Compartimentation et transfert de contaminants dans les milieux souterrains : interaction entre transport physique, réactivité chimique et activité biologique

Tristan Babey

ANNÉE 2016

THÈSE / UNIVERSITÉ DE RENNES 1
sous le sceau de l'Université Bretagne Loire

pour le grade de

DOCTEUR DE L'UNIVERSITÉ DE RENNES 1

Mention : Sciences de la Terre

Ecole doctorale Sciences de la Matière

présentée par

Tristan Babey

Préparée à l'unité de recherche Géosciences Rennes
(UMR CNRS 6118)
OSUR Observatoire des Sciences de l'Univers de Rennes

Compartimentation et transferts de contaminants dans les milieux souterrains : interaction entre transport physique, réactivité chimique et activité biologique.

Thèse soutenue à Rennes
le 8 décembre 2016

devant le jury composé de :

Philip BINNING
Professor, Technical University of Denmark / *rapporteur*

Fabrice GOLFIER
Maitre de conférences, Université de Lorraine / *rapporteur*

Hervé ANDRIEU
Directeur de recherche, IFSTTAR Nantes / *examinateur*

Naoise NUNAN
Chargé de recherches, AgroParisTech / *examinateur*

Luc AQUILINA
Professeur, Université de Rennes 1 / *examinateur*

Jean-Raynald DE DREUZY
Directeur de recherche, Université Rennes 1 / *directeur de thèse*

Résumé : Compartimentation et transfert de contaminants dans les milieux souterrains : interactions entre transport physique, réactivité chimique et activité biologique.

Classiquement le transfert des contaminants dans le milieu souterrain est modélisé par un couplage des processus de transport physiques (écoulements contrôlés par les structures géologiques poreuses) et des processus de dégradation ou d'immobilisation chimiques et biologiques. Tant sur les structures géologiques que sur la chimie et la physique, les modèles sont de plus en plus détaillés mais de plus en plus difficiles à calibrer sur des données toujours très parcellaires.

Dans cette thèse, nous développons une approche alternative basée sur des modèles parcimonieux sous la forme d'un simple graphe de compartiments interconnectés généralisant les modèles d'interaction de continuums (MINC) ou de transfert à taux multiples (MRMT). Nous montrons que ces modèles sont particulièrement adaptés aux milieux dans lesquels la diffusion de solutés occupe un rôle prépondérant par rapport à l'advection, tels les sols ou les aquifères très hétérogènes comme les aquifères fracturés. L'homogénéisation induite par la diffusion réduit les gradients de concentration, accélère les mélanges entre espèces et fait de la distribution des temps de résidence un excellent proxy de la réactivité. En effet, ces structures simplifiées reconstituées à partir d'informations de temps de résidence se révèlent également pertinentes pour des réactions chimiques non linéaires (e.g. sorption, précipitation/ dissolution). Nous montrons finalement comment ces modèles peuvent être adaptés automatiquement à des observations d'essais de traceurs ou de réactions de biodégradation.

Ces approches parcimonieuses présentent de nombreux avantages dont la simplicité de développement et de mise en œuvre. Elles permettent d'identifier les déterminants majeurs des échanges entre zones advectives et diffusives ou entre zones inertes et réactives, et d'extrapoler des processus de réactivité à des échelles plus larges. L'utilisation de données de fractionnement isotopique est proposée pour améliorer la dissociation entre l'effet des structures et de la réactivité.

Abstract : Compartmentalization and contaminant transfer in underground media : interaction between transport processes, chemical reactivity and biological activity

Modelling of contaminant transfer in the subsurface classically relies on a detailed representation of transport processes (groundwater flow controlled by geological structures) coupled to chemical and biological reactivity (immobilization, degradation). Calibration of such detailed models is however often limited by the small amount of available data on the subsurface structures and characteristics.

In this thesis, we develop an alternative approach of parsimonious models based on simple graphs of interconnected compartments, taken as generalized multiple interacting continua (MINC) and multiple rate mass transfer (MRMT). We show that this approach is well suited to systems where diffusion-like processes are dominant over advection, like for instance in soils or highly heterogeneous aquifers like fractured aquifers. Homogenization induced by diffusion reduces concentration gradients, speeds up mixing between chemical species and makes residence time distributions excellent proxies for reactivity. Indeed, simplified structures calibrated solely from transit time information prove to provide consistent estimations of non-linear reactivity (e.g. sorption and precipitation/dissolution). Finally, we show how these models can be applied to tracer observations and to biodegradation reactions.

Two important advantages of these parsimonious approaches are their facility of development and application. They help identifying the major controls of exchanges between advective and diffusive zones or between inert and reactive zones. They are also amenable to extrapolate reactive processes at larger scale. The use of isotopic fractionation data is proposed to help discriminating between structure-induced effects and reactivity.

Table des matières

Chapitre 1 : Introduction générale

Cette thèse s'inscrit dans le contexte du très fort sous-échantillonnage des transferts dans les milieux souterrains (Miller and Gray 2002, Dietrich et al. 2005, Refsgaard et al. 2010). Les milieux sont géologiquement complexes (Freeze and Cherry 1979, Clauser 1992), les transferts restent hétérogènes sur une large gamme d'échelles pouvant aller jusqu'à l'échelle kilométrique (Gelhar et al. 1992, de Marsily et al. 2005) et la densité de puits comme la couverture géophysique sont très faibles (Bear et al. 1993). Plusieurs approches ont été suivies allant des concepts de mélange entre pôles classiquement utilisés en géochimie (Hem 1985, Bethke and Johnson 2008) aux modèles de transferts physiques basés sur les lois fondamentales de la mécanique (Bear 1973, Anderson and Woessner 1990, Pinder and Celia 2006). De nombreux travaux ont cherché à adapter la complexité des modèles physiques à l'information disponible soit dans une approche parcimonieuse (McLaughlin and Townley 1996, de Marsily et al. 1999, Hill and Tiedeman 2006), soit automatiquement dans l'étude a posteriori de modèles à haute paramétrisation (Zimmerman et al. 1998, Doherty 2003). Une autre approche a consisté à adapter intuitivement l'échelle des modèles aux données disponibles comme dans le cas des modèles double poreux (Barenblatt et al. 1960, Warren and Root 1963) ou formellement avec des méthodes d'homogénéisation ou de renormalisation (Arbogast et al. 1990).

En dépit de leurs différences, ces approches sont systématiquement destinées à équilibrer la complexité des modèles à l'information disponible dans les données. Ici, nous nous inscrivons dans la dynamique d'établissement des modèles équivalents et parcimonieux, potentiellement adaptés à des milieux géologiquement complexes. Nous nous intéresserons particulièrement aux processus de transport de solutés pour lesquels la dispersion est essentiellement d'origine diffusive. Alors que les modèles parcimonieux ont été développés essentiellement pour le transport conservatif, nous étudierons leur pertinence pour du transport réactif.

1 Interface entre données parcellaires et modèles équivalents en hydrogéologie

La gestion de la ressource en eau requiert la capacité de comprendre et prédire le transfert de contaminants au sein des systèmes naturels. En hydrogéologie, cette capacité est confrontée à la forte hétérogénéité du milieu souterrain et des aquifères (de Marsily et al. 1999). Cette hétérogénéité est à la fois physique (variabilité des structures géologiques conditionnant les processus de transport) et chimique/biologique (e.g. présence ou absence de sites réactifs, de microorganismes dégradants) (Li et al. 2007, Englert et al. 2009). Il est généralement problématique d'en fournir une description précise et quantitative, soit à cause d'un manque d'information, soit à cause d'un manque d'intérêt pour l'ensemble des détails qui la composent. En effet, un observateur peut n'avoir accès ou n'être intéressé que par une donnée intégrant le fonctionnement de l'aquifère sur un certain volume, comme par exemple une concentration mesurée dans un puits (Freeze et al. 1990).

La méthodologie classique pour aborder cette question est celle du changement d'échelle (Dagan 1989, Hsieh 1998). Celle-ci cherche à extrapoler les lois et comportements connus à une certaine échelle à une échelle plus large, plus proche de l'échelle d'observation ou d'intérêt (Sposito 2008). Deux traitements différents de l'hétérogénéité peuvent être identifiés : l'approche multi-échelle et l'approche milieu équivalent (Battiato et al. 2011, Roubinet and Tartakovsky 2013). Dans l'approche multi-échelle, le comportement large échelle du système est donné sous la forme d'une gamme de comportements possibles, obtenue en faisant varier les paramètres de modèles simulant le transport et la réactivité des contaminants à haute résolution (Noetinger and Zargar 2004). Dans l'approche milieu effectif, l'effet de l'hétérogénéité petite échelle est incorporé dans un modèle équivalent déterministe, parcimonieux, pouvant être analytique. Chacune des deux approches présente des avantages et des inconvénients (Renard and de Marsily 1997, Hunt and Ewing 2009). Si l'approche multi-échelle est la plus exhaustive, elle est coûteuse en termes de puissance de calcul, et un faible nombre de données expérimentales peut la confronter à des problèmes d'équifinalité et de sur-paramétrisation (Hill and Tiedeman 2006, Tonkin et al. 2007). Un modèle équivalent est parcimonieux, facile à implémenter et à calibrer mais n'est valide que dans une gamme de conditions au final restrictive. Des modèles comme les modèles double poreux existent depuis déjà une cinquantaine d'années et donnent un certain recul sur ces approches équivalentes.

Malgré la complexité du milieu souterrain, des modèles équivalents, déterministes, possédant un faible nombre de paramètres calibrables sur des données de terrain, ont montré leur utilité pour certaines applications. C'est le cas des modèles double poreux (Barenblatt et al. 1960, Warren and Root 1963) discuté plus en détail dans la section 1.3. Ces modèles reposent sur une conceptualisation du milieu souterrain opposant une porosité primaire, bien connectée et perméable, "mobile" (niveaux sableux, fractures...), à une porosité secondaire, mal connectée et peu perméable, "immobile" (niveaux argileux, matrice rocheuse cristalline...) (*Figure 1.1*). Ces porosités sont caractérisées par un ou deux paramètres (volume poreux total, perméabilité) et reliées l'une à l'autre par un coefficient d'échange.

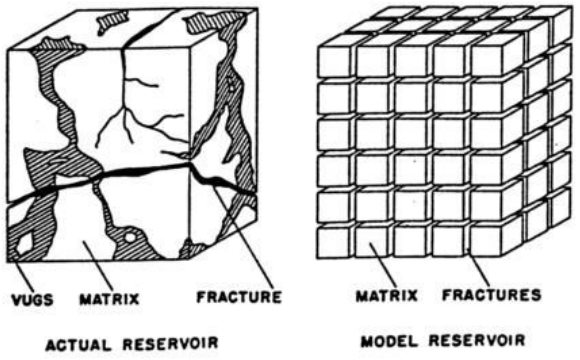

Figure 1.1: Représentation d'un milieu poreux hétérogène à gauche et son idéalisation sous la forme d'un modèle double poreux à droite (Warren and Root 1963).

Les modèles de mélange multi-pôles en hydrogéochimie constituent un autre exemple de modèles parcimonieux (Hem 1985, Bethke and Johnson 2008). Dans ces approches, la composition physico-chimique des eaux souterraines est interprétée comme résultant d'un mélange entre un nombre limité de pôles distincts (e.g. eau fraîche et intrusion saline). Ces pôles correspondent aux extrêmes des diagrammes de composition entre lesquels s'inscrivent l'ensemble des compositions mesurées dans un système (*Figure 1.2*). Un bilan de masse permet d'évaluer la contribution de chacun des pôles à la composition des zones de mélange. Les paramètres du modèle sont alors la composition chimique des différents pôles et la pondération de leur contribution. On pourra noter que cette approche partage une inspiration commune avec les modèles à l'échelle plus large du bassin versant de partitionnement des hydrographes entre différents pôles de compositions chimiques et biologiques distinctes (e.g. Johnson et al. 1969, Evans and Davies 1998, Burns et al. 2001).

Ces modèles parcimonieux s'obtiennent par une compréhension soit intuitive, soit formelle du fonctionnement d'un système dans son ensemble (Arbogast et al. 1996). Il n'est donc pas

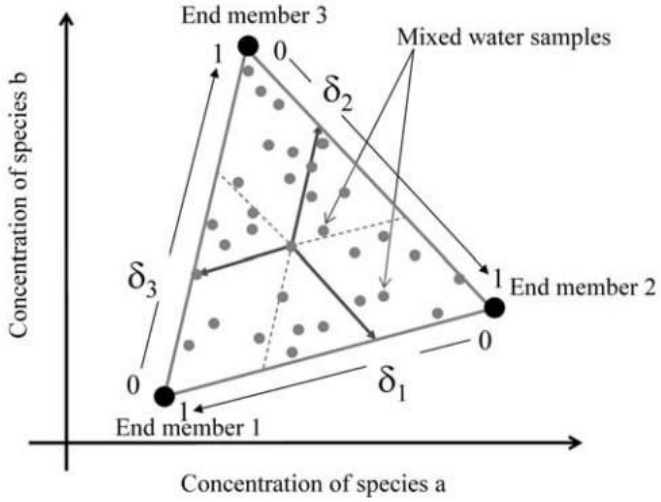

Figure 1.2: Définition des ratios de mélange dans un problème à trois pôles chimiques et deux concentrations (Carrera et al. 2004).

surprenant que l'usage des modèles parcimonieux devienne plus courant à mesure que l'échelle d'observation s'éloigne de celle des équations fondamentales (Quintard and Whitaker 1993, Hornung 1997). C'est le cas notamment pour le transport réactif (Wood et al. 2004, Golfier et al. 2009, Orgogozo et al. 2013). En effet, la réactivité prend place à l'échelle du pore, ou à l'échelle plus fine encore de l'interface lorsqu'il s'agit d'une réaction hétérogène entre phases. Le transport, quant à lui, est généralement décrit à une échelle bien supérieure comme celle de Darcy avec un concept de dispersion équivalente (Bear 1973, Zheng and Bennett 2002). De nombreux travaux, au travers d'approches théoriques et expérimentales, questionnent ainsi l'effet des structures géologiques ou de la dynamique du transport sur la réactivité et son intégration dans des modèles plus large échelle.

2 Structures de porosité diffusive

Dans cette partie, nous introduisons la notion de porosité (ou de structure) diffusive dans les milieux souterrains sur laquelle se concentre cette thèse. Nous présentons les contextes hydrogéologiques auxquels cette porosité correspond ainsi que son influence sur le transport conservatif et réactif de contaminants.

Classiquement en hydrogéologie, une distinction est faite entre la porosité totale d'un milieu et la porosité cinématique, ou effective, qui en représente une fraction plus ou moins importante et au sein de laquelle les écoulements prennent place (Fetter 2008) (*Figure 1.3*). La différence entre la porosité totale et la porosité cinématique donne la porosité non-circulante, qui elle

même peut être divisée entre la porosité non-connectée (enclavée) et la porosité de "bras morts", connectée mais accessible principalement par diffusion moléculaire. Cette dernière est ainsi appelée porosité diffusive, ou stagnante, ou immobile, par opposition à la porosité cinématique, ou advective, ou mobile.

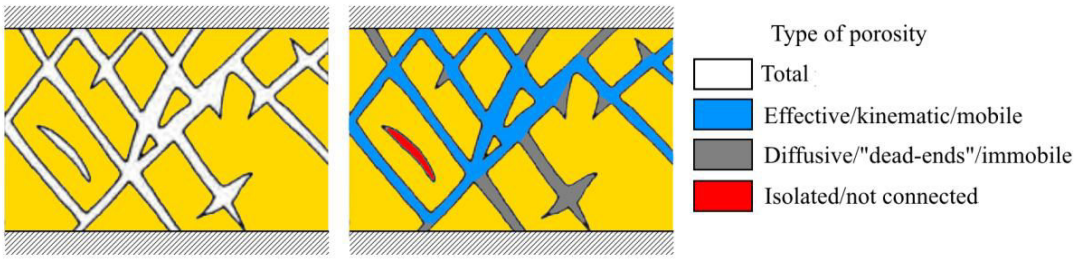

Figure 1.3: Types de porosité d'un réseau de fractures idéalisé d'après Freeze and Cherry (1979).

L'existence d'une porosité diffusive non-négligeable a été mise en évidence dans des contextes géologiques et à des échelles variés. Ainsi, la diffusion est le processus de transport principal au sein d'unités géologiques très peu perméables comme les argiles, ce qui fait de ceux-ci, entre autres, de bons candidats pour le confinement des sites de stockage géologique des déchets nucléaires (Johnson et al. 1989) (échelle du puits). Incidemment, des lithologies peu perméables incluses dans ou juxtaposées à des lithologies plus perméables tendront à se comporter comme une porosité immobile (e.g. niveaux de sables, de graviers et d'argiles au sein d'un même aquifère (Harvey and Gorelick 2000), inclusions d'argiles ou de sables fins dans des sables grossiers (Murphy et al. 1997, Levy and Berkowitz 2003, Knorr et al. 2016)) (*Figure 1.4*).

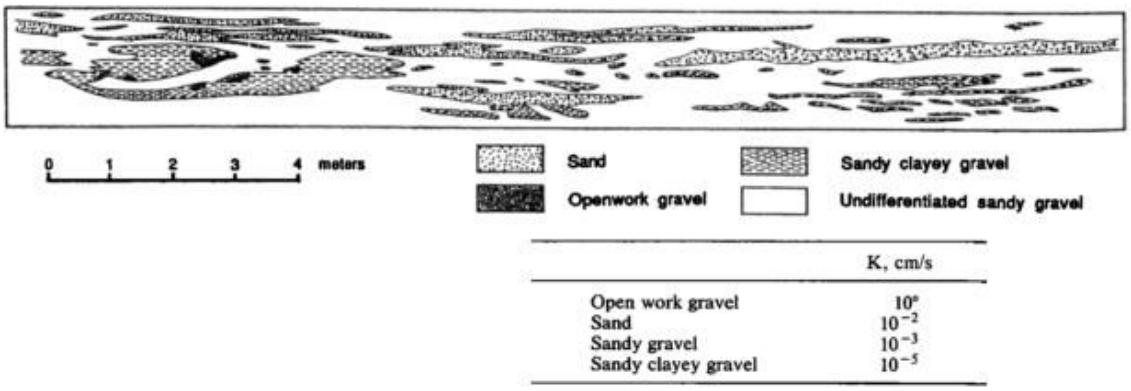

Figure 1.4: Coupe géologique représentant les différents faciès lithologiques constituant l'aquifère hétérogène du site expérimental MADE, d'après Rehfeldt et al. (1992).

Dans les milieux partiellement saturés comme les sols, l'importance de la diffusion comme moteur du transport augmente avec la diminution de la saturation en eau (Nye 1980, de Gennes 1983, Hu and Wang 2003, Conca and Wright 2012). A l'échelle du pore, la diffusion contrôle également l'accès à la porosité intra-particulaire (Rao et al. 1980, Wu and Gschwend 1986, Wood et al. 1990, Scheibe et al. 2013) ainsi qu'aux "bras morts" du réseau de porosité (Altman et al. 2004, Gouze et al. 2008) peu perméables et/ou hydrauliquement mal connectés (*Figure 1.5*).

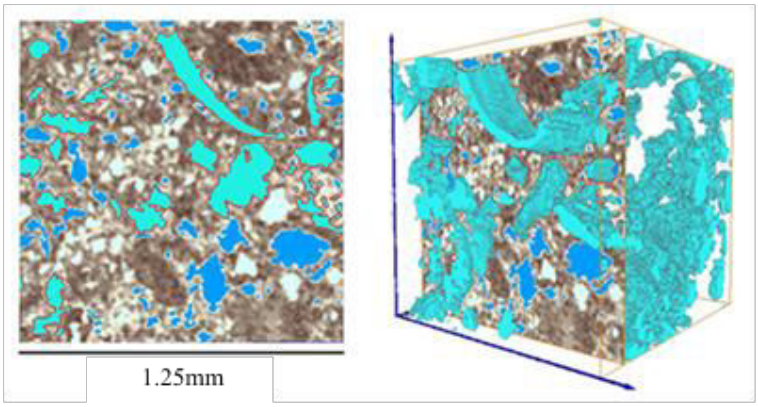

Figure 1.5: Section à gauche représentation 3D à droite d'une matrice calcaire poreuse obtenue par micro-tomographie (Gouze et al. 2008). La fraction mobile de la macroporosité est représentée en cyan, la fraction immobile en bleu, et la microporosité en niveaux de gris (sombre et clair pour une porosité faible et forte respectivement). Les différents types de porosité sont distingués par traitement numérique.

Enfin, les échanges entre porosités mobile et immobile sont caractéristiques des systèmes fractures-matrice. Dans ces systèmes, un petit nombre de fractures concentre le flux, mais les solutés peuvent être échangés par diffusion avec une porosité immobile étendue constituée de la matrice rocheuse peu perméable et des bras morts du réseau de fractures (échelle du puits, *Figure 1.6*) (Grisak and Pickens 1980, Neretnieks 1980, McKenna et al. 2001, Shapiro 2001, Andersson et al. 2004). Cette porosité immobile peut représenter une part variable de la porosité totale du milieu, depuis quelques pourcents pour la porosité intra-granulaire (Wood et al. 1990, Hay et al. 2011) à plusieurs dizaines de pourcents pour des milieux présentant des contrastes de perméabilité forts entre par exemple des niveaux de graviers, de sables et d'argiles (Harvey and Gorelick 2000).

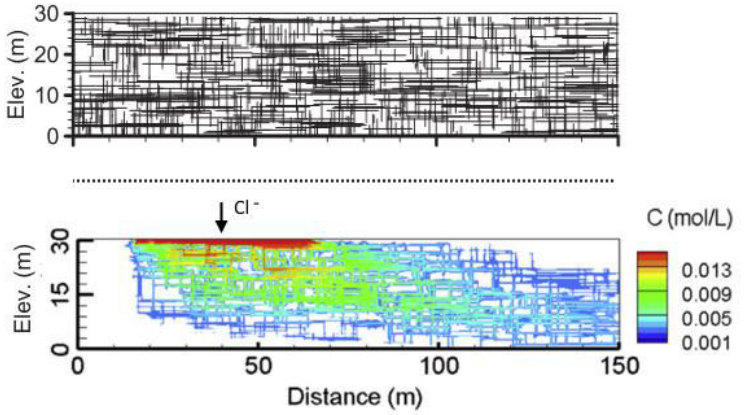

Figure 1.6: Réseau de fractures aléatoire généré au sein d'un matrice poreuse, en haut, et profil simulé de concentration en Cl⁻, en bas, d'après Molson et al. (2012). Ce profil est obtenu au terme d'une injection de Cl⁻ continue pendant huit ans sur une partie de la face supérieure du domaine. L'exutoire du système est la face droite du domaine. Cl⁻ est transporté par advection au sein des fractures, et par diffusion dans les bras morts du réseau de fractures ainsi que dans la matrice rocheuse environnante.

L'importance des structures diffusives pour le transport vient de leur rôle de piège hydrodynamique capable de retenir un soluté sur de longues périodes de temps, augmentant sa persistance dans le milieu (e.g. Grisak et al. 1980, Jardine et al. 1999, Harvey and Gorelick 2000, Meigs and Beauheim 2001, Wu et al. 2006a, Wu et al. 2006b) (*Figure 1.7*).

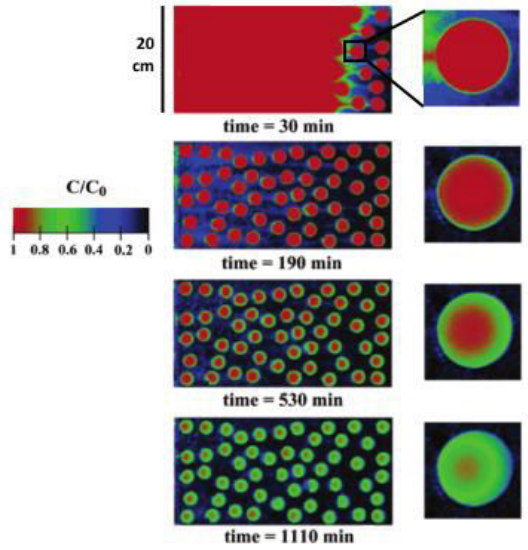

Figure 1.7: Série temporelle de profils de concentration d'un traceur conservation, mesurée dans un milieu poreux artificiel constitué de billes de verre, d'après Zinn et al. (2004). Les zones cylindriques sont constituées de billes de petit diamètre et présentent une perméabilité trois ordres de grandeur plus faible que la zone environnante constituée de billes de diamètre plus large. Le domaine est initialement occupé par une concentration uniforme de traceur C_0. A partir de t=0, une eau sans traceur est injectée continuellement sur la face droite du domaine, l'exutoire étant la face gauche. Le profil de concentration au sein des cylindres de faible perméabilité montre un transport dominé par la diffusion (zones immobiles), qui s'oppose à la porosité advective/mobile à l'extérieur des cylindres.

Le rôle de la diffusion dans une porosité immobile est par exemple au cœur de la stratégie de remédiation développée par Wu *et al.* (Wu et al. 2006a, Wu et al. 2006b) pour l'aquifère du site expérimental FRC. Sur ce site, le gradient hydraulique imposé entre un puits d'injection et un puits de pompage mobilise principalement une zone d'écoulement préférentielle dont les eaux résidentes sont remplacées à l'échelle de quelques heures (*Figure 1.8, haut*). Après l'arrêt des pompes, les concentrations mesurées dans l'aquifère retournent graduellement, après

plusieurs mois, à leur valeur d'origine du fait de la diffusion depuis la porosité stagnante environnante (*Figure 1.8, bas*). Ce lent phénomène de diffusion motivera une stratégie de remédiation s'étalant sur plus d'un an.

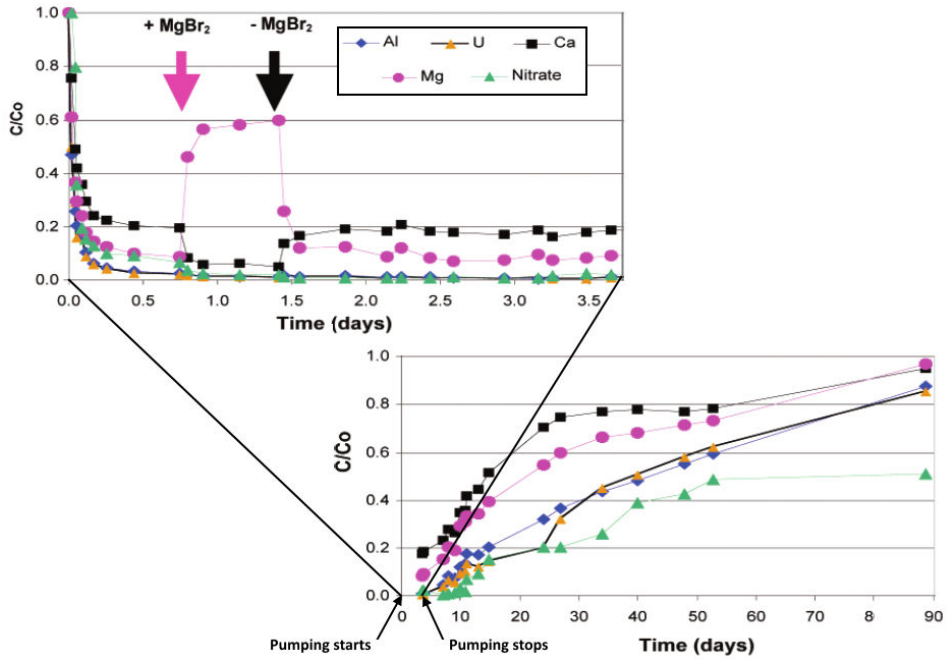

Figure 1.8: Concentrations mesurées dans l'aquifère du site expérimental FRC pendant et après la mise en place d'un gradient hydraulique imposé entre un puits d'injection et un puits de pompage, d'après Wu et al. (2006a). Les concentrations sont mesurées entre les deux puits environ 2m en aval du puits d'injection, et sont normalisées par leurs valeurs initiales dans l'aquifère. Les flèches marquées + $MgBr_2$ et - $MgBr_2$ correspondent respectivement au début à la fin d'une injection de $MgBr_2$ (traceur conservatif) dans le puits d'injection. Ces courbes mettent en évidence le retour graduel des concentrations des solutés mesurées dans le puits à leurs valeurs précédant le pompage, dû à la diffusion des solutés depuis le sol environnant.

Du point de vue des courbes de restitution des essais de traçage, la présence d'un porosité immobile non-négligeable se traduit par un transport dit anormal (ou non Fickien) sur une gamme assez large d'échelles, présentant des panaches de concentration non-gaussiens, une augmentation de la dispersion et du mélange, ainsi que l'apparition de temps de transit élevés (Dentz et al. 2004, Berkowitz et al. 2006) (*Figure 1.*9).

La diffusion dans la porosité immobile peut également conditionner l'accès à des sites réactifs provoquant l'immobilisation ou la dégradation des solutés. Un tel couplage a été étudié pour les phénomènes de sorption au sein de la porosité intra-particulaire (Ball and Roberts 1991, Hay et al. 2011) et de la matrice dans les milieux fracturés (Neretnieks 1980), ces deux porosités pouvant abriter une fraction significative des sites de sorption. Similairement, l'accès aux minéraux réactifs présents dans la matrice d'un milieu fracturé influence

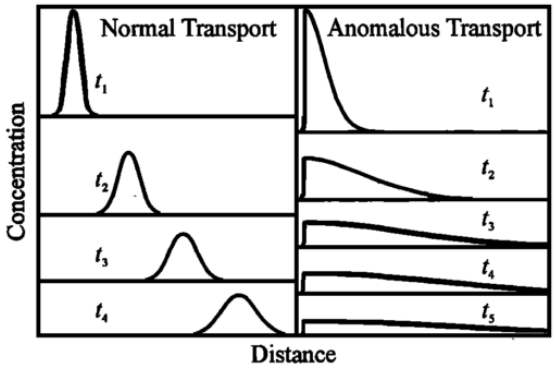

Figure 1.9: Illustration schématique du contraste entre transport gaussien (ou Fickien) et transport anormal pour l'avancée de la gauche vers la droite d'un panache de soluté (Berkowitz et al. 2000).

l'atténuation de fluides miniers acides à l'échelle du puits (Molson et al. 2012). La présence conjointe d'une porosité advective, aux temps de résidence courts, et d'une porosité diffusive, aux temps de résidence longs, entraîne également l'apparition de gradients de concentration pouvant aider voir conditionner la réactivité. C'est le cas par exemple pour une activité bactérienne nécessitant l'accès à deux substrats (échelle du pore (Briggs et al. 2015, Sawyer 2015), échelle du mètre (Murphy et al. 1997)) ainsi que pour les phénomènes de cémentation dus à la migration d'un panache hyperalcalin au sein de marnes (échelle du puits (Steefel and Lichtner 1994)). Enfin, lorsque la saturation en eau des sols diminue et devient défavorable au mouvement des microorganismes, la diffusion des nutriments au travers de l'eau résiduelle contrôle fortement l'activité bactérienne à l'échelle du pore (Or et al. 2007, Vogel et al. 2015). C'est également le cas à l'échelle du puits où la présence de zones peu perméables peut restreindre l'accès des microorganismes y résidant aux nutriments circulant dans la zone mobile (Scholl 2000). Les zones immobiles jouent ainsi un rôle important dans des problématiques de transport conservatif et réactif variées.

3 Modélisation de l'influence des zones diffusives sur le transport

3.1 Modèle double poreux

Dans cette partie, nous présentons les approches de modélisation classiques de l'influence des zones immobiles. Les premiers modèles équivalents cherchant à rendre compte de cette influence sont les modèles double poreux (Barenblatt et al. 1960, Warren and Root 1963, Coats and Smith 1964). Ces modèles sont proposés comme une amélioration des modèles poreux homogènes classiques à deux paramètres pour les flux (porosité effective et perméabilité) (Barenblatt et al. 1960, Warren and Root 1963) et le transport (vitesse

d'écoulement et coefficient de dispersion) (Coats and Smith 1964) appliqués aux milieux très hétérogènes. Dans le cas du flux, il s'agit de modéliser la propagation rapide des variations de pression le long des zones mobiles, suivie de la réponse plus lente des zones immobiles. Dans le cas du transport, il s'agit de modéliser le transfert rapide de solutés le long des zones mobiles et leur rétention dans les zones immobiles.

Pour le transport, les modèles double poreux rendent compte de déviations au modèle homogène (ou advection-dispersion, ou macro-dispersion (Bear et al. 1993)) observées sur les courbes de restitutions d'essais de traçage à l'échelle du mètre ou de la dizaine de mètres. Ces déviations consistent d'une part en des temps de première arrivée très courts pour des volumes de traceur injectés faibles par rapport à la porosité totale du milieu, dus à la chenalisation des écoulements dans un sous-ensemble de la porosité (i.e. mauvaise estimation de la porosité cinématique et des flux). Elles consistent d'autre part en des queues de restitution du traceur lourdes et une augmentation de la dispersion (*Figure 1.10*), dues à la diffusion du traceur dans

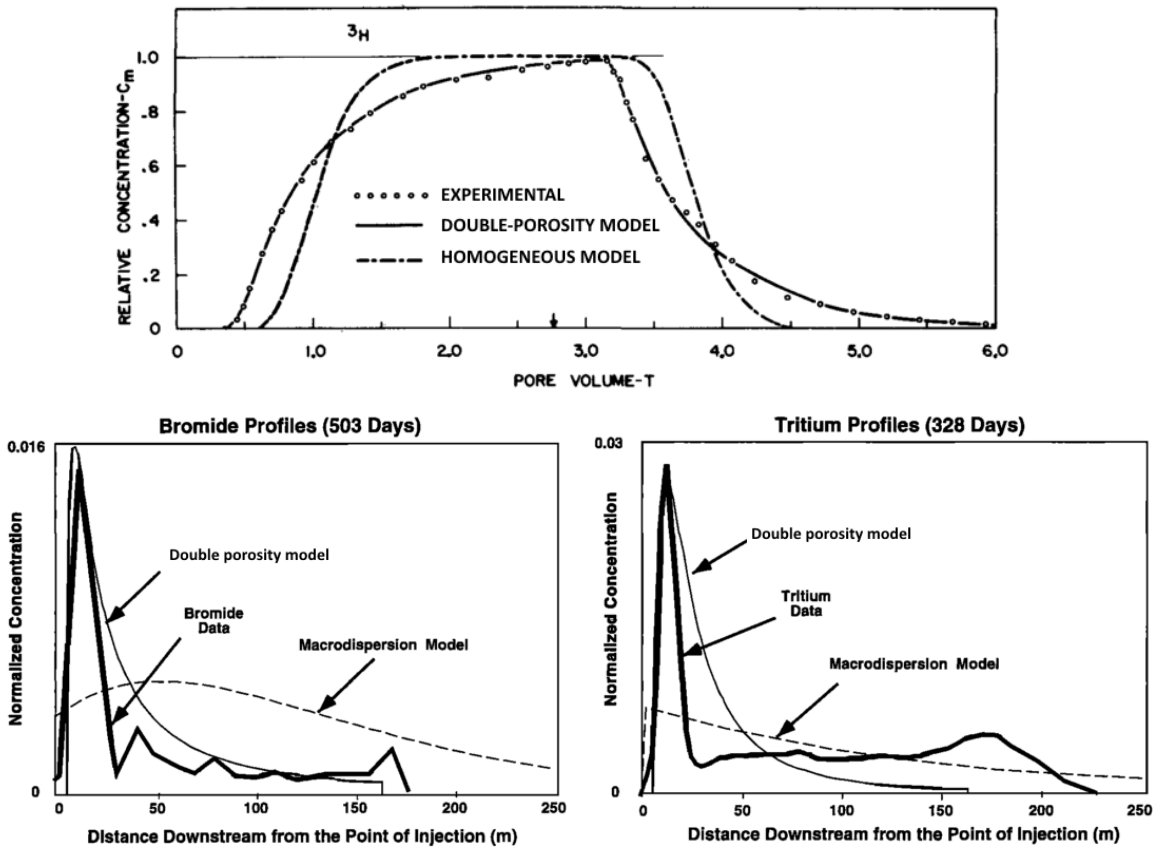

Figure 1.10: Haut: Concentrations effluentes en tritium (traceur) observées et simulées pour un essai de traçage dans une colonne de sol limono-argileux non saturé de 30 cm de long, d'après van Genuchten and Wierenga (1977). Bas: Profils de concentration longitudinaux de deux traceurs (bromure et tritium) mesurés et modélisés sur le site expérimental de MADE, d'après Harvey and Gorelick (2000).

les zones immobiles. Cette dernière déviation à une description fickienne du transport est caractéristique d'un transport qualifié classiquement d'anormal par les physiciens (Bouchaud and Georges 1990).

Le modèle double poreux proposé par Warren and Root (1963) pour les écoulements puis par Coats and Smith (1964) pour le transport repose sur une conceptualisation du milieu souterrain opposant une porosité bien connectée et perméable, "mobile", à une porosité mal connectée et peu perméable, "immobile". Pour le transport, le modèle proposé par Coats and Smith (1964) s'écrit :

$$(1-f)\frac{\partial c_m}{\partial t} + f\frac{\partial c_{im}}{\partial t} = -v\frac{\partial c_m}{\partial x} + D\frac{\partial^2 c_m}{\partial x^2} \qquad (1.1)$$

$$f\frac{\partial c_{im}}{\partial t} = k(c_m - c_{im}) \qquad (1.2)$$

où $c_m(x,t)$ et $c_{im}(x,t)$ sont les concentrations dans la zone mobile et immobile respectivement. v et D sont respectivement la vitesse d'écoulement et le coefficient de dispersion dans la zone mobile, et sont les paramètres classiques du modèle d'advection-dispersion homogène (Bear 1973). Dans leur synthèse (essais de traçage à échelle de 10^{-1} à 10^5 m), Gelhar et al. (1992) donnent une gamme de variabilité de v comprise entre 10^{-3} et 10^2 m/d, et de la dispersivité α avec $D = \alpha v$ comprise entre 10^{-2} et 10^4 m. f est la fraction de la porosité totale correspondant à la porosité immobile. k est le taux d'échange entre les zones mobile et immobile, justifiant l'autre dénomination de "modèle à taux unique" (single-rate model) de ce modèle. Haggerty et al. (2004) donnent une gamme de variabilité pour $f/(1-f)$ (ratio de la porosité immobile sur mobile) comprise entre 10^{-2} et 10^3, et pour le temps caractéristique d'échange $1/k$ des valeurs possibles comprises entre 10^{-2} et 10^5 h.

3.2 Modèles de transport anormal imitatifs

Ce concept de modèle double poreux "à taux unique" va par la suite être étendu à d'autres problématiques et inclus dans des modèles plus généralistes de transport anormal (Frippiat and Holeyman 2008). Ces modèles sont d'abord imitatifs, locaux, et reproduisent dans une certaine mesure les structures hydrogéologiques et les distributions de concentrations réelles. C'est le cas du modèle double perméabilité représentant des échanges diffusifs entre deux porosités advectives, l'une rapide et l'autre lente ("mobile"-"moins mobile") (Magnico et al. 1993). C'est aussi le cas du modèle triple porosité, où deux porosités mobiles échangent au

travers d'une porosité immobile ("mobile"-"immobile"-"moins mobile") (Wu et al. 2004) (*Figure 1.11*).

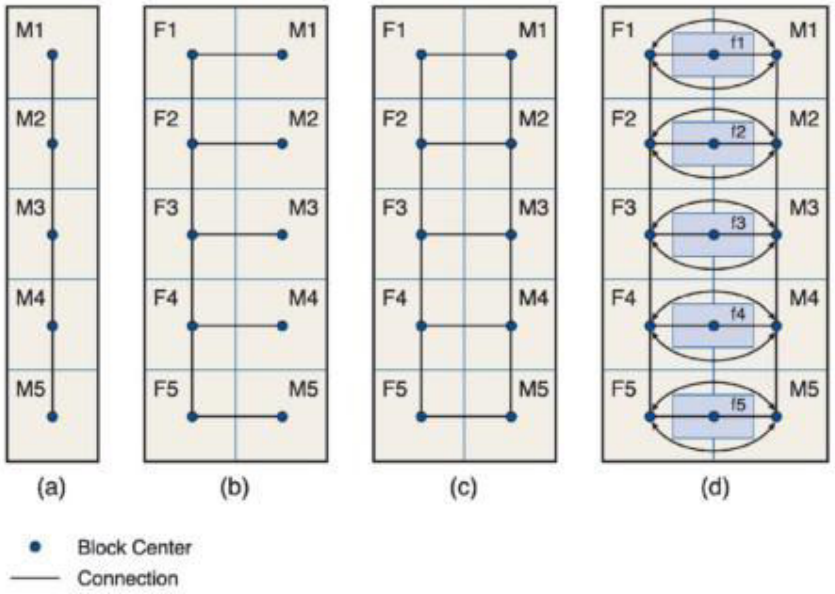

Figure 1.11: Représentation schématique de différents modèles de transport applicables à un système fracture-matrice (Wu et al. 2004): (a) modèle d'advection-dispersion homogène (Bear 1973) ; (b) modèle double poreux (Coats and Smith 1964) ; (c) modèle double perméabilité (Magnico et al. 1993) ; (d) modèle triple continua (Wu et al. 2004).

D'autres modèles proposent une représentation continue (Tang et al. 1981, Sudicky and Frind 1982, Maloszewski and Zuber 1985) ou discrète (modèle MINC, Multiple INteracting Continua) (Pruess and Narasimhan 1985, Karimi-Fard et al. 2006) de la diffusion transversale dans la matrice pour rendre compte d'effets transitoires dans la matrice comme le développement de gradients de pression ou de concentration. Enfin, Haggerty et Gorelick (1995) puis Carrera et al. (1998) généralisent le concept de porosité mobile en interaction avec une porosité immobile à celui d'échanges entre la porosité mobile et de multiples porosités immobiles (modèle MRMT, Multiple Rates Mass Transfer). Haggerty et Gorelick (1995) défendent l'idée que des structures géologiques diffusives de dimensions et de nature variées peuvent coexister au sein d'un même aquifère (*Figure 1.12*).

La coexistence de ces différentes zones immobile se traduit par une distribution de taux d'échange impactant les courbes de restitution d'un essai de traçage (*Figure 1.13*). Le modèle MRMT s'écrit ainsi pour un nombre fini N de zones immobiles (Haggerty and Gorelick 1995):

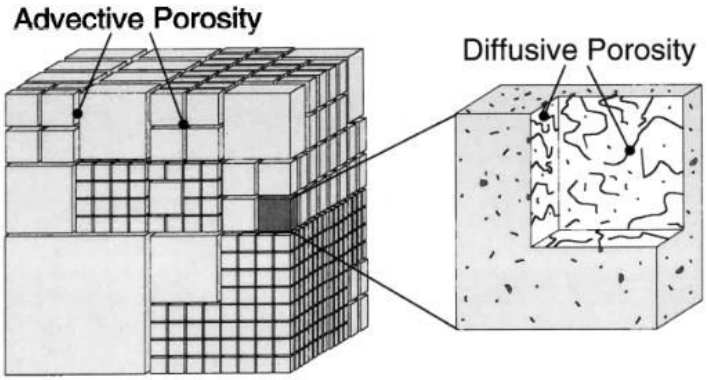

Figure 1.12: Haut : Modèle conceptuel du modèle à taux d'échanges multiples MRMT (Haggerty et al. 2001). Bien que les zones diffusives soient représentées par des cubes, elles peuvent avoir n'importe quelle forme. Le volume de roche représenté est plus petit que le volume élémentaire représentatif (Bear et al. 1993). L'aspect fractal de la distribution des volumes immobiles est à rapporter à la forme fractale de la porosité des lithologies peu perméables proches du seuil de percolation (Haggerty 2001).

$$(1-f)\frac{\partial c_m}{\partial t} + \sum_{j=1}^{N} \beta_j \frac{\partial c_{im,j}}{\partial t} = -v\frac{\partial c_m}{\partial x} + d_m \frac{\partial^2 c_m}{\partial x^2} \qquad (1.3)$$

$$\beta_j \frac{\partial c_{im,j}}{\partial t} = \alpha_j \left(c_m - c_{im,j}\right) \qquad (1.4)$$

où $c_{im,j}$ est la concentration dans la zone immobile j=1...N correspondant à la fraction de la porosité totale β_j avec $\sum_{j=1}^{N} \beta_j = f$ (*Eq. (1.1)-(1.2)*). α_j est le taux d'échange entre la zone immobile j et la zone mobile, et exprime la capacité à échanger de ces deux zones. On notera que dans ce modèle, toutes les zones immobiles échangent directement et exclusivement avec la zone mobile.

3.3 Modèles de transport anormal non-imitatifs (non locaux)

Les exemples précédents font ressortir la difficulté à modéliser l'influence de zones immobiles d'échelle et de structure variées, qui se traduisent par des conceptualisations différentes du milieu. Des modèles alternatifs, plus généralistes, ont ainsi été proposés qui s'affranchissent de la représentation de l'ensemble de la distribution des concentrations pour se concentrer sur la reproduction d'une donnée d'intérêt, comme les courbes de restitution des essais de traçage. Parce qu'ils n'évaluent pas les concentrations en tout point du temps et de l'espace, ces modèles sont qualifiés de non-locaux, par opposition aux modèles locaux ou imitatifs présentés dans la section précédente. Grâce à cette ambigüité, les modèles non-locaux peuvent

généraliser dans un même cadre formel différentes conceptualisations des processus menant à du transport anormal (Neuman and Tartakovsky 2009).

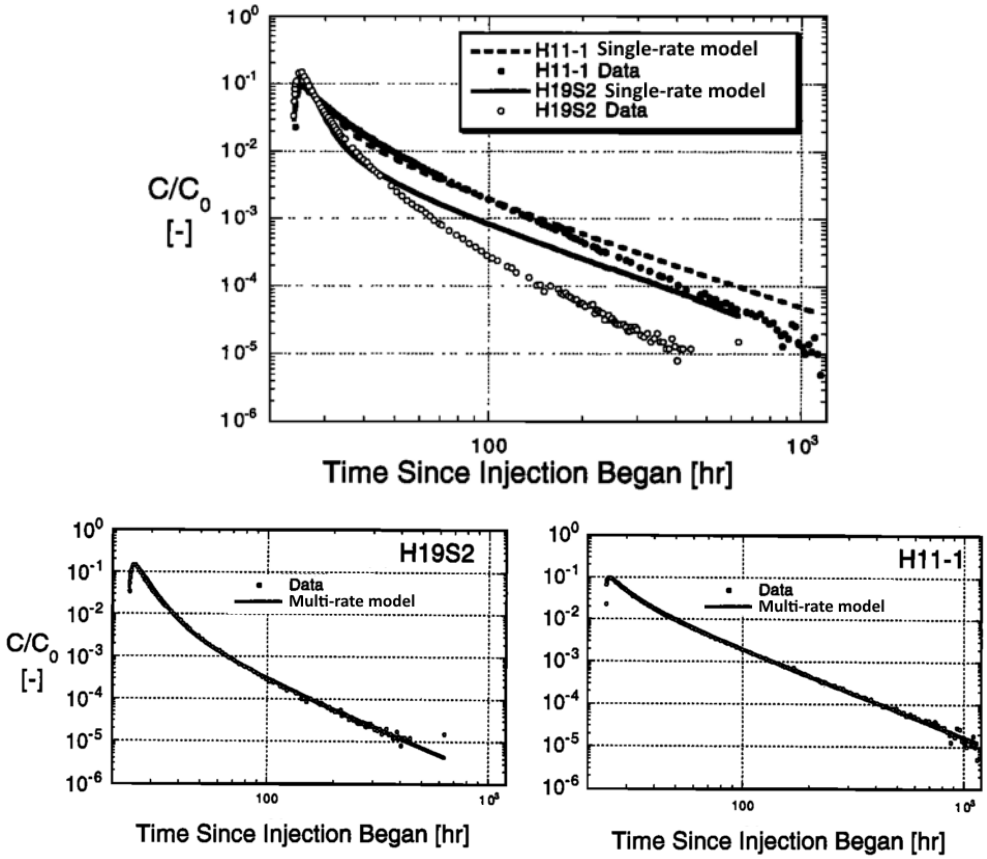

Figure 1.13: Haut : Courbes de restitution de deux essais de traçage, H11-1 et H19S2, sur le site expérimental SWIW et modèles à taux unique calibrés correspondants. Bas : Même courbes de restitution expérimentales, mais calibration avec un modèle à taux multiples MRMT (d'après Haggerty et al. (2001)).

L'intérêt des modèles MRMT est ainsi renforcé par la démonstration d'Haggerty et Gorelick (1995) et Carrera et al. (1998) de l'équivalence entre les modèles fracture-matrice de type MINC et les modèles MRMT pour la production de courbes de restitution. Ainsi, les modèles MRMT sont d'une part capables de représenter des milieux réellement "à taux d'échange multiples", où des zones immobiles de dimension et nature variées interagissent principalement avec la zone mobile (fonctionnement en "mode local"). Mais les modèles MRMT sont d'autre part capables de simuler l'empreinte sur les courbes de restitution d'effets transitoires au sein d'un domaine immobile de type MINC, comme le développement d'un gradient de concentration (fonctionnement en "mode non-local").

Cet aspect généraliste fait des modèles non-locaux un outil privilégié pour l'évaluation du transport. D'autres modèles non locaux que MRMT ont été proposés, liés à MRMT et entre eux par des relations d'équivalence pour certaines conditions (Neuman and Tartakovsky 2009). C'est le cas par exemple de Continuous Time Random Walk (CTRW) (Berkowitz and Scher 1998, Berkowitz et al. 2006) qui modélise la dispersion de soluté par des mouvements aléatoires de particules. C'est aussi le cas de Fractional Advection-Dispersion Equation (fADE) (Benson et al. 2000) qui fait appel à des dérivées spatiales fractionnées. Ces modèles de transport anormal seront appliqués avec succès à des problématiques de transport conservatif en milieu hétérogène sur le terrain et en laboratoire (e.g. Berkowitz and Scher 1998, Berkowitz et al. 2000, Benson et al. 2001, Haggerty et al. 2001, McKenna et al. 2001, Haggerty et al. 2004, Le Borgne and Gouze 2008).

4 Modèles de transport parcimonieux : du transport conservatif au transport réactif

Comme nous l'avons vu précédemment, des modèles équivalents tels que MRMT, parcimonieux et calibrables sur des données de terrain, fournissent de bonnes évaluations du transport conservatif. Cette efficacité rend fort l'intérêt d'étendre leur utilisation au transport réactif (Donado et al. 2009, de Dreuzy and Carrera 2015, Soler-Sagarra et al. 2016). Cependant, si ces modèles équivalents font sens pour le transport, le font-ils pour la réactivité ? La simplification du transport inhérente à leur formulation permet-elle encore de prendre en compte une chimie/biologie cohérentes ? Intuitivement, la structure de la porosité, dont une partie est perdue par ces modèles, contrôle la distribution des concentrations, les processus de mélange, et par conséquent la réactivité. A l'exception de réactions linéaires, auquel cas les opérateurs de transport et de réaction commutent (Haggerty and Gorelick 1995, Margolin et al. 2003), les modèles équivalents donneront une évaluation faussée des taux de réaction. Cependant, cette estimation pourrait se révéler malgré tout suffisamment proche des taux de réaction réels pour être exploitable. D'une part, l'obligation de reproduction des courbes de restitution en transport conservatif pose une contrainte forte sur les modèles équivalents. D'autre part, pour le cas d'une dispersion d'origine essentiellement diffusive auquel nous nous intéressons dans cette thèse, la diffusion réduit les gradients de concentration, homogénéise la répartition des solutés et réduit l'impact de la structure du milieu (Villermaux 1987, Haggerty and Gorelick 1995, Crank 2002).

La possibilité d'utiliser un modèle équivalent comme MRMT pour estimer du transport réactif non-linéaire a été évaluée dans quelques études (e.g. Willmann et al. 2010) mais reste encore incertaine. La première partie de la thèse (Chapitre 2) est ainsi consacrée à la comparaison du transport réactif entre un modèle de référence, le modèle MINC, et son modèle équivalent, le modèle MRMT, pour lesquels la relation d'équivalence en transport conservatif a été établie par Haggerty and Gorelick (1995). Dans le chapitre suivant (Chapitre 3), nous étendons cette relation d'équivalence à l'ensemble des organisations possibles des zones immobiles entre elles et avec la zone mobile (au-delà des trois types d'organisations étudiées par Haggerty and Gorelick (1995)). Nous renforçons ainsi l'intérêt du modèle MRMT comme modèle généraliste pour le transport conservatif. Cette relation d'équivalence est mise à profit dans le Chapitre 4 pour évaluer la capacité des modèles MRMT à reproduire des réactions de dissolution et de sorption non-linéaires dans des structures immobiles complexes. Finalement, le Chapitre 5 est consacré à la calibration d'un modèle couplant transport diffusif et réactivité biochimique sur des expériences de laboratoire traitant de la dégradation d'un pesticide dans le sol. Cette dernière partie met notamment en évidence l'impact des conditions initiales dans ces modèles de diffusion simplifiés et souligne leur nécessaire extension à d'autres processus, comme l'advection.

Chapitre 2 : Capacité d'un modèle de transport équivalent (MRMT) à évaluer une réactivité bimoléculaire à l'équilibre dans des inclusions planaires, cylindriques et sphériques (MINC)

1 Introduction

Une notion récurrente dans la suite de cette thèse est celle de modèle ou structure de référence, et celle de modèle équivalent. Nous nous concentrons sur l'influence de la diffusion dans des zones stagnantes/immobiles sur le transport et la réactivité de solutés. Par conséquent, "structure" réfère à l'organisation potentiellement complexe des zones stagnantes/immobiles entre elles et par rapport à une zone advective/mobile, qui par opposition présente une organisation simple et invariante (équation d'advection-dispersion 1D à vitesse d'écoulement et coefficient de dispersion constants et homogènes). Ainsi, le "modèle de référence" correspond à l'organisation "réelle" des zones immobiles, imitant les structures géologiques, et généralement considéré difficile à caractériser à partir de données expérimentales. Le "modèle équivalent" quant à lui est une approximation de ce modèle de référence, calibrable à partir d'une donnée de temps de transit comme la courbe de restitution d'un essai de traçage. La relation d'équivalence entre structures de référence et modèles simplifiés est l'identité des concentrations dans la zone mobile pour un traceur conservatif définie par Haggerty and Gorelick (1995), menant à l'identité des courbes de restitution.

Dans leur présentation du modèle MRMT (Multiple Rate Mass Transfer), Haggerty and Gorelick (1995) démontrent que ce modèle est formellement équivalent à des modèles de diffusion dans des inclusions immobiles planaires, cylindriques et sphériques par un choix approprié des coefficients d'échange et du volume des zones immobiles. Lorsque ces inclusions sont discrétisées, les modèles correspondants sont les modèles MINC (Multiple INteracting Continua) en 1D, 2D et 3D respectivement (Pruess and Narasimhan 1985, Pruess 1992, Karimi-Fard et al. 2003). Un modèle de référence MINC et son modèle équivalent MRMT donneront alors les mêmes courbes de restitution. L'organisation des concentrations immobiles est cependant très différente dans MINC et dans MRMT. Dans MINC, les zones immobiles forment une chaine reliée par une extrémité à la zone mobile (*Figure 2.1, gauche*). Dans MRMT, toutes les zones immobiles échangent exclusivement avec la zone mobile (*Figure 2.1, droite*). La notion même de concentration immobile dans MRMT est à considérer avec précaution car étant un produit de la relation d'équivalence.

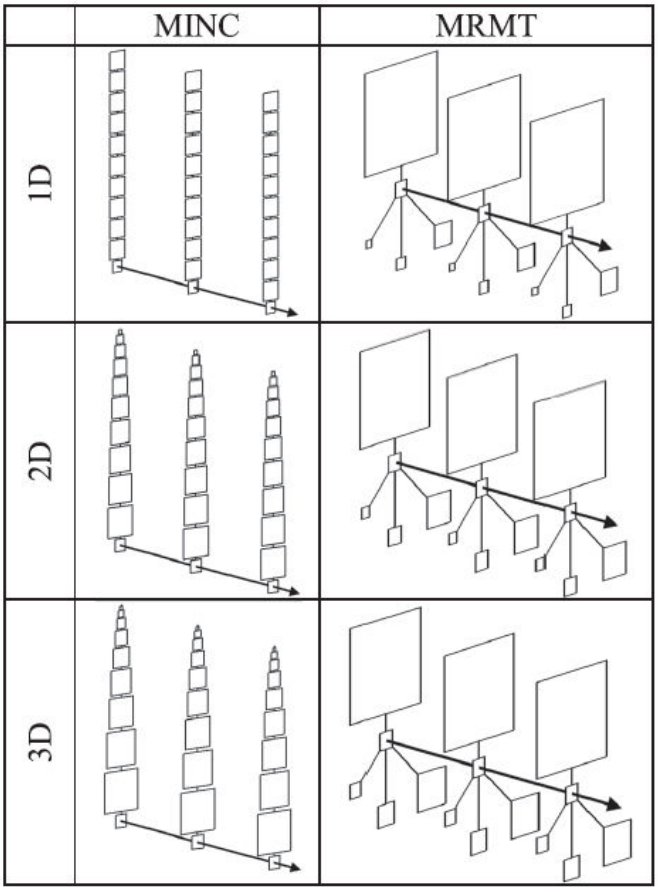

Figure 2.1: Représentation schématique de l'organisation des zones immobiles dans les modèles MINC (Multiple INteracting Continua) et MRMT (Multiple Rate Mass Transfer) pour des inclusions 1D, 2D et 3D. Les modèles sont représentés par trois coupes perpendiculaires à la zone mobile, identifiée par la flèche en gras. La surface des cellules est proportionnelle à leur porosité.

Dans l'article qui constitue le cœur de ce chapitre, nous évaluons la possibilité d'étendre l'usage de MRMT comme modèle équivalent à MINC pour du transport réactif. La réaction considérée est une réaction de précipitation bimoléculaire à l'équilibre de type A + B → C, où A et B sont des solutés et C est un minéral (Rubin 1983, de Simoni et al. 2005). Parce que cette réaction est non-linéaire ($c_A c_B = K$, où c_A et c_B sont les concentrations de A et B et K est la constante d'équilibre chimique), et que la relation d'équivalence entre MINC et MRMT n'assure pas la conservation de la distribution des concentrations immobiles, les taux de réaction dans MINC et MRMT peuvent être différents. Le modèle MRMT est utilisé comme modèle équivalent car présentant des "concentrations" pouvant être utilisées directement pour la réactivité, au contraire d'autres formalismes de transport anormal comme CTRW (Berkowitz and Scher 1998, Berkowitz et al. 2006) ou fADE (Benson et al. 2000).

2 Article : "*Influence of porosity structures on mixing-induced reactivity at chemical equilibrium in mobile/immobile Multi-Rate Mass Transfer (MRMT) and Multiple INteracting Continua (MINC) models*", par J.-R. de Dreuzy, A. Rapaport, T. Babey et J. Harmand, publié en 2013 dans Water Resources Research

En plus des discussions générales, ma contribution dans cet article a porté principalement sur le développement du code MINC-MRMT (peut-être publié prochainement...), et notamment l'implémentation et la visualisation des structures de porosité immobiles.

Influence of porosity structures on mixing-induced reactivity at chemical equilibrium in mobile/immobile Multi-Rate Mass Transfer (MRMT) and Multiple INteracting Continua (MINC) models

J.-R. de Dreuzy,[1,2] A. Rapaport,[3,4] T. Babey,[1] and J. Harmand[4,5]

Received 19 March 2013; revised 20 September 2013; accepted 5 November 2013.

[1] Trapping mechanisms and slow diffusion in poorly connected porosities are well modeled by several anomalous transport models including the Multi-Rate Mass Transfer framework (MRMT). In MRMT, solutes in fast mobile advective zones are slowed down by first-order exchanges with immobile zones. While MRMT models have been used essentially for conservative transport, we investigate their relevance to reactive transport. To this end, we analyze the influence of the structure of the diffusive porosity zone on the distribution of concentrations within the immobile zone and on the reactivity of simple precipitation/dissolution bimolecular reactions at equilibrium. We build Multi-Rate Mass Transfer (MRMT) and Multiple INteracting Continua (MINC) models with equivalent transport characteristics. Both models have the same mobile zone concentrations at any time. They, however, differ by the connectivity structure of their immobile zones. MRMT has a star-shaped connectivity structure with the mobile zone linked to all immobile zones and acting as the sole exchanger. MINC has a chained-type connectivity where immobile zones are mutually connected on a line. We show that both connectivity structures give the same concentration variance whatever the model parameters, dimensionality, and initial conditions. Reaction rates of bimolecular reaction at chemical equilibrium are also highly similar but not equal as long as concentration gradients within the diffusive zone remain low like in the uniform injection case, or at large times when high initial concentration gradients have been reduced. For high initial immobile concentration gradients in the diffusive zone, however, reaction rates are much lower in the star-shaped connectivity structure (MRMT), and consequently depend on the organization of the immobile porosity structure. Negative concentrations also occur in some of the immobile zones of the equivalent MRMT as a result of the direct connection of the mobile and immobile zones. While acceptable for conservative components, negative concentrations limit the relevance of MRMT to model reactivity at high immobile concentration gradients. The concept of immobile zone concentration should thus be taken with great care and systematically be assessed.

Citation: de Dreuzy, J.-R., A. Rapaport, T. Babey, and J. Harmand (2013), Influence of porosity structures on mixing-induced reactivity at chemical equilibrium in mobile/immobile Multi-Rate Mass Transfer (MRMT) and Multiple INteracting Continua (MINC) models, *Water Resour. Res.*, *49*, doi:10.1002/2013WR013808.

1. Introduction

[2] Solute exchanges between high and low-permeability zones are recognized as one of the key factors controlling solute transport in geological media. High-permeability zones promote fast solute transport with a dominance of advection over diffusion while transport is much slower and essentially diffusive in the low-permeability zones. Coexistence of these mobile and immobile zones and exchanges between them critically enhance solute spreading, breakthrough tailing and anomalous non-Fickian transport [*Benson et al*., 2000; *Berkowitz et al*., 2006; *Bouchaud and Georges*, 1990; *Dentz and Berkowitz*, 2003; *Neuman and Tartakovsky*, 2009]. It is widely observed in fractured media where the high-permeability zones are long and highly transmissive fractures while the low-permeability zones are the smaller fractures, the dead ends of the fracture network as well as the surrounding unfractured rock (matrix) [*Andersson et al*., 2004; *Gouze et al*., 2008; *Grisak and Pickens*, 1980; *McKenna et al*., 2001; *Neretnieks*, 1980; *Shapiro*, 2001]. It also prevails in

[1]Géosciences Rennes, UMR CNRS 6118, Campus de Beaulieu, Rennes, France.
[2]Institute of Environmental Analysis and Water Studies, CSIC, Barcelona, Spain.
[3]UMR 729 INRA SupAgro MISTEA, Montpellier, France.
[4]EPI INRA INRIA MODEMIC, Sophia-Antipolis, France.
[5]INRA-LBE, UR 0050, Avenue des étangs, Narbonne, France.

Corresponding author: J.-R. de Dreuzy, Géosciences Rennes, UMR CNRS 6118, Campus de Beaulieu, Université de Rennes 1, FR-35042 Rennes CEDEX, France. (Jean-Raynald.de-Dreuzy@univ-rennes1.fr)

0043-1397/13/10.1002/2013WR013808

porous media with high contrasts of lithologies [*Haggerty et al*., 2004; *LeBlanc et al*., 1991; *Sudicky*, 1986], in microscale inclusion models [*Golfier et al*., 2007; *Zinn et al*., 2004] and in radial diffusion in soils [*Rao et al*., 1980; *Wu and Gschwend*, 1986]. In fractured media, solute transport has been based on structure-imitating approaches like fracture-matrix concepts [*Maloszewski and Zuber*, 1985; *Sudicky and Frind*, 1982; *Tang et al*., 1981], Multiple INteracting Continua (MINC) [*Karimi-Fard et al*., 2006; *Pruess and Narasimhan*, 1985] and dual or triple-porosity concepts [*Magnico et al*., 1993; *Wu and Pruess*, 2000; *Wu et al*., 2004]. Regarding inert solute transport, these different approaches can all be accounted within the Multiple-Rate Mass Transfer framework (MRMT) [*Carrera et al*., 1998; *Ginn*, 2009; *Haggerty and Gorelick*, 1995; *Haggerty et al*., 2000; *Willmann et al*., 2008]. MRMT models consist of mobile zones exchanging solutes with several immobile zones according to a first-order exchange law. Despite their simplicity, MRMT models are highly general and can simultaneously model the interaction with different structures of diffusive zones and even different trapping mechanisms (e.g., diffusion in low-flow zones and sorption) [*Haggerty and Gorelick*, 1995].

[3] The equivalence between the MRMT models and the other fracture-matrix types of model is based on the equality of the concentrations in the mobile zone and, consequently, of the solute breakthrough curves [*Haggerty and Gorelick*, 1995]. Fundamentally, the diffusion in 1-D, 2-D, and 3-D inclusions is solved analytically in the Laplace domain, and the analytical solution is decomposed in partial fractions. Each partial fraction is further interpreted as a first-order exchange between the concentration in the mobile zone and an equivalent "virtual concentration" in the immobile zone. When keeping the focus on the transport properties, the important quantity is the concentration in the mobile zone and the status of the immobile "virtual concentrations" does not have to be further considered. However, it becomes a key issue when addressing reactivity in the immobile zone. It is tempting to use these immobile "virtual concentrations" as regular chemical concentrations of solutes that can be handled as concentrations of chemical compounds that can react chemically [*Donado et al*., 2009]. Nothing in the construction of the MRMT however ensures this, hence the term of "virtual concentration." The equivalence of *Haggerty and Gorelick* [1995] does not implicate anything on the distribution of concentrations nor on mixing capacities and reaction rates within the immobile zones. While the flux of concentration between the mobile and immobile zones is fully constrained, the concentration distributions in the immobile zones do not have any reason to be similar.

[4] Intuitively, the immobile concentration distribution does not only depend on the concentration in the mobile zone but also on the topological structure of the immobile zones, which are highly different in the MRMT and in the other approaches. In the multiple-interacting model (MINC), which can be considered as a discretization of the fracture-matrix model [*Pruess and Narasimhan*, 1985; *Pruess*, 1992], the immobile zones are connected in series and linked to the mobile zone by a single immobile zone (Figure 1a). This sketch is correct whatever the dimensionality of the fracture-matrix model (1-D layer, 2-D cylinder, and 3-D spheres) as long as initial conditions do not break their symmetry. For MRMT, all immobile zones are connected in parallel to the mobile zone (Figure 1b). The mobile zone can be seen as a mixer that distributes solutes directly to all immobile zones. For MINC, however, access to the immobile zones depends on their position in the series of the immobile zones. Solute exchange is more remote and critically depends on all the closer immobile zones. Interactions between immobile solute concentrations are expected to be more complex in MINC because of its linear topological structure than in the simpler topology of MRMT.

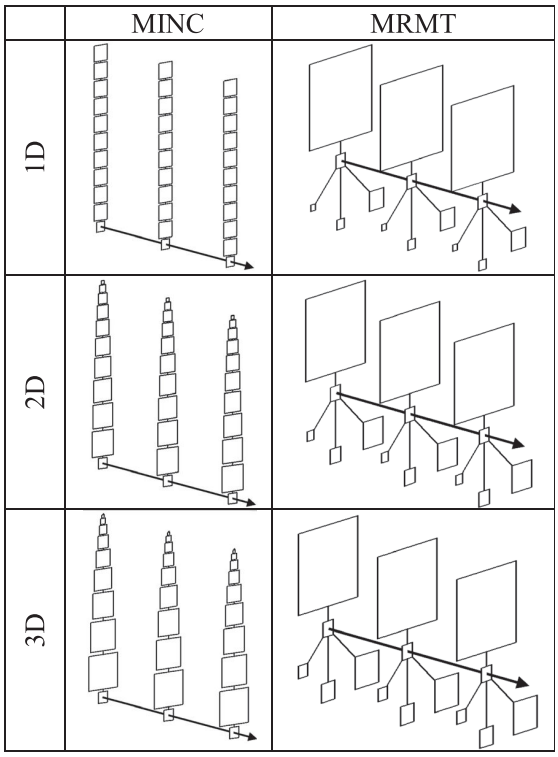

Figure 1. Sketches of the immobile zone organization for Multiple INteracting Continuum models (MINC) and Multiple-Rate Mass Transfer models (MRMT) for 1-D, 2-D, and 3-D inclusions. Mobile zones are identified by the connection arrow and their volume is exaggerated five times compared to the volume ratio taken for the simulation ($\beta = 100$). Comparison with the MRMT model shows the large dominance of the smallest rates having the largest volumes. Impact of the inclusion dimension intervenes in the rate values and on the rate of volume reduction smaller with higher dimensions.

[5] The dynamic of mixing also intuitively depends on the connectivity structure. The potential influence of structure is a priori not limited to the distribution of concentrations in the immobile zones but likely extends to mixing induced reactivity. Mixing can be characterized by the temporal derivative of the second moment of the concentration distribution M_2 [*Le Borgne et al*., 2010]

$$\chi(t) = -\frac{1}{2}\frac{dM_2}{dt}. \quad (1)$$

[6] This quantity defined as the scalar dissipation gives the rate of scalar mixing. As most of the porous volume is in the immobile zones rather than in the mobile zone [*Li et al*., 2011; *Willmann et al*., 2008], their concentration as well the dynamic of their exchanges are likely to impact the concentration variance and hence the reactivity in the absence of any mineralogical heterogeneity [*Glassley et al*., 2002]. In this article, we aim at exploring the influence of the organization of the immobile zones on the mixing characteristics and induced reactivity at chemical equilibrium at identical conservative solute transport.

[7] Previous studies are not answering directly this question as structures are all significantly more complex than the simpler MRMT and MINC configurations. Immobile zone organization is one parameter among others including the heterogeneity of the permeability field and the complexity of the flow structure (mobile zone organization, heterogeneous advection) [*Gramling et al*., 2002; *Luo and Cirpka*, 2008, 2011; *Willmann et al*., 2010]. However, in reaction-transport-diffusion dynamics, it is known that simple spatial structures can induce nonintuitive behaviors worth to be investigated [e.g., *Haidar et al*., 2011]. In this article, we focus on the sole effect of the immobile zone organization on the distribution of the immobile zone concentrations and on the mixing-induced reactivity on the basis of elementary connectivity structures.

2. Models and Methods

[8] We first recall the MRMT and MINC models, express them in dimensionless form and list the methods used to characterize conservative and reactive transport. We then detail the specificities of the numerical experiments including the initial conditions, the simulation parameters, and the computational methods.

2.1. Models

[9] We consider classical MRMT and MINC models that only differ by their immobile zone organization. The total porous volumes of the mobile and immobile zones are identical in both models. Even if they are not limited to diffusion in simple media, both MRMT and MINC models fundamentally derive from two different discretizations of the diffusion equation in homogeneous monodisperse inclusion zones of Euclidean dimension n in interaction with a 1-D mobile zone [*Haggerty and Gorelick*, 1995; *Pruess and Narasimhan*, 1985; *Sudicky and Frind*, 1982; *Tang et al*., 1981]. The fundamental set of equations for the 1-D mobile zone in interaction with diffusion in the immobile zone of dimension n are given in dimensional form

$$\frac{\partial c(x,t)}{\partial t} + \beta\frac{\partial \tilde{s}(x,t)}{\partial t} = -v\frac{\partial c(x,t)}{\partial x} + D_m\frac{\partial^2 c(x,t)}{\partial x^2}, \quad (2)$$

$$\frac{\partial s(x,r,t)}{\partial t} = \frac{d}{r^{n-1}}\frac{\partial}{\partial r}\left(r^{n-1}\frac{\partial s(x,r,t)}{\partial r}\right) \text{for } 0 \le r \le a, \quad (3)$$

$$\tilde{s}(x,t) = \int_0^a s(x,r,t)r^{n-1}dr \Big/ \int_0^a r^{n-1}dr, \quad (4)$$

where $c(x, t)$ is the mobile concentration at the scalar position x along the mobile domain $x \ge 0$, $s(x, r, t)$ is the immobile zone concentration at the microscopic distance r from the mobile zone and at the macroscopic position x, $\tilde{s}$ is the mean concentration in the immobile zone, a is the characteristic scale of the immobile zone (e.g., radius of spherical immobile inclusions in 3-D), v and D_m are the velocity and longitudinal dispersion coefficient in the mobile zone, d is the diffusion coefficient in the immobile zone and β is equal to the ratio of immobile to mobile porous volumes, also equal to the asymptotic repartition of the masses of solutes between the immobile and mobile zones. The concentration in the immobile zone is equal to the concentration of the mobile zone at the interface and no flow is imposed at the boundary $r = 0$

$$s(x, r=a, t) = c(x,t), \quad (5)$$

$$\left.\frac{\partial s}{\partial r}\right|_{r=0} = 0. \quad (6)$$

[10] Initial conditions are imposed in the mobile and immobile zones

$$s(x, r, t=0) = s_0(x,r), \quad (7)$$

$$c(x, t=0) = c_0(x). \quad (8)$$

[11] A dimensionless formulation of the problem can be obtained by choosing as the reference time the characteristic time of diffusion within the immobile zone $\tau = a^2/d$ and as the reference scale the characteristic immobile zone scale a

$$\frac{\partial c}{\partial \bar{t}} + \beta\frac{\partial \tilde{s}}{\partial \bar{t}} = -\frac{va}{d}\frac{\partial c}{\partial \bar{x}} + \frac{D_m}{d}\frac{\partial^2 c}{\partial \bar{x}^2}, \quad (9)$$

$$\frac{\partial s}{\partial \bar{t}} = \frac{1}{\bar{r}^{n-1}}\frac{\partial}{\partial \bar{r}}\left(\bar{r}^{n-1}\frac{\partial s}{\partial \bar{r}}\right) \text{for } 0 \le \bar{r} \le 1, \quad (10)$$

$$\tilde{s} = \int_0^1 s(x,\bar{r},t)\bar{r}^{n-1}d\bar{r} \Big/ \int_0^1 \bar{r}^{n-1}d\bar{r} \quad (11)$$

with $\bar{x} = x/a$, $\bar{r} = r/a$, and $\bar{t} = t/\tau$. The system of equations (9–11) depends on 3-D parameters, the capacity ratio β, the Damköhler number $Da = \frac{va}{d}$ that compares the characteristic diffusion time in the immobile zone with the characteristic advection time in the mobile zone and the ratio $R_d = \frac{D_m}{d}$ that compares the dispersion in the mobile zone and the diffusion in the immobile zone. In the following, R_d will be taken small enough ($R_d = 10^{-3}$) so that the effect of the dispersion in the mobile zone can be neglected as compared to the exchanges with the immobile zone. For convenience, all overbars will also be dropped as everything will be expressed in dimensionless form.

[12] In cases where both MINC and MRMT models result from a discretization of diffusion in 1-D, 2-D, or 3-D inclusions, equations (5–8) subjected to boundary and initial conditions (9–11) can be synthesized as (Appendix A)

$$M\left[\frac{\partial U}{\partial t} - L(RU)\right] = AU, \quad (12)$$

where $U = (\,C \quad S_1 \quad \ldots \quad S_N\,)^T$ is the vector of the mobile and N immobile concentrations $C(x, t)$ and $S_i(x, t)$

$(i=1,\ldots,N)$, where N is the number of immobile zones. Upper case letters are used for discretized quantities transversally to the mobile zone while lower case letters are used for continuous quantities. R is the restriction operator to the mobile zone. All elements of R are zero except for the element on the first row and first column equal to 1. L is the transport operator in the mobile zone

$$L(U)=-Da\frac{\partial U}{\partial x}+R_d\frac{\partial^2 U}{\partial x^2}. \quad (13)$$

[13] M is a diagonal matrix of the porous volumes of the mobile and immobile zones and A is a matrix characterizing their mutual interactions. The volume and interaction matrices M and A are derived for the MINC model and recalled for the MRMT model in Appendix A. Because diffusion is a nondirectional process and as the system of equation (12) is written in terms of solute mass conservation, A is a symmetrical Metzler matrix the sums across columns are equal to zero and all its off-diagonal elements are nonpositive. A characterizes a self-adjoint process.

[14] A is a kind of adjacency matrix weighted by the physical properties of the immobile inclusions [*Godsil and Royle*, 2001]. For MRMT models, A is an "arrow" type matrix where only the first line and the first column have nonzero off-diagonal elements because all the interactions occur between the mobile and immobile zones and none between immobile zones. For MINC models, A is a classical tridiagonal matrix traducing the interactions between neighboring immobile zones. Interaction with the mobile zone is performed only through the immobile zone next to the mobile zone and is expressed by the boundary condition (5).

2.2. Concentration Moments, Mixing Characteristics, and Reaction Rate

[15] We compare equivalent MRMT and MINC models on several different characteristics of the resulting concentration fields beginning first with the mean dimensionless velocity $V=d\langle x\rangle/dt=dm_1/dt$ and the dimensionless dispersion coefficient D with

$$D=\frac{1}{2}\frac{d\sigma_x^2}{dt}, \quad (14)$$

[16] Where

$$\sigma_x^2=m_2/m_0-(m_1/m_0)^2 \quad (15)$$

and the spatial moments m_k are

$$m_k=\int_{x=0}^{\infty}\sum_{i=1}^{N}x^k M(i,i)U_i(x)dx, \quad (16)$$

where we recall that $M(i, i)$ is the volume of the immobile zone i. $\langle x\rangle$ and σ_x^2 should be very close for equivalent MRMT and MINC models. They are not equal because of different discretization errors for the MINC method and truncation errors for the MRMT. Nonetheless, it will be used as a test of consistency of the numerical methods. Tests will be performed on the statistical quantities $\langle x\rangle$ and σ_x^2 rather than on their temporal derivatives V and D to avoid any loss of accuracy due to the derivation.

Table 1. Characteristic Time (α_i^{-1}), Relative Porosity Ratio of the Five First Rates of the MRMT Series for $n = 1$ (b_i) and Cumulative Relative Porosity Ratio of the First Few Rates $\sum_{k=1}^{i} b_k$

i	α_i^{-1}	b_i (%)	$\sum_{k=1}^{i} b_k$ (%)
1	0.4	81	81
2	0.045	9	90
3	0.016	3.3	93.3
4	0.0083	1.65	95
5	0.0050	1	96

[17] The second set of characteristics concerns the distribution of concentrations in the mobile and immobile zones. We build the histogram of the distribution of the decimal logarithm of concentrations ($p(\log C)$). The logarithm of concentrations is a priori more appropriate than the concentration itself because concentrations are expected to be broadly distributed over several orders of magnitude. To get more quantitative information, we compute the moments of the concentration distribution M_k

$$M_k=\int_{x=0}^{\infty}\sum_{i=1}^{N+1}M(i,i)[U_i(x)]^k dx \quad (17)$$

for the first integral values of k (k ranging from 1 to 5) where N is either equal to N_{MRMT} or N_{MINC}. The moments are less sensitive than the distribution itself to the strong dominance of the first rates in the MRMT model that make the distribution more discrete than continuous in the preasymptotic regime. They can also be computed whatever the concentration values.

[18] We shorten the denomination of "immobile zone with the kth rate" by the "kth rate." So the first rate designates the immobile zone with the smallest rate. It is also the immobile zone with the largest volume as the volume is decreasing with the rate. In the layered inclusion case, the first rate counts for 81 % of the total immobile porosity (Table 1). The five first rates count for 96 % of the total immobile porosity. Most of the porosity is thus concentrated in the very few first rates.

[19] The moments of the concentration distribution M_k should not be confused with the spatial moments of the concentration m_k. M_0 is the total porous volume of the domain simulated. M_1 is the mass within the domain. It is constant and expresses the conservation of mass as long as all the mass remains within the domain. As the total mass will be injected at the initial time and will be set at 1 (see section 2.3), M_k is numerically equal to the raw moment of order k and will be assimilated to it. We kept the nonnormalized equation (17) for M_k to systematically check that the total mass M_1 remains constant and equal to 1. Higher-order moments ($k > 1$) are nonlinear outputs of a linear model. M_2 gives an indication of the mixing-induced reactivity as it is linked to the scalar dissipation rate $\chi(t)$ by equation (1). We finally compute the reaction rate of a

bimolecular dissolution/precipitation reaction at chemical equilibrium from the concentration field of a conservative component. We assume the same diffusion coefficient for the two reactants, what might not be always the case [*Hochstetler et al*., 2013]. If A and B are the reactants and C_A and C_B their concentration vectors in the mobile and immobile zones, the conservative component $U = C_A - C_B$ follows equation (12) while the reaction rate R_C can be expressed by

$$R_C(t) = \int_{x=0}^{\infty} \sum_{i=1}^{N+1} R_{Ci}(x,t)dx \tag{18}$$

with

$$R_{Ci}(x,t) = M\left[\frac{\partial C_{Ai}(x,t)}{\partial t} - L(RC_{Ai}(x,t))\right] - AC_{Ai}(x,t) \tag{19}$$

and $C_{Ai}(x,t) = \frac{U_i(x,t)+\sqrt{U_i(x,t)^2+4K}}{2}$ where $C_{Ai}(x,t)\, C_{Bi}(x,t) = K$ for $i = 1, \ldots, N+1$ [*de Simoni et al*., 2005; *Rubin*, 1983]. K is the chemical equilibrium constant. The precipitated/dissolved mineral is assumed to have an activity equal to 1 and thus does not show up in the equations. To avoid any additional temporal derivative error, the derivative of C_A is directly determined from the derivative of the conservative component U rather than recomputed

$$\frac{\partial C_A}{\partial t} = \frac{\partial C_A}{\partial U}\frac{\partial U}{\partial t}. \tag{20}$$

[20] The reaction rate of equation (19) will be derived using the concentration of A and its derivative given by equation (20). Reactant concentrations are equal at equilibrium in most of the domain $C_{Ai} = C_{Bi} = \sqrt{K}$ corresponding to a zero value of the conservative component U_i ($U_i = 0$), outside of the narrow injection zone where the difference of their concentrations is strictly positive ($U_i > 0$). We derive the reaction rates in both MINC and MRMT models with this simple initial condition under the assumptions that the two species A and B are always present and that no kinetic reactions interfere with their activities [*Donado et al*., 2009]. In the case of the diffusion model, the reaction rate can be expressed as the product of a chemical and a physical factor [*de Simoni et al*., 2005]

$$R_{Ci} = \frac{\partial^2 C_{Ai}}{\partial U_i^2}\nabla^T U_i d_G \nabla U_i, \tag{21}$$

where $d_G = 1$ in the immobile zone ($i = 1$) and $d_G = R_d$ in the immobile zone ($i > 1$). The first chemical term can be simply expressed as

$$\frac{\partial^2 C_{Ai}}{\partial U_i^2} = \frac{2K}{(U_i^2+4K)^{3/2}}, \tag{22}$$

while the second physical factor integrated over the full domain is the scalar dissipation rate $\chi(t)$ related to the derivative of the integral of the squared concentration of the conservative component M_2 by equation (1). The reaction rate thus does not only depend on the M_2 value of the conservative component but also on the higher-order moments of the concentration distribution. Even if we distinguish physical and chemical factors in the reaction rate, all the reactivity remains physically driven by mixing processes of solutes with different concentrations.

2.3. Injection Conditions

[21] To model initial continuous concentration profiles with potentially large gradients, initial concentrations follow a Gaussian profile along the mobile zone centered at the position x_0 sufficiently distant from the system inflow to prevent any spurious boundary effect from the upstream boundary conditions

$$c(x, t=0) = c_0(x) = \frac{1}{\sigma_0\sqrt{2\pi}} e^{-\frac{(x-x_0)}{2\sigma_0^2}}. \tag{23}$$

[22] The standard deviation of the Gaussian is fixed at σ_0 and is five times larger than the initial discretization step. Under these initial conditions, concentrations are normalized so that the total mass injected in the system is equal to 1. For the initial concentrations in the immobile zone, we consider two cases. In the first uniform case, concentrations in the immobile zones are all equal to the concentration in the mobile zone at the same position x

$$s(x, r, t=0) = c(x, t=0). \tag{24}$$

[23] The initial ratio of mass in the mobile and immobile zones is equal to the capacity ratio β and hardly evolves throughout the simulation. The mean velocity remains also constant. The concentration gradients are initially zero in the immobile zone and are later solely induced by the transport in the mobile zone. We also consider a second case with nonuniform initial concentrations in the immobile zone that highlight the mixing mechanisms. The concentration of the reactant (A) is much larger than the concentration of the other reactant (B) away from the mobile zone. Such cases occur for example when young waters percolate within deeper formations of resident water of composition determined by long-term water-rock interactions [*Aquilina et al*., 2011; *Aquilina and de Dreuzy*, 2011; *Fourcade et al*., 2007; *Techer et al*., 2012].

[24] Concentrations of the conservative component are distributed along the immobile zone according to a uniform profile $g(r)$ in the whole domain

$$s(x, r, t=0) = g(r)c(x, t=0). \tag{25}$$

[25] The profile $g(r)$ is chosen in such a way that the ratio of mass in the immobile and mobile zones remains equal to the capacity ratio so that the velocity remains as close as possible to its asymptotic; F_s value

$$\frac{\int_{r=0}^{r=1} s(x, r, t=0)g(r)dr}{\int_{r=0}^{r=1} g(r)dr} = \frac{c(x, t=0)}{\beta}. \tag{26}$$

[26] We will use this second type of conditions only for $n = 1$, a case for which we derive simple analytical

Table 2. Simulation Parameters Used in Sections 3 and 4[a]

Name	Description	Section 3	Section 4
β	Ratio of immobile to mobile porous volumes	10^2	10^2
D_a	Characteristic diffusion time in the immobile zone to advection time in the mobile zone	10^2	10, 10^2, 10^3
R_d	Ratio of diffusion in the mobile and immobile zones	10^{-3}	10^{-3}
n	Euclidean dimension of immobile zones	1, 2, 3	2
N_{MRMT}	Truncation order in MRMT model	20, 40	20
N_{MINC}	Discretization order in MINC model	20, 40	20
σ_0	Characteristic extension of the initial conditions along the mobile zone	0.1	0.1
Δ_0	Characteristic extension of the initial conditions along to the immobile zone	0.2	0.2
$\overline{K}$	Chemical equilibrium constant	10^{-2}	10^{-1}

[a]Parameters different in section 4 from section 3 are highlighted in bold.

relations between the initial immobile concentrations in the MRMT and MINC frameworks (Appendix B). In this case, we consider a Gaussian profile such as

$$g(r)=\frac{1}{\Delta_0\sqrt{2\pi}}e^{-\frac{r^2}{2\Delta_0^2}} \quad 0\le r\le\Delta_0 \qquad (27)$$
$$g(r)=0 \quad \Delta_0 < r < 1.$$

[27] The maximum initial concentration value $u^0_{\max}$ depends on the injection shape and is either

$$u^0_{\max}=\frac{1}{\sigma_0\sqrt{2\pi}} \qquad (28)$$

in the uniform case or

$$u^0_{\max}\approx\frac{1}{\sigma_0\Delta_0\pi} \qquad (29)$$

in the distributed case if Δ_0 is much smaller than 1. The magnitude of the initial concentration is important when considering reactivity as the chemical factor intervening in the reaction rate (equation (22)) depends both on the magnitude of the concentration u and on the equilibrium constant K. Initially, the influence of concentration is dominant over K if

$$u^0_{\max}\gg\sqrt{2K}. \qquad (30)$$

[28] Thus, the ratio $\overline{K}=K/(u^0_{\max})^2$ is a key control parameter of reactivity. If it is very high, reactivity will be exclusively controlled by the scalar dissipation rate with an almost uniform chemical factor. If it is very low, the chemical factor can be highly variable and control reactivity as well as the physical factor.

2.4. Simulation Parameters

[29] We have performed simulations with the following set of common parameters: $\beta=100$, $N_{MINC}=N_{MRMT}=20$. The discretization of the MINC model (N_{MINC}) as well as the truncation of the MRMT model (N_{MRMT}) have a minor influence as long as they are high enough as will be shown in section 3.2. N_{MINC} and N_{MRMT} are more numerical parameters than controlling physical parameters. As a result, the key parameters are the Damköhler number (Da) that compares the characteristic diffusion time in the immobile zone and the characteristic advection time in the mobile zone and the capacity ratio β that characterizes the relative proportion of the immobile to the mobile porous volumes. The influence of the immobile zones increases both with β and Da. Larger β values reduce the velocity and larger Da enhances the global dispersion. In sections 3 and 4, we will investigate the effect of the inclusion dimensionality n ($n=1$, 2, and 3) and of the Damköhler number ($Da=10$, 10^2, and 10^3).

[30] Initial conditions (23–29) are taken with $\sigma_0=0.1$ and $\Delta_0=0.2$. The maximum initial concentration $u^0_{\max}$ is close to either 4 for uniform injection conditions or 15 for distributed injection conditions. The dimensionless equilibrium constant $\overline{K}$ is set at small values of 10^{-2} and 10^{-1} to highlight the possible impact of the concentration variations. All parameter values for sections 3 and 4 are synthesized in Table 2.

2.5. Transport Simulation Methods

[31] Numerous numerical methods have been developed for MRMT and MINC models that either preserve mass [*Başağaoğlu et al.*, 2002] or improve precision [*Willmann et al.*, 2008]. Here we have chosen a time and space-adaptive method that preserves mass to make simulations over a broad range of temporal scales. For the diffusion model in the immobile zones, the system of equations (10) and (11) with boundary conditions (5) and (6) and initial conditions (8) are discretized with a finite difference scheme as shown in Appendix A. The advection-diffusion equation (9) is handled as the noniterative sequential coupling of the diffusive operator simulated with a finite-difference discretization and of the advective operator simulated with a Lagrangian method. The mobile and immobile methods are sequentially coupled. Temporal integration is performed with an implicit scheme. To simulate transport on a large range of temporal and spatial scales, we use a simple time control method that increases consistently the temporal and spatial steps when the coarse and fine solutions are sufficiently close. The coarsening condition is based on the squared difference of the concentrations divided by the maximal concentration. When it is smaller than a threshold value (10^{-7}), the temporal and spatial steps are simultaneously increased. This method is much faster and almost as accurate as a more classical fully coupled constant time-step Eulerian scheme because of the amplitude of the diffusion induced by the exchanges between the mobile and immobile zones. We have compared it with a more classical Galerkin finite element

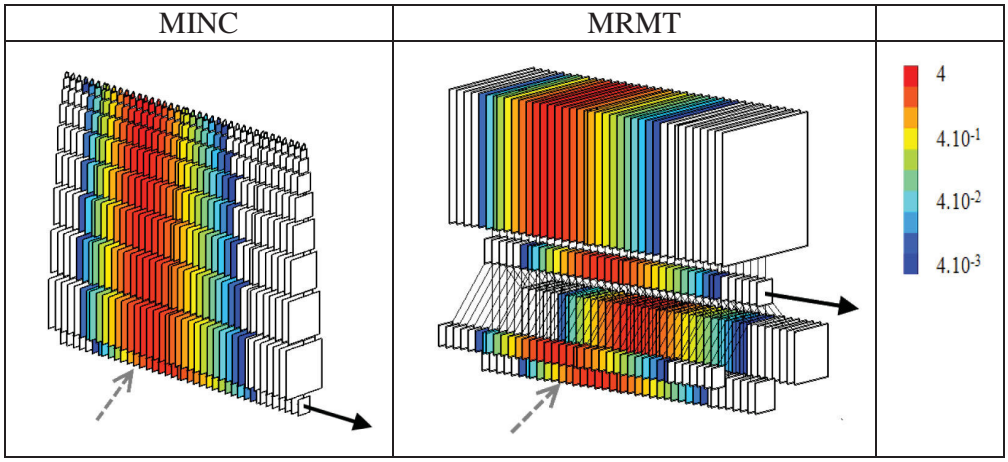

Figure 2. Logarithm of concentration fields in the mobile and 3-D immobile zones with $\beta = 100$ at $t = 0.1$ on 1.5 spatial units for equivalent MINC and MRMT models under uniform injection conditions centered at the location pointed out by the gray arrow. Representation of system structure follows the one given in Figure 1.

method in the mobile zone [*Daus et al*., 1985] fully coupled to the immobile zone for the set of the parameters of section 3 given by Table 2 under uniform initial conditions. Integration of the resulting system of ordinary differential equation was performed with the fourth-order Runge-Kutta method implemented in the ode45 function of MATLAB with the default tolerance values. Both methods lead to the same dispersion, moment and reaction rate results within a relative difference of at most 10^{-3} %. Actual behavior of immobile porous structures with MINC diffusion and equilibrium reactions among the reactants may also be simulated with coarse representation of transport but with realistic chemical reaction(s) in PhreeqC using the MIX and EQUILIBRIUM_PHASES functionalities [*Charlton and Parkhurst*, 2011; *Parkhurst and Appelo*, 1999].

3. Results

[32] Dispersion, concentration moments, and reaction rates are systematically compared as a function of the immobile zone dimensionality under uniform and nonuniform injection conditions both qualitatively and quantitatively.

3.1. Influence of Inclusion Dimensionality Under Uniform Injection Conditions

[33] We first simulate transport starting with classical uniform injection conditions in the mobile and immobile zones (equations (24) and (25)). Exchanges between mobile and immobile zones quickly spread out the concentrations downstream even at one-tenth of the characteristic diffusion time ($t = 0.1$) (Figure 2). Concentrations are broadly distributed over several orders of magnitude. Both MINC and MRMT models display qualitatively the same concentration patterns despite their different connectivity structure.

[34] With these initial conditions, dispersion sharply increases because of the quickly progressing concentration in the mobile zone and because of the trailing concentration trapped in the immobile zone (Figure 3a). About the characteristic dimensionless diffusion time in the immobile zone ($t = 1$), it reaches its asymptotic value D_A. In the asymptotic regime, dispersion fully controls the M_2 value of the concentration field [*de Dreuzy et al*., 2012a; *Le Borgne et al*., 2010]. The larger dimensions induce a faster decrease of the concentration second moment, i.e., the reverse tendency to the asymptotic regime. A crossover occurs before $\bar{t} = 1$. Initially, it is the largest surface to volume ratio for the spherical inclusions that promotes more mixing and faster decrease of M_2. Eventually, it is the largest volume to surface ratio of the layered inclusions that promotes more mixing.

[35] The overall behavior of the reaction rate R_c is more complex than M_2 (Figure 3c). It first slightly increases before steeply decreasing. The increasing trend comes from the chemical factor (equation (22)) while the decreasing trend comes from the physical factor (equation (21)). In fact the chemical factor monotonously increases because the reaction will be highest for equal concentrations of reactants ($U_i = 0$). However, the physical factor monotonously decreases because it is a function of the concentration gradients constantly reduced by the diffusion processes. At first, the increase of the chemical factor dominates the decrease of the physical factor, while, at larger times ($t > 0.1$), the system behavior is dominated by the decrease of the physical factor. In fact, at late times, the reaction rate is directly proportional to the scalar dissipation rate (inset of Figure 3c) as the chemical factor (equation (22)) becomes uniform for values of the conservative component concentration U_i much smaller than $\sqrt{2K}$. Especially, the reaction rate increases with the Euclidean dimension because of the larger surface to volume ratio. At smaller times, the interplay between the chemical and physical factors of reactivity induces several inversions of tendencies of the effect of inclusion dimensionality. At early times, the increase of dimensionality reduces the reaction rate as opposed to what occurs at later times. Reaction rates depend thus not only on M_2 but also on higher-order moments of the concentration distribution.

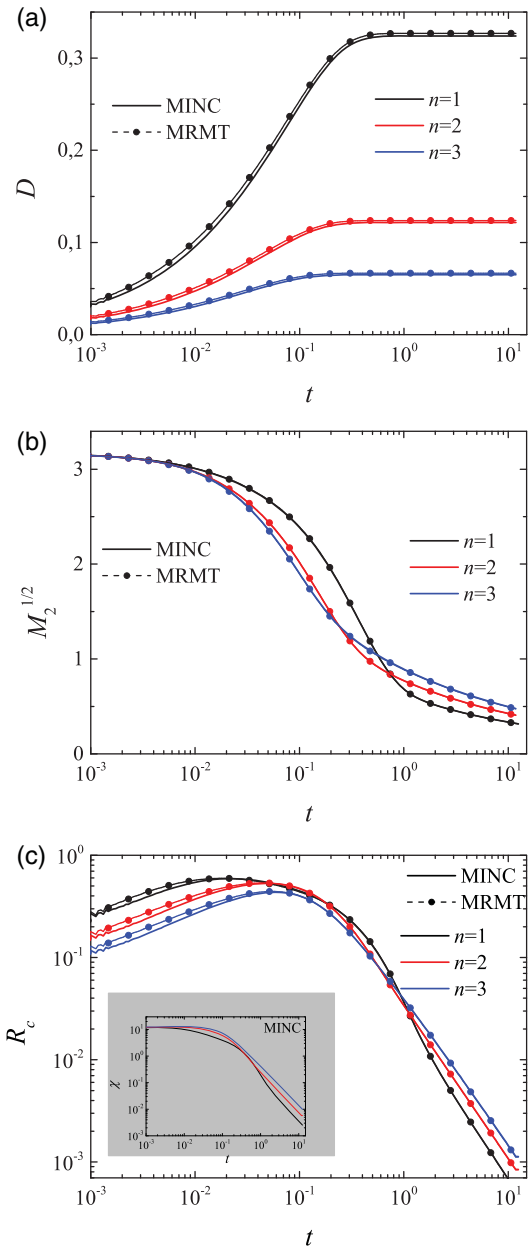

Figure 3. Evolution for equivalent MRMT and MINC models of (a) the dispersion coefficient D, (b) the square root of the second moment concentration moments $M_2^{1/2}$, and (c) the reaction rate R_c and in the gray insert the scalar dissipation rate χ with an initial Gaussian concentration profile uniform in the mobile and immobile zones (n = 1, $Pe = 100$, $\beta = 100$, $R_d = 10^{-3}$, $N = N_{MRMT} = N_{MINC} = 20$).

[36] In fact, $M_k^{1/k}$ display differing temporal evolutions as a function of k (Figure 4). Their initial value $M_k(t{=}0)$ depends on the characteristic width of the injection σ_0

$$M_k(t{=}0) = {\sigma_0}^{1-k}. \tag{31}$$

[37] M_1 remains constant equal to 1 because of mass conservation while the higher-order moments monotonically decrease (Figure 4). The decrease is very sharp between 0.1 and 1 while the concentrations initially trapped in the immobile zone are progressively released in the mobile zone and spread back in the downstream immobile zones. An asymptotic decreasing tendency is reached for $t = 1$. The relative magnitude of the $M_k^{1/k}$ values is reversed around $t = 1$. Around $t = 1$, $M_k^{1/k}$ almost all intersect together. Their asymptotic behavior becomes close when increasing the order k. While the first moments are very close together, concentration distributions are not equal as shown in Figure 5. They differ mostly at intermediary times (Figure 5b, $t = 0.1$) when the dispersion coefficient is steeply increasing. MINC has higher probabilities for the extremes of the distribution. At much earlier and later times (Figures 5a and 5c, $t = 0.025$ and $t = 0.8$), distributions become closer together. High frequency variations of the distribution for the MRMT case come from the quantified volumes of the immobile zones.

[38] The spatial distribution of the reaction rates $R_{Ci}(x, t)$ integrated over time also shows the proximity of the reactivities between MRMT and MINC models (Figure 3). Reactivity sharply decreases downgradient of the injection zone following the reduction of the concentrations and concentration gradients. Reactivity is also more correlated to the volume of the immobile zone rather than to the distance to the immobile zone in MINC or to the reaction rate in MRMT. We note that the reactivities in the mobile zone are not equal as they depend both on the concentrations in the mobile zone and on their relation to the concentrations in the immobile zone (equation (19)). Despite nonobvious relations between reaction rates in the immobile zones for the MRMT and MINC models, the overall variations of the reactivity patterns remain visually very close together.

3.2. Comparison of MRMT and MINC Models

[39] Quite surprisingly, all previously studied quantities remain very close between MRMT and MINC models (Figure 3, lines compared to dots). More quantitatively, we evaluate their relative differences by computing

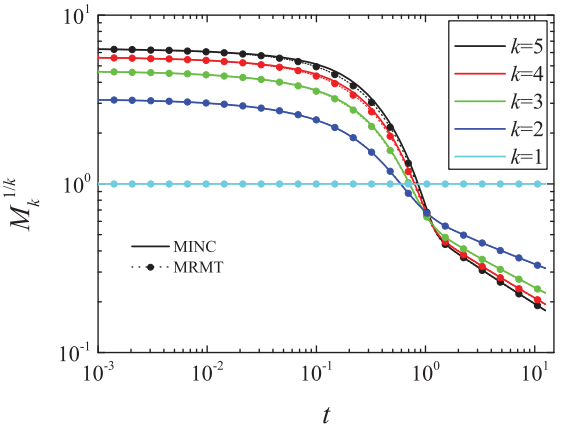

Figure 4. Time evolution of the first five moments of the concentration distribution $M_k^{1/k}$ for the layered case (n = 1) (equation (13)).

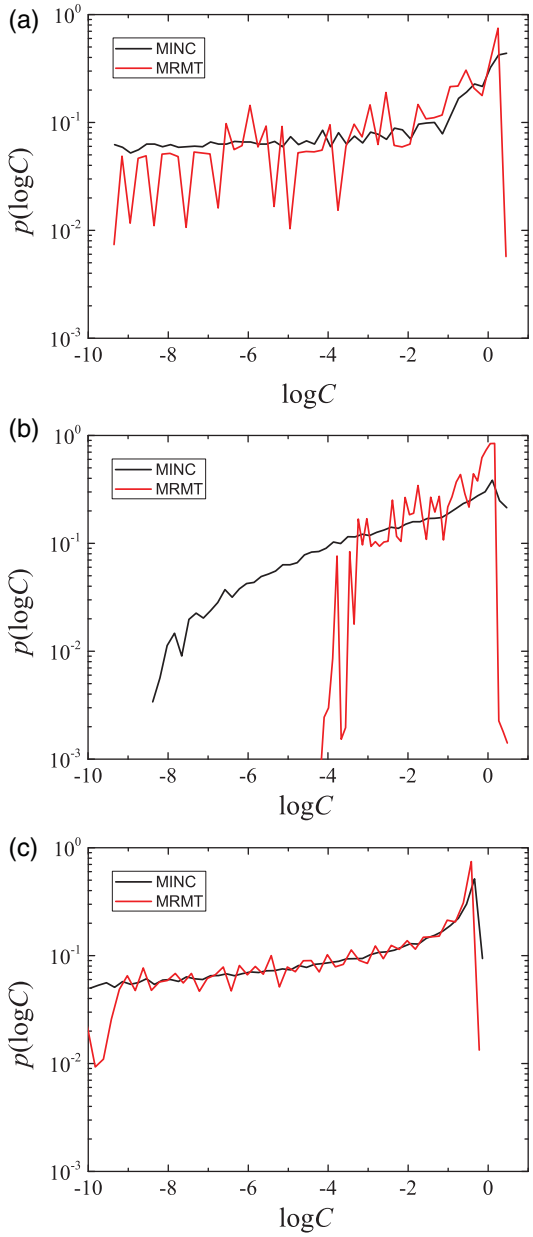

Figure 5. Distribution of the decimal logarithm of concentrations of the mobile and immobile zones at three evolving times $t = 2.5 \times 10^{-2}$, 0.1 and 0.8 for uniform injection conditions.

$$diff(X) = \sqrt{\sum_{i_t=1}^{i_t=n_t} \left[\frac{X^{MINC}(i_t) - X^{MRMT}(i_t)}{(X^{MINC}(i_t) + X^{MRMT}(i_t))/2} \right]^2}, \qquad (32)$$

where X is successively σ_x, $M_k{}^{1/k}$, and R_c (Table 3). While small, differences remain much larger than the estimated numerical accuracy of 10^{-3}%. All quantities are very close whatever the dimensionality of the immobile zone (layered inclusions for $n = 1$, cylindrical inclusions for $n = 2$ and spherical inclusions for $n = 3$). Dispersion values (σ_x) are theoretically equal in both models. Their slight differences decrease with the discretization of the immobile zones. For $N = N_{MRMT} = N_{MINC} = 20$, the mean squared difference is around 1.5%. A refinement of the discretization by a factor of 2 to $N = 40$ reduces the dispersion difference by a factor of around 1.75 to 0.8% − 0.87% (Table 3). Differences in the integrals $M_k{}^{1/k}$ are also small with a maximum at 2.6% and increase with the order k. For $M_2{}^{1/2}$, differences are <0.4% and are reduced by a factor of 2 when refining the immobile zone discretization. For the higher-order moments, differences are not modified by the refined discretization. The M_2 values converge in the MRMT and MINC models while the higher-order integrals slightly differ. They differ by around 0.6% for $M_3{}^{1/3}$, 1.5% for $M_4{}^{1/4}$, and 2.2% for $M_5{}^{1/5}$. Distributions of concentrations are thus not equal but highly close. As a consequence, differences in reaction rates R_c remain small between 2.4% and 5.1% and do not decrease with N as illustrated by the cumulative reaction rates in Figure 6. Differences in reaction rates for the bimolecular reaction are considered to come from the chemical factor rather than from the scalar dissipation rate and the concentration second moment M_2. Because the reaction rate is the product of a physical factor by a chemical factor, the reaction rate depends not only on the scalar dissipation rate but also on higher-order moments of the concentration distribution. Differences in reaction rate depend on the reactivity type and may be larger for more complex reactions.

3.3. Nonuniform Injection Conditions ($n = 1$, Layered Inclusions)

[40] To highlight the possible differences between the concentration distributions and the compensation mechanism within the MRMT model, we analyze the full mobile/immobile problem with nonuniform initial concentrations within the immobile zone described by equations (25–27). Compared to uniform initial conditions, nonuniform initial conditions with injections in the mobile zone and in the remote immobile zone have been chosen to underline possible mixing between immobile concentrations far from the

Table 3. Temporally Integrated Differences *diff*(*X*) Between Equivalent MRMT and MINC Models as Defined by Equation (32) for Two Levels of Discretization of the Immobile Zones ($N = N_{MRMT} = N_{MINC}$) Equal to 20 and 40

	n	$diff(\sigma_x)$	$diff(M_2{}^{1/2})$	$diff(M_3{}^{1/3})$	$diff(M_4{}^{1/4})$	$diff(M_5{}^{1/5})$	$diff(R_c)$
$N = 20$	1	0.014	9×10^{-4}	7.8×10^{-3}	0.017	0.026	0.11
	2	0.015	2.5×10^{-3}	6.6×10^{-3}	0.016	0.025	0.090
	3	0.015	4.3×10^{-3}	6.8×10^{-3}	0.011	0.018	0.080
$N = 40$	1	8.0×10^{-3}	4.2×10^{-4}	7.0×10^{-3}	0.016	0.024	0.10
	2	8.5×10^{-3}	1.3×10^{-3}	6.3×10^{-3}	0.016	0.025	0.087
	3	8.7×10^{-3}	2.4×10^{-3}	4.8×10^{-3}	0.01	0.017	0.081

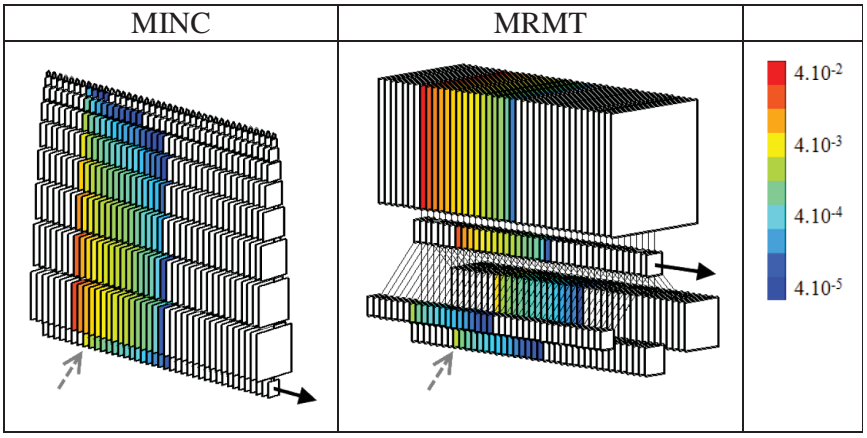

Figure 6. Reactivity integrated between $t = 0$ and $t = 10$. Parameters correspond to those of Figure 2, but with a spatial extension of 30 units.

mobile zone and mobile concentrations. Other parameters are identical to those of the previous section and given in Table 2.

[41] To maintain the comparison between the MINC and MRMT models, the relations between initial conditions in both of these frameworks are developed in Appendix B on the basis of the analytical solution obtained by the separation of variables method. As discussed in Appendix B, some of the initial "virtual concentrations" in the equivalent MRMT model can be negative depending on the shape of the initial conditions in the diffusion model. It is indeed the case for the nonuniform injection conditions as shown by Figure 9. We underline that these negative "virtual concentrations" cannot be considered as numerical errors as they fundamentally come from the sinusoidal function of equation (B3).

[42] The occurrence of the negative "virtual concentrations" in MRMT can be explained in relation to their MINC counterpart. In MINC, the immobile zones void of any concentration between the mobile zone and the remote immobile zones of nonzero concentration act as a "buffer" that must be invaded before the immobile concentration feeds the mobile zone. This lag time is natural in the MINC model where the topology of the connections delays the diffusion of the remote initial immobile concentrations to the mobile zone. In the MRMT model however, all immobile zones start to exchange concentrations at once. To maintain the equivalence between the MRMT and MINC models, the MRMT model introduces negative "virtual concentrations" that offset the contribution of the rates with positive initial concentrations. Initially, successive MRMT zones have opposite signs and the compensation mechanism of the positive and negative incoming "virtual concentrations" in the mobile zone extend over all the immobile zones (Figure 9, black dashed line and disks). The negative "virtual concentrations" progressively vanish as the immobile "virtual concentrations" break through to the mobile zone (Figure 9, solid lines). At $t = 1$, the concentration has broken through to the mobile zone in the MINC model (Figure 9, solid green line) and there is only one negative "virtual concentration" left in the MRMT model (Figure 9, dashed green line and disks). At that same time, almost all of the immobile MRMT zones but the two first ones have uniform concentrations already in equilibrium with the mobile zone because of their high exchange rate.

[43] It should be noted that the negative "virtual concentrations" show up in quite specific cases. They would not occur with uniform injections at any time of the simulation. In fact immobile concentration profiles decreasing from the mobile zone always lead to positive "virtual concentrations" in the MRMT immobile zones (Appendix B). Flat concentration profiles typical of those observed in the retreating concentration from the immobile zone after an initial invasion from the mobile zone also lead to positive concentrations in the MRMT model. In fact, no immobile zone "virtual concentration" can become negative with positive surrounding concentrations because all off-diagonal coefficients of the matrix A of equation (12) are positive or null. The negative "virtual concentrations" thus concern only the injection zone, i.e., the zone where initial concentrations in the immobile zone are nonzero.

[44] Nonetheless the existence of negative "virtual concentrations" induced by the nonuniform injection conditions, dispersions remain very close together in both the MRMT and MINC models (Figure 10a) as well as the second moment of the concentration distribution (Figure 10b) as in the uniform injection case. At later times, the same behavior as for uniform initial conditions is recovered. Reaction rates however strongly differ at early times (i.e., for $t < 0.5$), when concentrations are still influenced by the initial conditions. Differences in reaction rates (Figure 10c) are simultaneous to differences in the high order moments of the concentration distribution $M_k^{1/k}$ $(k > 2)$ (Figure 11). Like in the diffusive flush of the layered inclusion (section 1.1), the distribution of concentrations is narrower in the MRMT case than in the MINC case with a dominance of the concentrations of the smaller rates as shown by the moments of the concentration distribution for $k > 2$ (Figure 11). Even though these concentrations are smaller than the maximal concentrations of the MINC models (Figure 9), their contribution strongly determines the chemical factor of the reaction rate (equation (22)) and leads to 10 times smaller values than in the MINC case (Figure 10c).

[45] Despite the existence of negative "virtual concentrations," the MRMT model is still highly close to the

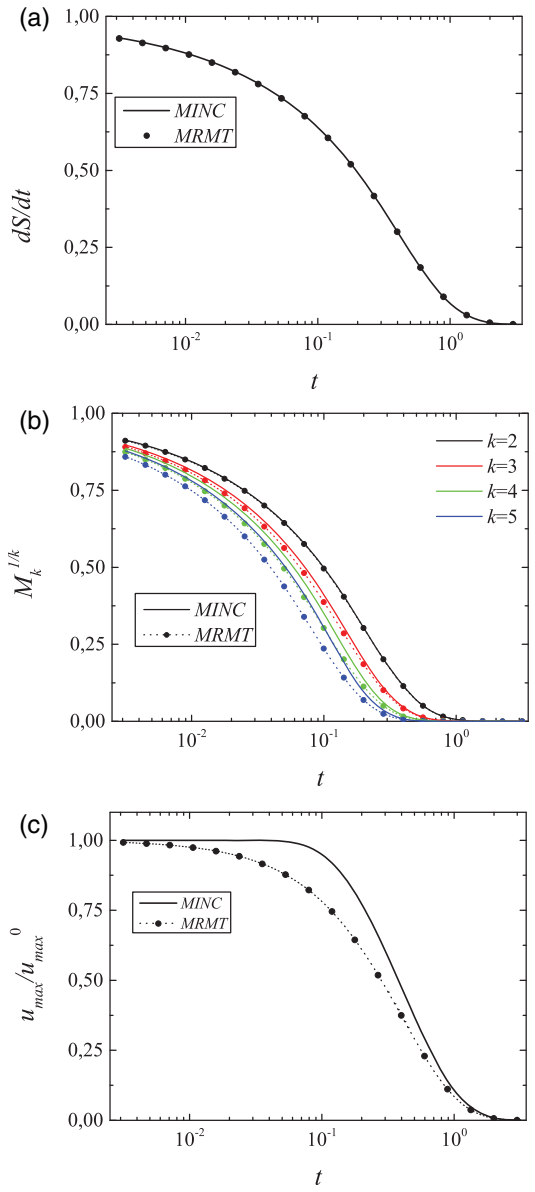

Figure 7. Temporal evolution of (a) the total concentration variation in the immobile zone dS/dt, (b) the $M_k^{1/k}$ for k = 2, . . ., 5, and (c) the maximum concentration $u_{\max}$ normalized by its initial value $u^0_{\max}$ for equivalent MRMT and MINC models in the diffusive flush of a 1-D immobile zone.

diffusion model for the dispersion and the second moment of the concentration distribution M_2. The other characteristics (reaction rates and higher-order integrals) however largely differ at early times when the influence of the initial conditions remain nonnegligible. At later times, MRMT and MINC models are again almost equivalent from all respects like in the uniform injection case.

4. Discussion

[46] We discuss successively the conservation of the concentration variance between MRMT and MINC models, the relevance of MRMT models to chemical reactivity, and the influence of the immobile porosity structure on reactivity.

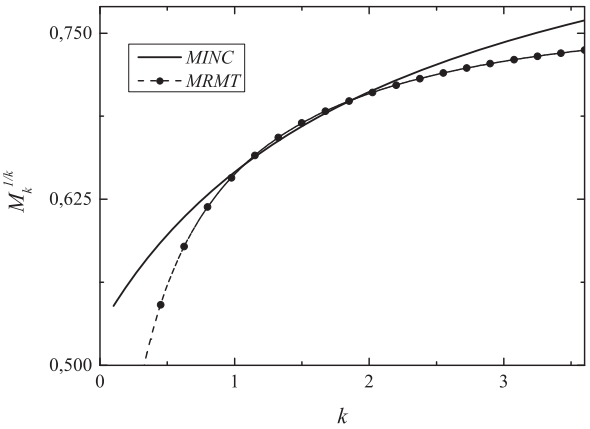

Figure 8. $M_k^{1/k}$ as a function of k for t = 0.1 in the diffusive flush of a 1-D immobile zone.

4.1. Equivalence of Concentration Variance and Scalar Dissipation Rate

[47] The equivalence of the MRMT and MINC models for the second moment of the concentration distribution, a nonlinear output of the linear transport process, was not expected. It can be analytically proven only for layered inclusions ($n = 1$) (Appendix D). The equivalence is hardly affected by the discretization and truncation orders of the MINC and MRMT models as shown by Table 3 as long as the discretization is not too small. We have also checked that the results of the previous section are general and do not depend on the main dimensionless parameters of the model (Da, β, R_d, $\overline{K}$, σ_0, Δ_0) (Table 2). While the influence of these parameters is critical on the outputs observed, the equivalence is not modified. We illustrate this by analyzing systems at different Damköhler number values Da (10, 10^2, 10^3) with other parameters fixed at their values given by Table 2 for $n = 2$ (Figure 12). Larger Da values enhance

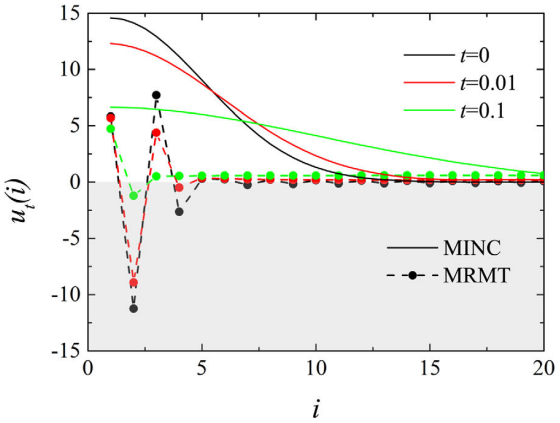

Figure 9. Concentration profiles in the immobile zone for the MRMT and MINC models at initial time ($t = 0$) and at time $t = 0.1$ for the nonuniform injection case. The gray zone underlines the negative concentration area.

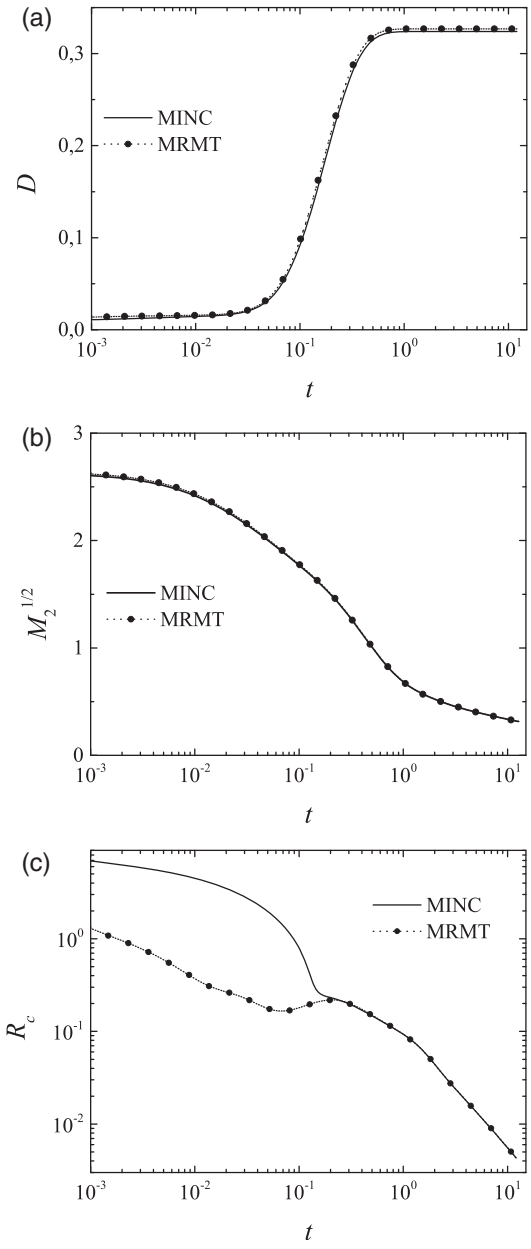

Figure 10. Same as Figure 3 for the nonuniform injection conditions along the immobile zone described by equations (25), (26), and (27). Parameters are given in Table 2, column section 3.

dispersion, mixing and initial reactivity, but do not change the equivalence between MINC and MRMT models.

[48] The equivalence of the second moment of the concentration distribution M_2 is robust as it holds whatever the model parameters, whatever the inclusion dimensionality and for different initial conditions. As M_2 is directly linked to the scalar dissipation rate (equation (1)), MRMT models do not only give consistent breakthrough curves but also consistent concentration variances and scalar dissipation rates. By itself, this result is important as it reinforces the relevance of MRMT models for modeling more complex systems. MRMT models are increasingly used for modeling large-scale transport in heterogeneous media [*Fernandez-Garcia et al.*, 2009; *Li et al.*, 2011; *Willmann et al.*, 2008] and their relevance to inert transport might be generically extended to at least some mixing characteristics like the scalar dissipation rate.

4.2. Relevance of Immobile Concentrations for Chemical Reactions in MRMT Models

[49] The previous analysis shows that the concentration distributions coming from MRMT and MINC models are close together for uniform injection conditions. What we have called in introduction the "virtual concentrations" can be handled as effective chemical concentrations of elements that can react with other elements. It was not granted from the onset, as the "virtual concentrations" are a byproduct of the derivation of the MRMT model from the analytical solutions of the diffusion equation in inclusions of different dimensionalities. In more complex cases however, the relevance of the "virtual concentrations" for reactivity is limited by several factors. The strict equivalence of MRMT and MINC models ends up at the scalar dissipation rate. Both models have different higher-order concentration moments $M_k^{1/k}$ (equation (17)) and different reaction rates (equation (18)) for simple bimolecular reactions at chemical equilibrium. If differences remain small (of the order of a few percents) for uniform injection conditions along the immobile zone, differences can be quite large with nonuniform injection conditions in the time range where the influence of the initial conditions remains nonnegligible. It is especially the case when initial conditions are nonzero far from the mobile zone.

[50] The largest differences come from the initial negative "virtual concentrations" of some of the MRMT rates in the nonuniform injection case. These negative "virtual concentrations" are necessary to ensure the initial delay of the concentration breakthrough to the mobile zone. They could be acceptable for conservative components. In the case of the bimolecular reaction previously described, positive and negative concentrations would correspond to one of the reactant concentration either higher or lower than the

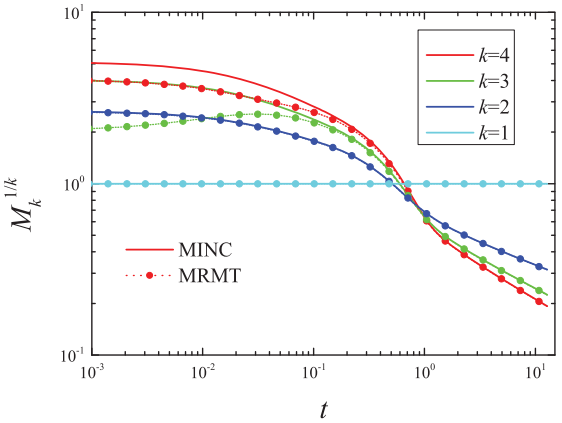

Figure 11. Temporal evolution of the first five moments of the concentration distribution $M_k^{1/k}$ for the layered case (n = 1) with nonuniform injection conditions along the immobile zone. Same parameters as in Figure 10.

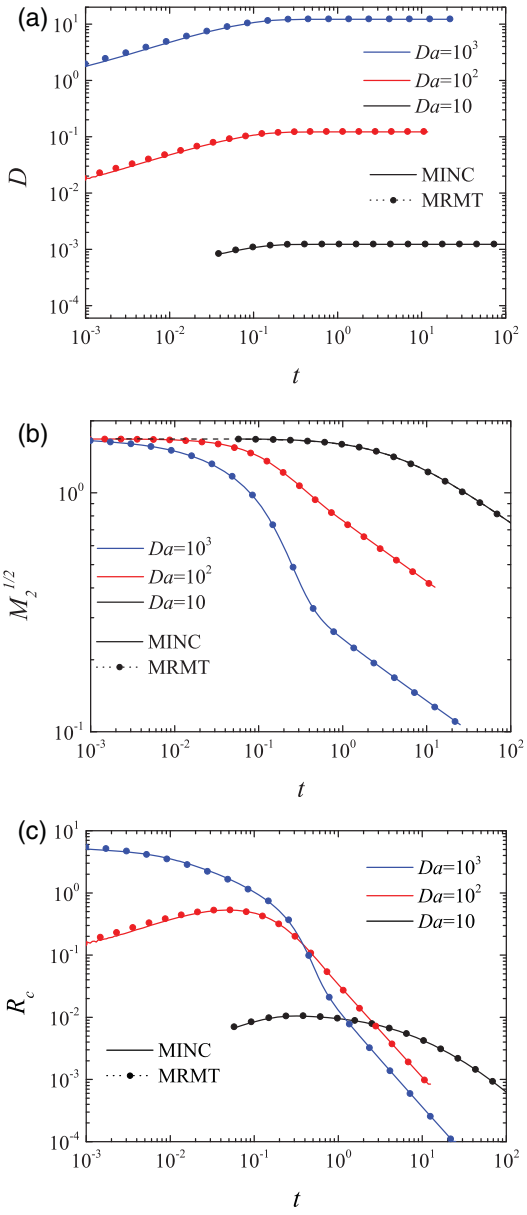

Figure 12. Temporal evolution of the (a) dispersion coefficient, (b) square root of the second moment of the concentration distribution, and (c) the reaction rate as functions of the Damköhler number (ratio of the characteristic diffusion time in the immobile zone to the characteristic advection time in the mobile zone). Parameters are synthesized in Table 2, column section 4.

other one. However, it is a severe limitation when considering that the transported species are directly chemical elements. The concept of immobile zone concentration should then be taken with great care and systematically assessed when modifying the initial conditions.

4.3. Influence of Immobile Porosity Structure on Reactivity

[51] The case of the nonuniform injection conditions shows that a more complex initial organization of the concentration field highlights the topological differences between the MRMT and MINC models (Figure 1) and that these differences can be nonnegligible as long as the concentration field retains the memory of the initial organization. Differences in reactivity might be even higher with more complex topological structures of the immobile zones. We have so far considered only two cases. Either all immobile zones are connected to the mobile zone, or the immobile zones (MRMT) are linearly connected between themselves (MINC). Inclusion dimensionality does not change the topology but the distribution of the volumes affected to the immobile zones. More complex topological structure may however occur in natural media. While, in fractured media, the observed wide-range distribution of the diffusion times [*Liu et al.*, 2004, 2007; *Zhou et al.*, 2007] has been related to the distribution of matrix-block sizes [*Haddad et al.*, 2012; *Kfoury et al.*, 2006; *Roubinet et al.*, 2010, 2012, 2013; *Zhan et al.*, 2009], it might also come from the topology of dead end and poorly linked fractures, which extension sharply increases from 2-D to 3-D [*de Dreuzy et al.*, 2001, 2012b]. Such secondary structures occur on a large range of scales from the fracture scale because of fracture aperture heterogeneities and from the

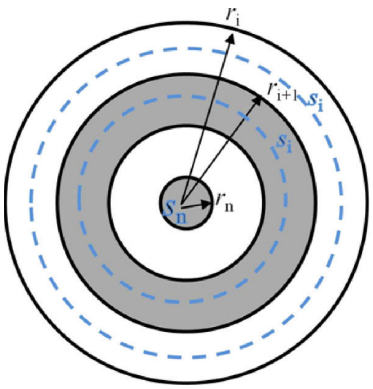

Figure 13. Sketch of the annuli and concentrations for cylindrical immobile zones ($n = 2$). The concentration s_i is defined at the middle of the two successive annuli r_i and r_{i+1}.

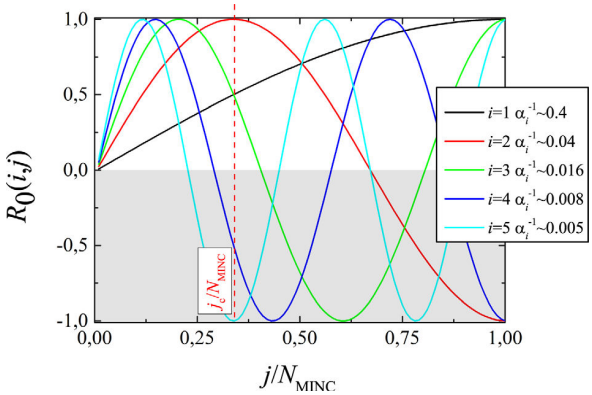

Figure 14. R_0(i, j) (equation (B9)) as a function of j/N_{MINC} for the five smallest MRMT rates (i = 1, . . ., 5).

complexity of the fracture gouge [*Andersson et al*., 2004; *Auradou et al*., 2006; *Brown et al*., 1998; *Méheust and Schmittbuhl*, 2001] to the network scale [*Davy et al*., 2006, 2010; *Odling*, 1997]. Multiple INteracting Continua result essentially from a discretization of the nonfractured part of the rock (matrix) according to the sole metric of the distance to the mobile zone [*Karimi-Fard et al*., 2006]. A topological characteristic might however be necessary for modeling reactive transport shifting the Multiple INteracting Continua framework (MINC) to a Structure INteracting Continua framework (SINC). Structure can be straightforwardly embedded in the developed formalism by simply modifying the matrix A of equation (12) characterizing the interaction between the immobile zones to include branching and dead ends parameters controlling the metric and topological organization of the immobile zones like what has classically been done for fractals or networks [*Barrat et al*., 2012; *Bouchaud and Georges*, 1990; *Havlin and Ben-Avraham*, 1987]. The range of possible topological structures may be further extended to those resulting from connectivity structures in porous media [*Le Goc et al*., 2009; *Renard and Allard*, 2012], or resulting from reactive transport processes like wormholes and dissolution patterns [*Andreani et al*., 2009; *Daccord et al*., 1993; *Fredd and Folger*, 1998; *Golfier et al*., 2002].

[52] Although incomplete, simplified interaction models like the Multi-Rate Mass Transfer (MRMT), the Multiple INteracting Continua (MINC), or the Structured INteracting Continua (SINC) are of interest as they propose an intermediary level of complexity to analyze nonlinear processes as mixing and the induced reactivity. On one hand, they maintain some structure in the model. On the other hand, they are not as complex as fully heterogeneous models for which analytical approximations still rely on some complex numerical closure assumptions [*Chiogna et al*., 2011; *de Dreuzy et al*., 2012a; *Jha et al*., 2011a, 2011b; *Kapoor and Kitanidis*, 1998; *Tennekes and Lumley*, 1972].

[53] While diffusion has a strong homogenization effect on transport processes and practically removes the details of the structures including most of the topological characteristics [*Haggerty and Gorelick*, 1995; *Villermaux*, 1987], chemical reactions coupled to diffusion may lead to significantly more localization and segregation as observed on the influence of concentration fluctuations [*de Anna et al*., 2011] and in geochemical self-organization, auto-catalytic reactions and where dimensionality has a critical influence [*Ortoleva*, 1994; *Pearson*, 1993; *Renard et al*., 1998]. Reactivity is, however, expected to differ from these pure diffusion-reaction processes because of the coupling induced by the mobile zone. Solute at evolving concentrations are constantly either brought up or removed from the immobile zone. If connections with the immobile zone are strong like in the MRMT model, the mobile zone will be likely more important than in more linear and ramified structures for which mobile/immobile interactions are limited to a single immobile zone. Interaction with the mobile zone is also expected to have more complex effects because of the strong organization of the velocity field induced by permeability heterogeneities [*Chiogna et al*., 2011; *Le Borgne et al*., 2007, 2008; *Luo and Cirpka*, 2008, 2011] that cannot be reduced to diffusion-like processes [*Becker and Shapiro*, 2000].

5. Conclusion

[54] We investigate numerically the influence of the immobile zone structure on mixing characteristics, concentration distribution, and reaction rate of a simple bimolecular reaction at chemical equilibrium in the framework of mobile/immobile models. The comparison relies on the MRMT and MINC immobile zone organizations both based on the diffusion in one-dimensional diffusive inclusions. In Multi-Rate Mass Transfer models (MRMT), all immobile zones are directly linked to the mobile zone, and this mobile zone is the only exchanger between the immobile zones (star connectivity). In Multiple INteracting Continua models (MINC), immobile zones are linked as a regular chain with a single element in relation with the immobile zone whatever the dimensionality of the immobile zone (chained connectivity). As both models derive from the same equation, they are equivalent in terms of transport in the mobile zone. Immobile zone concentrations in the MRMT model are a byproduct of the equivalence and are denominated "virtual concentrations" before checking their relevance to model real chemical concentrations. We use the simple bimolecular reaction at equilibrium as a typical example of chemical reactivity.

[55] We show that both MRMT and MINC models have the same concentration variance whatever the model parameters, dimensionality, and initial conditions. While their concentration variance strongly evolves with the model parameters and immobile zone dimensionality, they do not depend on the organization of the immobile zone, star connectivity in MRMT and chained connectivity in MINC. We confirm analytically this result for the flush of an n-dimensional immobile zone. When chemical reactivity is dominated by characteristics derived from the concentration variance (like the scalar dissipation rate), reactivity is independent of the structure of immobile porosity, and immobile zone "virtual concentrations" in the MRMT models can be handled as real chemical concentrations.

[56] However, the porosity structure has a critical influence on chemical reactivity when initial conditions induce more complex mixing patterns. It is especially the case for high initial concentration gradients in the immobile zone. Differences in higher moments of the immobile concentration distributions are amplified by the nonlinearity of the chemical reaction. Some of the immobile zone "virtual concentrations" in the MRMT model are negative to offset the direct connectivity of all immobile zones to the mobile zone. When high initial "virtual concentrations" are distant from the mobile zone, the immediate exchange with positive immobile zone concentrations is offset by exchanges with negative immobile zone "virtual concentrations" ensuring some delay of the concentration breakthrough to the mobile zone. Negative "virtual concentrations" may not be a fundamental problem for conservative components, which are linear combination of species concentrations. Yet they imply a severe limitation to MRMT models for the transport of real chemical concentrations. The concept of immobile zone concentration should then be taken with great care and systematically assessed when modifying the initial conditions.

[57] Strong immobile concentration gradients highlight the role of immobile porosity structure on chemical

reactivity and on the limits of the relevance of the MRMT to model chemical reactivity. Further evaluations are needed for more complex topological structures of the immobile zones and for complete chemical systems.

Appendix A: Mass and Interaction Matrix for the MRMT and MINC Models With Diffusion in Dimension *n*

[58] We discretize equations (9–11) according to a finite volume scheme for which the unknown concentrations S_i are taken at the middle between the annuli of radii r_i and r_{i+1} (Figure 13)

$$v_n\left(r_i^n - r_{i+1}^n\right)\frac{\partial S_i}{\partial t} = Q_{i+1} - Q_i \quad \text{for} \quad i = 1, \ldots, N_{MINC} - 1, \tag{A1}$$

where $r_1, \ldots, r_{N_{MINC}+1}$ is a concentric discretization starting at the interface between the mobile and immobile zones $r_1 = 1$ and ending at the immobile zone center $r_{N_{MINC}+1} = 0$, v_n is the volume of the unit sphere in dimension n (v_n is equal to 1, π, and $4/3\pi$ for $n = 1$, 2, and 3) and the fluxes Q_i are given by

$$\begin{aligned} Q_1 &= -a_n \frac{2r_1^{n-1}}{r_1 - r_2}(C - S_1) \\ Q_i &= -a_n \frac{2r_i^{n-1}}{r_{i-1} - r_{i+1}}(S_{i-1} - S_i) \quad \text{for} \quad i = 2 \ldots N_{MINC} - 1 \\ Q_{N_{MINC}+1} &= 0, \end{aligned} \tag{A2}$$

where a_1 is the surface of the unit sphere in dimension n (a_n is equal to 1, 2π, and 4π for $n = 1$, 2, and 3). The concentration c is considered homogeneous in the mobile zone at position x. Equation (9) is rewritten to integrate the continuity of solute flux at the mobile/immobile interface and modified to keep symmetrical expressions for the diffusive fluxes

$$\left(\frac{\sigma}{a_n r_1^{n-1}}\right)^{-1}\left(\frac{\partial C(x,t)}{\partial t} - L(C)\right) = Q_1, \tag{A3}$$

where σ is the ratio of the porous surface of the mobile/immobile interface per unit mobile volume [*Carrera et al.*, 1998] and L is the transport operator defined in equation (13). With the additional knowledge of the mean surface to volume ratio of the matrix blocks S_{im}/V_{im}, σ can straightforwardly be related to the porous volume ratio β of equation (2) by

$$\sigma = \frac{S_{im}}{V_{im}}\beta. \tag{A4}$$

[59] The surface to volume ratio in dimension n is $S_{im}/V_{im} = n/r_1$. The diagonal mass matrix defined by equation (12) is deduced with some rearrangement of the mobile equation (A3) to express A_{MINC} as a symmetrical matrix. As diffusion is a nondirectional process, A_{MINC} can in fact be expressed as a symmetrical matrix

$$\begin{aligned} M_{MINC}(1,1) &= \frac{v_n r_1^n}{\beta} \\ M_{MINC}(i,i) &= v_n\left(r_{i-1}^n - r_i^n\right) \quad \text{for} \quad i = 2, \ldots, N_{MINC} + 1, \end{aligned} \tag{A5}$$

where we also accounted for the shift of indices in the immobile zone. Note that $\frac{v_n r_1^n}{\beta}$ is simply the volume of the mobile zone expressed as a function of the capacity ratio β and of the characteristic volume of the immobile zone. The immobile to mobile porosity ratio is contained in β. Using (12) and (A1–A4), we deduce the interaction matrix

$$\begin{aligned} A_{MINC}(2,1) &= 2a_n \frac{r_1^{n-1}}{r_1 - r_2} \\ A_{MINC}(1,2) &= A_{MINC}(2,1) \\ A_{MINC}(1,1) &= -A_{MINC}(1,2) \\ A_{MINC}(i-1,i) &= 2a_n \frac{r_{i-1}^{n-1}}{r_{i-2} - r_i} \quad \text{for} \quad i = 3, \ldots, N_{MINC} \\ A_{MINC}(i,i+1) &= A_{MINC}(i-1,i) \quad \text{for} \quad i = 3, \ldots, N_{MINC} \\ A_{MINC}(i,i) &= -\left(A_{MINC}(i,i+1) + A_{MINC}(i,i-1)\right) \quad \text{for} \quad i = 2, \ldots, N_{MINC} - 1 \\ A_{MINC}(i,i) &= -A_{MINC}(i,i-1) \quad \text{for} \quad i = N_{MINC}. \end{aligned} \tag{A6}$$

[60] A_{MINC} is a tri-diagonal matrix. All elements outside of the three central diagonals are equal to zero.

[61] Multi-Rate Mass Transfer models are expressed by equation (9) in the mobile zone and the following equation in the immobile zone

$$\frac{\partial S_i}{\partial t} = \alpha_i (C - S_i) \quad \text{for} \quad i = 2, \ldots, N_{MRMT} + 1. \tag{A7}$$

[62] The derivation of the Multi-Rate Mass Transfer model equivalent to the diffusion within an immobile zone of dimension n leads to the following mass and interaction matrices [*Carrera et al.*, 1998; *Haggerty and Gorelick*, 1995]

$$\begin{aligned} M_{MRMT}(1,1) &= \frac{v_n r_1^n}{\beta} \\ M_{MRMT}(i,i) &= V_N^n b_{i-1} \text{for} \quad i = 2, , \ldots, N_{MRMT} + 1 \end{aligned} \tag{A8}$$

and

$$\begin{cases} A_{MRMT}(1,i) = 2nV_N^n \\ A_{MRMT}(i,i) = -2n\ V_N^n \quad \text{for} \quad i = 2, \ldots, N_{MRMT} + 1 \\ A_{MRMT}(i,1) = 2nV_N^n \end{cases} \tag{A9}$$

$$A_{MRMT}(1,1) = -\sum_{i=2}^{N_{MRMT}+1} A(1,i),$$

where only the first N_{MRMT} elements of the infinite series have been kept

$$V_N^n = \frac{v_n r_1^n}{\sum_{i=1}^{N} b_i} \tag{A10}$$

and the exchange rate of the immobile porosity of α_i is denoted b_i. The series of α_i and b_i can directly be derived from *Haggerty and Gorelick* [1995, Table 1]

$$\begin{aligned} n=1 \;\; \alpha_i &= \frac{(2i-1)^2\pi^2}{4} \\ n=2 \;\; \alpha_i &= u_i^2 \\ n=3 \;\; \alpha_i &= i^2\pi^2 \end{aligned} \tag{A11}$$

with u_i the ith root of the zero-order Bessel function of the first kind and

$$b_i = \frac{2n}{\alpha_i}. \tag{A12}$$

[63] The normalization by the sum of b_i coefficients is required to enforce that the ratio of the immobile to mobile porous volumes be equal to β. The interaction matrix A_{MRMT} is an arrow-type of matrix with only nonzero elements in the first line, in the first column and in the diagonal expressing a star-shaped connectivity structure.

Appendix B: Relation Between Initial Immobile-Zone Concentrations in the Diffusive Flush of a 1-D Immobile Zone

[64] This appendix considers the simpler case of a 1-D diffusion with simplified initial and boundary conditions. In 1-D, the dimensionless diffusion equation is

$$\frac{\partial s}{\partial t} = \frac{\partial^2 s}{\partial y^2} \text{for } 0 \le y \le 1, \tag{B1}$$

where $s(y, t)$ is the concentration in the immobile zone at the distance 1-y from the mobile zone. Under more specific initial and boundary conditions, a fully analytical solution may also be derived using the method of separation of variables. Assuming $c(t) = 0$

$$s(y,t) = \sum_{i=1}^{\infty} \gamma_i \sin\left(\sqrt{\alpha_i} y\right) e^{-\alpha_i t} \tag{B2}$$

with

$$\gamma_i = 2\int_0^1 s_0(y) \sin\left(\sqrt{\alpha_i} y\right) dy. \tag{B3}$$

[65] Integrating over y leads to the classical expression of the MRMT model in 1-D. We derive the relation between the initial concentrations in the MRMT and MINC models from the general expressions (B2) and (B3). For MINC, we simply average the concentration along the immobile zone in N_{MINC} elements of equal dimension $1/N_{MINC}$

$$S_0^{MINC}(j) = N_{MINC} \int_{\frac{j-1}{N_{MINC}}}^{\frac{j}{N_{MINC}}} s_0(y) dy \tag{B4}$$

for $j = 1, \ldots, N_{MINC}$. We recall that lower and upper case concentrations stand, respectively, for continuous and integrated quantities. For MRMT, we express that the exchanges between mobile and immobile zones are equal to that in the diffusion solution and find

$$S_0^{MRMT}(i) = \frac{1}{2}\sqrt{\alpha_i}\gamma_i \tag{B5}$$

for $i = 0, \ldots, N_{MRMT}$, where γ_i is given by (B3). If we further assume that the initial concentration is discretized as in the MINC model, we can express from (B5) a relation between the initial concentrations in the MINC and MRMT models

$$S_0^{MRMT}(i) = 2\sin\left(\frac{\sqrt{\alpha_i}}{2N_{MINC}}\right) \sum_{j=1}^{N_{MINC}} \sin\left(\frac{\sqrt{\alpha_i}}{2N_{MINC}}(2j-1)\right) S_0^{MINC}(j), \tag{B6}$$

which can also be expressed in algebraic form

$$S_0^{MRMT} = 2D_0 R_0 S_0^{MINC} \tag{B7}$$

with D_0 the square diagonal matrix of size N_{MRMT}^2

$$D_0(i,j) = \sin\left(\frac{\sqrt{\alpha_i}}{2N_{MINC}}\right)\delta(i,j) \tag{B8}$$

[66] R_0 the full rectangular matrix N_{MRMT}. N_{MINC} of coefficients

$$R_0(i,j) = \sin\left(\frac{\sqrt{\alpha_i}}{2N_{MINC}}(2j-1)\right) \tag{B9}$$

and $S_0^{MRMT} = \left(s_0^{MRMT}(1), \ldots, s_0^{MRMT}(N_{MRMT})\right)^T$ and $S_0^{MINC} = \left(s_0^{MINC}(1), \ldots, s_0^{MINC}(N_{MINC})\right)^T$. Aside from the discretization and truncation errors in the MINC and MRMT models, the algebraic relation holds not only at the initial time but at all times and shows how the concentrations in the immobile zones are related in the MRMT and MINC frameworks.

[67] The diagonal matrix D_0 expresses a global weighting function of the discretization step of the MINC model while each element (i, j) of the matrix R_0 can be considered as the relative weight of the concentration at the position j/N_{MINC} in the MINC model to the concentration of the characteristic rate α_i in the MRMT model. As shown by Figure 14, the weight $R_0(i, j)$ strongly evolves with j/N_{MINC} and, apart from the smallest rate α_1 ($i = 1$), take both positive and negative values (in the white and gray parts of the graph, respectively). Depending on the initial concentrations in the MINC model, some of the initial concentrations in the MRMT model can be negative. The case of a uniform injected concentration in the MINC model is quite specific as it induces a uniform concentration in the MRMT model with all initial MRMT concentrations positive [*Haggerty and Gorelick*, 1995]. We can indeed show that $2D_0(i,i)\sum_{j=1}^{N_{MINC}} R_0(i,j)$ tends to 1 when N_{MINC} tends to infinity whatever the value of i. The uniform injection case gives also some indications on the relative contribution of the MINC zones to the MRMT transfer rates. For a given rate α_i of index i, only the first quarter period of $R(i, j)$ as a

function of j is nonzero as the remaining of the sum is performed over an integer number of half periods. The critical value of j below which the sum gives a nonzero contribution is denoted j_c (Figure 14) and is approximately equal to

$$\frac{j_c}{N_{MINC}} \approx \frac{1}{2i-1}. \tag{B10}$$

[68] For $i = 1$, the full immobile zone contributes positively to the first MRMT rate α_1, while, for $i = 2$, only the first third closest to the mobile zone contributes positively to the second MRMT rate α_2. For higher rates (smaller characteristic times), the positive contribution to the MRMT concerns always a smaller part of the immobile zone next to the mobile zone. Globally, the first transfer rate of the MRMT model is the sole rate that accounts positively for around the two-thirds of the immobile zone remote from the mobile zone. It is a large percentage that is reflected by the importance in volume of the first rate relatively to the other rates ($b_1 \sim 0.8$).

Appendix C: Second Moment of the Concentration Distribution in the Diffusive Flush of a 1-D Immobile Zone

[69] We start by computing the mean of the concentration squared in the MINC framework from its expression derived in Appendix B in the particular case of the same number of terms for the MINC and MRMT models $N_{MINC} = N_{MRMT}$. As the solution (B2) has been obtained using the method of separation of variables, we express it as

$$\int_{y=0}^{1} s^2(y,t)dy = \sum_{k=1}^{N_{MINC}} \sum_{i'=1}^{N_{MINC}} \gamma_i \gamma_{i'} e^{-(\alpha_i+\alpha_{i'})\bar{t}} \int_0^1 \sin(\sqrt{\alpha_i}y)\sin(\sqrt{\alpha_{i'}}y)dy \tag{C1}$$

which simplifies to

$$\int_{y=0}^{1} s^2(y,t)dy = \sum_{i=1}^{N_{MINC}} b_i \left(s_0^{MRMT}(k)e^{-\alpha_i t}\right)^2 \tag{C2}$$

by using (A11), (B5) and the orthogonality of the sine functions

$$\int_0^1 \sin(\sqrt{\alpha_i}y)\sin(\sqrt{\alpha_{i'}}y)dy = \frac{1}{2}\delta(i,i') \tag{C3}$$

[70] The right-hand side term of equation (C2) is precisely the solution of the MRMT model with an initial nonuniform concentration S_0^{MRMT}. The equality (C2) of the mean squared concentration directly derives from the orthogonality of the basis function used to express the analytical solution with the method of separation of variables. This argument does no longer hold for higher-order moments for which the product of more than three sine functions does not integrate necessarily to 0.

Appendix D: Flush of a 1-D Immobile Zone

[71] To get some additional insights into the conservation of the concentration variance, we consider the simpler problem of the flush by diffusion of 1-D immobile zone corresponding to equations (3), (5), and (6) with uniform initial conditions

$$s(r, t=0) = 1. \tag{D1}$$

[72] The concentration in the mobile zone is set to zero at all times. Solutions to this simpler problem are fully analytical both for the diffusion problem (Appendix B, equations (B2) and (B3)) and for the MRMT model

$$s_i(t) = \exp(-\alpha_i t) \tag{D2}$$

for $i = 1, \ldots, \infty$ and where the coefficients α_i are given by equation (A11). Both solutions are expressed as infinite series that we truncate at a large enough index (200) so that the truncation error can be neglected. Parameters are otherwise identical to those used in the previous section. We check that the total variation of masses in the immobile zone are equal for the MRMT and diffusion models (Figure 7a). The $M_2^{1/2}$ values are also equal between both models (Figure 7b, black lines). This equality can be demonstrated analytically in this specific 1-D diffusion case whatever the initial conditions (Appendix C). The equality fundamentally comes from the orthogonality of the family of functions used to construct the solution within the variable separation method. The higher-order integrals $M_k^{1/k}$ however differ (Figure 7b, colored lines). The full evolution of $M_k^{1/k}$ with k is shown in Figure 8 for k ranging from 0.1 to 3.5. It shows that $M_k^{1/k}$ values are equal between both models for $k = 1$ and $k = 2$. Between 1 and 2, $M_k^{1/k}$ remain very similar while they slightly differ for lower and higher k values. As the moments only slightly differ, the distributions of concentration remain close between the diffusion and the MRMT models.

[73] Concerning now the differences between the distributions, the higher differences occur for the lower and higher values of the order k, which are more sensitive to the extreme of the distribution. In fact, the maximum concentrations differ and their difference can reach 25% (Figure 7c). They remain higher in the diffusion model than in the MRMT model as, at early times, they are away from the mobile zone and unaffected by the evolution of its concentration. In the MRMT model, however, the mobile/immobile exchanges affect all concentrations including their maximum at once. Minimal concentrations have also higher probabilities in the diffusion model than in MRMT (Figure 8). The concentration distribution is wider in the diffusion model than in MRMT. The stronger importance of intermediary concentrations in the MRMT model fundamentally comes from the extreme dominance of the concentrations of the lowest rates with the highest porosity ratios (Table 1). The concentration distribution dominated by these few discrete values is narrower with smaller probability of occurrence of its extremes. To maintain an equivalent exchange between mobile and immobile zones, MRMT thus includes a compensation mechanism where less smaller concentrations are compensated by less larger concentrations.

[74] **Acknowledgments.** The European Union is acknowledged for its funding through the Marie-Curie fellowship PIEF-GA-2009–251710 and the ANR through its project H2MNO4 under ANR-12-MONU-0012-01. The INRA-INRIA "VITELBIO" is also acknowledged to have supported the collaboration between the first, second, and fourth authors. We thank Tim Ginn and Ahmed Ali for their careful review and relevant contribution to the paper and Daniel Fernandez-Garcia for his editorial work.

References

Andersson, P., J. Byegård, E.-L. Tullborg, T. Doe, J. Hermanson, and A. Winberg (2004), In situ tracer tests to determine retention properties of a block scale fracture network in granitic rock at the Aspo Hard Rock Laboratory, Sweden, *J. Contam. Hydrol.*, *70*(3–4), 271–297.

Andreani, M., L. Luquot, P. Gouze, M. Godard, E. Hoisé, and B. Gibert (2009), Experimental study of carbon sequestration reactions controlled by the percolation of CO_2-rich brine through peridotites, *Environ. Sci. Technol.*, *43*(4), 1226–1231.

Aquilina, L., and J.-R. de Dreuzy (2011), Relationship of present saline fluid with paleomigration of basinal brines at the basement/sediment interface (Southeast basin of France), *Appl. Geochem.*, *26*(12), 1933–1945.

Aquilina, L., P. Boulvais, and J.-R. Mossmann (2011), Fluid migration at the basement/sediment interface along the margin of the Southeast basin (France): Implications for Pb-Zn ore formation, *Miner. Deposita*, *46*(8), 959–979, doi:10.1007/s00126-011-0360-9.

Auradou, H., G. Drazer, A. Boschan, J. P. Hulin, and J. Koplik (2006), Flow channeling in a single fracture induced by shear displacement, *Geothermics*, *35*(5–6), 576–588.

Barrat, A., M. Barthélemy, and A. Vespignani (2012), *Dynamical Processes on Complex Networks*, Cambridge Univ. Press, Cambridge, U. K.

Başağaoğlu, H., B. J. McCoy, T. R. Ginn, F. J. Loge, and J. P. Dietrich (2002), A diffusion limited sorption kinetics model with polydispersed particles of distinct sizes and shapes, *Adv. Water Resour.*, *25*(7), 755–772.

Becker, M. W., and A. M. Shapiro (2000), Tracer transport in fractured crystalline rock: Evidence of nondiffusive breakthrough tailing, *Water Resour. Res.*, *36*(7), 1677–1686.

Benson, D. A., S. W. Wheatcraft, and M. M. Meerschaert (2000), Application of a fractional advection-dispersion equation, *Water Resour. Res.*, *36*(6), 1403–1412.

Berkowitz, B., A. Cortis, M. Dentz, and H. Scher (2006), Modeling non-Fickian transport in geological formations as a continuous time random walk, *Rev. Geophys.*, *44*, RG2003, doi:10.1029/2005RG000178.

Bouchaud, J.-P., and A. Georges (1990), Anomalous diffusion in disordered media: Statistical mechanisms, models and physical applications, *Phys. Rep.*, *195*(4–5), 127–293.

Brown, S., A. Caprihan, and R. Hardy (1998), Experimental observation of fluid flow channels in a single fracture, *J. Geophy. Res.*, *103*(B3), 5125–5132.

Carrera, J., X. Sanchez-Vila, I. Benet, A. Medina, G. Galarza, and J. Guimera (1998), On matrix diffusion: Formulations, solution methods and qualitative effects, *Hydrogeol. J.*, *6*(1), 178–190.

Charlton, S. R., and D. L. Parkhurst (2011), Modules based on the geochemical model PHREEQC for use in scripting and programming languages, *Comput. Geosci.*, *37*(10), 1653–1663.

Chiogna, G., O. A. Cirpka, P. Grathwohl, and M. Rolle (2011), Transverse mixing of conservative and reactive tracers in porous media: Quantification through the concepts of flux-related and critical dilution indices, *Water Resour. Res.*, *47*, W02505, doi:10.1029/2010WR009608.

Daccord, G., O. Lietard, and R. Lenormand (1993), Chemical dissolution of a porous-medium by a reactive fluid. 1. Model for the wormholing phenomenon, *Chem. Eng. Sci.*, *48*(1), 169–178.

Daus, A. D., E. O. Frind, and E. A. Sudicky (1985), Comparative error analysis in finite-element formulations of the advection-dispersion equation, *Adv. Water Resour.*, *8*(2), 86–95.

Davy, P., O. Bour, J.-R. de Dreuzy, and C. Darcel (2006), Flow in multiscale fractal fracture networks, *Geol. Soc. Spec. Publ.*, *261*(1), 31–45.

Davy, P., R. Le Goc, C. Darcel, O. Bour, J. R. de Dreuzy, and R. Munier (2010), A likely universal model of fracture scaling and its consequence for crustal hydromechanics, *J. Geophys. Res.*, *115*, B10411, doi:10.1029/2009JB007043.

de Anna, P., T. Le Borgne, M. Dentz, D. Bolster, and P. Davy (2011), Anomalous kinetics in diffusion limited reactions linked to non-Gaussian concentration probability distribution function, *J. Chem. Phys.*, *135*(17), 174104.

de Dreuzy, J.-R., P. Davy, and O. Bour (2001), Hydraulic properties of two-dimensional random fracture networks following a power law length distribution: 1. Effective connectivity, *Water Resour. Res.*, *37*(8), 2065–2078.

de Dreuzy, J.-R., J. Carrera, M. Dentz, and T. Le Borgne (2012a), Time evolution of mixing in heterogeneous porous media, *Water Resour. Res.*, *48*, W06511, doi:10.1029/2011WR011360.

de Dreuzy, J.-R., Y. Méheust, and G. Pichot (2012b), Influence of fracture scale heterogeneity on the flow properties of three-dimensional Discrete Fracture Networks (DFN), *J. Geophys. Res.*, *117*, B11207, doi:10.1029/2012JB009461.

Dentz, M., and B. Berkowitz (2003), Transport behavior of a passive solute in continuous time random walks and multirate mass transfer, *Water Resour. Res.*, *39*(5), 1111, doi:10.1029/2001WR001163.

de Simoni, M., J. Carrera, X. Sánchez-Vila, and A. Guadagnini (2005), A procedure for the solution of multicomponent reactive transport problems, *Water Resour. Res.*, *41*, W11410, doi:10.1029/2005WR004056.

Donado, L. D., X. Sanchez-Vila, M. Dentz, J. Carrera, and D. Bolster (2009), Multicomponent reactive transport in multicontinuum media, *Water Resour. Res.*, *45*, W11402, doi:10.1029/2008WR006823.

Fernàndez-Garcia, D., G. Llerar-Meza, and J. J. Gómez-Hernández (2009), Upscaling transport with mass transfer models: Mean behavior and propagation of uncertainty, *Water Resour. Res.*, *45*, W10411, doi:10.1029/2009WR007764.

Fourcade, S., L. Trotignon, P. Boulvais, I. Techer, M. Elie, D. Vandamme, E. Salameh, and H. Khoury (2007), Cementation of kerogen-rich marls by alkaline fluids released during weathering of thermally metamorphosed marly sediments. Part I: Isotopic (C,O) study of the Khushaym Matruk natural analogue (central Jordan), *Appl. Geochem.*, *22*(7), 1293–1310.

Fredd, C. N., and H. S. Folger (1998), Alternative stimulation fluids and their impact on carbonate acidizing, *Soc. Pet. Eng. J.*, *13*(34), 34–41.

Ginn, T. R. (2009), Generalization of the multirate basis for time convolution to unequal forward and reverse rates and connection to reactions with memory, *Water Resour. Res.*, *45*, W12419, doi:10.1029/2009WR008320.

Glassley, W. E., A. M. Simmonsb, and J. R. Kercher (2002), Mineralogical heterogeneity in fractured, porous media and its representation in reactive transport models, *Appl. Geochem.*, *17*(6), 699–708.

Godsil, C., and G. F. Royle (2001), Algebraic Graph Theory, Springer, New York.

Golfier, F., C. Zarcone, B. Bazin, R. Lenormand, D. Lasseux, and M. Quintard (2002), On the ability of a Darcy-scale model to capture wormhole formation during the dissolution of a porous medium, *J. Fluid Mech.*, *457*, 213–254.

Golfier, F., M. Quintard, F. Cherblanc, B. A. Zinn, and B. D. Wood (2007), Comparison of theory and experiment for solute transport in highly heterogeneous porous medium, *Adv. Water Resour.*, *30*(11), 2235–2261.

Gouze, P., Y. Melean, T. Le Borgne, M. Dentz, and J. Carrera (2008), Non-Fickian dispersion in porous media explained by heterogeneous microscale matrix diffusion, *Water Resour. Res.*, *44*, W11416, doi:10.1029/2007WR006690.

Gramling, C. M., C. F. Harvey, and L. C. Meigs (2002), Reactive transport in porous media: A comparison of model prediction with laboratory visualization, *Environ. Sci. Technol.*, *36*(11), 2508–2514.

Grisak, G. E., and J. F. Pickens (1980), Solute transport through fractured media. 1. The effect of matrix diffusion, *Water Resour. Res.*, *16*(4), 719–730.

Haddad, A. S., H. Hassanzadeh, and J. Abedi (2012), Advective-diffusive mass transfer in fractured porous media with variable rock matrix block size, *J. Contam. Hydrol.*, *133*, 94–107.

Haggerty, R., and S. M. Gorelick (1995), Multiple-rate mass transfer for modeling diffusion and surface reactions in media with pore-scale heterogeneity, *Water Resour. Res.*, *31*(10), 2383–2400.

Haggerty, R., S. A. McKenna, and L. C. Meigs (2000), On the late-time behavior of tracer test breakthrough curves, *Water Resour. Res.*, *36*(12), 3467–3479.

Haggerty, R., C. F. Harvey, C. Freiherr von Schwerin, and L. C. Meigs (2004), What controls the apparent timescale of solute mass transfer in aquifers and soils? A comparison of experimental results, *Water Resour. Res.*, *40*, W01510, doi:10.1029/2002WR001716.

Haidar, I., A. Rapaport, and F. Gérard (2011), Effects of spatial structure and diffusion on the performances of the chemostat, *Math. Biosci. Eng.*, *8*(4), 953–971.

Havlin, S., and D. Ben-Avraham (1987), Diffusion in disordered media, *Adv. Phys.*, *36*(6), 695–798.

Hochstetler, D. L., M. Rolle, G. Chiogna, C. M. Haberer, P. Grathwohl, and P. K. Kitanidis (2013), Effects of compound-specific transverse mixing on steady-state reactive plumes: Insights from pore-scale simulations and Darcy-scale experiments, *Adv. Water Resour.*, *54*, 1–10.

Jha, B., L. Cueto-Felgueroso, and R. Juanes (2011a), Fluid mixing from viscous fingering, *Phys. Rev. Lett.*, *106*(19), 194–502.

Jha, B., L. Cueto-Felgueroso, and R. Juanes (2011b), Quantifying mixing in viscously unstable porous media flows, *Phys. Rev. A*, *84*(6 Pt 2), 066312.

Kapoor, V., and P. K. Kitanidis (1998), Concentration fluctuations and dilution in aquifers, *Water Resour. Res.*, *34*(5), 1181–1193.

Karimi-Fard, M., B. Gong, and L. J. Durlofsky (2006), Generation of coarse-scale continuum flow models from detailed fracture characterizations, *Water Resour. Res.*, *42*, W10423, doi:10.1029/2006WR005015.

Kfoury, M., R. Ababou, B. Noetinger, and M. Quintard (2006), Upscaling fractured heterogeneous media: Permeability and mass exchange coefficient, *J. Appl. Mech.*, *73*(1), 41–46.

LeBlanc, D. R., S. P. Garabedian, K. M. Hess, L. W. Gelhar, R. D. Quadri, K. G. Stollenwerk, and W. W. Wood (1991), Large-scale natural gradient tracer test in sand and gravel, Cape Cod, Massachusetts, 1. Experimental design and observed tracer movement, *Water Resour. Res.*, *27*(5), 895–910.

Le Borgne, T., J.-R. de Dreuzy, P. Davy, and O. Bour (2007), Characterization of the velocity field organization in heterogeneous media by conditional correlations, *Water Resour. Res.*, *43*, W02419, doi:10.1029/2006WR004875.

Le Borgne, T., M. Dentz, and J. Carrera (2008), Spatial Markov processes for modeling Lagrangian particle dynamics in heterogeneous porous media, *Phys. Rev. A*, *78*(2 Pt 2), 9.

Le Borgne, T., M. Dentz, D. Bolsterc, J. Carrera, J.-R. de Dreuzy, and P. Davy (2010), Non-Fickian mixing: Temporal evolution of the scalar dissipation rate in heterogeneous porous media, *Adv. Water Resour.*, *33*(12), 1468–1475.

Le Goc, R., J.-R. de Dreuzy, and P. Davy (2009), Statistical characteristics of flow as indicators of channeling in heterogeneous porous and fractured media, *Adv. Water Resour.*, *33*(3), 257–269.

Li, L., H. Zhoua, and J. J. Gómez-Hernández (2011), Transport upscaling using multi-rate mass transfer in three-dimensional highly heterogeneous porous media, *Adv. Water Resour.*, *34*(4), 478–489.

Liu, H. H., G. S. Bodvarsson, and G. Zhang (2004), Scale dependency of the effective matrix diffusion coefficient, *Vadose Zone J.*, *3*(1), 312–315.

Liu, H. H., Y. Q. Zhang, Q. Zhou, and F. J. Molz (2007), An interpretation of potential scale dependence of the effective matrix diffusion coefficient, *J. Contam. Hydrol.*, *90*(1–2), 41–57.

Luo, J., and O. A. Cirpka (2008), Traveltime-based descriptions of transport and mixing in heterogeneous domains, *Water Resour. Res.*, *44*, W09407, doi:10.1029/2007WR006035.

Luo, J., and O. A. Cirpka (2011), How well do mean breakthrough curves predict mixing-controlled reactive transport?, *Water Resour. Res.*, *47*, W02520, doi:10.1029/2010WR009461.

Magnico, P., C. Leroy, J. P. Bouchaud, C. Gauthier, and J. P. Hulin (1993), Tracer dispersion in porous media with a double porosity, *Phys. Fluids A*, *5*(1), 46–57.

Maloszewski, P., and A. Zuber (1985), On the theory of tracer experiments in fissured rocks with a porous matrix, *J. Hydrol.*, *79*(3–4), 333–358.

McKenna, S. A., L. C. Meigs, and R. Haggerty (2001), Tracer tests in a fractured dolomite 3. Double-porosity, multiple-rate mass transfer processes in convergent flow tracer tests, *Water Resour. Res.*, *37*(5), 1143–1154.

Méheust, Y., and J. Schmittbuhl (2001), Geometrical heterogeneities and permeability anisotropy of rough fractures, *J. Geophy. Res.*, *106*(B2), 2089–2102.

Neretnieks, I. (1980), Diffusion in the rock matrix: An important factor in radionucleside retardation?, *J. Geophy. Res.*, *85*(B8), 4379–4397.

Neuman, S. P., and D. M. Tartakovsky (2009), Perspective on theories of non-Fickian transport in heterogeneous media, *Adv. Water Resour.*, *32*(5), 670–680.

Odling, N. E. (1997), Scaling and connectivity of joint systems in sandstones from western Norway, *J. Struct. Geol.*, *19*(10), 1257–1271.

Ortoleva, P. J. (1994), *Geochemical Self-Organization*, Oxford Univ. Press, Oxford, U. K.

Parkhurst, D. L., and C. A. J. Appelo (1999), User's guide to PHREEQC (version 2)—A computer program for speciation, batch-reaction, one-dimensional transport, and inverse geochemical calculations, U.S. Geol. Surv. Water Resour. Invest. Rep., 99–4259. 321 p.

Pearson, J. E. (1993), Complex patterns in a simple system, *Science*, *261*(5118), 189–192.

Pruess, K. (1992), *Brief Guide to the MINC—Method for Modeling Flow and Transport in Fractured Media*, Lawrence Berkeley Natl. Lab., Earth Sci. Div., Berkeley, Calif.

Pruess, K., and T. N. Narasimhan (1985), A practical method for modeling fluid and heat-flow in fractured porous-media, *Soc. Pet. Eng. J.*, *25*(1), 14–26.

Rao, P. S. C., D. E. Rolston, R. E. Jessup, and J. M. Davidson (1980), Solute transport in aggregated porous-media—Theoretical and experimental evaluation, *Soil Sci. Soc. Am. J.*, *44*(6), 1139–1146.

Renard, F., J.-P. Gratier, P. Ortoleva, E. Brosse, and B. Bazin (1998), Self-organization during reactive fluid flow in a porous medium, *Geophys. Res. Lett.*, *25*(3), 385–388.

Renard, P., and D. Allard (2012), Connectivity metrics for subsurface flow and transport, *Adv. Water Resour* 168–196.

Roubinet, D., H.-H. Liu, and J.-R. de Dreuzy (2010), A new particle-tracking approach to simulating transport in heterogeneous fractured porous media, *Water Resour. Res.*, *46*, W11507, doi:10.1029/2010WR009371.

Roubinet, D., J.-R. de Dreuzy, and D. M. Tartakovsky (2012), Semi-analytical solutions for solute transport and exchange in fractured porous media, *Water Resour. Res.*, *48*, W01542, doi:10.1029/2011WR011168.

Roubinet, D., J.-R. de Dreuzy, and D. M. Tartakovsky (2013), Particle-tracking simulations of anomalous transport in hierarchically fractured rocks, *Comput. Geosci.*, *50*(0), 52–58.

Rubin, J. (1983), Transport of reacting solutes in porous-media—Relation between mathematical nature of problem formulation and chemical nature of reactions, *Water Resour. Res.*, *19*(5), 1231–1252.

Shapiro, A. (2001), Effective matrix diffusion in kilometer-scale transport in fractured crystalline rock, *Water Resour. Res.*, *37*(3), 507–522.

Sudicky, E. A. (1986), A natural gradient experiment on solute transport in a sand aquifer: Spatial variability of hydraulic conductivity and its role in the dispersion process, *Water Resour. Res.*, *22*(13), 2069–2082.

Sudicky, E. A., and E. O. Frind (1982), Contaminant transport in fractured porous-media—Analytical solutions for a system of parallel fractures, *Water Resour. Res.*, *18*(6), 1634–1642.

Tang, D. H., E. O. Frind, and E. A. Sudicky (1981), Contaminant transport in fractured porous-media—Analytical solution for a single fracture, *Water Resour. Res.*, *17*(3), 555–564.

Techer, I., D. Bartier, Ph. Boulvais, E. Tinseau, K. Suchorski, J. Cabrera, and A. Dauzères (2012), Tracing interactions between natural argillites and hyper-alkaline fluids from engineered cement paste and concrete: Chemical and isotopic monitoring of a 15-years old deep-disposal analogue, *Appl. Geochem.*, *27*(7), 1384–1402.

Tennekes, H., and J. L. Lumley (1972), *A First Course in Turbulence*, MIT Press, Cambridge, Mass.

Villermaux, J. (1987), Chemical-engineering approach to dynamic modeling of linear chromatography—A flexible method for representing complex phenomena from simple concepts, *J. Chromatogr.*, *406*, 11–26.

Willmann, M., J. Carrera, and X. Sánchez-Vila (2008), Transport upscaling in heterogeneous aquifers: What physical parameters control memory functions?, *Water Resour. Res.*, *44*, W12437, doi:10.1029/2007WR006531.

Willmann, M., J. Carrera, X. Sanchez-Vila, O. Silva, and M. Dentz (2010), Coupling of mass transfer and reactive transport for nonlinear reactions in heterogeneous media, *Water Resour. Res.*, *46*, W07512, doi:10.1029/2009WR007739.

Wu, S. C., and P. M. Gschwend (1986), Sorption kinetics of hydrophobic organic-compounds to natural sediments and soils, *Environ. Sci. Technol.*, *20*(7), 717–725.

Wu, Y.-S., and K. Pruess (2000), Numerical simulation of non-isothermal multiphase tracer transport in heterogeneous fractured porous media, *Adv. Water Resour.*, *23*(7), 699–723.

Wu, Y. S., H. H. Liu, and G. S. Bodvarsson (2004), A triple-continuum approach for modeling flow and transport processes in fractured rock, *J. Contam. Hydrol.*, *73*(1–4), 145–179.

Zhan, H. B., Z. Wen, G. Huang, and D. Sun (2009), Analytical solution of two-dimensional solute transport in an aquifer-aquitard system, *J. Contam. Hydrol.*, *107*(3–4), 162–174.

Zhou, Q. L., H. H. Liu, F. J. Molz, Y. Zhang, and G. S. Bodvarsson (2007), Field-scale effective matrix diffusion coefficient for fractured rock: Results from literature survey, *J. Contam. Hydrol.*, *93*(1–4), 161–187.

Zinn, B., L. C. Meigs, C. F. Harvey, R. Haggerty, W. J. Peplinski, and C. F. von Schwerin (2004), Experimental visualization of solute transport and mass transfer processes in two-dimensional conductivity fields with connected regions of high conductivity, *Environ. Sci. Technol.*, *38*(14), 3916–3926.

3 Bilan

Comme nous l'avons vu dans l'article précédent, en dépit de l'organisation très différente de leur zones immobiles, les modèles MINC et MRMT donnent des taux de réaction qui bien que différents restent très similaires. Cette capacité des modèles MRMT à reproduire le transport réactif tient à leur très bonne évaluation des distributions de concentrations. En particulier, la relation d'équivalence apparaît conserver le second moment de la distribution des concentrations, ce que nous avons montré analytiquement pour le cas MINC 1D. Les différences entre MINC et MRMT apparaissent principalement en cas de forts gradients de concentration initiaux dans la zone immobile. Dans le cas où un soluté se trouve initialement dans la zone immobile loin de la zone mobile, ce soluté va mettre un certain temps à traverser la zone immobile avant d'atteindre la zone mobile. Hors, dans MRMT, toutes les zones immobiles échangent directement avec la zone mobile. Afin d'assurer l'identité des concentrations dans la zone mobile, des "concentrations" négatives apparaissent dans MRMT pour compenser les contributions des "concentrations" positives et rendre compte du délai nécessaire au soluté pour atteindre la zone mobile. Ce cas souligne le fait que les "concentrations" MRMT sont avant tout des produits mathématiques de la relation d'équivalence entre MINC et MRMT, et que leur utilisation en tant que concentrations réelles doit être évaluée avec précaution. Il met aussi en évidence le rôle de l'organisation des zones immobiles et une des limites de la simplification de cette organisation opérée par le modèle MRMT.

Chapitre 3 : Généralisation de l'équivalence entre modèles diffusifs et modèles MRMT à tout type de structure des zones immobiles

1 Introduction

Dans le chapitre précédent, nous avons vu que des modèles simplifiés de type MRMT pouvaient estimer correctement une réactivité non-linéaire à l'équilibre dans des structures diffusives de type MINC, i.e. dans des inclusions diffusives planaires, cylindriques et sphériques. Cette capacité tient à la bonne évaluation des distributions de concentrations par MRMT, et notamment la reproduction du second moment de ces distributions. La question se pose cependant de savoir si l'usage de MRMT comme proxy pour le transport réactif peut s'étendre à des structures de porosité immobile plus complexes que l'organisation linéaire de MINC. Ces structures peuvent être par exemple les bras morts d'un réseau de fractures (Sornette et al. 1993, Flekkøy et al. 2002), d'un réseau de pores au sein d'une matrice (Altman et al. 2004, Gouze et al. 2008) ou d'une figure de dissolution (Golfier et al. 2002, Luquot et al. 2014) (*Figure 3.1*). Avant cependant de vérifier si MRMT peut être utilisé pour reproduire du transport réactif dans ces structures, nous démontrons qu'il peut reproduire du transport conservatif.

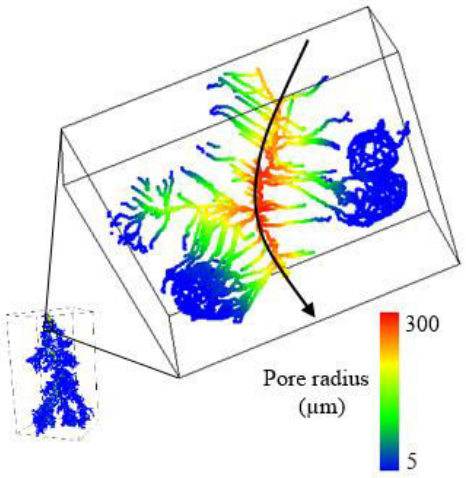

Figure 3.1: (a) Squelette d'une figure de dissolution dans un calcaire à oolites, observée par micro-tomographie à rayons X, d'après Luquot et al. (2014). Cette porosité est obtenue par injection d'une solution acide percolant depuis le haut vers le bas de la vue générale (coin inférieur gauche). Le pH de la solution augmente du haut vers le bas et de l'intérieur vers l'extérieur du chemin d'infiltration préférentiel indiqué par la flèche sur la vue détaillée (coin supérieur droit). L'acide dissous préférentiellement le ciment de calcite entourant les oolithes, la taille des pores diminue progressivement à distance du chemin d'infiltration préférentiel et l'organisation des pores devient plus complexe.

Dans l'article suivant, nous présentons le modèle SINC (Structured INteracting Continua) qui étend le modèle MINC (Multiple INteracting Continua) en introduisant une structure de l'organisation des zones immobiles. Les interactions entre zones immobiles forment un graphe décrit algébriquement par une matrice d'interactions. Cette formulation permet de représenter

des structures immobiles variées, possédant des boucles, des jonctions et des ramifications. Les quatre structures immobiles de la *Figure 3.2* sont choisies comme exemples de référence pour illustrer la comparaison entre SINC et MRMT. Ces structures sont considérées comme représentatives d'une large gamme d'organisations immobiles du fait de leurs géométries très différentes. Nous évaluons alors la capacité du modèle MRMT à reproduire le transport dans ce modèle SINC.

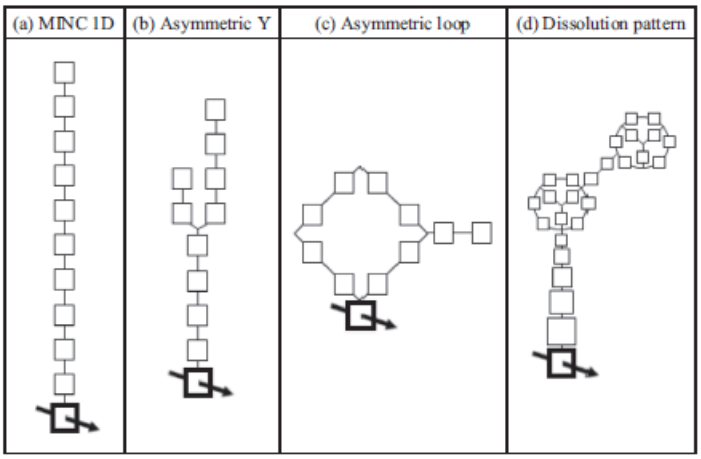

Figure 3.2: Exemples de structures SINC utilisées pour illustrer la comparaison entre SINC et MRMT. Ces structures sont (a) le modèle classique Multiple INteracting Continua (MINC) 1D, (b) un Y asymétrique avec une seule jonction, (c) une boucle asymétrique et (d) une structure plus complexe inspirée de la figure de dissolution présentée sur la Figure 3.1. Ces structures sont représentées selon une coupe transverse à la zone mobile, représentée en gras avec une flèche. La porosité totale de toutes ces structures est identique.

2 Article: "*Multi-Rate Mass Transfer (MRMT) models for general diffusive porosity structures*", par T. Babey, J.-R. de Dreuzy et C. Casenave, publié en 2015 dans Advances in Water Resources

Advances in Water Resources 76 (2015) 146–156

Contents lists available at ScienceDirect

Advances in Water Resources

journal homepage: www.elsevier.com/locate/advwatres

Multi-Rate Mass Transfer (MRMT) models for general diffusive porosity structures

Tristan Babey [a,*], Jean-Raynald de Dreuzy [a], Céline Casenave [b,c]

[a] Géosciences Rennes (UMR CNRS 6118), Campus de Beaulieu, Université de Rennes 1, 35042 Rennes cedex, France
[b] UMR INRA-SupAgro 0729 MISTEA, 2 place Viala, 34060 Montpellier, France
[c] MODEMIC Project-Team, INRA/INRIA, Sophia-Antipolis, France

ARTICLE INFO

Article history:
Received 22 August 2014
Received in revised form 13 December 2014
Accepted 15 December 2014
Available online 25 December 2014

Keywords:
Porous media
Solute transport
Mobile–immobile models
Multi-Rate Mass Transfer

ABSTRACT

We determine the relevance of Multi-Rate Mass Tansfer (MRMT) models (Haggerty and Gorelick, 1995) to general diffusive porosity structures. To this end, we introduce Structured INteracting Continua (SINC) models as the combination of a finite number of diffusion-dominated interconnected immobile zones exchanging with an advection-dominated mobile domain. It directly extends Multiple INteracting Continua framework (Pruess and Narasimhan, 1985) by introducing a structure in the immobile domain, coming for example from the dead-ends of fracture clusters or poorly-connected dissolution patterns. We demonstrate that, whatever their structure, SINC models can be made equivalent in terms of concentration in the mobile zone to a unique MRMT model. We develop effective shape-free numerical methods to identify its few dominant rates, that comply with any distribution of rates and porosities. We show that differences in terms of macrodispersion are not larger than 50% for approximate MRMT models with only one rate (double porosity models), and drop down to less than 0.1% for five rates MRMT models. Low-dimensional MRMT models accurately approach transport in structured diffusive porosities at intermediate and long times and only miss early responses.

1. Introduction

Transport in complex geological environments results in part from the interactions between fast advective-dominated transport in a localized "mobile porosity" and slow diffusive-dominated transport in extensive "immobile porosities". It is the case of the fracture–matrix systems [30,38] and of the highly heterogeneous porous media [12,15,17,42]. When diffusive times in the immobile zones become much larger than the characteristic advective time in the mobile zone, transport becomes anomalous with non-Gaussian concentration plumes, more extensive spreading and mixing, slow transit times, and broad ranges of solute retardation times [4,11]. Such transport mechanisms and exchanges are at the root of numerous anomalous transport modeling frameworks [1,3,5,7,8,21] and can be highly effective in the interpretative and predictive phases of laboratory and field experiments [2,6,18,20,22]. Anomalous transport ultimately stems from some extended distribution whether it is a waiting time distribution as in Continuous Time Random Walk (CTRW) or a rate-porosity distribution as in Mutli-Rate Mass Transfert (MRMT) [10,31,35]. For MRMT models, while these distributions can take very different shapes [23], only some power-law distributions are effectively related to diffusive processes in 1D, 2D or 3D inclusions [7,21] or to anomalous diffusive processes in fractal-like structures [19]. Diffusive structures may however be topologically more complex like for example fracture dead ends [13,36], fracture–matrix interactions [25,26,37–39], or dissolution patterns in porous media [16,28] (Fig. 1).

In this article, we show that the MRMT framework is general to all diffusive architectures that can be modeled as a finite number of interconnected continua (Fig. 1). The notion of continuum comes from the double porosity and Multiple INteracting Continua (MINC) concepts introduced initially for fracture–matrix systems [34,41]. The double porosity model is the classical diffusive interaction of advective–diffusive processes in a mobile zone with a single immobile zone [41]. The Multiple INteracting Continua (MINC) framework models matrix diffusion as diffusive-like exchanges within a succession of "continua", identified to the elementary cells issued by a finite-difference discretization of the diffusion process in the matrix (Fig. 2a) [33,34]. The denomination of multiple continua is a direct generalization of the double porosity concept of [41]. We propose to further generalize the notion of interacting continua to any immobile zones structure where

* Corresponding author. Tel.: +33 646204318.
E-mail address: tristan.babey@univ-rennes1.fr (T. Babey).

http://dx.doi.org/10.1016/j.advwatres.2014.12.006
0309-1708/

diffusive-like exchanges intervene between any connected zones or continua. Because of the potential importance of structure on diffusion, we denote these models as Structured INteracting Continua (SINC). SINC models include a wide range of structures going from elementary branching and loops (Fig. 2b and c) to more involved dissolution patterns (Fig. 2d). They would typically be derived from the coarse discretization of diffusion processes in dead-end porosity structures [18,32]. We define SINC models in Section 2, with their exact relation to the MRMT and MINC models. We show in Section 3 that any SINC model is equivalent in terms of transport to a unique MRMT model of the same dimension, i.e. with the same number of immobile zones. We develop efficient numerical methods in Section 4 to identify lower-dimension but highly accurate approximate MRMT models.

2. Structured INteracting Continua (SINC)

We present the Structured INteracting Continua framework (SINC) and show how it relates to existing models like Multi-Rate Mass Transfer (MRMT) and Multiple INteracting Continua (MINC).

The SINC model is made up of a continuous 1-D mobile zone in interaction with a finite number of interconnected immobile zones (Fig. 1). In the continuous mobile zone, solutes are transported by advection, dispersion and diffusion. Between the mobile zone and the immobile zones as well as between the immobile zones, concentration exchanges are diffusive-like, i.e. directly proportional to the difference of concentrations. This model can be generically expressed as:

$$\frac{\partial U}{\partial t} - AU = L(R_m U), \tag{1}$$

where $U = \left[c_m(x,t) \quad c^1_{im}(x,t) \quad \cdots \quad c^N_{im}(x,t)\right]^T$ is the vector of dimension $N+1$ made up of the concentrations in the mobile zone $c_m(x,t)$ and in the N immobile zones $c^i_{im}(x,t)$ with $i = 1,\ldots,N$. A is the $(N+1, N+1)$ interaction matrix characterizing the diffusive-like concentration exchanges between the immobile zones and with the mobile zone. R_m is the restriction matrix to the mobile zone:

$$R_m(i,j) = \delta(i-1)\delta(j-1). \tag{2}$$

L is the transport operator in the mobile zone:

$$L(c_m) = -\frac{q}{\phi_m}\frac{\partial c_m}{\partial x} + d_m \frac{\partial^2 c_m}{\partial x^2}, \tag{3}$$

with q, ϕ_m and d_m the Darcy flow, porosity and dispersion coefficient in the mobile zone. The physical properties of the mobile and immobile domains are homogeneous along the mobile domain. The interaction matrix A is equal to the matrix M deriving from the diffusive-like mass exchanges between the different zones, corrected by the porosities of the zones:

$$A = -\Phi^{-1} M, \tag{4}$$

with Φ the diagonal matrix whose diagonal elements are the porosities associated to the mobile zone ϕ_m and to the N immobile zones ϕ^i_{im} with $i = 1,\ldots,N$:

$$\begin{cases} \Phi(1,1) = \phi_m \\ \Phi(i,j) = \phi^{i-1}_{im}\delta(i,j) \text{ for } (i,j) \neq (1,1) \end{cases}. \tag{5}$$

The matrix M expresses rates of mass exchange. The dimension of its elements is therefore the inverse of a time. As exchanges are diffusive-like, M is a M-matrix, i.e. M is symmetric, its diagonal elements are positive, its off-diagonal elements are negative or equal to zero, and the sum of its elements along each of its rows is equal to zero. We underline that it is the matrix M that is symmetric and generally not the interaction matrix A that also integrates the differences in porosities. The interaction matrix A registers the connectivity of the different zones through the position of its non-zero off-diagonal elements, the strength of the interactions is determined by porosity ratios and exchange rates. Fig. 3a shows the example of the interaction matrix for the asymmetric Y structure (cf Fig. 2b). The branching architecture leads to a compact interaction matrix, which values are all on the three principal diagonals except at the branching node. The interaction matrix is scaled by the inverse of the mean diffusion time in the immobile structure τ. We define τ as the quadratic mean distance of the immobile zones to the mobile zone divided by the diffusion coefficient between two zones.

The SINC framework generalizes Multiple INteracting Continua (MINC) [34]. MINC models are obtained by the finite-difference

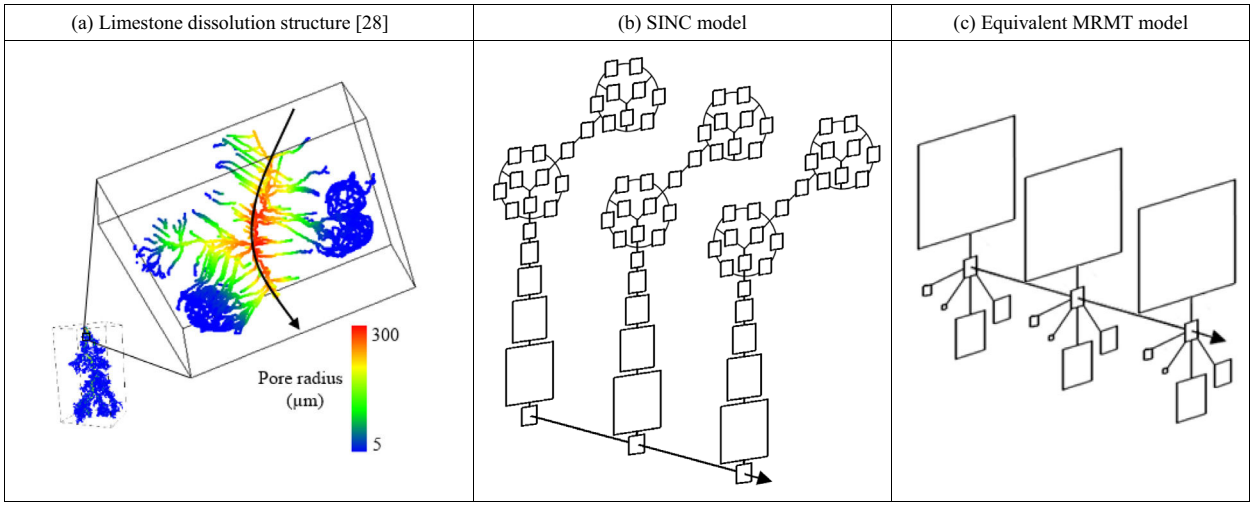

Fig. 1. (a) Skeleton of a dissolution feature in an oolitic limestone, observed by X-ray micro-tomography [28]. The dissolving acidic solution percolates from top to bottom on the general view (bottom left). Its pH increases from top to bottom and from inside out of the main flow path indicated by the curved arrow on the detailed view (top right). The acid dissolves preferentially the calcite cement surrounding the oolites, the size of the pores progressively decreases away from the main flow path, and the organization of the pores becomes more complex. (b) Structured INteracting Continua model (SINC) sketched from the dissolution pattern of (a) with three cross sections transversal to the mobile zone materialized by the arrow. (c) Equivalent MRMT model with the 5 most important rates as determined by the numerical methods set up in Section 4. The size of the boxes scales with the porosity affected to the rates labeled by triangles in Fig. 7.

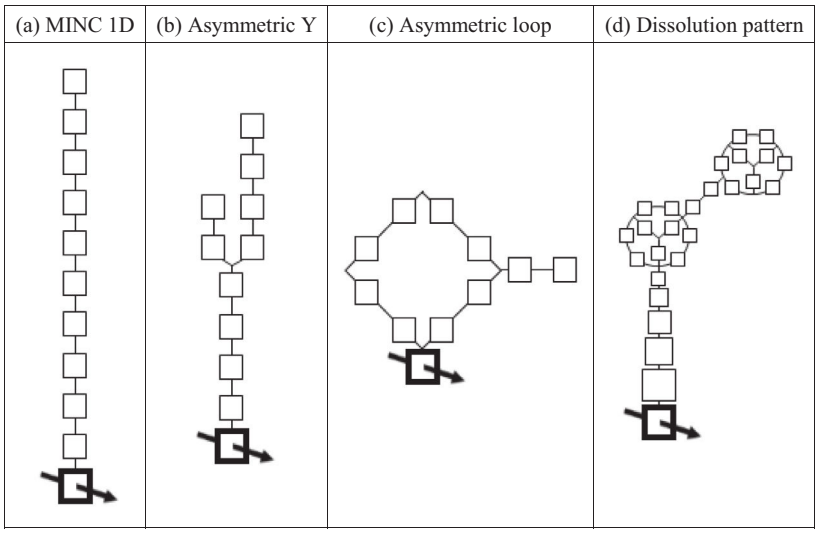

Fig. 2. Examples of Structured INteracting Continua (SINC) used to illustrate and validate the numerical identification methods of the equivalent MRMT models. From left to right, the diffusive porosity structures are (a) the classical Multiple INteracting Continua (MINC) [34], (b) an asymmetric *Y* with a single junction, (c) an asymmetric loop, and (d) the dissolution structure presented in Fig. 1. The size of the immobile cells is proportional to their porosity and the distance along the immobile structure is to scale. The mobile zone is represented by the thick black box with the crossing arrow. Its size has been exaggerated 10 times to be clearly marked. To be comparable, the four structures have the same total porous volume and the same radius of gyration taken with respect to the mobile zone.

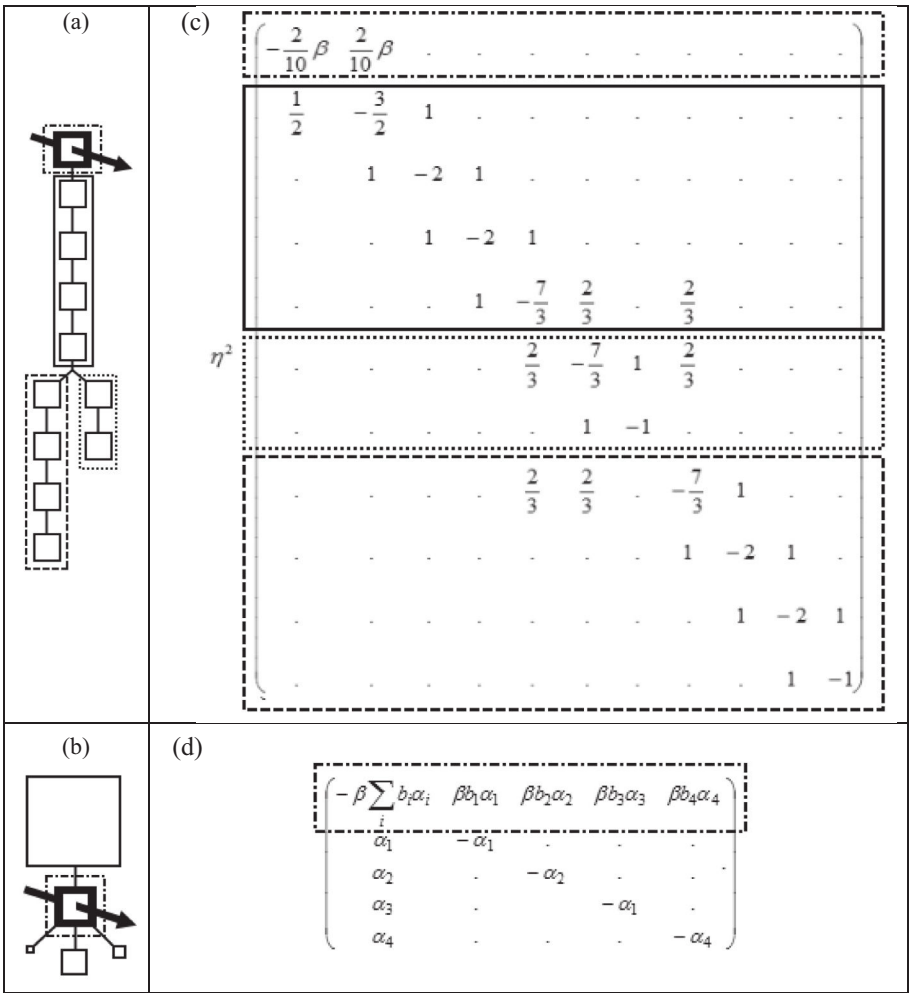

Fig. 3. Diffusive porosity structures represented as cross-sections transversal to the mobile zone direction ((a) and (b)), with their associated interaction matrix *A* ((c) and (d)) for the asymmetric *Y* (*top*) and MRMT structures (*bottom*). Dotted frames around subsets of the immobile porosity structures ((a) and (b)) and around matrix lines ((c) and (d)) show how structures are expressed in matrix form. Parameters for the asymmetric *Y* structure are taken from Table 1 and the multiplicative factor η (η = 5.015) is equal to the ratio of the distance between two consecutive immobile zones to the radius of gyration of the immobile domain to the mobile zone. β is the ratio of the total immobile porosity to the mobile porosity.

discretization of diffusion in a 1-D homogeneous medium. In such a case, the interaction matrix A is simply tri-diagonal. The term "continuum" comes from the continuity along the mobile zone like in the dual-porosity concept [41]. It is consistent with our concept of a continuous formalism of transport along the mobile zone and a finite number of interacting continua in the immobile direction.

The SINC framework also generalizes Multiple-Rate Mass Transfer models with a finite number of rates [7,21]. In MRMT models as defined by Haggerty and Gorelick [21], the immobile domain consists in a distribution of sub-domains exchanging exclusively with the mobile domain. The star-like connectivity structure leads to an arrow-type broad-width interaction matrix (Fig. 3b). Each subdomain is characterized by its rate of transfer α_i and its porosity ϕ^i_{im}, with $\alpha_i < \alpha_{i+1}$ [21]. When defined with a finite number of rates, MRMT models can be recovered by fixing

$$\begin{cases} M(i,j) = 0 \quad \text{for} \quad i > 1, \quad j > 1 \text{ and } i \neq j \\ M(i,1) = M(1,i) = -\phi_{im}^{i-1}\alpha_{i-1} \quad \text{for} \quad i > 1 \\ M(i,i) = -\sum_{j,j\neq i} M(i,j) \end{cases} . \qquad (6)$$
$$\begin{cases} \Phi(1,1) = \phi_m \\ \Phi(i,j) = \phi_{im}^{i-1}\delta(i,j) \quad \text{for} \quad (i,j) \neq (1,1) \end{cases}$$

Because they are defined in algebraic terms, SINC models can only represent MRMT models with finite number of rates. They are rigorously not equivalent to 1D, 2D and 3D diffusion models that themselves correspond to an infinite number of exchange rates [21]. However they offer very accurate approximations when taking only a finite number of rates, especially as the porosities ϕ^i_{im} decrease as a power law of i. SINC models generalize MRMT models defined with a finite number of rates but remain different to MRMT models defined by an infinite series of rates or by a continuous rate-porosity function. Our objective in this article is not to produce any kind of generalization of MRMT models but rather to determine how complex diffusive porosity structures can be approached by simpler reduced models.

3. Proof of equivalence of SINC to MRMT model

Following up the work of [21], we define the equivalence relation to a MRMT model as the identity of the mobile concentration at any time. To prove the equivalence of the SINC model to a MRMT model, we first decompose the interaction matrix A in two parts, consisting in the exchanges between the immobile zones only for the first part and in the exchanges between the mobile zone and the immobile zones for the second one:

$$A = \begin{pmatrix} 0 & \cdots & \cdots & 0 \\ \vdots & & & \\ \vdots & & \widehat{A} & \\ 0 & & & \end{pmatrix} + \begin{pmatrix} A_{11} & A_{12} & \cdots & A_{1,N+1} \\ A_{21} & & & \\ \vdots & & 0 & \\ A_{N+1,1} & & & \end{pmatrix}, \qquad (7)$$

with $\widehat{A} = A(2\ldots N+1, 2\ldots N+1)$. As shown in Appendix A, the matrix $\widehat{A}$ can be diagonalized

$$\widehat{A} = \widehat{R}\,\Lambda\widehat{R}^{-1}, \qquad (8)$$

with Λ the diagonal matrix made up of the eigenvalues of $\widehat{A}$, which are all real and negative, and $\widehat{R}$ the matrix of the eigenvectors of $\widehat{A}$, defined each up to a multiplicative constant. To fix the eigenvalues decomposition, as Λ is defined up to a permutation of its diagonal elements, we sort the eigenvalues according to their absolute value by increasing order $|\Lambda_{i,i}| \leqslant |\Lambda_{i+1,i+1}|$. In the new coordinate system defined by the eigenvectors, there are no more exchanges between the immobile zones. All exchanges are made directly between the immobile zones and the mobile zone. To characterize the precise nature and extent of these exchanges, we propagate the change of the coordinate system to the exchanges with the mobile zone

$$\begin{pmatrix} A_{11} & A_{12} & \cdots & A_{1,N+1} \\ A_{21} & & & \\ \vdots & & 0 & \\ A_{N+1,1} & & & \end{pmatrix} = R \begin{pmatrix} A_{11} & B_{12} & \cdots & B_{1,N+1} \\ B_{21} & & & \\ \vdots & & 0 & \\ B_{N+1,1} & & & \end{pmatrix} R^{-1}, \qquad (9)$$

with the $(N+1, N+1)$ matrix R and its inverse R^{-1} defined as

$$R = \begin{pmatrix} 1 & 0 & \cdots & 0 \\ 0 & & & \\ \vdots & & \widehat{R} & \\ 0 & & & \end{pmatrix} \text{ and } R^{-1} = \begin{pmatrix} 1 & 0 & \cdots & 0 \\ 0 & & & \\ \vdots & & \widehat{R}^{-1} & \\ 0 & & & \end{pmatrix}. \qquad (10)$$

In this transformation, the mobile zone remains unchanged consistently with our objective to reorganize only the immobile zones without interfering with the concentration in the mobile zone. The full transformation defined by R is applied to the matrix A following its decomposition in Eq. (7)

$$A = R \begin{pmatrix} 0 & \cdots & \cdots & 0 \\ \vdots & & & \\ \vdots & & \Lambda & \\ 0 & & & \end{pmatrix} R^{-1} + R \begin{pmatrix} A_{11} & B_{12} & \cdots & B_{1,N+1} \\ B_{21} & & & \\ \vdots & & 0 & \\ B_{N+1,1} & & & \end{pmatrix} R^{-1}, \qquad (11)$$

which can be finally expressed by a simple factorization as

$$A = RBR^{-1} \text{ with } B = \begin{pmatrix} A_{11} & B_{12} & \cdots & B_{1,N+1} \\ B_{21} & & & \\ \vdots & & \Lambda & \\ B_{N+1,1} & & & \end{pmatrix}. \qquad (12)$$

Finally, as the restriction matrix to the mobile zone R_m (Eq. (2)) commutes with R^{-1}, we can write the full model as

$$\frac{\partial R^{-1}U}{\partial t} - BR^{-1}U = L\left(R_m R^{-1}U\right). \qquad (13)$$

To be representative of a MRMT model, B should be an arrow matrix, the sum of its elements over each of its rows should be zero, and all its non-diagonal elements should be either positive or equal to zero. In Appendix B, we show that this can be obtained by adjusting the norm of the eigenvectors in $\widehat{R}$. The characteristics of this MRMT model are then determined by a simple identification of Eq. (6) with Eq. (12):

$$\begin{cases} \alpha_i = -\Lambda_i \\ \phi^i_{im} = \phi_m \dfrac{B_{1,i+1}}{B_{i+1,1}} = \phi_m \dfrac{B_{1,i+1}}{-\Lambda_i} \end{cases}. \qquad (14)$$

While this algebraic identification method can already be widely used to determine equivalent MRMT models, it faces some numerical limitations. The diagonalization process becomes challenging when $\hat{A}$ becomes large, limiting the range of the identification to not too complex architectures and/or coarse discretizations of the immobile domain. The immobile porosity structure may be composed of a large number of cells, while a much smaller number of rates may be necessary to get highly accurate equivalent MRMT models. To address these limitations, we propose an alternative approximate numerical identification method.

4. Approximate numerical identification method of the MRMT model equivalent to a SINC model

We first develop the numerical methodology and secondly apply it to the four examples of Fig. 2. Because of their widely differing structures, these four SINC examples are thought to be a good basis for testing and illustrating the numerical methods. The first one is the classical MINC taken as reference. The two next ones were chosen for their elementary branching and looping connectivity patterns (Fig. 2b and c). Any more involved patterns like the dissolution pattern of Fig. 2d will be some kind of combination of these elementary structures. These four examples are comparable in the sense that they have the same mobile properties, the same overall immobile to mobile porosity ratio β, and the same mean quadratic diffusion time τ as defined in Section 2 (Table 1). The dispersivity in the mobile zone $d_m/(q/\phi_m)$ divided by the effective dispersivity due to the exchanges with the immobile zone defined as $\tau(q/\phi_m)$ is taken equal to $5\cdot10^{-5}$, i.e. much smaller than 1, so that dispersive effects come predominantly from the mobile/immobile exchanges. For the same reason, β is taken much larger than 1 ($\beta = 100$).

4.1. Methodology

To numerically approximate the MRMT model equivalent to a SINC model, we consider the particular case of the discharge of the immobile zones to the mobile zone. The mass discharged to the mobile zone from an initially homogeneous immobile concentration c_0 is fitted by a combination of exponential functions typical of the MRMT model. The residual mass per unitary volume $m(t)$ in the immobile domains is fitted by its MRMT counterpart $\gamma(t)$ given by:

$$\gamma(t) = \sum_{i=1}^{N} c_0 \phi_{im}^i \exp(-\alpha_i t), \tag{15}$$

where α_i and ϕ_{im}^i, $i = 1\ldots N$ are the N rates and immobile porosities defined in Eq. (6). In Appendix C, we develop an optimization method to identify the α and ϕ_{im} series. We further illustrate its application to the cases $N = 1$ and $N = 2$ in Appendix D.

The advantage of this method over the previous algebraic method is to be flexible in terms of the number of rates N to identify. It also prioritizes the identification of the rates and immobile porosities having a significant impact on transport. In the following we determine the number of rates that should be identified to model accurately macrodispersive processes.

4.2. Simulations and results

We analyze the influence of the number of rates N on the reproduction of macrodispersion for the four structures displayed in Fig. 2 for N ranging from 1 to 5. Identification is performed according to the methodology presented before and with a logarithmic sampling of times starting at the time for which the relative mass discharge to the mobile zone is lower than 10^{-3} and ending at the time for which the relative residual mass itself is lower than 10^{-4}.

Table 1
Parameters used for the simulation of Section 4.2 with the characteristic diffusion time τ and the consecutive distance covered by advection in the mobile zone $q\tau/\phi_m$ as temporal and spatial dimensional parameters. β is the immobile to mobile porosity ratio. $d_m/\left(\tau(q/\phi_m)^2\right)$ is the dimensionless dispersion in the mobile zone. $\sigma_0/(q\tau/\phi_m)$ is the dimensionless standard deviation of the initial Gaussian concentration profile. x_{max} is the extension of the simulation domain in the direction of the mobile zone, dx is the spatial step along the mobile zone and dt is the time step.

Parameter	Value
β	100
$d_m/\left(\tau(q/\phi_m)^2\right)$	$5\cdot10^{-5}$
$\sigma_0/(q\tau/\phi_m)$	$3\cdot10^{-3}$
x_{max}/σ_0	100
dx/σ_0	0.2
dt/τ	$5\cdot10^{-4}$

Simulations of transport for the SINC and approximate MRMT models are further performed with identical Gaussian concentration profiles in the mobile and immobile domains

$$c_m(x, t=0) = c_{im}(x, t=0) = \frac{c_{max}}{\sigma_0\sqrt{2\pi}} \exp\left(-\frac{(x-x_0)^2}{2\sigma_0^2}\right), \tag{16}$$

where x_0, σ_0 and c_{max} are the mean, standard deviation and maximum concentration of the Gaussian profile. σ_0 is taken small enough so that the initial plume size has minor effects on the overall dispersion (Table 1).

We compute for all models the effective dispersion coefficient D as

$$D = \frac{1}{2}\frac{d\sigma_x^2}{dt}, \tag{17}$$

with σ_x the plume spreading

$$\sigma_x^2 = m_2/m_0 - (m_1/m_0)^2. \tag{18}$$

The spatial moments of concentration m_k are given by

$$m_k(t) = \int_{x=0}^{\infty} \sum_{i=1}^{N+1} x^k \Phi(i,i) U(x,t,i) dx. \tag{19}$$

We assess the quality of the MRMT model for modeling dispersion through the quadratic mean of the relative difference in effective dispersion of the SINC and MRMT models:

$$diff(D_{SINC}, D_{MRMT}) = \sqrt{\int_t \left[\frac{D_{SINC}(t) - D_{MRMT}(t)}{(D_{SINC}(t) + D_{MRMT}(t))/2}\right]^2 dt \Big/ \int_t dt}. \tag{20}$$

This criterion is sensitive to differences in dispersion on a broad time range from the initial time to the time at which dispersion becomes constant.

Classical numerical methods were used to solve both the exchanges within the immobile zones and the advective–dispersive transport in the mobile zone [9]. They were validated on a set of immobile structures rigorously equivalent to the MINC model (Fig. 4). In those cases, $diff(D_{SINC}, D_{MINC})$ was of the order of 10^{-11} and much smaller than any differences recorded in the analysis performed hereafter.

For the structures displayed on Fig. 2, the effective dispersion obtained with the MRMT models converges quickly to the reference dispersion of the corresponding SINC model as the number of MRMT rates N increases (Fig. 5). The equivalent MRMT model with only one immobile zone ($N = 1$), equivalent to the double porosity model [41], already gives the right order of magnitude of dispersion. With $N = 2$, the error of the MRMT model is close to 10%. With $N = 4$, it is close to 1% and with $N = 5$, it is close to 0.1%. A very limited number of rates is thus sufficient to represent even the complex diffusive structure displayed on Fig. 2d. This fundamentally comes from the homogenization due to diffusion that systematically removes the extremes of the concentration distributions as previously noted in numerous studies [21,40].

In addition, the equivalent MRMT model with only one rate reproduces well the tailing of the breakthrough curve (Fig. 6). As expected, introducing higher rates progressively improves the accuracy of the MRMT model at earlier times. The double peak observed for $N = 1$ is a classical feature of double porosity models

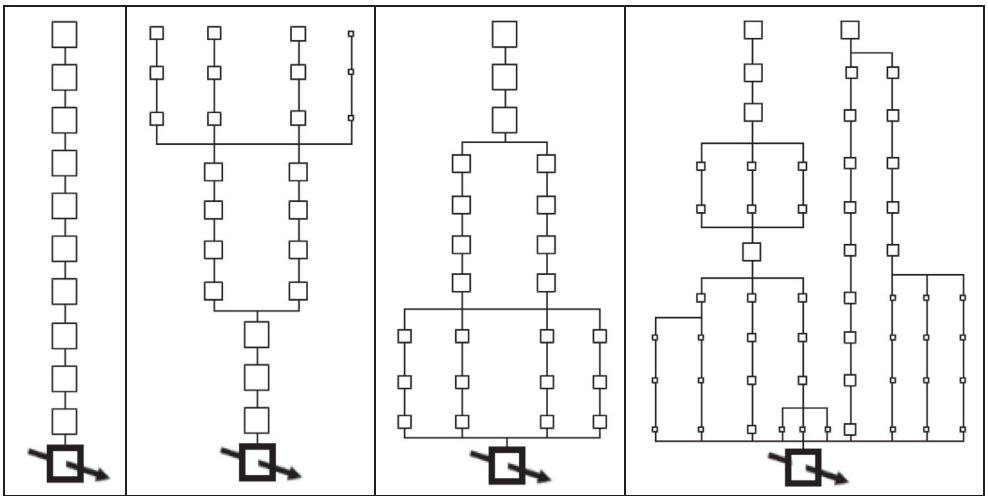

Fig. 4. Diffusive porosity structures used to check the numerical implementation of the SINC model. These structures display the same behavior as the "MINC 1D" structure (*left column*) for homogeneous initial concentrations in the immobile zones. The mobile zone is the bold box with the arrow. The size of the boxes is proportional to the porosity of the zones. Only the vertical distance of an immobile zone to the mobile zone is to scale.

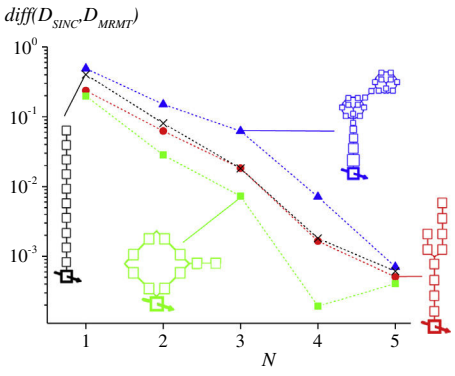

Fig. 5. Differences in macrodispersions $diff(D_{SINC},D_{MRMT})$ as defined by equation (20) between SINC models and their approximate equivalent MRMT models with a limited number of N rates, for the four diffusive porosity structures presented in Fig. 2. Determination of the MRMT rates and porosities is achieved with the numerical identification method in the temporal domain (Section 4.1 and Appendix C).

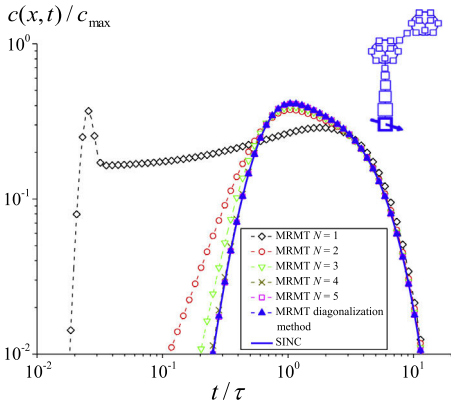

Fig. 6. Breakthrough curves for the dissolution-like SINC model (Fig. 2d) and for its equivalent MRMT models, either determined by the diagonalization method (Section 3), or by the numerical method in the temporal domain with a limited number of N rates (Section 4.1 and Appendix C). The concentrations are measured at the position $x = 20\sigma_0$.

where advection is much faster than diffusion in the immobile porosity [29]. It vanishes for higher-order MRMT models ($N = 2$–5), as higher rates enhance short-term mobile–immobile exchanges and remove early breakthroughs.

The quality of the MRMT model with only very few rates fundamentally comes from the dominating role of the smaller rates (i.e. larger transfer times). In fact the whole rate series as determined by the algebraic diagonalization method shows that the lowest rate dominates in every case by accounting for 70–85% of the total immobile porosity (Fig. 7). The five lowest rates represent at least 95% of the total immobile porosity for all the studied structures. The evolution of the porosities ϕ_{im}^i with the rates α_i is monotonic only for the MINC model and becomes much more variable for more complex structures, highlighting the need of identification methods that do not assume any *a priori* repartition of the immobile porosity among the rates. We finally note that our results pertain to complex diffusive structures observed on a given range of scales. If not close to the mobile zone, finer details would be fast homogenized by diffusion and are unlikely to modify the identified rates. If close to the mobile zone, finer details should be treated independently in the same way as for the larger-scale structures and the MRMT models obtained at different scales should be eventually superposed.

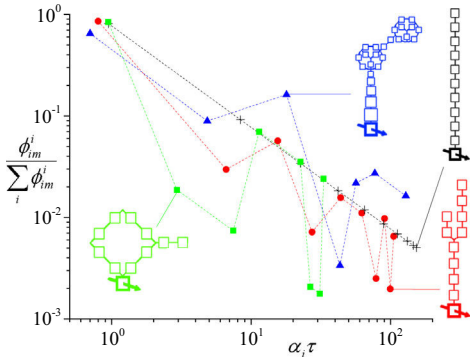

Fig. 7. Normalized rates $\alpha_i\tau$ versus normalized porosities $\phi_{im}^i \big/ \sum_i \phi_{im}^i$ for the MRMT models equivalent to the four diffusive porosity structures presented in Fig. 2, as determined by the diagonalization method (Section 3). Normalized rates larger than 200 or corresponding to normalized porosities smaller than 10^{-3} have been truncated.

5. Conclusion

We define a general mobile/immobile Structured INteracting Continua (SINC) transport framework accounting for a broad variety of immobile porosity structures. Like in more classical double porosity, Multi-Rate Mass Transfer (MRMT), and Multiple INteracting Continua (MINC) frameworks, solute transport is dominated by advection in the mobile porosity and is diffusion-like in the immobile porosity. The SINC framework introduces a connectivity pattern within the immobile domain covering a broad range of diffusive geological structures including cluster of dead-end fractures, irregular matrix shapes and dissolution patterns. Immobile structures are based on branching and looping structures, and on any combination of them. Solute transport is expressed as an advection–diffusion equation coupled to algebraically defined exchanges with a finite number of immobile zones. Interactions among the immobile zones and with the mobile zone are fully determined by a simple interaction matrix, which corresponds to an arrow type of matrix in the MRMT case and to a tri-diagonal matrix in the MINC case. The graph of the matrix registers the connectivity pattern while the value of its coefficients is determined by porosity ratios and rates of mass exchanges between zones.

We show that any Structured INteracting Continua model is equivalent to a unique MRMT model, where the equivalence is defined as the strict identity of the concentrations in the mobile zone, whatever the initial and boundary conditions. The rates of the equivalent MRMT model are the eigenvalues of the subset of the interaction matrix where the line and column corresponding to the mobile zone are removed. The diagonalization method gives a first identification method of the equivalent MRMT with the same dimension, i.e. with the same number of immobile zones. Because of limitations coming essentially from the dimension of the immobile porosity structure, we set up alternative numerical methods designed to identify the most important rates controlling the transport of solute. Developed both in the temporal and Laplace domains, these methods seek for the combination of a finite number of exponential functions that best matches a simple discharge of the immobile zones into a quickly flushed mobile zone.

A simple sensitivity study on representative diffusive structures shows that very few rates are needed for accurately modeling the solute transport in a 1D advection-dominated mobile zone exchanging with an immobile porosity structure. Double porosity models (MRMT models with a single rate) already give the right order of magnitude of macrodispersion. Differences in macrodispersion drop down to around 10% for two rates, to 1% for four rates, and to less than 0.1% for five rates. Simplified models based on only five rates approach accurately the behavior of the system at intermediate to large times and only miss the very early responses. While only few rates are necessary, their distribution and associated porosities are highly variable, the complexity of the structure being transferred to the identified rates and associated porosities. We thus conclude that MRMT models can be very efficient for modeling diffusion-like transport in a broad range of porosity structures with only very few rates. Even though numerical simulations have been performed in 1D mobile domains, results are likely to be also valid in 3D. Additional simulations should also be performed to investigate the behavior of mixing and chemical reactivity both between different SINC structures and between SINC structures and their simplified MRMT counterparts.

Acknowledgements

The ANR is acknowledged for its funding through its Project H2MNO4 under the No. ANR-12-MONU-0012-01. The authors are also grateful to Linda Luquot, Alain Rapaport and Jesús Carrera for stimulating discussions, and additionally to Linda Luquot for providing the illustrative dissolution patterns. We also thank the four anonymous reviewers for their insightful and critical review of the manuscript, as well as Cass Miller for his editorial work.

Appendix A. Diagonalization of $\widehat{A}$

We show that the eigenvalues of the matrix $\widehat{A}$ are real and negative and that they correspond to the opposites of the rates of the equivalent MRMT model ($-\alpha_i$). As displayed by Eqs. (4) and (7), $\widehat{A} = -\widehat{\Phi}^{-1}\widehat{M}$ where $\widehat{\Phi} = \Phi(2\dots N+1, 2\dots N+1)$ and $\widehat{M} = M(2\dots N+1, 2\dots N+1)$. $\widehat{\Phi}^{-1}$ is diagonal and its diagonal elements are all positive. Thus $\widehat{\Phi}^{-1}$ is positive definite, i.e. for every non-zero and real column vector x, $x^T\widehat{\Phi}^{-1}x = \sum_i \frac{x(i)^2}{\Phi(i,i)} > 0$. $\widehat{M}$ is symmetrical, real, diagonally dominant $\left|\widehat{M}(i,i)\right| \geqslant \sum_{j,j\neq i}\left|\widehat{M}(i,j)\right|$, and strictly diagonally dominant $\left|\widehat{M}(i,i)\right| > \sum_{j,j\neq i}\left|\widehat{M}(i,j)\right|$ on its rows corresponding to the immobile zones connected to the mobile zone, due to the removal of the column corresponding to the mobile zone in the extraction of $\widehat{A}$ from A (Eq. (7)). If $\widehat{A}$ is additionally of rank N, then $\widehat{A}$ is diagonalizable, has real eigenvalues, and has the same number of positive and negative eigenvalues as $-\widehat{M}$ [24].

We moreover show that $-\widehat{M}$ and equivalently $\widehat{A}$ have strictly negative, real eigenvalues. It is the direct consequence [24] of $-\widehat{M}$ being symmetrical, real, having only negative diagonal elements, and also being irreducible diagonally dominant. The diagonally dominance has been shown previously. The irreducibility property is more involved but can be proved by studying the properties of the graph defined by $\widehat{M}$. When $\widehat{M}$ represents an immobile structure connected to the mobile structure by a single link, at least one path exists from any immobile cell to any other immobile cell that does not cross the mobile zone, then the graph defined by $\widehat{M}$ is strongly connected, so $\widehat{M}$ is irreducible [24]. When several immobile zones are independently connected to the mobile zone, each of these immobile zones is associated to a strongly connected graph and to an irreducible diagonally dominant matrix, itself a sub-matrix of $\widehat{M}$. The eigenvalues and eigenvectors of $\widehat{M}$ are then obtained by clustering the ones of the sub-matrices.

Appendix B. Construction of the matrix B

The norm of each eigenvector in $\widehat{R}$ is defined up to a constant. A first straightforward step is to adjust these norms so that the sum along the $2\dots N+1$ rows of B is equal to zero. It is achieved by taking $B_{i+1,1} = -\Lambda_i$, which writes in matrix form

$$\begin{bmatrix} B_{2,1} \\ \vdots \\ B_{N+1,1} \end{bmatrix} = -\Lambda \begin{bmatrix} 1 \\ \vdots \\ 1 \end{bmatrix}. \tag{B1}$$

Given this choice and the properties of the matrices A and $\widehat{R}$, we demonstrate that the sum of the elements of the first line of B is also zero. We express the relation between the first columns of A and B from Eq. (12):

$$\begin{bmatrix} B_{2,1} \\ \vdots \\ B_{N+1,1} \end{bmatrix} = \widehat{R}^{-1} \begin{bmatrix} A_{2,1} \\ \vdots \\ A_{N+1,1} \end{bmatrix}. \tag{B2}$$

As the sum of the elements of each line of A is zero

$$\begin{bmatrix} A_{2,1} \\ \vdots \\ A_{N+1,1} \end{bmatrix} = -\widehat{A} \begin{bmatrix} 1 \\ \vdots \\ 1 \end{bmatrix}. \tag{B3}$$

Eq. (B2) rewrites

$$\begin{bmatrix} B_{2,1} \\ \vdots \\ B_{N+1,1} \end{bmatrix} = -\widehat{R}^{-1}\widehat{A}\begin{bmatrix} 1 \\ \vdots \\ 1 \end{bmatrix} = -\Lambda\widehat{R}^{-1}\begin{bmatrix} 1 \\ \vdots \\ 1 \end{bmatrix}. \tag{B4}$$

By substituting equation (B4) into Eq. (B1), we deduce that the eigenvectors comply with

$$\begin{bmatrix} 1 \\ \vdots \\ 1 \end{bmatrix} = \widehat{R}\begin{bmatrix} 1 \\ \vdots \\ 1 \end{bmatrix}. \tag{B5}$$

As $R^{-1}U$ corresponds to the concentrations in the equivalent model (Eq. (13)), Eq. (B5) implies that a homogeneous immobile concentration profile in SINC remains unchanged in the equivalent model. We finally express the sum of the $2\dots N+1$ elements of the first row of B and use the result of Eq. (B5):

$$\begin{aligned}\sum_{j=2}^{N+1} B_{1,j} &= [\,B_{1,2} \quad \dots \quad B_{1,N+1}\,]\begin{bmatrix} 1 \\ \vdots \\ 1 \end{bmatrix} = [\,A_{1,2} \quad \dots \quad A_{1,N+1}\,]\widehat{R}\begin{bmatrix} 1 \\ \vdots \\ 1 \end{bmatrix} \\ &= [\,A_{1,2} \quad \dots \quad A_{1,N+1}\,]\begin{bmatrix} 1 \\ \vdots \\ 1 \end{bmatrix} = \sum_{j=2}^{N+1} A_{1,j} = -A_{1,1}.\end{aligned} \tag{B6}$$

An additional condition for B to be representative of a MRMT model is $B_{1,j} > 0$ for $j = 2\dots N+1$. In the following we show that the adjustment of the norms of the eigenvectors is sufficient to ensure this condition. Equations (12) and (B2) give:

$$\begin{aligned}&[\,B_{1,2} \quad \dots \quad B_{1,N+1}\,] \\ &= [\,A_{1,2} \quad \dots \quad A_{1,N+1}\,]\widehat{R} \\ &= -\tfrac{1}{\phi_m}[\,M_{1,2} \quad \dots \quad M_{1,N+1}\,]\widehat{R} \\ &= -\tfrac{1}{\phi_m}[\,M_{2,1} \quad \dots \quad M_{N+1,1}\,]\widehat{R} \text{ because } M \text{ is symmetric} \\ &= -\tfrac{1}{\phi_m}[\,\phi_{im}^1 A_{2,1} \quad \dots \quad \phi_{im}^N A_{N+1,1}\,]\widehat{R} \\ &= -\tfrac{1}{\phi_m}[\,A_{2,1} \quad \dots \quad A_{N+1,1}\,]\begin{bmatrix} \phi_{im}^1 & & \\ & \ddots & \\ & & \phi_{im}^N \end{bmatrix}\widehat{R} \\ &= \tfrac{1}{\phi_m}[\,B_{2,1} \quad \dots \quad B_{N+1,1}\,]\widehat{R}^T\begin{bmatrix} \phi_{im}^1 & & \\ & \ddots & \\ & & \phi_{im}^N \end{bmatrix}\widehat{R}\end{aligned} \tag{B7}$$

We now show that the matrix $\widehat{R}^T\widehat{\Phi}\widehat{R}$ with $\widehat{\Phi} = \Phi(2\dots N+1, 2\dots N+1)$ is diagonal with only positive diagonal elements.

We note $\widehat{A} = -\widehat{\Phi}^{-1}\widehat{M}$ with $\widehat{M} = M(2\dots N+1, 2\dots N+1)$. $\widehat{M}$ is symmetric, its diagonal elements are positive, its non-zero off-diagonal elements are negative, but the sum of its elements over each of its rows is not equal to zero. As the ϕ_{im}^i are positive, we can consider the square root of the matrix $\widehat{\Phi}$:

$$\widehat{A} = \widehat{\Phi}^{-1/2}\underbrace{(-1)\widehat{\Phi}^{-1/2}\widehat{M}\widehat{\Phi}^{-1/2}}_{\widehat{C}}\widehat{\Phi}^{1/2}. \tag{B8}$$

$\widehat{C}$ is similar (in the mathematical sense) to $\widehat{A}$, so it is diagonalizable and has the same eigenvalues as $\widehat{A}$. Moreover $\widehat{C}$ is symmetric, so it can be diagonalized by an orthogonal matrix S:

$$\widehat{C} = S\Lambda S^{-1}. \tag{B9}$$

As a consequence, Eq. (B9)rewrites:

$$\widehat{A} = \widehat{\Phi}^{-1/2}S\Lambda S^{-1}\widehat{\Phi}^{1/2} = \widehat{\Phi}^{-1/2}S\Lambda\left(\widehat{\Phi}^{-1/2}S\right)^{-1}. \tag{B10}$$

As the norms of the eigenvectors in $\widehat{R}$ are adjusted so that Eq. (B1) is verified, there exists a unique orthogonal matrix S such that

$$S = \widehat{\Phi}^{1/2}\widehat{R}. \tag{B11}$$

As S is orthogonal, S^TS is diagonal with only positive diagonal elements and writes

$$S^TS = \left(\widehat{\Phi}^{1/2}\widehat{R}\right)^T\widehat{\Phi}^{1/2}\widehat{R} = \widehat{R}^T\widehat{\Phi}^{1/2}\widehat{\Phi}^{1/2}\widehat{R} = \widehat{R}^T\widehat{\Phi}\widehat{R}. \tag{B12}$$

The matrix $\widehat{R}^T\widehat{\Phi}\widehat{R}$, which is present in Eq. (B7), is thus diagonal with only positive diagonal elements. Consequently, as the $B_{1,j}$ are positive for $j = 2\dots N+1$, so are the $B_{j,1}$.

Appendix C. Numerical identification method of MRMT models equivalent to a SINC model

We set up an optimization scheme to approximate the MRMT model equivalent to a SINC model. We first consider the case where the remaining mass per unitary volume $m(t)$ in the immobile domain during its discharge into a quickly flushed mobile domain can effectively be modeled by a series of N exponential functions with rates α_i and associate porosities ϕ_{im}^i ($m(t) = \gamma(t)$, see Eq. (15)). We derive a set of equivalent expressions in the Laplace domain with simple dependences on α_i and ϕ_{im}^i. We then deduce optimization strategies both in the Laplace and temporal domains.

We assume first that the SINC model is strictly equivalent to a given MRMT model as in Section 2 ($m(t) = \gamma(t)$). It is the case when initial concentrations are homogeneous in the immobile zone and when the immobile zones are constantly discharging to a quickly flushed mobile zone where concentration is assumed to remain negligible ([21], Appendix B). In the Laplace domain, exponential functions become simple rational functions and $\tilde{m}(p) = \tilde{\gamma}(p)$ is expressed as

$$\tilde{m}(p) = \sum_{i=1}^{N}\frac{\phi_{im}^i c_0}{\alpha_i}\frac{1}{1+\frac{p}{\alpha_i}}, \tag{C1}$$

where p is the Laplace variable and $\tilde{m}(p)$ (respectively $\tilde{\gamma}(p)$) is the Laplace transform of $m(t)$ (respectively $\gamma(p)$). We multiply Eq. (C1) by the polynomial $P(p)$ of degree N

$$P(p) = \prod_{i=1}^{N}\left(1+\frac{p}{\alpha_i}\right) = 1 + a_1p + a_2p^2 + \dots + a_Np^N, \tag{C2}$$

and obtain

$$\left(1 + a_1p + a_2p^2 + \dots + a_Np^N\right)\tilde{m}(p) = \sum_{i=1}^{N}\left[\frac{\phi_{im}^i c_0}{\alpha_i}\prod_{\substack{j=1\\ j\neq i}}^{N}\left(1+\frac{p}{\alpha_j}\right)\right]. \tag{C3}$$

If we now consider the polynomial $Q_i(p)$ of degree $N-1$

$$Q_i(p) = \prod_{\substack{j=1\\ j\neq i}}^{N}\left(1+\frac{p}{\alpha_j}\right) = 1 + a_{i,1}p + a_{i,2}p^2 + \dots + a_{i,N-1}p^{N-1}, \tag{C4}$$

and substitute equation (C4) into Eq. (C3), we obtain:

$$\begin{aligned}&\left(a_1p + a_2p^2 + \dots + a_Np^N\right)\tilde{m}(p) + \tilde{m}(p) \\ &= \sum_{i=1}^{N}\frac{\phi_{im}^i c_0}{\alpha_i}\left(1 + a_{i,1}p + a_{i,2}p^2 + \dots + a_{i,N-1}p^{N-1}\right).\end{aligned} \tag{C5}$$

The interest of Eq. (C5) is to be linear in the a_i (polynomial coefficients of $P(p)$) and in ϕ^i_{im}/α_i with $i = 1 \dots N$. We isolate these quantities from the Laplace parameter-dependant elements to obtain the linear system

$$\varphi^T(p)\theta = y(p), \tag{C6}$$

with

$$\varphi(p) = \begin{bmatrix} p\tilde{m}(p) \\ p^2\tilde{m}(p) \\ \vdots \\ p^N\tilde{m}(p) \\ -1 \\ -p \\ \vdots \\ -p^{N-1} \end{bmatrix}, \quad \theta = \begin{bmatrix} a_1 \\ a_2 \\ \vdots \\ a_N \\ \sum_{i=1}^{N} \frac{\phi^i_{im} c_0}{\alpha_i} \\ \sum_{i=1}^{N} \frac{\phi^i_{im} c_0}{\alpha_i} a_{i,1} \\ \vdots \\ \sum_{i=1}^{N} \frac{\phi^i_{im} c_0}{\alpha_i} a_{i,N-1} \end{bmatrix}, \quad y(p) = -\tilde{m}(p). \tag{C7}$$

Both $\varphi(p)$ and θ are vectors of dimension $2N$. The rates $-\alpha_i$ are directly obtained from the roots of the polynomial $P(p)$ of Eq. (C2), whose coefficients are given by $\theta_1 \dots \theta_N$. The porosities ϕ^i_{im} are further deduced from $\theta_{N+1} \dots \theta_{2N}$ by inversing the $N+1 \dots 2N$ equations of (C7):

$$\begin{bmatrix} \phi^1_{im} \\ \phi^2_{im} \\ \vdots \\ \phi^N_{im} \end{bmatrix} = G^{-1} \begin{bmatrix} \theta_{N+1} \\ \theta_{N+2} \\ \vdots \\ \theta_{2N} \end{bmatrix}, \tag{C8}$$

with

$$G = \begin{bmatrix} c_0/\alpha_1 & \cdots & c_0/\alpha_N \\ c_0 a_{1,1}/\alpha_1 & \cdots & c_0 a_{N,1}/\alpha_N \\ \vdots & & \vdots \\ c_0 a_{1,N-1}/\alpha_1 & \cdots & c_0 a_{N,N-1}/\alpha_N \end{bmatrix}, \tag{C9}$$

where the values of $a_{i,j}$ are deduced from the identified values of α_i. In the case of strict equivalence between MRMT and SINC models, the equivalent MRMT model can be found through (C6)–(C9).

In the case where MRMT and SINC models are not strictly equivalent, we seek for the composition of N exponential functions that best matches $\tilde{m}(p)$ on a given sampling of the Laplace parameter p_k, $k = 1, \dots, K$ of p by using a least-square method, minimizing the mismatch objective function J [14,27]:

$$J = \sum_{k=1}^{K} \left(y(p_k) - \phi^T(p_k)\theta\right)^2. \tag{C10}$$

The sampling should be extensive enough to contain all the information necessary to identify the different rates. If α_N is the largest rate, the initial time sampling should be smaller than $\alpha_N^{-1}/2$ following the spirit of Shannon's theorem. Adequate time sampling could then increase with time for determining the smaller rates.

The minimum $\tilde{\theta}$ of J is explicitly given by:

$$\tilde{\theta} = \left(\sum_{k=1}^{K} \varphi(p_k)\varphi^T(p_k)\right)^{-1} \sum_{k=1}^{K} \varphi(p_k) y(p_k), \tag{C11}$$

and the α_i and ϕ^i_{im} coefficients can be determined from the approximate $\tilde{\theta}_i$ coefficients and (C6)–(C9).

$\tilde{\theta}$ can also be obtained in the temporal domain. We first divide equation (C5) by p^N (which is equivalent to integrate N times over t in the temporal domain) because of the better numerical stability of integration compared to derivation

$$\left(\frac{1}{p^N} + a_1 \frac{1}{p^{N-1}} + a_2 \frac{1}{p^{N-2}} + \cdots + a_N\right)\tilde{m}(p) = \sum_{i=1}^{N} \frac{\phi^i_{im} c_0}{\alpha_i} \left(\frac{1}{p^N} + a_{i,1} \frac{1}{p^{N-1}} + a_{i,2} \frac{1}{p^{N-2}} + \cdots + a_{i,N-1} \frac{1}{p}\right). \tag{C12}$$

For convenience, we note

$$\int^{(n)} m(u)du = \int_0^t \int_0^{u_1} \int_0^{u_2} \cdots \int_0^{u_{n-1}} m(u_n) du_n \dots du_2 du_1. \tag{C13}$$

The inverse Laplace transform of equation (C12) gives

$$\int^{(N)} m(u)du + a_1 \int^{(N-1)} m(u)du + a_2 \int^{(N-2)} m(u)du + \cdots + a_N m(t) = \sum_{i=1}^{N} \frac{\phi^i_{im} c_0}{\alpha_i} \left(\frac{t^{N-1}}{(N-1)!} + a_{i,1} \frac{t^{N-2}}{(N-2)!} + a_{i,2} \frac{t^{N-3}}{(N-3)!} + \cdots + a_{i,N-1}\right). \tag{C14}$$

As done previously in the Laplace domain, we separate the time-dependent elements from the quantities depending on ϕ^i_{im} and α_i

$$\varphi(t) = \begin{bmatrix} \int^{(N-1)} m(u)du \\ \int^{(N-2)} m(u)du \\ \vdots \\ m(t) \\ -\frac{t^{N-1}}{(N-1)!} \\ -\frac{t^{N-2}}{(N-2)!} \\ \vdots \\ -1 \end{bmatrix}, \quad \theta = \begin{bmatrix} a_1 \\ a_2 \\ \vdots \\ a_N \\ \sum_{i=1}^{N} \frac{\phi^i_{im} c_0}{\alpha_i} \\ \sum_{i=1}^{N} \frac{\phi^i_{im} c_0}{\alpha_i} a_{i,1} \\ \vdots \\ \sum_{i=1}^{N} \frac{\phi^i_{im} c_0}{\alpha_i} a_{i,N-1} \end{bmatrix},$$

$$y(t) = -\int^{(N)} m(u)du. \tag{C15}$$

θ may also be obtained with a similar least-square method by considering a discretization of time t_k ($k = 1 \dots K$) and by minimizing the objective function

$$J = \sum_{k=1}^{K} \left(y(t_k) - \varphi^T(t_k)\theta\right)^2. \tag{C16}$$

The minimum $\tilde{\theta}$ is given by

$$\tilde{\theta} = \left(\sum_{k=1}^{K} \varphi(t_k)\varphi^T(t_k)\right)^{-1} \sum_{k=1}^{K} \varphi(t_k) y(t_k). \tag{C17}$$

Appendix D. Application of the numerical identification method to cases $N = 1$ and $N = 2$

We recall the expression of $m(t)$, the remaining mass of solute per unitary volume in the immobile domain, during a discharge into a mobile zone of constant concentration zero (Eq. (C1)):

$$m(t) = \sum_{i=1}^{N} c_0 \phi_{im}^i \exp(-\alpha_i t), \tag{D1}$$

where c_0 is the initial homogeneous immobile concentration.

D.1. Case $N = 1$

In Laplace domain, Eq. (D1) rewrites:

$$\tilde{m}(p) = \frac{\phi_{im}^1 c_0}{\alpha_1} \frac{1}{1+\frac{p}{\alpha_1}}, \tag{D2}$$

$$\left(1+\frac{p}{\alpha_1}\right)\tilde{m}(p) = \frac{\phi_{im}^1 c_0}{\alpha_1}. \tag{D3}$$

Dividing equation (D3) by p and then using the inverse Laplace transform, we obtain:

$$\int_0^t m(u)du + \frac{m(t)}{\alpha_1} = \frac{\phi_{im}^1 c_0}{\alpha_1}. \tag{D4}$$

Equations (D3) and (D4) are both linear in quantities depending on the unknown parameters α_1 and ϕ_{im}^1 to be identified. Equation (D4) can be written under the form:

$$\phi^T(t)\theta = y(t) \tag{D5}$$

with:

$$\phi(t) = \begin{bmatrix} m(t) \\ -1 \end{bmatrix}, \quad \theta = \begin{bmatrix} 1/\alpha_1 \\ c_0\phi_{im}^1/\alpha_1 \end{bmatrix}, \quad y(t) = -\int_0^t m(u)du. \tag{D6}$$

The vector $\tilde{\theta}$ which minimizes the quantity:

$$J = \sum_{k=1}^{K} \left(y(t_k) - \varphi^T(t_k)\theta\right)^2 \tag{D7}$$

with a discretization t_k, $k = 1, \ldots, K$ of t, is given by:

$$\tilde{\theta} = \left(\sum_{k=1}^{K} \varphi(t_k)\varphi^T(t_k)\right)^{-1} \sum_{k=1}^{K} \varphi(t_k) y(t_k), \tag{D8}$$

where

$$\varphi(t_k)\varphi^T(t_k) = \begin{bmatrix} m(t_k)^2 & -m(t_k) \\ -m(t_k) & 1 \end{bmatrix},$$
$$\varphi(t_k)y(t_k) = \begin{bmatrix} -m(t_k)\int_0^{t_k} m(u)du \\ \int_0^{t_k} m(u)du \end{bmatrix} \tag{D9}$$

so

$$\tilde{\theta} = \begin{bmatrix} \sum_{k=1}^{K} m(t_k)^2 & -\sum_{k=1}^{K} m(t_k) \\ -\sum_{k=1}^{K} m(t_k) & K \end{bmatrix}^{-1} \begin{bmatrix} -\sum_{k=1}^{K} m(t_k)\int_0^{t_k} m(u)du \\ \sum_{k=1}^{K} \int_0^{t_k} m(u)du \end{bmatrix}. \tag{D10}$$

We then get α_1 and ϕ_{im}^1:

$$\alpha_1 = \frac{1}{\tilde{\theta}_1}, \phi_{im}^1 = \frac{\tilde{\theta}_2 \alpha_1}{c_0}. \tag{D11}$$

D.2. Case $N = 2$

In Laplace domain, Eq. (D1) rewrites:

$$\tilde{m}(p) = \frac{\phi_{im}^1 c_0}{\alpha_1} \frac{1}{1+\frac{p}{\alpha_1}} + \frac{\phi_{im}^2 c_0}{\alpha_2} \frac{1}{1+\frac{p}{\alpha_2}}, \tag{D12}$$

which gives, when multiplied by $(1+p/\alpha_1)(1+p/\alpha_2)$:

$$(1+p/\alpha_1)(1+p/\alpha_2)\tilde{m}(p) = \frac{\phi_{im}^1 c_0}{\alpha_1}(1+p/\alpha_2) + \frac{\phi_{im}^2 c_0}{\alpha_2}(1+p/\alpha_1). \tag{D13}$$

We divide then Eq. (D13) by p^2 (which is equivalent to integrate two times over t) and get:

$$\frac{1}{\alpha_1\alpha_2}\tilde{m}(p) + \left(\frac{1}{\alpha_1}+\frac{1}{\alpha_2}\right)\frac{\tilde{m}(p)}{p} + \frac{\tilde{m}(p)}{p^2} = \frac{\phi_{im}^1 c_0}{\alpha_1}\left(\frac{1}{p^2}+\frac{1}{p\alpha_2}\right) + \frac{\phi_{im}^2 c_0}{\alpha_2}\left(\frac{1}{p^2}+\frac{1}{p\alpha_1}\right). \tag{D14}$$

Then, by using the inverse Laplace transform, we obtain:

$$\frac{1}{\alpha_1\alpha_2}m(t) + \left(\frac{1}{\alpha_1}+\frac{1}{\alpha_2}\right)\int_0^t m(u)du + \int_0^t\int_0^u m(v)dvdu = \frac{\phi_{im}^1 c_0}{\alpha_1}\left(t+\frac{1}{\alpha_2}\right) + \frac{\phi_{im}^2 c_0}{\alpha_2}\left(t+\frac{1}{\alpha_1}\right). \tag{D15}$$

Again Eqs. (D12) and (D13) are both linear in quantities depending on the unknown parameters α_i and ϕ_{im}^i to be identified. Equation (D15) and can be written under the form:

$$\varphi^T(t)\theta = y(t) \tag{D16}$$

with:

$$\varphi(t) = \begin{bmatrix} \int_0^t m(u)du \\ m(t) \\ -t \\ -1 \end{bmatrix}, \quad \theta = \begin{bmatrix} 1/\alpha_1 + 1/\alpha_2 \\ 1/(\alpha_1\alpha_2) \\ \frac{\phi_{im}^1 c_0}{\alpha_1} + \frac{\phi_{im}^2 c_0}{\alpha_2} \\ \frac{\phi_{im}^1 c_0}{\alpha_1\alpha_2} + \frac{\phi_{im}^2 c_0}{\alpha_1\alpha_2} \end{bmatrix},$$
$$y(t) = -\int_0^t\int_0^u m(v)dvdu. \tag{D17}$$

The vector $\tilde{\theta}$ which minimizes the quantity:

$$J = \sum_{k=1}^{K} \left(y(t) - \varphi^T(t)\theta\right)^2 \tag{D18}$$

with a discretization t_k, $k = 1, \ldots, K$ of t, is given by:

$$\tilde{\theta} = \left(\sum_{k=1}^{K} \varphi(t_k)\varphi^T(t_k)\right)^{-1} \sum_{k=1}^{K} \varphi(t_k) y(t_k). \tag{D19}$$

We then have the following relations:

$$\begin{cases} 1/\alpha_1 + 1/\alpha_2 = \tilde{\theta}_1 \\ 1/(\alpha_1\alpha_2) = \tilde{\theta}_2 \\ \frac{\phi_{im}^1 c_0}{\alpha_1} + \frac{\phi_{im}^2 c_0}{\alpha_2} = \tilde{\theta}_3 \\ \frac{\phi_{im}^1 c_0}{\alpha_1\alpha_2} + \frac{\phi_{im}^2 c_0}{\alpha_1\alpha_2} = \tilde{\theta}_4 \end{cases}, \tag{D20}$$

from which we can identify the unknown parameters $-\alpha_1$ and $-\alpha_2$ that may be obtained as the roots of the polynomial $1 + \tilde{\theta}_1 x + \tilde{\theta}_2 x^2$. Once α_1 and α_2 are identified, ϕ_{im}^1 and ϕ_{im}^2 are given by:

$$\begin{bmatrix} \phi_{im}^1 \\ \phi_{im}^2 \end{bmatrix} = \frac{1}{c_0}\begin{bmatrix} 1/\alpha_1 & 1/\alpha_2 \\ 1/\alpha_1\alpha_2 & 1/\alpha_1\alpha_2 \end{bmatrix}^{-1}\begin{bmatrix} \tilde{\theta}_3 \\ \tilde{\theta}_4 \end{bmatrix}. \tag{D21}$$

References

[1] Benson DA, Meerschaert MM. A simple and efficient random walk solution of multi-rate mobile/immobile mass transport equations. Adv Water Resour 2009;32(4):532–9. http://dx.doi.org/10.1016/j.advwatres.2009.01.002.

[2] Benson DA, Schumer R, Meerschaert MM, Wheatcraft SW. Fractional dispersion, Lévy motion, and the MADE tracer test. Transp Porous Media 2001;42(1–2):211–40. http://dx.doi.org/10.1007/978-94-017-1278-1_11.

[3] Benson DA, Wheatcraft SW, Meerschaert MM. Application of a fractional advection–dispersion equation. Water Resour Res 2000;36(6). http://dx.doi.org/10.1029/2000WR900031.
[4] Berkowitz B, Cortis A, Dentz M, Scher H. Modeling non-Fickian transport in geological formations as a continuous time random walk. Rev Geophys 2006;44(2). http://dx.doi.org/10.1029/2005rg000178.
[5] Berkowitz B, Scher H. Theory of anomalous chemical transport in random fracture networks. Phys Rev E 1998;57(5). http://dx.doi.org/10.1103/PhysRevE.57.5858.
[6] Berkowitz B, Scher H, Silliman S. Anomalous transport in laboratory-scale, heterogeneous porous media. Water Resour Res 2000;36(1). http://dx.doi.org/10.1029/1999WR900295.
[7] Carrera J, Sánchez-Vila X, Benet I, Medina A, Galarza G, Guimerà J. On matrix diffusion: formulations, solution methods and qualitative effects. Hydrogeol J 1998;6(1). http://dx.doi.org/10.1007/s100400050143.
[8] Cushman JH, Ginn TR. Fractional advection–dispersion equation: a classical mass balance with convolution-Fickian flux. Water Resour Res 2000;36(12). http://dx.doi.org/10.1029/2000WR900261.
[9] de Dreuzy JR, Rapaport A, Babey T, Harmand J. Influence of porosity structures on mixing-induced reactivity at chemical equilibrium in mobile/immobile Multi-Rate Mass Transfer (MRMT) and Multiple INteracting Continua (MINC) models. Water Resour Res 2013;49(12):8511–30. http://dx.doi.org/10.1002/2013WR013808.
[10] Dentz M, Berkowitz B. Transport behavior of a passive solute in continuous time random walks and multirate mass transfer. Water Resour Res 2003;39(5):1111. http://dx.doi.org/10.1029/2001WR001163.
[11] Dentz M, Cortis A, Scher H, Berkowitz B. Time behavior of solute transport in heterogeneous media: transition from anomalous to normal transport. Adv Water Resour 2004;27(2):155–73. http://dx.doi.org/10.1016/j.advwatres.2003.11.002.
[12] Fernandez-Garcia D, Llerar-Meza G, Gomez-Hernandez JJ. Upscaling transport with mass transfer models: mean behavior and propagation of uncertainty. Water Resour Res 2009;45. http://dx.doi.org/10.1029/2009wr007764.
[13] Flekkøy EG, Malthe-Sørenssen A, Jamtveit B. Modeling hydrofracture. J Geophys Res 2002;107(B8):2151. http://dx.doi.org/10.1029/2000JB000132.
[14] Garnier H, Wang L, Young P. Direct identification of continuous-time models from sampled data: issues, basic solutions and relevance. In: Garnier H, Wang L, editors. Identification of continuous-time models from sampled data. London: Springer; 2008. p. 1–29. http://dx.doi.org/10.1007/978-1-84800-161-9_1.
[15] Golfier F, Quintard M, Cherblanc F, Zinn BA, Wood BD. Comparison of theory and experiment for solute transport in highly heterogeneous porous medium. Adv Water Resour 2007;30(11):2235–61. http://dx.doi.org/10.1016/j.advwatres.2007.05.004.
[16] Golfier F, Zarcone C, Bazin B, Lenormand R, Lasseux D, Quintard M. On the ability of a Darcy-scale model to capture wormhole formation during the dissolution of a porous medium. J Fluid Mech 2002;457:213–54. http://dx.doi.org/10.1017/s0022112002007735.
[17] Gotovac H, Cvetkovic V, Andricevic R. Flow and travel time statistics in highly heterogeneous porous media. Water Resour Res 2009;45:24. http://dx.doi.org/10.1029/2008WR007168.
[18] Gouze P, Melean Y, Le Borgne T, Dentz M, Carrera J. Non-Fickian dispersion in porous media explained by heterogeneous microscale matrix diffusion. Water Resour Res 2008;44(11):19. http://dx.doi.org/10.1029/2007wr006690.
[19] Haggerty R. Matrix diffusion – heavy-tailed residence time distributions and their influence on radionuclide retention. In: Paper presented at 5th GEOTRAP workshop on radionuclide retention in geologic media, May 7–9, 2001, Organisation for Economic Co-Operation and Development, Nuclear Energy Agency, 75 – Paris (France), Oskarshamn, Sweden, 2002. http://dx.doi.org/10.1787/9789264196148-en.
[20] Haggerty R, Fleming SW, Meigs LC, McKenna SA. Tracer tests in a fractured dolomite 2. Analysis of mass transfer in single-well injection-withdrawal tests. Water Resour Res 2001;37(5). http://dx.doi.org/10.1029/2000WR900334.
[21] Haggerty R, Gorelick SM. Multiple-rate mass transfer for modeling diffusion and surface reactions in media with pore-scale heterogeneity. Water Resour Res 1995;31(10):2383–400. http://dx.doi.org/10.1029/95WR10583.
[22] Haggerty R, Harvey CF, von Schwerin CF, Meigs LC. What controls the apparent timescale of solute mass transfer in aquifers and soils? A comparison of experimental results. Water Resour Res 2004;40(1). http://dx.doi.org/10.1029/2002wr001716.
[23] Haggerty R, McKenna SA, Meigs LC. On the late-time behavior of tracer test breakthrough curves. Water Resour Res 2000;36(12):3467–79. http://dx.doi.org/10.1029/2000WR900214.
[24] Horn RA, Johnson CR. Matrix analysis. Cambridge, New York: Cambridge University Press; 1985, ISBN 0-521-30586-1.
[25] Jardine PM, Sanford WE, Gwo JP, Reedy OC, Hicks DS, Riggs JS, Bailey WB. Quantifying diffusive mass transfer in fractured shale bedrock. Water Resour Res 1999;35(7):2015–30. http://dx.doi.org/10.1029/1999WR900043.
[26] Karimi-Fard M, Gong B, Durlofsky LJ. Generation of coarse-scale continuum flow models from detailed fracture characterizations. Water Resour Res 2006;42(10). http://dx.doi.org/10.1029/2006WR005015.
[27] Ljung L. System identification: theory for the user. Upper Saddle River: Prentice Hall; 1999, ISBN 0-13-656695-2.
[28] Luquot L, Rodriguez O, Gouze P. Experimental characterization of porosity structure and transport property changes in limestone undergoing different dissolution regimes. Transp Porous Media 2014;101(3):507–32. http://dx.doi.org/10.1007/s11242-013-0257-4.
[29] Michalak AM, Kitanidis PK. Macroscopic behavior and random-walk particle tracking of kinetically sorbing solutes. Water Resour Res 2000;36(8):2133–46. http://dx.doi.org/10.1029/2000wr900109.
[30] Neretnieks I. Diffusion in the rock matrix: an important factor in radionuclide retardation? J Geophys Res 1980;85(B8):4379–97. http://dx.doi.org/10.1029/JB085iB08p04379.
[31] Neuman SP, Tartakovsky DM. Perspective on theories of non-Fickian transport in heterogeneous media. Adv Water Resour 2009;32(5):670–80. http://dx.doi.org/10.1016/j.advwatres.2008.08.005.
[32] Noetinger B, Estebenet T. Up-scaling of double porosity fractured media using continuous-time random walks methods. Transp Porous Media 2000;39(3). http://dx.doi.org/10.1023/A:1006639025910.
[33] Pruess K. Brief guide to the MINC – method for modeling flow and transport in fractured MediaRep., Earth Sciences Division, Lawrence Berkeley National Laboratory. Berkeley CA USA; 1992. http://dx.doi.org/10.2172/6951290.
[34] Pruess K, Narasimhan TN. A practical method for modeling fluid and heat-flow in fractured porous-media. Soc Pet Eng J 1985;25(1):14–26. http://dx.doi.org/10.2118/10509-PA.
[35] Silva O, Carrera J, Dentz M, Kumar S, Alcolea A, Willmann M. A general real-time formulation for multi-rate mass transfer problems. Hydrol Earth System Sci 2009;13(8):1399–411. http://dx.doi.org/10.5194/hess-13-1399-2009.
[36] Sornette A, Davy P, Sornette D. Fault growth in brittle–ductile experiments and the mechanics of continental collisions. J Geophys Res Solid Earth 1993;98(B7):12111–39. http://dx.doi.org/10.1029/92JB01740.
[37] Sudicky EA, Frind EO. Contaminant transport in fractured porous-media – analytical solutions for a system of parallel fractures. Water Resour Res 1982;18(6):1634–42. http://dx.doi.org/10.1029/WR018i006p01634.
[38] Tang DH, Frind EO, Sudicky EA. Contaminant transport in fractured porous-media – analytical solution for a single fracture. Water Resour Res 1981;17(3):555–64. http://dx.doi.org/10.1029/WR017i003p00555.
[39] Tsang YW. Study of alternative tracer tests in characterizing transport in fractured rocks. Geophys Res Lett 1995;22(11):1421–4. http://dx.doi.org/10.1029/95GL01093.
[40] Villermaux J. Chemical-engineering approach to dynamic modeling of linear chromatography – a flexible method for representing complex phenomena from simple concepts. J Chromatogr 1987;406:11–26. http://dx.doi.org/10.1016/s0021-9673(00)94014-7.
[41] Warren JE, Root PJ, Aime M. The behavior of naturally fractured reservoirs. Soc Pet Eng J 1963:245–55. http://dx.doi.org/10.2118/426-PA.
[42] Willmann M, Carrera J, Sanchez-Vila X. Transport upscaling in heterogeneous aquifers: What physical parameters control memory functions? Water Resour Res 2008;44(12). http://dx.doi.org/10.1029/2007wr006531.

3 Bilan

Nous avons démontré dans l'article précédent que n'importe quel modèle SINC (i.e. peu importe l'organisation de sa porosité immobile) est algébriquement équivalent en termes de concentration d'un soluté conservatif dans la zone mobile à un modèle MRMT unique. Ce modèle MRMT peut être déterminé par une transformation algébrique de la matrice d'interactions décrivant les échanges entre les zones immobiles du modèle SINC original. Un modèle MRMT équivalent possède un nombre de taux d'échange égal au nombre de zones immobiles du modèle SINC de référence. L'application de cette méthode aux quatre structures SINC de référence de la *Figure 3.2* a en outre montré que, dû à l'homogénéisation opérée par la diffusion, un petit nombre de taux d'échange concentre la majorité de la porosité diffusive (typiquement, 5 taux d'échange correspondent à plus de 95% de la porosité immobile). Nous avons donc également proposé deux méthodes permettant d'approximer le modèle MRMT équivalent par un nombre limité de taux d'échange, fixé par l'utilisateur, à partir d'une donnée de type courbe de restitution. Les modèles MRMT réduits ainsi obtenus (3-5 taux d'échange) parviennent à reproduire la macrodispersion observée dans SINC avec une erreur de seulement quelques pourcents, voire moins. Nos résultats renforcent ainsi l'intérêt du modèle MRMT comme proxy pour le transport conservatif. Le lien entre les caractéristiques des structures SINC (présence d'une jonction, d'une boucle...) et la distribution des rates dans le modèle MRMT équivalent n'a pas été étudié. Il pourrait l'être au travers de simulation numériques extensives ou en s'intéressant aux propriétés de la transformation algébrique de SINC en MRMT.

Chapitre 4 : Du transport conservatif au transport réactif en régime dominé par la diffusion

1 Introduction

Nous avons vu précédemment que le modèle MRMT pouvait être utilisé pour reproduire l'impact de structures diffusives complexes sur les courbes de restitution d'un essai de traçage pour du transport conservatif (Babey et al. 2015). Nous avons également proposé plusieurs méthodes afin d'identifier ce modèle MRMT équivalent. Dans ce chapitre, nous évaluons la possibilité d'étendre l'utilisation de MRMT à la prédiction d'une réactivité non-linéaire. Nous commençons par utiliser les méthodes développées précédemment pour identifier les modèles MRMT équivalents à quatre structures immobiles SINC de référence (*Figure 3.2*). Puis nous utilisons les "concentrations" MRMT comme des concentrations réelles de réactants pour simuler des taux de réaction que nous comparons à ceux de SINC. Les deux réactions considérées sont la dissolution d'un minéral et la sorption de type Freundlich, toutes deux non-linéaires et sous contrôle cinétique. SINC et MRMT sont comparés sur une expérience de flush, où un minéral / une concentration sorbée initialement répartis de manière homogène dans le milieu sont mobilisés par l'injection continue d'une solution sous-saturée à l'entrée de la zone mobile. Les taux de réaction dans SINC et MRMT seront a priori différents. En effet, la relation d'équivalence entre SINC et MRMT ne préserve pas la distribution des concentrations immobiles, et les opérateurs de transport et de réaction ne commutent pas pour une réaction non-linéaire.

2 Article: "*From conservative to reactive transport under diffusion-controlled conditions*", par T. Babey, J.-R. de Dreuzy et T.R. Ginn, publié en 2016 dans Water Resources Research

AGU PUBLICATIONS

Water Resources Research

RESEARCH ARTICLE
10.1002/2015WR018294

From conservative to reactive transport under diffusion-controlled conditions

Tristan Babey[1], Jean-Raynald de Dreuzy[1], and Timothy R. Ginn[2]

[1]Géosciences Rennes UMR CNRS 6118, Campus de Beaulieu, Université de Rennes 1, Rennes, France, [2]Department of Civil and Environmental Engineering, Washington State University, Pullman, Washington, USA

Key Points:
- Simulation of nonlinear fluid-rock interactions under diffusive-controlled transport
- Derivation of concentration distributions from conservative transport by MRMT models
- Mono-component reactivity accurately estimated by parsimonious MRMT models

Correspondence to:
T. Babey,
tristan.babey@univ-rennes1.fr

Citation:
Babey, T., J.-R. de Dreuzy, and T. R. Ginn (2016), From conservative to reactive transport under diffusion-controlled conditions, *Water Resour. Res.*, *52*, doi:10.1002/2015WR018294.

Received 28 OCT 2015
Accepted 16 APR 2016
Accepted article online 25 APR 2016

Abstract We assess the possibility to use conservative transport information, such as that contained in transit time distributions, breakthrough curves and tracer tests, to predict nonlinear fluid-rock interactions in fracture/matrix or mobile/immobile conditions. Reference simulated data are given by conservative and reactive transport simulations in several diffusive porosity structures differing by their topological organization. Reactions includes nonlinear kinetically controlled dissolution and desorption. Effective Multi-Rate Mass Transfer models (MRMT) are calibrated solely on conservative transport information without pore topology information and provide concentration distributions on which effective reaction rates are estimated. Reference simulated reaction rates and effective reaction rates evaluated by MRMT are compared, as well as characteristic desorption and dissolution times. Although not exactly equal, these indicators remain very close whatever the porous structure, differing at most by 0.6% and 10% for desorption and dissolution. At early times, this close agreement arises from the fine characterization of the diffusive porosity close to the mobile zone that controls fast mobile-diffusive exchanges. At intermediate to late times, concentration gradients are strongly reduced by diffusion, and reactivity can be captured by a very limited number of rates. We conclude that effective models calibrated solely on conservative transport information like MRMT can accurately estimate monocomponent kinetically controlled nonlinear fluid-rock interactions. Their relevance might extend to more advanced biogeochemical reactions because of the good characterization of conservative concentration distributions, even by parsimonious models (e.g., MRMT with 3–5 rates). We propose a methodology to estimate reactive transport from conservative transport in mobile-immobile conditions.

1. Introduction

Transit time distributions obtained from conservative tracer testing are often used to predict chemically active transport [e.g., *Becker and Shapiro*, 2000; *Charbeneau*, 2006; *Cirpka and Kitanidis*, 2000; *Ginn*, 2001; *Hadermann and Heer*, 1996; *Haggerty et al*., 2001; *LeBlanc et al*., 1991; *Ptak and Schmid*, 1996]. Conservative transport models are then coupled to simple chemical models to investigate contaminant fate involving kinetically degrading compounds [*Bohlke*, 2002; *Green et al*., 2014; *Heße et al*., 2014], radioactively decaying species [*Cvetkovic et al*., 1999; *Neretnieks*, 1980], or sorbing solutes [*Brusseau*, 1992; *Vereecken et al*., 1999; *Wels and Smith*, 1994]. Reactivity can be straightforwardly inferred for linear approximation of reactivity, a case for which transport and chemical operators commute [*Bahr and Rubin*, 1987; *Michalak and Kitanidis*, 2000; *Valocchi*, 1990], as well as for more involved biogeochemical hysteretic cases through exposure time concepts [*Ginn*, 1999; *Murphy and Ginn*, 2000]. Similar approximations are also used at larger watershed and continental scales with more limited hydrological tracer information to constrain long-term fluid-rock interactions like weathering and dissolution rates [*Clark and Fritz*, 1997; *Maher*, 2010, 2011; *Mukhopadhyay et al*., 2014; *Steefel and Maher*, 2009; *Yoo and Mudd*, 2008]. However, for nonlinear sorption/desorption or precipitation/dissolution, bulk fluid-rock interactions cannot be inferred solely from transit time information and require some additional approximation of the concentration distribution [*Attinger et al*., 2009; *Brusseau and Srivastava*, 1997; *Vereecken et al*., 2002].

In some highly heterogeneous media, reactivity is controlled by the slow diffusion to the reactive sites located aside from the main advective channels, as in the case of fractured media in which solutes are quickly advected along the main connected fractures that account only for a minor part of the porosity and

slowly diffuse in the extensive but less connected fractures and in the large volume of surrounding rock [*MacQuarrie and Mayer*, 2005; *Molson et al*., 2012; *Neretnieks*, 1980; *Steefel and Lichtner*, 1994]. Similar behavior occurs in the case of inclusions of almost impervious structures in more pervious media and at smaller scales of complex dissolution patterns or clay aggregates [*Luquot et al*., 2014b; *Murphy et al*., 1997; *Poonoosamy et al*., 2015; *Tyagi et al*., 2013]. These slow diffusion processes have been identified as a source of failure of the advection-dispersion equation to model transport in heterogeneous formations motivating the development of alternative anomalous transport frameworks [*Benson et al*., 2000; *Berkowitz et al*., 2006; *Berkowitz and Scher*, 1998; *Carrera et al*., 1998; *Haggerty and Gorelick*, 1995]. Conceptually consistent with retardation and broad residence times, anomalous transport models have also been shown to model adequately field-scale breakthrough curves obtained from conservative tracer tests [e.g., *Benson et al*., 2001; *Berkowitz and Scher*, 1998; *Haggerty et al*., 2004; *Le Borgne and Gouze*, 2008; *McKenna et al*., 2001]. Once successfully calibrated on field data, they may offer a preferential way to assess the effect of slow transport processes on bulk reactivity. This has been demonstrated extensively for linear reaction processes using the commutativity of the transport and reaction operators [*Haggerty and Gorelick*, 1995; *Margolin et al*., 2003]. For nonlinear reactions, commutativity no longer holds and there is no guarantee that anomalous transport can be relevantly coupled to chemical reactions. Bulk reactivity is no longer determined by the sole time distribution at the basis of anomalous transport but also by the concentration distribution.

Despite this barrier, we investigate the capacity of anomalous transport to model nonlinear reactivity for the two following motivations. First, extending transport that appears anomalous due to diffusion to cases controlled by realistic chemical reactions is a major issue [*Bolster et al*., 2010; *de Anna et al*., 2011; *de Dreuzy and Carrera*, 2015]. Therefore we focus on effective pore scale modeling that honors genuine diffusion and nonlinear kinetically controlled reactions, unlike prior investigations [e.g., *Willmann et al*., 2010] which consider advection-controlled dispersion and equilibrium reactions. Second, one of the anomalous transport frameworks, the Multi-Rate Mass Transfer models (MRMT), has recently been shown numerically to conserve the concentration variance in the slow-diffusing zones (also called immobile or diffusive zones) for the specific 1D, 2D and 3D inclusion cases [*de Dreuzy et al*., 2013]. MRMT construction ensures only the conservation of the concentrations in the mobile zone and does not involve any constraint on the diffusive concentration distribution [*Carrera et al*., 1998; *Haggerty and Gorelick*, 1995; *Willmann et al*., 2008]. For 1D inclusions where analytical demonstration has been achieved, the conservation of immobile concentration variance is a byproduct of the mobile concentration conservation relation. Equivalent immobile MRMT concentrations are expressed as the product of the inclusion concentrations with orthogonal functions derived from the solution of the 1D diffusion equation [*de Dreuzy et al*., 2013]. This result is however limited to the concentration variance in layered inclusions. Nothing can be implied a priori for more complex structure or for chemical reactivity metrics other than concentration variance.

We thus evaluate the possibility to predict nonlinear kinetically controlled reactivity on the basis of conservative transport information in diffusion-dominated conditions, i.e., when access to the reactive sites is explicitly controlled by diffusion within poorly connected porosity structures ("diffusive zones"). Aside from the motivations mentioned above, the choice of MRMT is also instrumental as it gives a spatiotemporal distribution of concentrations in the immobile zones from conservative transport information. We simulate transport coupled to fluid-rock interactions in a broad range of diffusion-dominated porosity structures taken as ground-truth reference data, and compare it to MRMT equivalent models. While simple, our ground-truth model is an explicit porescale model that would require information about geological structures to be used in practical modeling. On the contrary, MRMT can be built solely from conservative transport information (e.g., breakthrough curves) and as such is commonly used as a practical model for passive tracers. Our purpose here is to continue to explore its use for reactive transport. We frame our results in a global methodology to approach chemical transport from conservative transport information. We eventually discuss its limitations and potential extensions to more general contexts.

2. Models and Methods

We present the reference reactive transport model with the transport processes, the diffusive porosity structures and the chemical reactions. We show how equivalent Multi-Rate Mass Transfer models (MRMT) are

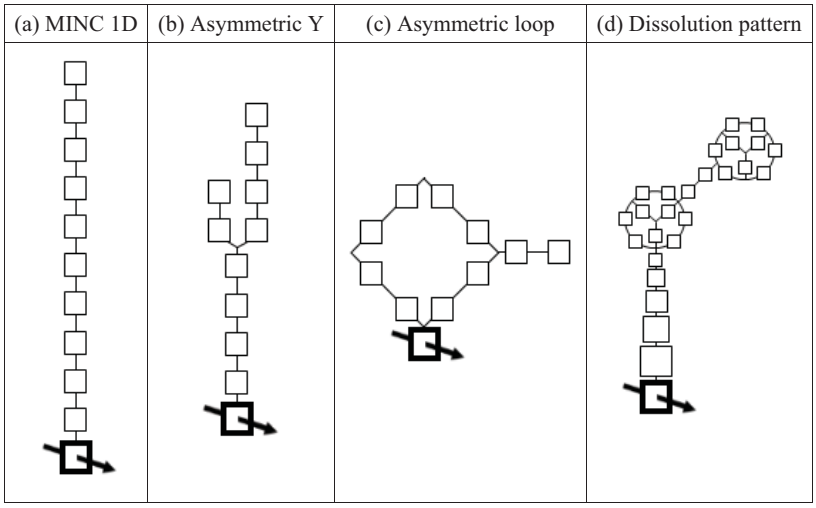

Figure 1. SINC structures used to evaluate the relevance of MRMT models for reactive transport. The mobile zone is represented by the thick black cell with the crossing arrow and the diffusive zones by the thin lined cells. From left to right, the diffusive porosity structures are (a) the classical 1-D Multiple INteracting Continua (MINC) model [*Pruess and Narasimhan*, 1985], (b) an asymmetric Y with a single junction, (c) an asymmetric loop, and (d) a structurally more involved pattern inspired by a dissolution feature in an oolitic limestone [*Babey et al*., 2015; *Luquot et al*., 2014a]. The area of the different cells is proportional to their porosity. The distance along the diffusive structure is to scale. The four structures have the same total porous volume, the same diffusive to mobile porosity ratio and the same quadratic mean distance of the diffusive zones to the mobile zone.

built from conservative transport information. We describe the synthetic experiments, criteria and numerical methods used to compare the reference and equivalent MRMT models.

2.1. Reference Reactive Transport Model

The reference reactive transport model is the Structured INteracting Continua (SINC) [*Babey et al*., 2015] taken as an extension of the Multiple INteracting Continua (MINC) introduced by *Pruess and Narasimhan* [1985]. In MINC, transport is mostly advective in one of the continua also called the mobile zone and diffusive across a finite number of continua connected in series to the mobile zone, here referred as the diffusive zones (Figure 1a). SINC is based on the same advectively controlled transport in the mobile zone interacting with a finite number of diffusive continua. These diffusive continua however differ by their connectivity (Figures 1b–1d). Organization may come from poorly connected fractures [*Andersson et al*., 2004; *Davy et al*., 2010] (Figure 1b), heterogeneous porosities [*Gouze et al*., 2008; *Robinet et al*., 2012] (Figure 1c), or dissolution patterns (Figure 1d) [*Luquot et al*., 2014b]. The four SINC structures of Figure 1 are the same used as references in *Babey et al*. [2015], except for their total diffusive porosity which is 10 times smaller. Because of their very distinct topologies, they are considered as characteristic of a large range of diffusive porosity structures. The finite number of diffusive zones would typically derive from a coarse description of the porosity or from a finite-difference discretization of diffusion within porous or fracture structures. The exchanges between the mobile and diffusive continua as well as the connectivity patterns are expected to determine the characteristic transport times, the mixing of water of different solute concentrations, the accessibility to the reactive sites and, eventually, the overall concentration distribution and dynamics.

In the SINC framework, aqueous species are transported by advection and dispersion along the mobile zone, and undergo diffusive-like exchanges (i.e., proportional to the difference of concentrations) between the mobile zone and some of the diffusion zones as well as between the diffusive zones. As in the MINC framework, the model is continuous along the mobile zone and discretized across the diffusive porosity. We assume that the transported aqueous species are reactive and interact by adsorption/desorption or precipitation/dissolution with the rock. Reactions are kinetically controlled. For the sake of simplicity, we assume that all stoichiometric coefficients are equal to one, and that the activities of all nonmineral species are equal to their concentrations. We do not consider feedbacks of reactivity on transport like induced porosity, diffusivity or velocity variations. Following classical multiporosity and reactive transport formalisms, the model then is formulated as [*de Dieuleveult and Erhel*, 2010; *Steefel and Maher*, 2009]:

$$\frac{\partial C}{\partial t} = \mathcal{L}(\boldsymbol{F}_m C) + \boldsymbol{A} C - R, \tag{1}$$

$$\frac{\partial S}{\partial t} = R. \tag{2}$$

$C(x,t) = [\, c_1(x,t) \quad \dots \quad c_{n+1}(x,t) \,]^T$ and $S(x,t) = [\, s_1(x,t) \quad \dots \quad s_{n+1}(x,t) \,]^T$ are the vectors of size $n+1$ made up of the aqueous and fixed (sorbed or precipitated) concentrations in the mobile zone for the first index ($c_1(x,t)$ and $s_1(x,t)$) and in the n diffusive zones for indices 2 to $n+1$. Both aqueous and fixed concentrations are taken as masses divided by the equivalent volume of fluid [ML^{-3}] (hereafter dimensions are given in dimension of mass [M], of length [L] and of time [T] [*Yoo and Mudd*, 2008]). x is the direction along the mobile zone with $0 \leq x \leq x_{\max}$. R is the reactive sink-source term further expressed in section 2.2. $\boldsymbol{F}_m$ is the restriction matrix to the mobile zone:

$$\boldsymbol{F}_m(i,j) = \delta(i-1)\delta(j-1) \tag{3}$$

where δ is the Kronecker delta

$$\delta(i) = \begin{cases} 0 & \text{if} \quad i \neq 0 \\ 1 & \text{if} \quad i = 0 \end{cases}. \tag{4}$$

$\mathcal{L}$ is the transport operator in the mobile zone

$$\mathcal{L}(c) = -\frac{q}{\phi_1}\frac{\partial c}{\partial x} + d_m \frac{\partial^2 c}{\partial x^2} \tag{5}$$

with q, ϕ_1 and d_m the Darcian flow [LT^{-1}], porosity and diffusive-dispersive coefficient [*Bear*, 1972; *Scheidegger*, 1954] [L^2T^{-1}] in the mobile zone.

The interaction matrix $\boldsymbol{A}$ of size $(n+1, n+1)$ expresses the diffusive exchanges between the diffusive zones and with the mobile zone [*Babey et al.*, 2015]. $\boldsymbol{A}$ would typically be derived from a coarse discretization of the diffusive porosity. Its nonzero off-diagonal coefficients correspond to exchange rates [T^{-1}] between connected zones. Because $\boldsymbol{A}$ integrates the porosity of the different zones, it is symmetrical only when all zones have the same porosity. It decomposes as

$$\boldsymbol{A} = -\boldsymbol{\Phi}^{-1}\boldsymbol{M} \tag{6}$$

with $\boldsymbol{M}$ the M-matrix expressing rates of exchanges of mass, and $\boldsymbol{\Phi}$ the diagonal matrix made up of the porosities of the different zones ϕ_i:

$$\boldsymbol{\Phi}(i,j) = \phi_i \delta(i-j). \tag{7}$$

2.2. Heterogeneous Reactions

We consider the two classical cases of nonlinear kinetically controlled Freundlich sorption and mineral dissolution. The Freundlich sorption isotherm has been widely used to describe the nonlinear, reversible adsorption of metals and organic compounds by soils [*Fetter*, 2008; *Weber et al.*, 1991]. Under kinetic control, it is generally expressed as:

$$R_i(c_i, s_i) = \frac{1}{\tau_r}((k c_i)^{\nu} - s_i) \tag{8}$$

where τ_r [T] is the characteristic reaction time, k is a sorption capacity constant and ν is an exponent related to sorption intensity. Observed values of ν are commonly smaller or equal to 1. We use $\nu = 1/2$ (desorption of order 1/2) corresponding to a common value for metals [*Adhikari and Singh*, 2003; *Paikaray et al.*, 2005]. In this specific case, k is of the dimension of a concentration [ML^{-3}].

For dissolution, we study the case of the kinetically controlled dissolution of a mineral AB into two aqueous species A and B of concentrations c_i^A and c_i^B. We assume that the initial and boundary conditions are such that at all times $c_i^A = c_i^B = c_i$ and $s_i^{AB} = s_i$. While restrictive, this assumption enhances the sensitivity of the reaction to the concentration distribution by maximizing the availability of the reactants and thus reactions

rates [*de Simoni et al.*, 2005]. The reaction is expressed as [*Appelo and Postma*, 2005; *Steefel and Maher*, 2009]:

$$R_i(c_i, s_i) = \begin{cases} 0 & \text{if} \quad s_i = 0 \quad \text{and} \quad \dfrac{c_i}{k} < 1, \\ \dfrac{k}{\tau_r}\left(\left(\dfrac{c_i}{k}\right)^2 - 1\right) & \text{otherwise.} \end{cases} \tag{9}$$

τ_r [T] is the characteristic reaction time and k [ML^{-3}] is the square root of the solubility product. This dissolution reaction is of order 2. We choose consistent definitions for the reaction constant and characteristic time k and τ_r for desorption (equation (8)) and dissolution (equation (9)) because of their consistent dimensions and similar influence on reactivity (section 2.4). Finally, we underline that the kinetic control of the reactions precludes the use of the conservative component framework [*de Simoni et al.*, 2007; *Gramling et al.*, 2002; *Rubin*, 1983].

2.3. Equivalent MRMT Models

In the Multi-Rate Mass Transfer (MRMT) framework [*Carrera et al.*, 1998; *Haggerty and Gorelick*, 1995], all the diffusive zones exchange exclusively with the mobile zone. Each diffusive zone is characterized by its porosity ϕ_i and its rate of exchange α_i [T^{-1}]. MRMT models can be expressed within the framework of SINC by imposing connections exclusively between the mobile and diffusive zones such that the exchange matrix of equation (6) writes:

$$\begin{cases} \boldsymbol{M}(i,j) = 0 \quad \text{for } i > 1\,,\ j > 1 \quad \text{and } i \neq j \\ \boldsymbol{M}(i,1) = \boldsymbol{M}(1,i) = -\phi_i \alpha_{i-1} \quad \text{for } i > 1 \\ \boldsymbol{M}(i,i) = -\sum_{j j \neq i} \boldsymbol{M}(i,j) \end{cases}. \tag{10}$$

Following up the work of *Haggerty and Gorelick* [1995], the equivalence between SINC and MRMT models is defined via identification of the mobile concentrations for a passive tracer. *Babey et al.* [2015] have shown that any SINC model (i.e., whatever the connectivity pattern of the diffusive zones) is algebraically equivalent to a unique MRMT model with the same number of diffusive zones. This equivalent MRMT can be identified algebraically using a linear transformation of the SINC exchange matrix (equation (6)). We use this identification method to derive equivalent MRMT for each of the four SINC structures of Figure 1. Chemical reactions are then applied on the MRMT concentrations of the mobile and diffusive zones.

2.4. Synthetic Experiments

We simulate desorption and dissolution (equations (8) and (9)) in the four diffusive structures displayed on Figure 1. To ensure temporal responses of the same order of magnitude, the total porosity of the diffusive zones as well as the characteristic diffusion time τ_d are taken equal. τ_d is defined as the mean diffusive time from the diffusive zones to the mobile zone. Initially, sorbed or precipitated species are uniformly distributed in the domain with a concentration s^0 at chemical equilibrium with the fluid:

$$s_1(x, t=0) = \ldots = s_{n+1}(x, t=0) = s^0 \tag{11}$$

$$R_1(x, t=0) = \ldots = R_{n+1}(x, t=0) = 0. \tag{12}$$

"Pure water" (i.e., with a solute concentration equal to zero) is then continuously injected at the inlet of the mobile zone

$$c_1(x=0, t>0) = 0. \tag{13}$$

Fixed elements are progressively desorbed or dissolved, and then transported throughout the domain until they reach the downstream adsorbing boundary condition:

$$c_1(x=x_{\max}, t) = 0. \tag{14}$$

Continuous chemical interaction with the rock is maintained during transport.

Focusing on the coupling of the physical and chemical processes, we fix the hydraulic parameters and investigate the relative influence of the chemical processes. The dispersion coefficient in the mobile zone is

Table 1. Transport, Reaction and Numerical Parameters Used for the Simulations of Section 3 With the Characteristic Diffusion Time τ_d and the Consecutive Distance Covered by Advection in the Mobile Zone $q\tau_d/\phi_1$ Taken as Temporal and Spatial Reference Scales[a]

Parameter	Value
$\sum_{i=2}^{n+1}\phi_i/\phi_1$	10
$d_m/\left(\tau_d(q/\phi_1)^2\right)$	10^{-8}
$Da=\tau_d/\tau_r$	0.1; 1; 10
s^0/k	0.1; 1; 10
$x_{max}/(q\tau_d/\phi_1)$	1.5×10^{-3}
$dx/(q\tau_d/\phi_1)$	3×10^{-5}
dt/τ_d	4×10^{-4}

[a] $\sum_{i=2}^{n+1}\phi_i/\phi_1$ is the diffusive to mobile porosity ratio. $d_m/\left(\tau_d(q/\phi_1)^2\right)$ is the dimensionless dispersion in the mobile zone. $Da=\tau_d/\tau_r$ is the Damköhler number for the kinetically controlled Freundlich desorption and mineral dissolution. s^0/k is the dimensionless ratio of the initial concentration of sorbed species to the sorption capacity constant for desorption, and of the initial concentration of precipitated species to the square root of the solubility product for dissolution. x_{max} is the extension of the simulation domain in the direction of the mobile zone, dx is the spatial step along the mobile zone and dt is the time step.

classically taken much smaller than the characteristic multi-domain diffusion induced by the mobile-immobile exchanges ($\tau_d(q/\phi_m)^2$) and the ratio of the total diffusive to mobile porosity is taken much larger than one $\left(\sum_{i=2}^{n+1}\phi_i/\phi_1=10\right)$ [*Carrera et al.*, 1998; *Willmann et al.*, 2008]. For both the chosen desorption and dissolution processes (equations (8) and (9)), the key parameters are the ratio of the characteristic diffusion to reaction times τ_d/τ_r and the normalized initial concentration s^0/k. The ratio of characteristic times is generally called Damköhler number $Da=\tau_d/\tau_r$ [*Steefel and Maher*, 2009]. Results are also a function of the initial condition s^0/k because the chemical reactions are nonlinear. We investigate the effect of both these parameters over two orders of magnitude around 1 [0.1;10]. Model parameters and their values are synthesized in Table 1.

2.5. Comparison Criteria

We assess the ability of MRMT models to capture the mobilization rates through the five first moments of the aqueous concentration distribution taken over the whole domain (mobile and diffusive porosities)

$$m^j(C,t)=\int_{x=0}^{x_{max}}\sum_{i=1}^{n+1}\phi_i[c_i(x,t)]^j dx \tag{15}$$

with j the order of the moment $j=1,\ldots,5$. Complementary comparison is provided by the mobilization time t_m [T] defined as the time at which 95% of the total initial mass of fixed species have been mobilized, such that with $\eta=0.05$:

$$m(S,t=t_m)/m(S,t=0)=\eta \tag{16}$$

with

$$m(S,t)=\int_{x=0}^{x_{max}}\sum_{i=1}^{n+1}\phi_i s_i(x,t)dx. \tag{17}$$

2.6. Numerical Methods

Finite-difference discretization of the advection-dispersion processes in the mobile zone, exchanges within the diffusive zones, and chemical reactions are sequentially coupled [*de Dreuzy et al.*, 2013; *Steefel and MacQuarrie*, 1996]. Reaction rates are integrated with the fourth-order Runge-Kutta ode45 method of MATLAB [*Shampine and Reichelt*, 1997]. SINC implementation is validated against a set of diffusive structures strictly equivalent to Multiple Interacting Continua (MINC) taken as a discretization of 1D diffusion in an homogeneous layered inclusion (Figure 1a) [*Babey et al.*, 2015]. Coupling between transport and reactivity is validated against PHREEQC on a single dual porosity structure ($n=1$) by using the STAGNANT functionality [*Parkhurst and Appelo*, 1999].

3. Results

Mobilization times and concentration moments in SINC and MRMT are compared as functions of diffusive zone structure, reaction type and reaction parameters. We assess the possibility to use parsimonious MRMT models (with only 1–5 rates) to estimate reaction rates.

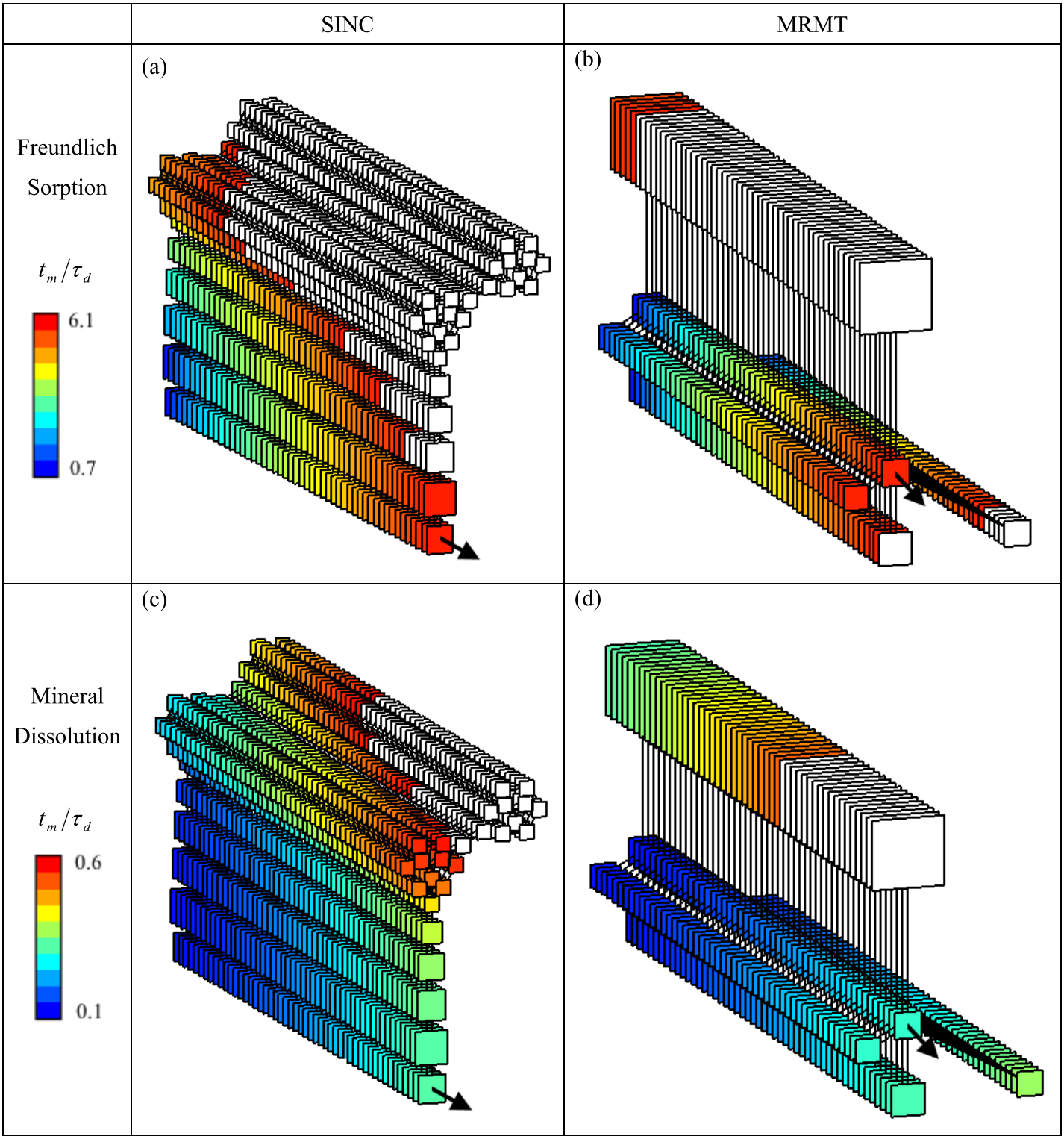

Figure 2. Mobilization times t_m/τ_d (section 2.5) for the Freundlich sorption (equation (9)) and the mineral dissolution (equation (10)) with $Da=\tau_d/\tau_r=10$ and $s^0/k=1$, for the SINC dissolution pattern (Figure 1d) and its equivalent MRMT model represented by its four zones with the largest porosities (out of 25), depicted as cross sections transverse to the mobile zone identified by the arrow. For the MRMT of the right column, the distances between the mobile and immobile zones are proportional to log $(1/\alpha_i)$, and the porosities of the mobile and diffusive zones are proportional to the area of the cells.

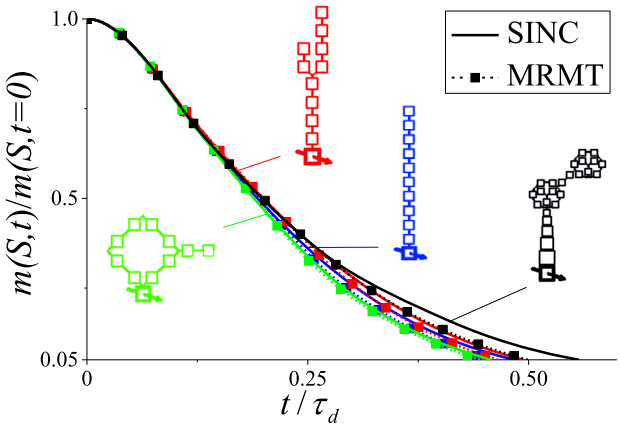

Figure 3. Remaining mass of mineral in the domain $m(S,t)$ for the four SINC structures of Figure 1 and their equivalent MRMT models. The dimensionless reaction parameters are $Da=\tau_d/\tau_r=10$ and $s^0/k=1$.

3.1. Mobilization Times

The reaction front can be traced by the spatial repartition of the mobilization time t_m. Figure 2 represents t_m across the diffusive porosity and along the mobile zone for the SINC structure of Figure 1d and its equivalent MRMT model, for both the dissolution and the desorption cases. SINC and MRMT models both have 25 diffusive zones. In Figure 2, only the four MRMT diffusive zones with the largest porosities ϕ_i are represented as they account for more than 95% of the total diffusive porosity. The desorption and dissolution fronts progress quickly downstream the mobile zone but more slowly across the diffusive porosity. MRMT zones with large exchange rates (small cells on Figure 2b) reproduce well the mobilization rates in the SINC zones close to the mobile porosity (Figure 2a). Both SINC and MRMT models display visually the same diffuse increase of the mobilization time in the few closest zones to the mobile zone. Diffusive zones away from the mobile zone in SINC are flushed much later (Figures 2a and 2c) like the zone with the smallest exchange rate for MRMT (largest cell more distant from the central mobile zones of Figures 2b and 2d). Mobilization times t_m for dissolution are intermediary between τ_r and τ_d $(0.1 \leq t_m/\tau_d \leq 0.6)$ and about one order of magnitude smaller than mobilization times for desorption. For this parameterization, desorption is slower than dissolution because of its lower order (1/2) and its dependency on the sorbed species concentration.

The most apparent difference between SINC and MRMT on Figure 2 does not come from the mobilization time but from the nature of the discretization. All non-represented MRMT zones account for less than 5% of the overall diffusive porosity and are characteristic of extremely short exchange times. Nonetheless, diffusive zones next to the mobile porosity are well characterized and discretized by MRMT as they control fast

		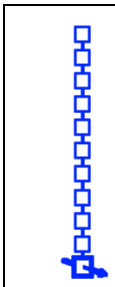	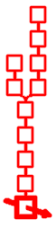	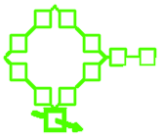	
1	1	-2 x 10^{-3}	-2 x 10^{-3}	-9 x 10^{-4}	-4 x 10^{-3}
0.1	1	-6 x 10^{-4}	-6 x 10^{-4}	-3 x 10^{-4}	-1 x 10^{-3}
10	1	-3 x 10^{-3}	-2 x 10^{-3}	-1 x 10^{-3}	-6 x 10^{-3}
1	0.1	-3 x 10^{-3}	-2 x 10^{-3}	-2 x 10^{-3}	-6 x 10^{-3}
1	10	-8 x 10^{-4}	-7 x 10^{-4}	-3 x 10^{-4}	-2 x 10^{-3}
Da	s^0/k	$\left(t_m^{MRMT}-t_m^{SINC}\right)/t_m^{SINC}$			

Figure 4. Relative differences on the mobilization time $\left(t_m^{MRMT}-t_m^{SINC}\right)/t_m^{SINC}$ between the four SINC models presented on Figure 1 and their equivalent MRMT models for the kinetically controlled Freundlich desorption (section 2.2). The dimensionless reaction parameters are the Damköhler number Da and the normalized initial concentration of fixed species s^0/k.

		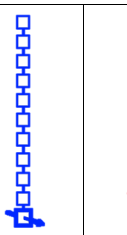	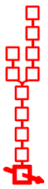	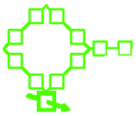	
1	1	-2 x 10^{-3}	-2 x 10^{-3}	-6 x 10^{-4}	-5 x 10^{-3}
0.1	1	< 10^{-5}	< 10^{-5}	< 10^{-5}	4 x 10^{-5}
10	1	-6 x 10^{-2}	-6 x 10^{-2}	-3 x 10^{-2}	-1 x 10^{-1}
1	0.1	-3 x 10^{-2}	-3 x 10^{-2}	-1 x 10^{-2}	-6 x 10^{-2}
1	10	2 x 10^{-4}	3 x 10^{-4}	4 x 10^{-5}	7 x 10^{-4}
Da	s^0/k	$\left(t_m^{MRMT}-t_m^{SINC}\right)/t_m^{SINC}$			

Figure 5. Relative differences on the mobilization time $\left(t_m^{MRMT}-t_m^{SINC}\right)/t_m^{SINC}$ between the four SINC models presented on Figure 1 and their equivalent MRMT models for the kinetically controlled mineral dissolution (section 2.2). The dimensionless reaction parameters are the Damköhler number Da and the normalized initial concentration of fixed species s^0/k.

exchanges between the mobile and the diffusive zones. On the opposite, at late times, discretization of MRMT is extremely coarse. The late-time contribution to mobile-diffusive exchanges by the SINC porosity structure is represented by a single large lumped porosity zone in MRMT. This follows from the essence of diffusion. Late-time responses are smoothed out by diffusion and are dominated by more remote parts of the diffusive porosity. They do not need to be finely discretized and their contribution to mobile-diffusive exchanges can be represented by a single large lumped porosity zone. In synthetic terms, MRMT models discretize the exchanges with the diffusive porosity at early times and homogenize them at late times. Hence, the mobilization time in the large MRMT zone with the smallest exchange rate corresponds to an average value for the more remote zones of the SINC structure.

The accurate description of the early-time exchanges is confirmed by the close integrated desorbed and dissolved masses between SINC and MRMT models (Figure 3, lines for SINC and symbols for MRMT). MRMT models give observable differences only in the dissolution case and for the more complex diffusive structure of Figure 1d when more than 50% of the originally precipitated species have been dissolved. Still these differences remain small as shown by the relative difference in mobilization times between the SINC and MRMT models. Relative errors on the mobilization time t_m are commonly less than 1% with maximum values obtained for $Da=10$ and $s^0/k=1$, i.e., when the reaction becomes transport-limited. In this case errors increase from the better-connected asymmetric loop structure (0.1% for desorption (Figure 4), 3% for dissolution (Figure 5)) to the asymmetric Y and the MINC structures (0.3% and 6% each) and eventually to the less-connected dissolution pattern structure

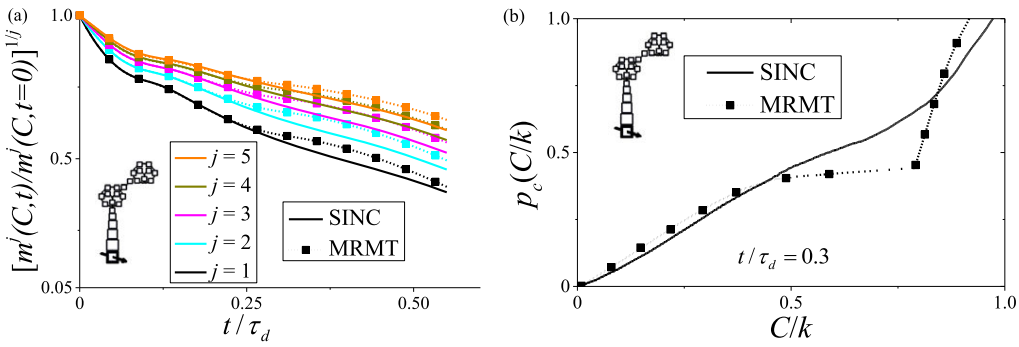

Figure 6. For the mineral dissolution with $Da=\tau_d/\tau_r=10$ and $s^0/k=1$: (a) Moments of the concentration distribution of the aqueous species $m^j(C,t)$ for the dissolution pattern SINC model (Figure 1d) and its equivalent MRMT model; (b) Cumulated concentration distribution of the aqueous species $p_c(C/k)$ at $t/\tau_d=0.3$ for the dissolution pattern SINC model (Figure 1d) and its equivalent MRMT model.

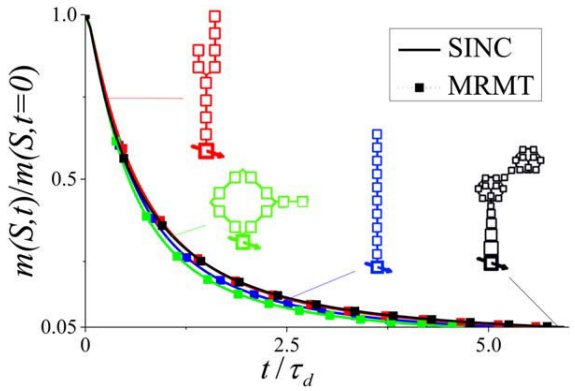

Figure 7. Remaining mass of sorbed species in the domain $m(S,t)$ for the four SINC structures of Figure 1 and their equivalent MRMT models. The dimensionless reaction parameters are $Da=\tau_d/\tau_r=10$ and $s^0/k=1$.

(0.6% and 10%). To summarize, errors by MRMT remain lower than 10% in all cases and decrease when mobilization times increase (i.e., slower reactions (smaller *Da*), larger initial amounts of fixed species (larger s^0/k), desorption instead of dissolution) as homogenization of concentrations by diffusion is more important and reduces the influence of porosity structures on bulk reactivity.

3.2. Concentration Distributions

The largest deviations occur in the SINC case of Figure 1d. Although limited, these differences are worth investigating as they illustrate the effect of the MRMT discretization pattern displayed by Figure 2. Lower values of precipitated mass observed at intermediary times ($0.2 \leq t/\tau_d \leq 0.6$) on Figure 3 directly translate to higher values of the aqueous concentration moments (Figure 6a). A closer inspection of the distribution of solute concentrations taken over the entire domain at $t/\tau_d=0.3$ (Figure 6b) shows important deviations at large concentration values ($C/k > 0.5$) characteristic of the remote diffusive zones where mineral is more slowly flushed. The largest lumped zone of the MRMT cannot fully capture the complex concentration patterns of the SINC structure. While the lumped representation of the complex SINC structure far from the mobile zone leads to accurate predictions for conservative transport, it gives some differences for reactive transport at intermediary times. At late times ($t/\tau_d \geq 0.6$), the strong homogenization effect of diffusion eventually dominates and reduces the differences. While qualitatively also present in the desorption case, deviations between SINC and MRMT are much more limited than in the dissolution case (Figures 7 and 8). Desorption is better matched than dissolution because it occurs more progressively and does not present the reaction rate discontinuity when the mineral vanishes.

The relevance of MRMT for reactive transport is consistent with its good characterization of the concentration distribution for conservative transport. By construction MRMT models reproduce the moments of the concentration distribution of order zero and one for a nonreactive tracer (conservation of the total porous volume and of the total mass of conservative solute respectively). MRMT models also reproduce the second moment of the concentration distribution for MINC diffusive structures as the one shown on Figure 1a [*de Dreuzy et al.*, 2013]. We check that it is also the case for the four studied SINC structures as shown for the dissolution pattern on Figure 9. Moments of order three and above are not equal, but remain very close.

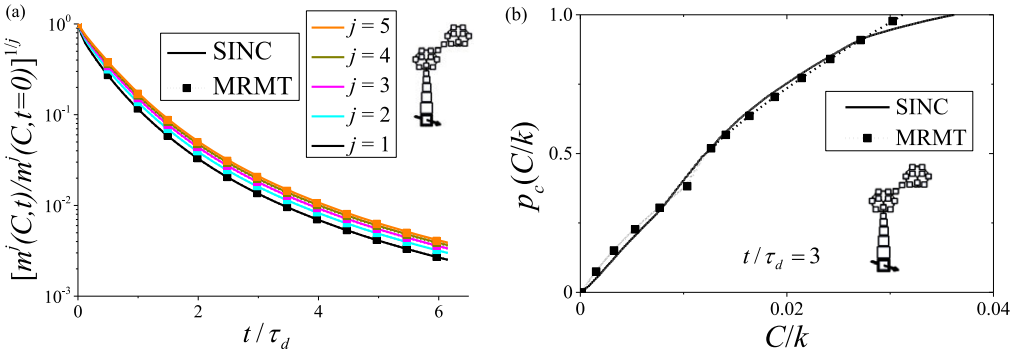

Figure 8. For the Freundlich desorption with $Da=\tau_d/\tau_r=10$ and $s^0/k=1$: (a) Moments of the concentration distribution of the aqueous species $m^j(C,t)$ for the dissolution pattern SINC model (Figure 1d) and its equivalent MRMT model; (b) Cumulated concentration distribution of the aqueous species $p_c(C/k)$ at $t/\tau_d=3$ the for the dissolution pattern SINC model (Figure 1d) and its equivalent MRMT model.

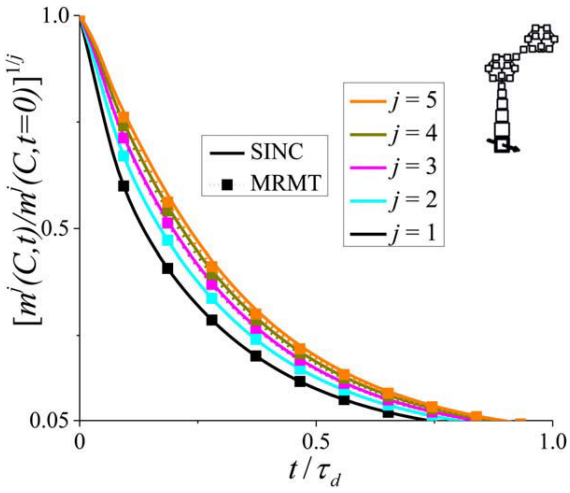

Figure 9. Moments of the concentration distribution $m^j(C,t)$ of a non-reactive tracer for the dissolution pattern SINC model (Figure 1d) and its equivalent MRMT model. The tracer is initially uniformly distributed in the domain and is flushed out by a continuous injection of a solution with a concentration equal to zero at the mobile inlet. The transport and numerical parameters used in the simulation are listed in Table 1.

Except in the extreme cases of complex diffusive porosity structures far away from the mobile zone, where errors can be as high as 10% on the mobilization time for dissolution, errors remain smaller than a few percent. As previously noted for conservative transport [*Haggerty and Gorelick*, 1995; *Villermaux*, 1987], the relevance of MRMT models comes from their ability to accurately represent rapid exchanges with numerous exchange rates and from the homogenization nature of diffusion. The strong diffusive-induced homogenization is also reflected in the restricted dispersion of the precipitated and sorbed masses between the four SINC structures (Figures 3 and 7). All structures display close reaction rates. It is first and foremost the diffusive volume and the mean diffusion time to the mobile zone τ_d that determine the reactivity within the diffusive zones. The large geometrical and topological differences between the structures of Figures 1a–1c do not induce significant differences in reactivity. Only very marked structures like the weak connections within the dissolution pattern (Figure 1d) have some limited impact on reactivity (Figure 3) as they restrain the access to some of the immobile zones and delay the dissolution within them.

3.3. Simplified MRMT Models

For conservative transport, SINC models are algebraically equivalent to MRMT models having the same number of zones [*Babey et al.*, 2015]. It is precisely these equivalent MRMT models that have been used so far in this study. They have as many zones as the original SINC models. Approximate MRMT models with fewer zones can alternatively be built based on numerical flushing experiments of the diffusive zones [*Babey et al.*, 2015]. The MRMT with a single zone or single rate ($n=1$) is the classical double porosity model with one mobile zone and one immobile zone [*Warren et al.*, 1963]. With 2 exchange rates ($n=2$), it is the triple porosity model [e.g., *Wu et al.*, 2004] .

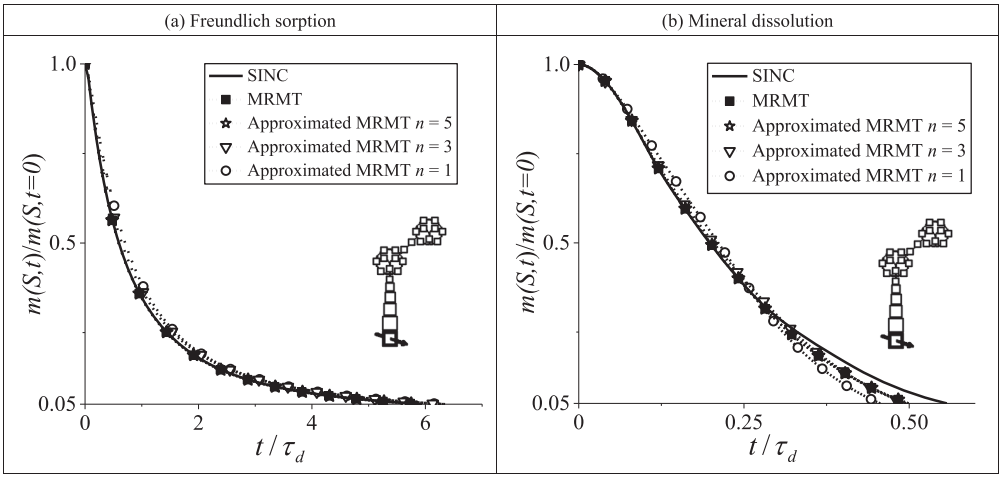

Figure 10. Remaining mass of (a) adsorbed species and (b) mineral in the domain $m(S,t)$ for the dissolution pattern SINC model (Figure 1d) and its equivalent MRMT model, either determined algebraically (section 2.3) or approximated with a limited number of n rates (section 3.3). The dimensionless reaction parameters are $Da=\tau_d/\tau_r=10$ and $s^0/k=1$.

We assess the performances of these approached MRMT models according to their number of diffusive porosities (n) on the reactive transport experiment considered above, first on the remaining sorbed and precipitated masses (Figure 10). The double porosity model remains in the range of the full MRMT and reference SINC. Simplified MRMT models with increasing number of diffusive zones then rapidly converge to the behavior of the full MRMT. Quantitatively, for dissolution, $Da=10$ and $s^0/k=1$, errors on t_m drop down from a maximum of 20% for $n=1$ (double porosity model) to 11% for $n=3$ and 10% for $n=5$. Increasing the number of rates to the full MRMT ($n=25$) does not improve the approximation of t_m. Results are comparable for desorption where approximate values of t_m converge to the reference SINC value with relative differences of 7% ($n=1$), 6% ($n=3$) and 0.2% ($n=5$). The fast convergence comes from the dominance of the five first rates of the full MRMT that account for more than 95% of the diffusive porosity. The remaining rates characterize rapid exchanges that can be important only at very early times. It is consistent with the already discussed picture of diffusion where rapid interactions concern only the immediate volume next to the concentration injection, while longer-term exchanges are homogenized and can be represented by simple models with few parameters [*Crank*, 2002]. As for conservative transport (as shown in *Haggerty and Gorelick* [1995]), to increase the number of MRMT rates only marginally improves the approximation of short-term reactivity.

4. Discussion

The previous section has shown that MRMT models give good estimates of mono-component fluid-rock interactions over multiple complex porosity topologies. This consistency is fundamentally linked to the homogenization nature of diffusion and to the ability of MRMT models to capture concentration patterns beyond mass conservation. As the variability induced by the diffusive porosity structure is limited, even parsimonious MRMT models with a limited number of rates (3–5) can provide accurate predictions of reaction rates. Reactivity is primarily controlled by the ratio of diffusive to mobile porosity and by the quadratic mean transfer time to the diffusive zones. From a more applied point of view within the context of our present study, we propose the following methodology to approach reaction rates from breakthrough curves of conservative tracers. We eventually discuss the limitations and potential extensions of such approaches.

4.1. From Conservative Tracer Tests to Reactive Transport Estimates

We propose a three-step methodology to derive reactive MRMT simulations from conservative tracer test data. We choose MRMT among other anomalous transport frameworks like CTRW [*Berkowitz et al*., 2006; *Berkowitz and Scher*, 1998], fADE [*Benson et al*., 2000], or exposure-time mass transfer [*Ginn*, 2009], because it provides readily usable concentrations for reactions. Step one consists in verifying whether dispersion is diffusion-induced, for which our previous analysis pertains. Step two corresponds to the calibration of MRMT parameters upon the breakthrough curve (BTC) of a conservative tracer. In step three, reactions are simulated in the MRMT model.

4.1.1. Verification of Diffusion-Induced Dispersion Conditions

In this paper, we have considered diffusion-induced dispersion typical of fracture/matrix systems [*Neretnieks*, 1980; *Roubinet et al*., 2013, 2010; *Sudicky and Frind*, 1982; *Tang et al*., 1981; *Zhou et al*., 2007] or mobile/immobile media [*Golfier et al*., 2007; *Haggerty et al*., 2004; *Zinn et al*., 2004]. Transport variability also comes from local hydrodynamic effects [*Bear*, 1972] that contribute to the macro-dispersion typically observed in tracer experiments. As local dispersion has a similar expression as diffusion [*Sánchez-Vila and Carrera*, 2004], MRMT models could remain consistent as an intermediary between tracer experiments and reactivity estimates [*Willmann et al*., 2010]. This should be analyzed and checked. If local dispersive effects require some specific treatment, their signature should be distinguished from diffusion. This could be done by varying the hydrodynamic parameters [*Guiheneuf et al*., 2014] or the tracer diffusivity [*Becker and Shapiro*, 2000, 2003].

4.1.2. MRMT Model Calibration From BTC

MRMT parameters are calibrated from breakthrough curve information of a conservative tracer using any conventional procedure [e.g., *Haggerty et al*., 2001]. *Willmann et al*. [2008] have also proposed a generic methodology where mobile and diffusive porosity parameters are identified successively. First mobile porosity ϕ_1 and diffusion-dispersion coefficient d_m (equation (5)) are obtained by fitting an advection-dispersion equation upon the first arrival and the peak of the BTC. Second, MRMT rates α and porosities ϕ (equation (10)) are calibrated by fitting the heavy tail of the BTC. The main difficulty lies in the potentially

large and irregular distributions of α and ϕ required to fit the BTC. It may be overcome by assuming an a priori density function $\phi(\alpha)$. For example, *Haggerty et al.* [2000] have related the commonly observed power-law tailing of the breakthrough concentration c according to time t ($c \sim t^{-\kappa}$) to the power-law density function $\phi \sim \alpha^{\kappa-3}$. However, complex diffusive porosity architectures are typically related to nonmonotonous density functions and nonparametric identification methods may have to be used [*Babey et al.*, 2015].

4.1.3. Using MRMT Concentrations for Reactions

Chemical reactions are applied on the MRMT concentrations of the mobile and diffusive zones. This can be achieved by using either the method presented in this article or alternatives like PHREEQC [*Parkhurst and Appelo*, 1999] that might give way to include more advanced reactive processes, as discussed in the next section. The model could be validated by comparing simulated and experimental breakthrough curves of a reactive species. It would typically be used to predict the apparent reduction of the reaction rates due to delayed access to the reactive surfaces, using for example spatially integrated reaction rates between an injection point and an observation point as an indicator of reaction advancement.

4.2. Extensions and Limitations of MRMT Approaches

While we study the overall capability of the MRMT modeling approach to handle kinetically controlled nonlinear reactions, it is important to keep in mind the limitations of this upscaling approach in field application. The parameters of the MRMT model are effective rate coefficients and capacities used to mimic collectively delayed transport associated with range of possible causes including anomalous dispersion, truly multi-rate diffusion, multiple sorption site types of different equilibria, and intermediate scale nonuniformities in advective transport. Determining the physical sense of MRMT parameters is a critical point to assess the predictive capabilities of MRMT models overall. However, in this paper we focus on whether MRMT can be used to predict reactivity in the first place under the conditions of the calibration. Investigation of the relations between MRMT fitted parameters and structural porosity features could be achieved through extensive numerical simulation of diverse SINC structures and by studying the algebraic transformation of SINC to MRMT.

Previous works have also shown the relevance of MRMT approaches to predict homogeneous and mixing-induced reactivity [*de Dreuzy et al.*, 2013; *Donado et al.*, 2009; *Willmann et al.*, 2010]. In addition to our results for heterogeneous reactions, this supports an extended validity of MRMT to a broader range of reactions. Fundamentally the very good characterization of the concentration distribution for a conservative solute extends to reactive solutes. Limitations would come from highly nonlinear reactions with strong positive feedbacks like auto-catalysis [*de Anna et al.*, 2010; *Gray and Scott*, 1983] or high initial concentration gradients in the diffusive porosity that cannot be recovered by MRMT [*de Dreuzy et al.*, 2013]. MRMT and beyond conservative tracers capture the physical constraint of reactivity as long as concentration patterns within the diffusive zones remain weakly correlated to the reaction process.

5. Conclusions

In this study we assess the possibility to use conservative transport information, like breakthrough curves from conservative tracer tests, to predict nonlinear fluid-rock interactions when reactivity is limited by slow diffusion to the reactive sites. For reference ground-truth data, we use the Structured INteracting Continua (SINC) framework where solute dispersion is primarily driven by exchanges between a fast, advective 1D mobile zone and an extensive diffusive porosity architecture coming from poorly connected fractures, low-permeability inclusions/matrix or dissolution patterns. The internal organization of the diffusive porosity and its connectivity to the mobile zone control the accessibility to the reactive sites. We select four reference SINC structures representative of different geological contexts and porous structure geometries. Reactions are taken as nonlinear kinetically controlled Freundlich sorption and mineral dissolution. The Multi-Rate Mass Transfer (MRMT) model is used as an intermediary between conservative transport information and reactive transport estimates. Reference and estimated reaction rates in SINC and their equivalent MRMT are compared for a flushing experiment.

Despite the noncommutativity of the reaction and transport operators for the nonlinear desorption and dissolution considered, MRMT models are shown to provide surprisingly close estimations of the bulk solubilization rates for both desorption and dissolution whatever the tested diffusive porosity structure. Errors are commonly less than 1% with maxima of 0.6% for sorption and 10% for dissolution obtained for fast

reactions, i.e., when the reaction becomes transport-limited. The first five moments of the aqueous reactant concentration distribution and the distributions themselves are similarly well approached. This is consistent with the very good characterization of the concentration distribution for conservative transport. Moments of order one and two for a passive tracer are equal in SINC and MRMT, and moments of higher order remain very close. The relevance of MRMT comes from its ability to accurately represent rapid exchanges between the mobile and diffusive porosities with numerous exchange rates, as well as from the homogenizing nature of diffusion itself. On one hand, diffusive zones next to the mobile porosity are well characterized and discretized by MRMT as they control short-term mobile-diffusive interactions. On the other hand, the coarse discretization of large-time exchanges reflects the homogenization operated by diffusion in the remote parts of the diffusive porosity. Deviations mainly occur in the case of complex diffusive porosity structures far away from the mobile zone where MRMT cannot capture persistent concentration gradients. While different, mobilization rates in the cases examined remain nonetheless close with differences smaller than a few percent or less.

Anomalous transport models derived solely from conservative transport information may thus be used to estimate nonlinear fluid-rock interactions when transport processes are dominated by slow diffusion to the reactive sites. Because conservative concentration distributions are well estimated, more advanced homogeneous and heterogeneous reactivities are likely to be also well captured. Additionally, we show that those models may not require an extensive parameterization, as parsimonious MRMT models with only a few diffusive zones remain highly effective. Dual-porosity models (MRMT with one diffusive zone) already give the proper order of magnitude of the mobilization times (maximum of 20% of error) and maximum precision is reached using a reduced five rates MRMT. For these reasons, we frame our results with a general methodology to estimate reaction rates from conservative transport information through anomalous transport models, using MRMT as an example. While highly effective for reaction under diffusion-controlled transport, the necessary extension to hydrodynamic-issued dispersion remains challenging.

Acknowledgments
The ANR is acknowledged for its funding through its project H2MNO4 under the number ANR-12-MONU-0012-01. This work was supported in part by NSF/EAR Project 1417495, "A practical upscaling of subsurface reactive transport." While the manuscript does not make use of experimental data, the Matlab numerical codes that have been used for the reactive transport simulations and MRMT identification are available by contacting the authors (tristan.babey@univ-rennes1.fr).

References

Adhikari, T., and M. V. Singh (2003), Sorption characteristics of lead and cadmium in some soils of India, *Geoderma*, *114*(1–2), 81–92, doi:10.1016/S0016-7061(02)00352-X.

Andersson, P., J. Byegard, E.-L. Tullborg, T. Doe, J. Hermanson, and A. Winberg (2004), In situ tracer tests to determine retention properties of a block scale fracture network in granitic rock at the Aspo Hard Rock Laboratory, Sweden, *J. Contam. Hydrol.*, *70*(3-4), 271–297.

Appelo, C. A. J., and D. Postma (2005), *Geochemistry, Groundwater and Pollution*, 2nd ed., CRC Press, Leiden, Netherlands.

Attinger, S., J. Dimitrova, and W. Kinzelbach (2009), Homogenization of the transport behavior of nonlinearly adsorbing pollutants in physically and chemically heterogeneous aquifers, *Adv. Water Resour.*, *32*(5), 767–777, doi:10.1016/j.advwatres.2009.01.011.

Babey, T., J. R. de Dreuzy, and C. Casenave (2015), Multi-Rate Mass Transfer (MRMT) models for general diffusive porosity structures, *Adv. Water Resour.*, *76*, 146–156, doi:10.1016/j.advwatres.2014.12.006.

Bahr, J. M., and J. Rubin (1987), Direct comparison of kinetic and local equilibrium formulations for solute transport affected by surface-reactions, *Water Resour. Res.*, *23*(3), 438–452, doi:10.1029/WR023i003p00438.

Bear, J. (1972), *Dynamics of Fluids in Porous Media*, Dover, N. Y.

Becker, M. W., and A. M. Shapiro (2000), Tracer transport in fractured crystalline rock: Evidence of nondiffusive breakthrough tailing, *Water Resour. Res.*, *36*(7), 1677–1686.

Becker, M. W., and A. M. Shapiro (2003), Interpreting tracer breakthrough tailing from different forced-gradient tracer experiment configurations in fractured bedrock, *Water Resour. Res.*, *39*(1), 1024, doi:10.1029/2001WR001190.

Benson, D. A., S. W. Wheatcraft, and M. M. Meerschaert (2000), Application of a fractional advection-dispersion equation, *Water Resour. Res.*, *36*(6), 1403–1412, doi:10.1029/2000WR900031.

Benson, D. A., R. Schumer, M. M. Meerschaert, and S. W. Wheatcraft (2001), Fractional dispersion, Lévy motion, and the MADE tracer test, *Transp. Porous Media*, *42*(1-2), 211–240, doi:10.1007/978-94-017-1278-1_11.

Berkowitz, B., and H. Scher (1998), Theory of anomalous chemical transport in random fracture networks, *Phys. Rev. E*, *57*(5), 5858–5869, doi:10.1103/PhysRevE.57.5858.

Berkowitz, B., A. Cortis, M. Dentz, and H. Scher (2006), Modeling non-Fickian transport in geological formations as a continuous time random walk, *Rev. Geophys.*, *44*, RG2003, doi:10.1029/2005RG000178.

Bohlke, J. K. (2002), Groundwater recharge and agricultural contamination, *Hydrogeol. J.*, *10*(1), 153–179, doi:10.1007/s10040-001-0183-3.

Bolster, D., D. A. Benson, T. Le Borgne, and M. Dentz (2010), Anomalous mixing and reaction induced by superdiffusive nonlocal transport, *Phys. Rev. E*, *82*(2), 021119.

Brusseau, M. L. (1992), Transport of rate-limited sorbing solutes in heterogeneous porous media: Application of a one-dimensional multifactor nonideality model to field data, *Water Resour. Res.*, *28*(9), 2485–2497.

Brusseau, M. L., and R. Srivastava (1997), Nonideal transport of reactive solutes in heterogeneous porous media 2. Quantitative analysis of the Borden natural-gradient field experiment, *J. Contam. Hydrol.*, *28*(1-2), 115–155.

Carrera, J., X. Sánchez-Vila, I. Benet, A. Medina, G. Galarza, and J. Guimerà (1998), On matrix diffusion: Formulations, solution methods and qualitative effects, *Hydrogeol. J.*, *6*(1), 178–190, doi:10.1007/s100400050143.

Charbeneau, R. J. (2006), *Groundwater Hydraulics and Pollutant Transport*, Waveland Press, Long Grove, Ill.

Cirpka, O. A., and P. K. Kitanidis (2000), An advective-dispersive stream tube approach for the transfer of conservative-tracer data to reactive transport, *Water Resour. Res.*, *36*(5), 1209–1220, doi:10.1029/1999WR900355.

Clark, I. D., and P. Fritz (1997), *Environmental Isotopes in Hydrogeology*, CRC Press, N. Y.
Crank, J. (2002), *The Mathematics of Diffusion*, Oxford Univ. Press, Oxford.
Cvetkovic, V., J. O. Selroos, and H. Cheng (1999), Transport of reactive tracers in rock fractures, *J. Fluid Mech.*, *378*, 335–356.
Davy, P., R. Le Goc, C. Darcel, O. Bour, J. R. de Dreuzy, and R. Munier (2010), A likely universal model of fracture scaling and its consequence for crustal hydromechanics, *J. Geophys. Res.*, *115*, B10411, doi:10.1029/2009JB007043.
de Anna, P., F. Di Patti, D. Fanelli, A. J. McKane, and T. Dauxois (2010), Spatial model of autocatalytic reactions, *Phys. Rev. E*, *81*(5), 056110.
de Anna, P., T. Le Borgne, M. Dentz, D. Bolster, and P. Davy (2011), Anomalous kinetics in diffusion limited reactions linked to non-Gaussian concentration probability distribution function, *J. Chem. Phys.*, *135*(17), 174104, doi:10.1063/1.3655895.
de Dieuleveult, C., and J. Erhel (2010), A global approach to reactive transport: Application to the MoMas benchmark, *Comput. Geosci.*, *14*(3), 451–464, doi:10.1007/s10596-009-9163-9.
de Dreuzy, J. R., and J. Carrera (2015), On the validity of effective formulations for transport through heterogeneous porous media, *Hydrol. Earth Syst. Sci. Discuss.*, *12*(11), 12,281–12,310, doi:10.5194/hessd-12-12281-2015.
de Dreuzy, J. R., A. Rapaport, T. Babey, and J. Harmand (2013), Influence of porosity structures on mixing-induced reactivity at chemical equilibrium in mobile/immobile Multi-Rate Mass Transfer (MRMT) and Multiple INteracting Continua (MINC) models, *Water Resour. Res.*, *49*, 8511–8530, doi:10.1002/2013WR013808.
de Simoni, M., J. Carrera, X. Sanchez-Vila, and A. Guadagnini (2005), A procedure for the solution of multicomponent reactive transport problems, *Water Resour. Res.*, *41*, W11410, doi:10.1029/2005WR004056.
de Simoni, M., X. Sanchez-Vila, J. Carrera, and M. W. Saaltink (2007), A mixing ratios-based formulation for multicomponent reactive transport, *Water Resour. Res.*, *43*, W07419, doi:10.1029/2006WR005256.
Donado, L. D., X. Sanchez-Vila, M. Dentz, J. Carrera, and D. Bolster (2009), Multicomponent reactive transport in multicontinuum media, *Water Resour. Res.*, *45*, W11402, doi:10.1029/2008WR006823.
Fetter, C. W. (2008), *Contaminant Hydrogeology*, 2nd ed., Waveland Press Inc., N. Y.
Ginn, T. R. (1999), On the distribution of multicomponent mixtures over generalized exposure time in subsurface flow and reactive transport: Foundations, and formulations for groundwater age, chemical heterogeneity, and biodegradation, *Water Resour. Res.*, *35*(5), 1395–1407.
Ginn, T. R. (2001), Stochastic–convective transport with nonlinear reactions and mixing: Finite streamtube ensemble formulation for multicomponent reaction systems with intra-streamtube dispersion, *J. Contam. Hydrol.*, *47*(1), 1–28, doi:10.1016/S0169-7722(00)00167-4.
Ginn, T. R. (2009), Generalization of the multirate basis for time convolution to unequal forward and reverse rates and connection to reactions with memory, *Water Resour. Res.*, *45*, W12419, doi:10.1029/2009WR008320.
Golfier, F., M. Quintard, F. Cherblanc, B. A. Zinn, and B. D. Wood (2007), Comparison of theory and experiment for solute transport in highly heterogeneous porous medium, *Adv. Water Resour.*, *30*(11), 2235–2261, doi:10.1016/j.advwatres.2007.05.004.
Gouze, P., Y. Melean, T. Le Borgne, M. Dentz, and J. Carrera (2008), Non-Fickian dispersion in porous media explained by heterogeneous microscale matrix diffusion, *Water Resour. Res.*, *44*, W11416, doi:10.1029/2007WR006690.
Gramling, C. M., C. F. Harvey, and L. C. Meigs (2002), Reactive transport in porous media: A comparison of model prediction with laboratory visualization, *Environ. Sci. Technol.*, *36*(11), 2508–2514, doi:10.1021/es0157144.
Gray, P., and S. K. Scott (1983), Autocatalytic reactions in the isothermal continuous, stirred-tank reactor: isolas and other forms of multistability, *Chem. Eng. Sci.*, *38*, 29–43.
Green, C. T., Y. Zhang, B. C. Jurgens, J. J. Starn, and M. K. Landon (2014), Accuracy of travel time distribution (TTD) models as affected by TTD complexity, observation errors, and model and tracer selection, *Water Resour. Res.*, *50*, 6191–6213, doi:10.1002/2014WR015625.
Guiheneuf, N., A. Boisson, O. Bour, B. Dewandel, J. Perrin, A. Dausse, M. Viossanges, S. Chandra, S. Ahmed, and J. C. Marechal (2014), Groundwater flows in weathered crystalline rocks: Impact of piezometric variations and depth-dependent fracture connectivity, *J. Hydrol.*, *511*, 320–334, doi:10.1016/j.jhydrol.2014.01.061.
Hadermann, J., and W. Heer (1996), The Grimsel (Switzerland) migration experiment: Integrating field experiments, laboratory investigations and modelling, *J. Contam. Hydrol.*, *21*(1-4), 87–100.
Haggerty, R., and S. M. Gorelick (1995), Multiple-rate mass transfer for modeling diffusion and surface reactions in media with pore-scale heterogeneity, *Water Resour. Res.*, *31*(10), 2383–2400.
Haggerty, R., S. A. McKenna, and L. C. Meigs (2000), On the late-time behavior of tracer test breakthrough curves, *Water Resour. Res.*, *36*(12), 3467–3479, doi:10.1029/2000WR900214.
Haggerty, R., S. W. Fleming, L. C. Meigs, and S. A. McKenna (2001), Tracer tests in a fractured dolomite 2. Analysis of mass transfer in single-well injection-withdrawal tests, *Water Resour. Res.*, *37*(5), 1129–1142, doi:10.1029/2000WR900334.
Haggerty, R., C. F. Harvey, C. F. von Schwerin, and L. C. Meigs (2004), What controls the apparent timescale of solute mass transfer in aquifers and soils? A comparison of experimental results, *Water Resour. Res.*, *40*, W01510, doi:10.1029/2002WR001716.
Heße, F., V. Prykhodko, S. Attinger, and M. Thullner (2014), Assessment of the impact of pore-scale mass-transfer restrictions on microbially-induced stable-isotope fractionation, *Adv. Water Resour.*, *74*, 79–90, doi:10.1016/j.advwatres.2014.08.007.
LeBlanc, D. R., S. P. Garabedian, K. M. Hess, L. W. Gelhar, R. D. Quadri, K. G. Stollenwerk, and Wood (1991), Large-scale natural gradient tracer test in sand and gravel, Cape Cod, Massachusetts, 1, Experimental design and observed tracer movement, *Water Resour. Res.*, *27*(5), 895–910.
Le Borgne, T., and P. Gouze (2008), Non-Fickian dispersion in porous media: 2. Model validation from measurements at different scales, *Water Resour. Res.*, *44*, W06427, doi:10.1029/2007WR006279.
Luquot, L., O. Rodriguez, and P. Gouze (2014a), Experimental characterization of porosity structure and transport property changes in limestone undergoing different dissolution regimes, *Transp. Porous Media*, *101*(3), 507–532, doi:10.1007/s11242-013-0257-4.
Luquot, L., T. S. Roetting, and J. Carrera (2014b), Characterization of flow parameters and evidence of pore clogging during limestone dissolution experiments, *Water Resour. Res.*, *50*, 6305–6321, doi:10.1002/2013WR015193.
MacQuarrie, K. T. B., and K. U. Mayer (2005), Reactive transport modeling in fractured rock: A state-of-the-science review, *Earth Sci. Rev.*, *72*(3-4), 189–227, doi:10.1016/j.earscirev.2005.07.003.
Maher, K. (2010), The dependence of chemical weathering rates on fluid residence time, *Earth Planet. Sci. Lett.*, *294*(1–2), 101–110, doi:10.1016/j.epsl.2010.03.010.
Maher, K. (2011), The role of fluid residence time and topographic scales in determining chemical fluxes from landscapes, *Earth Planet. Sci. Lett.*, *312*(1–2), 48–58, doi:10.1016/j.epsl.2011.09.040.
Margolin, G., M. Dentz, and B. Berkowitz (2003), Continuous time random walk and multirate mass transfer modeling of sorption, *Chem. Phys.*, *295*(1), 71–80.
McKenna, S. A., L. C. Meigs, and R. Haggerty (2001), Tracer tests in a fractured dolomite 3. Double-porosity, multiple-rate mass transfer processes in convergent flow tracer tests, *Water Resour. Res.*, *37*(5), 1143–1154.

Michalak, A. M., and P. K. Kitanidis (2000), Macroscopic behavior and random-walk particle tracking of kinetically sorbing solutes, *Water Resour. Res.*, *36*(8), 2133–2146, doi:10.1029/2000WR900109.
Molson, J., M. Aubertin, and B. Bussière (2012), Reactive transport modelling of acid mine drainage within discretely fractured porous media: Plume evolution from a surface source zone, *Environ. Modell. Software*, *38*, 259–270, doi:10.1016/j.envsoft.2012.06.010.
Mukhopadhyay, S., H. H. Liu, N. Spycher, and B. M. Kennedy (2014), Gaining insights into reactive fluid-fractured rock systems using the temporal moments of a tracer breakthrough curve, *J. Contam. Hydrol.*, *158*, 23–37, doi:10.1016/j.jconhyd.2013.12.003.
Murphy, E. M., and T. R. Ginn (2000), Modeling microbial processes in porous media, *Hydrogeol. J.*, *8*, 142–158.
Murphy, E. M., T. R. Ginn, A. Chilakapati, C. T. Resch, J. L. Phillips, T. W. Wietsma, and C. M. Spadoni (1997), The influence of physical heterogeneity on microbial degradation and distribution in porous media, *Water Resour. Res.*, *33*(5), 1087–1103.
Neretnieks, I. (1980), Diffusion in the rock matrix: An important factor in radionucleside retardation?, *J. Geophys. Res.*, *85*(B8), 4379–4397, doi:10.1029/JB085iB08p04379.
Paikaray, S., S. Banerjee, and S. Mukherji (2005), Sorption behavior of heavy metal pollutants onto shales and correlation with shale geochemistry, *Environ. Geol.*, *47*(8), 1162–1170, doi:10.1007/s00254-005-1262-x.
Parkhurst, D. L., and C. A. J. Appelo (1999), User's guide to PHREEQC (version 2)—A computer program for speciation, batch-reaction, one-dimensional transport, and inverse geochemical calculations, Report 99-4259, U.S. Geol. Surv., Denver, Colo.
Poonoosamy, J., G. Kosakowsld, L. R. Van Loon, and U. Mader (2015), Dissolution-precipitation processes in tank experiments for testing numerical models for reactive transport calculations: Experiments and modelling, *J. Contam. Hydrol.*, *177*, 1–17, doi:10.1016/j.jconhyd.2015.02.007.
Pruess, K., and T. N. Narasimhan (1985), A practical method for modeling fluid and heat-flow in fractured porous-media, *SPEJ Soc. Pet. Eng. J.*, *25*(1), 14–26, doi:10.2118/10509-PA.
Ptak, T., and G. Schmid (1996), Dual-tracer transport experiments in a physically and chemically heterogeneous porous aquifer: Effective transport parameters and spatial variability, *J. Hydrol.*, *183*(1-2), 117–138.
Robinet, J.-C., P. Sardini, D. Coelho, J.-C. Parneix, D. Prêt, S. Sammartino, E. Boller, and S. Altmann (2012), Effects of mineral distribution at mesoscopic scale on solute diffusion in a clay-rich rock: Example of the Callovo-Oxfordian mudstone (Bure, France), *Water Resour. Res.*, *48*, W05554, doi:10.1029/2011WR011352.
Roubinet, D., H. Liu, and J.-R. de Dreuzy (2010), A new particle-tracking approach to simulating transport in heterogeneous fractured porous media, *Water Resour. Res.*, *46*, W11507, doi:10.1029/2010WR009371.
Roubinet, D., J.-R. de Dreuzy, and D. Tartakovsky (2013), Particle-tracking simulations of anomalous transport in hierarchically fractured rocks, *Comput. Geosci.*, *50*, 52–58, doi:10.1016/j.cageo.2012.07.032.
Rubin, J. (1983), Transport of reacting solutes in porous-media-–Relation between mathematical nature of problem formulation and chemical nature of reactions, *Water Resour. Res.*, *19*(5), 1231–1252, doi:10.1029/WR019i005p01231.
Sánchez-Vila, X., and J. Carrera (2004), On the striking similarity between the moments of breakthrough curves for a heterogeneous medium and a homogeneous medium with a matrix diffusion term, *J. Hydrol.*, *294*(1-3), 164–175.
Scheidegger, A. E. (1954), Statistical hydrodynamics in porous media, *J. Appl. Phys.*, *25*(8), 994–1001, doi:10.1063/1.1721815.
Shampine, L. F., and M. W. Reichelt (1997), The MATLAB ODE Suite, *SIAM J. Sci. Comput.*, *18*(1), 1–22, doi:10.1137/S1064827594276424.
Steefel, C. I., and P. C. Lichtner (1994), Diffusion and reaction in rock matrix bordering a hyperalkaline fluid-filled fracture, *Geochim. Cosmochim. Acta*, *58*(17), 3595–3612, doi:10.1016/0016-7037(94)90152-X.
Steefel, C. I., and K. T. B. MacQuarrie (1996), Approaches to modeling of reactive transport in porous media, *Rev. Mineral.*, *34*(1), 85–129.
Steefel, C. I., and K. Maher (2009), Fluid-Rock Interaction: A Reactive Transport Approach, in *Thermodynamics and Kinetics of Water-Rock Interaction*, edited by E. H. Oelkers and J. Schott, pp. 485–532, Mineral. Soc Am., Chantilly, Va, doi:10.2138/rmg.2009.70.11.
Sudicky, E. A., and E. O. Frind (1982), Contaminant transport in fractured porous-media - analytical solutions for a system of parallel fractures, *Water Resour. Res.*, *18*(6), 1634–1642, doi:10.1029/WR018i006p01634.
Tang, D. H., E. O. Frind, and E. A. Sudicky (1981), Contaminant transport in fractured porous-media - analytical solution for a single fracture, *Water Resour. Res.*, *17*(3), 555–564, doi:10.1029/WR017i003p00555.
Tyagi, M., T. Gimmi, and S. V. Churakov (2013), Multi-scale micro-structure generation strategy for up-scaling transport in clays, *Adv. Water Resour.*, *59*, 181–195, doi:10.1016/j.advwatres.2013.06.002.
Valocchi, A. J. (1990), Use of temporal moment analysis to study reactive solute transport in aggregated porous-media, *Geoderma*, *46*(1-3), 233–247.
Vereecken, H., U. Jaekel, O. Esser, and O. Nitzsche (1999), Solute analysis of bromide, uranin and LiCl using breakthrough curves from aquifer sediment, *J. Contam. Hydrol.*, *39*, 7–34.
Vereecken, H., U. Jaekel, and H. Schwarze (2002), Analysis of the long-term behavior of solute transport with nonlinear equilibrium sorption using breakthrough curves and temporal moments, *J. Contam. Hydrol.*, *56*(3-4), 271–294.
Villermaux, J. (1987), Chemical-engineering approach to dynamic modeling of linear chromatography - a flexible method for representing complex phenomena from simple concepts, *J. Chromatogr.*, *406*, 11–26, doi:10.1016/s0021-9673(00)94014-7.
Warren, J. E., P. J. Root, and M. Aime (1963), The behavior of naturally fractured reservoirs, *Soc. Pet. Eng. J.*, *3*(3), 245–255, doi:10.2118/426-PA.
Weber, W. J., P. M. McGinley, and L. E. Katz (1991), Sorption phenomena in subsurface systems- concepts, models and effects on contaminant fate and transport, *Water Res.*, *25*(5), 499–528.
Wels, C., and L. Smith (1994), Retardation of sorbing solutes in fractured media, *Water Resour. Res*, *30*(9), 2547–2563.
Willmann, M., J. Carrera, and X. Sanchez-Vila (2008), Transport upscaling in heterogeneous aquifers: What physical parameters control memory functions?, *Water Resour. Res.*, *44*, W12437, doi:10.1029/2007WR006531.
Willmann, M., J. Carrera, X. Sanchez-Vila, O. Silva, and M. Dentz (2010), Coupling of mass transfer and reactive transport for nonlinear reactions in heterogeneous media, *Water Resour. Res.*, *46*, W07512, doi:10.1029/2009WR007739.
Wu, Y. S., H. H. Liu, and G. S. Bodvarsson (2004), A triple-continuum approach for modeling flow and transport processes in fractured rock, *J. Contam. Hydrol.*, *73*(1-4), 145–179, doi:10.1016/j.jconhyd.2004.01.002.
Yoo, K., and S. M. Mudd (2008), Discrepancy between mineral residence time and soil age: Implications for the interpretation of chemical weathering rates, *Geology*, *36*(1), 35–38, doi:10.1130/g24285a.1.
Zhou, Q. L., H. H. Liu, F. J. Molz, Y. Q. Zhang, and G. S. Bodvarsson (2007), Field-scale effective matrix diffusion coefficient for fractured rock: Results from literature survey, *J. Contam. Hydrol.*, *93*(1-4), 161–187.
Zinn, B., L. C. Meigs, C. F. Harvey, R. Haggerty, W. J. Peplinski, and C. F. Von Schwerin (2004), Experimental visualization of solute transport and mass transfer processes in two-dimensional conductivity fields with connected regions of high conductivity, *Environ. Sci. Technol.*, *38*(14), 3916–3926, doi:10.1021/es034958g.

3 Bilan

Les modèles MRMT sont donc capables non seulement de reproduire l'effet de structures immobiles complexes sur le transport conservatif (Chapitre 3), mais également de fournir de très bonnes estimations d'une réactivité hétérogène, cinétique et non-linéaire. Les taux de dissolution d'un minéral et de désorption d'un soluté dans SINC et MRMT diffèrent généralement de moins de 1% et au maximum de 10%. Ce résultat s'explique d'une part par la bonne représentation par MRMT des échanges mobile-immobiles rapides par un grand nombre de taux d'échange, d'autre part par l'homogénéisation opérée aux temps longs par la diffusion dans les parties plus reculées de la structure immobile. De plus, comme dans le Chapitre 3, nous avons montré que des modèles MRMT simplifiés, ne possédant qu'un faible nombre de taux d'échange (< 5), donnent déjà de très bonnes estimations des taux de réaction. Nous proposons donc une méthode de calibration d'un modèle MRMT réactif à partir d'une courbe de restitution.

Deux limitations à l'usage de MRMT comme proxy pour du transport réactif méritent d'être soulignées. La première est que notre étude est restreinte à une dispersion d'origine principalement diffusive. Hors la dispersion possède également une composante advective due aux variations hydrodynamiques locales. L'extension de l'usage de MRMT à une dispersion dominée par l'advection reste à être validée.

D'autre part, les déviations observées entre SINC et MRMT, quoique limitées, apparaissent principalement lorsque des gradients de concentration forts persistent dans les parties reculées de la structure, par exemple dans le cas où une large part de la porosité n'est accessible que par un goulot d'étranglement. MRMT fournit donc des estimations correctes des taux de réaction tant que les gradients de concentrations dans la structure immobile restent d'abord déterminés par les échanges mobile-immobiles. Les déviations entre SINC et MRMT deviennent ainsi plus importantes lorsque le temps caractéristique de diffusion augmente par rapport au temps caractéristique de réaction, i.e. lorsque la réaction devient davantage transport-limitée. L'utilisation de MRMT pour du transport réactif pourrait alors être invalidée par des réactions fortement non-linéaires, comme des réactions auto-catalytiques, ou par une réaction qui ne prendrait place que dans une partie seulement de la structure immobile. Ce dernier cas rejoindrait les limitations de l'approche MRMT pour du transport réactif mises en évidence dans le Chapitre 2, où l'existence de conditions initiales non-homogènes pouvait

invalider l'usage des "concentrations" MRMT comme de véritables concentrations chimiques (notamment toujours positives).

Chapitre 5 : Contrôle temporel de la biodégradation d'un pesticide dans les sols : rôle d'une distribution hétérogène de dégradeurs microbiens modélisée à partir d'expériences de laboratoire

1 Introduction

Dans le chapitre précédent, nous avons vu que des modèles de transport équivalents, à quelques degrés de liberté, donnent de bonnes estimations d'une réactivité non-linéaire lorsque le transport est dominé par la diffusion. Ces modèles sont de plus calibrables à partir de données de terrain comme une distribution de temps de transit. Nous avons également souligné comment une des limites de ces modèles est leur difficulté à prendre en compte des conditions initiales non-homogènes.

Le rôle des conditions initiales dans le couplage entre transport diffusif et réactivité biochimique est central dans ce chapitre et prolonge cette réflexion. Notre étude ici se base sur une série d'expériences de laboratoire réalisée par Pinheiro et al. (2015) sur la dégradation d'un pesticide, le 2,4-D, dans des colonnes de sol d'échelle centimétrique (*Figure 5.1*). Dans cette série de quatre expériences, l'évolution d'un apport de pesticide marqué au ^{14}C est suivi pour différentes répartitions initiales de pesticide et de dégradeurs microbiens (*Figure 5.2*). En effet, la dégradation de pesticides dans les sols varie à l'échelle centimétrique due à la distribution des dégradeurs microbiens en hotspots (Gonod et al. 2003, Gonod et al. 2006). L'accessibilité des dégradeurs au pesticide est alors un contrôle majeur de la dégradation (Dechesne et al. 2010).

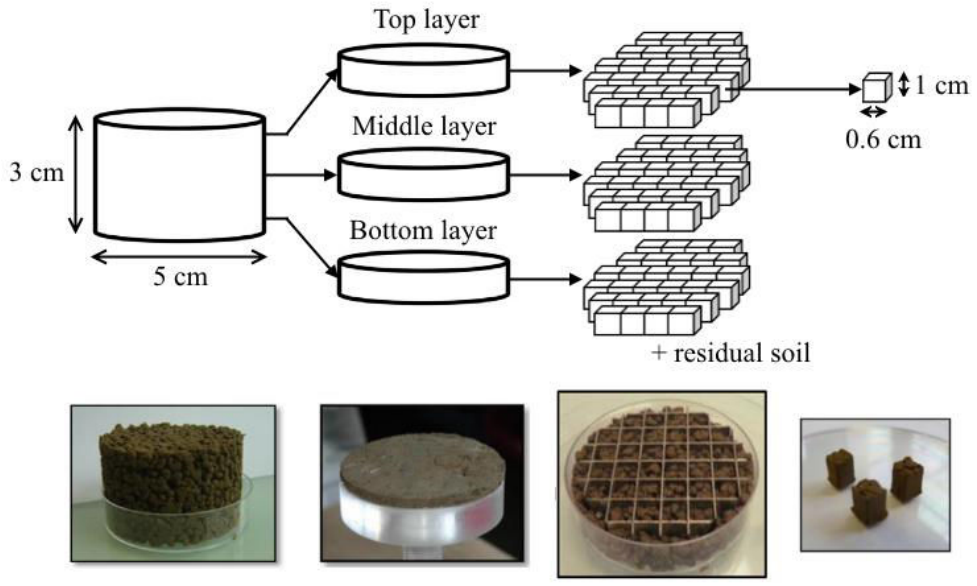

Figure 5.1 : Procédure de découpe des colonnes de sol mise en œuvre par Pinheiro et al. (2015) afin de suivre l'évolution d'un amendement en 2,4-D (pesticides). La construction des colonnes de sol suit une procédure symétrique, où l'utilisation d'une grille permet de contrôler l'emplacement initial du pesticide et des microorganismes dégradants.

Dans un premier temps, nous chercherons à utiliser la complémentarité des différentes expériences afin de calibrer de manière univoque un modèle de transport réactif. Ce modèle couple transport par diffusion, sorption et dégradation par une communauté bactérienne du pesticide, cette communauté évoluant dynamiquement dans le temps (croissance et mort). Dans un second temps, le modèle calibré servira de base à une étude de sensibilité basée sur différents scénarios d'extrapolation (influence de la saturation en eau, de la distance de séparation initiale entre le pesticide et les microorganismes...). L'objectif est de mettre en évidence les contrôles du couplage entre diffusion et réactivité biochimique.

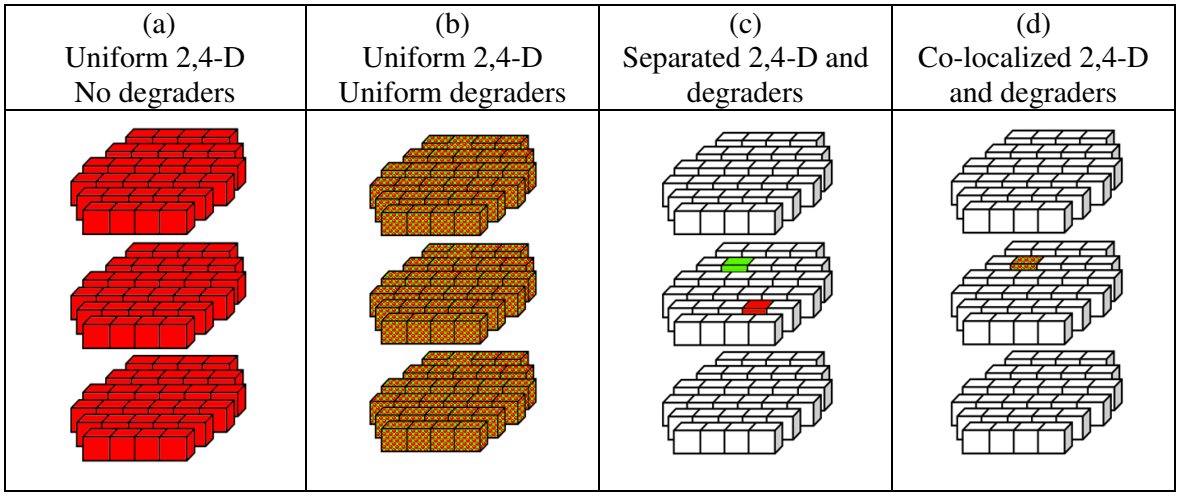

Figure 5.2 : Répartition initiale du pesticide (rouge) et des dégradeurs (vert) dans les quatre expériences de Pinheiro et al. (2015).

2 Article: "*Simulations and temporal-control of 2,4-D pesticide degradation by spatially distributed microorganisms in 3D soil-core experiments*", par T. Babey, L. Vieublé-Gonod, A. Rapaport, M. Pinheiro, P. Garnier et J.-R. de Dreuzy, publié en 2017 dans Ecological Modelling

Ecological Modelling 344 (2017) 48–61

Contents lists available at ScienceDirect

Ecological Modelling

journal homepage: www.elsevier.com/locate/ecolmodel

Spatiotemporal simulations of 2,4-D pesticide degradation by microorganisms in 3D soil-core experiments

Tristan Babey[a,*], Laure Vieublé-Gonod[b], Alain Rapaport[c], Marc Pinheiro[d], Patricia Garnier[d], Jean-Raynald de Dreuzy[a]

[a] Géosciences Rennes UMR CNRS 6118, Campus de Beaulieu, Université de Rennes 1, 35042 Rennes Cedex, France
[b] AgroParisTech, UMR Ecologie Fonctionnelle et Ecotoxicologie des Agrosystèmes, Av. L. Brétignières, 78850 Thiverval Grignon, France
[c] UMR 729 INRA SupAgro MISTEA, Montpellier, France
[d] INRA, UMR Ecologie Fonctionnelle et Ecotoxicologie des Agrosystèmes, Av. L. Brétignières, 78850 Thiverval Grignon, France

ARTICLE INFO

Article history:
Received 4 May 2016
Received in revised form 7 November 2016
Accepted 8 November 2016

Keywords:
Pesticide degradation
Spatial heterogeneity
Reactive transport model
Diffusion-controlled microbial activity
2,4-D

ABSTRACT

We investigate the temporal constraints of 2,4-D degradation by spatially distributed soil microorganisms. Based on a complementary set of laboratory experiments (Pinheiro et al., 2015), we determine the characteristic temporal scales of the involved chemical, biological and diffusion processes from the calibration of a biochemical transport model. Reversible sorption is the fastest process with characteristic sorption and desorption rates $k_{SA} = 0.09\,d^{-1}$ and $k_{AS} = 4.4\,d^{-1}$ respectively, but remains limited to a minor amount of pesticides. Microbial mineralization is slower and is well described by a Monod formulation ($\mu_{max} = 0.6\,d^{-1}$, $\kappa_S = 0.37$ $\mu gC/g_{soil}$, $y = 0.5$) complemented by the characteristic accommodation rate $\alpha = 0.93\,d^{-1}$, the microbial mortality rate $m_t = 0.06\,d^{-1}$ and the recycling coefficient for dead biomass $\chi = 0.6$. Irreversible abiotic attachment and 2,4-D diffusion are the slowest processes, with the estimated attachment rate $k_c = 0.01\,d^{-1}$ and diffusion coefficient $d = 6.10^{-6}\,m^2/d$. We use the calibrated biochemical transport model to explore the influence of the initial 2,4-D repartition and of the water potential. When added next to the microorganisms, pesticides that are not diffused away are efficiently degraded in the first few days. The pesticides diffused away are diluted, sorbed and hardly get back to the microorganisms, limiting the overall degradation. In this case degradation is more efficient for smaller diffusion and water content conditions. When initially separated, pesticides diffuse slowly everywhere in the soil core. The small part reaching the microorganisms is not efficiently degraded due to a low biological activity. The larger part becomes abiotically trapped before reaching the degraders. We hypothesize that transport mechanisms like pesticide convection or microbial mobility might be more decisive than pesticide diffusion to establish contact between pesticides and microorganisms.

1. Introduction

Biodegradation in soils is controlled by physical, biological and chemical processes interacting on a broad range of scales. Furthermore, the complex soil structure generates a heterogeneous spatial distribution of pesticides and microorganisms. Consequently pesticide degradation varies spatially at the scale of the agricultural field (Filipović et al., 2014) but also at the scale of microbial habitats (Gonod et al., 2003, 2006). Accessibility and availability of pesticides to degraders are key processes controlling biodegradation in soil (Dechesne et al., 2010). Microscale structures like tortuosity or poor pore connectivity reduce the probability of contact between the microorganisms and the organic substrates (Or et al., 2007; Vogel et al., 2015). At the macroscale, higher water content or porosity have been linked to increased pesticide accessibility (Chenu et al., 2001; Monard et al., 2012). Biodegradation is also controlled by chemical sorption and other trapping processes that may temporarily or definitively reduce the bioavailability of organic compounds (Barriuso et al., 2008; Kästner et al., 2013; Sims et al., 1991). Effective biodegradation additionally depends on the nature and state of the microorganisms inherited from the previous soil activity as well as on the previous exposure to varying substrate sources (Filipović et al., 2014; Murphy and Ginn, 2000; Murphy et al., 1997). However, most of the pesticide models in soil do not consider the explicit location of pollutants and degraders, as well as the coupling between biotic and abiotic processes. The mod-

* Corresponding author.
E-mail address: tristan.babey@univ-rennes1.fr (T. Babey).

http://dx.doi.org/10.1016/j.ecolmodel.2016.11.006
0304-3800/

els of Dechesne et al. (2010) and Villaverde et al. (2009) simulate respectively benzoate and atrazine behavior under diffusion conditions, and the model of Rosenbom et al. (2014) simulate MCPA degradation during convection. Models by Monga et al. (2014) and Vogel et al. (2015) consider the spatial heterogeneity of microbial degradation at pore scale but not chemical processes associated to pesticide such as adsorption.

Using extensive pore-scale simulations, Vogel et al. (2015) show that the initial repartition of substrates and microorganisms is the first factor conditioning the variability of biodegradation under diffusion-controlled transport. Similar conclusions are reached from cm-scale laboratory experiments performed with varying initial distributions of 2,4-dichlorophenoxyacetic acid (2,4-D) and degraders (Pinheiro et al., 2015). To further investigate the relative importance of the different processes and initial conditions, we thus develop a 3D model coupling diffusion, biological degradation, microorganism growth, and chemical reversible and irreversible trappings. This model is calibrated and validated on the experiments of Pinheiro et al. (2015). It is then used to simulate the influence of key factors controlling the degradation of pesticides in real soils including the concentration of pesticides, the distance between pesticides and degrading microorganisms that may be affected by agricultural practices, and the water potential linked to the degree of water filling of the porosity impacting pesticide mobility in soils.

2. Experiments, models and methods

We present concisely the experiments carried out in Pinheiro et al. (2015) and show how their complementarity can be used to determine unambiguously the chemical, biological and physical components of an integrated model of 2,4-D reactivity in soils. Then we detail the methods used for numerical simulations and model calibration. Effective calibration of the model is presented in the results section. Finally, we show the assumptions used to extrapolate the calibrated model to different physical, chemical and biological conditions.

2.1. Experiments

Pinheiro et al. (2015) performed laboratory experiments in 5 cm diameter x 3 cm height reconstructed soil cores from 2 to 3.15 mm soil aggregates, sterilized or not by gamma-irradiation. Each core was considered as physically homogeneous and was composed of $0.6 \times 0.6 \times 1$ cm cubes (Appendix A). Each cube was considered as chemically and biologically homogeneous. Experiments were identified by their initial spatial repartition of ^{14}C-labeled 2,4-D and degrading microorganisms (first 4 rows of Fig. 1). Soil cores were incubated for 14 days under laboratory-controlled conditions at 20 °C and with a constant water potential of −31.6 kPa (field capacity). Cumulated $^{14}CO_2$ emissions resulting from ^{14}C-2,4-D mineralization were measured daily at the core scale. At days 1, 7 and 14, soil cores were analyzed for ^{14}C-$CaCl_2$-extractable residues, ^{14}C-methanol-extractable residues, ^{14}C-non-extractable residues and degrading microorganisms. For the two heterogeneous initial distributions of 2,4-D and microorganisms (Fig. 1, columns c and d), cores were cut back into mm-sized cubes and analyses were performed independently on each cube. The total recovery of added ^{14}C label ranged from 95 to 130% for all experiments.

2.2. Model

2.2.1. 2,4-D chemical interaction with the soil matrix

2,4-D interacts with the soil matrix either reversibly or irreversibly. Reversible interactions come from sorption to the surface of particles and organic matter. Irreversible attachment comes from the formation of more stable linkages like covalent bonds (Gevao et al., 2000). The mass balance model for the different compartments writes (Kästner et al., 2013):

$$\frac{dS}{dt} = -k_{SA}S + k_{AS}A - k_cS \quad (1)$$

$$\frac{dA}{dt} = k_{SA}S - k_{AS}A \quad (2)$$

$$\frac{dR_c}{dt} = k_cS \quad (3)$$

$S(t)$ is the 2,4-D concentration in solution at time t expressed in micrograms of carbon per gram of soil [$\mu gC\, g_{soil}^{-1}$]. $A(t)$ is the reversibly sorbed 2,4-D concentration [$\mu gC\, g_{soil}^{-1}$] with k_{SA} and k_{AS} the sorption and desorption rates [day^{-1}]. $R_c(t)$ is the concentration of irreversibly attached abiotic residues [$\mu gC{\cdot}g_{soil}^{-1}$] with k_c the irreversible attachment rate [day^{-1}]. We define $\tau_c = 1/k_c$ as the characteristic time of formation of irreversibly attached abiotic residues. Similarly, $\tau_{sorption} = 1/k_{SA}$ and $\tau_{desorption} = 1/k_{AS}$ are defined as the characteristic sorption and desorption times for reversible sorption.

We will calibrate the reaction rates k_{SA}, k_{AS} and k_c on the experiment where 2,4-D is initially uniformly distributed in a sterilized soil core (Fig. 1, column a). The calibration is achieved by assimilating S to the ^{14}C $CaCl_2$-extractable residues, A to the ^{14}C methanol-extracted residues and R_c to the ^{14}C non-extractable residues (*NER*).

2.2.2. 2,4-D biodegradation

In addition to its chemical interactions with the soil matrix, 2,4-D can also be mineralized by soil microorganisms (Barriuso et al., 2008; Gonod et al., 2006). Labile 2,4-D in the soil solution is mineralized preferentially due to its greater availability to micro-organisms (Greer and Shelton, 1992; Ogram et al., 1985). Reversibly sorbed pesticide of concentration A is indirectly available to biodegradation through its potential release into the soil solution. These assumptions are consistent with the findings of Barriuso et al. (2004) who showed that atrazine bioavailability to soil microorganisms can be estimated from the $CaCl_2$-methanol extractable fraction. We also assume that the ^{14}C microbial uptake not used for biomass growth is only released as CO_2 emissions. We do not explicitly consider the formation of metabolites due to the lack of specific measurements. Under these assumptions, 2,4-D degradation and sorption writes (Kästner et al., 2013; Manzoni and Porporato, 2007; Patarinska et al., 2000; Pirt, 1975):

$$\frac{dS}{dt} = -k_{SA}S + k_{AS}A - k_cS - \frac{\mu}{y}B + m_t\chi B \quad (4)$$

$$\frac{dB}{dt} = \mu B - m_tB \quad (5)$$

$$\frac{dR_b}{dt} = m_t(1-\chi)B \quad (6)$$

$$\frac{dCO_2}{dt} = (1-y)\frac{\mu}{y}B \quad (7)$$

$B(t)$ is the degrading biomass concentration [$\mu gC\, g_{soil}^{-1}$]. $R_b(t)$ is the biotic residue concentration formed by non-recycled dead biomass [$\mu gC\, g_{soil}^{-1}$]. $CO_2(t)$ is the emitted CO_2 expressed in equivalent mass of carbon by gram of soil [$\mu gC\, g_{soil}^{-1}$]. With this non-classical choice of unit for the partial pressure of CO_2, all observed quantities have the same units and dimensions, and biological parameters units remain simple. y is the dimensionless yield coefficient ($0 < y < 1$). m_t is the mortality rate [day^{-1}]. χ is the partition coefficient between recycled and non-recycled dead biomass ($0 < \chi < 1$). We assume that the recycled biomass fraction consists in soluble 2,4-D stored inside the cells of degraders and released

	(a) Uniform 2,4-D No degraders	(b) Uniform 2,4-D Uniform degraders	(c) Separated 2,4-D and degraders	(d) Co-localized 2,4-D and degraders
	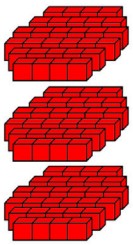	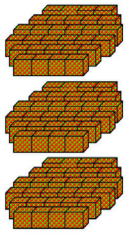	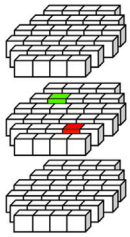	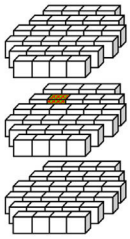
Initial 2,4-D location [x y z]	All cubes	All cubes	[5 5 2]	[2 2 2]
Initial 2,4-D concentration [μgC.g$_{soil}^{-1}$]	0.66	0.66	0.66	0.66
Initial degraders location [x y z]	Nowhere	All cubes	[2 2 2]	[2 2 2]
Initial degraders concentration [μgC.g$_{soil}^{-1}$]	0	0.13	0.13	0.13
Reference experimental data (Pinheiro et al., 2015)	$m_{tot}(X,t)$ with $X = S, A$ and NER	$m_{tot}(X,t)$ with $X = S, A, NER$ and CO_2	Repartition maps of S, A and NER and $m_{tot}(CO_2,t)$	Repartition maps of S, A and NER and $m_{tot}(CO_2,t)$
Fixed parameters	-	k_{SA}, k_{AS}, k_c	k_{SA}, k_{AS}, k_c, α, μ_{max}, κ_S, y, m_t, χ	
Calibrated parameters	k_{SA}, k_{AS}, k_c	α, μ_{max}, κ_S, y, m_t, χ	d	
	Calibration			Validation

Fig. 1. Rows 1 to 4: Initial location and concentration for 2,4-D (Red) and degraders (Green) for the four laboratory experiments from Pinheiro et al. (2015). All other initial concentrations are equal to zero. Cube positions are given in matrix coordinates. Rows 5 to 8: Calibration-validation sequence of the model defined in Section 2.1. Calibration is performed progressively on the experiments of columns (a) to (c) and validated against the experiment of column (d). (For interpretation of the references to colour in this figure legend, the reader is referred to the web version of this article.)

in soil solution upon their death. μ is the specific growth rate of degraders [day^{-1}] accounting for the microbial lag phase in substrate availability conditions (Patarinska et al., 2000):

$$\frac{d\mu}{dt} = \alpha\left(\mu_{\max}\frac{S}{\kappa_S + S} - \mu\right) \tag{8}$$

with $\mu(t=0)=0$ (no previous growth at initial state for degraders). α is the characteristic accommodation rate [day^{-1}], $\mu_{\max}$ is the maximum growth rate for degraders [day^{-1}] and κ_S is the half-saturation concentration in 2,4-D [μgC g$_{soil}^{-1}$]. The ratio μ/y in Eq. (4) corresponds to the substrate uptake rate by degraders [day^{-1}]. The overall model structure is shown on Fig. 2. We define the characteristic biodegradation time τ_{bio} as the instantaneous capacity at time t of the biomass of concentration $B(t)$ to degrade the substrate of concentration $S(t)$:

$$\tau_{bio}(t) = \frac{S(t)}{\mu B(t)/y} \tag{9}$$

τ_{bio} is equal to the substrate concentration $S(t)$ divided by the microbial substrate uptake rate $\mu B(t)/y$. While τ_{bio} evolves with the biomass and substrate, it gives a first approximation of the degraders activity that can be compared to the characteristic time of the other processes. The characteristic death time for biomass is also defined as the inverse of the mortality rate $\tau_{death} = 1/m_t$.

The six biological parameters (y, α, $\mu_{\max}$, κ_S, m_t, χ) will be calibrated on the experiment where 2,4-D and degraders are uniformly distributed in the soil core (optimal conditions for biodegradation) (Fig. 1, column b). Initial degrader concentration is calculated from

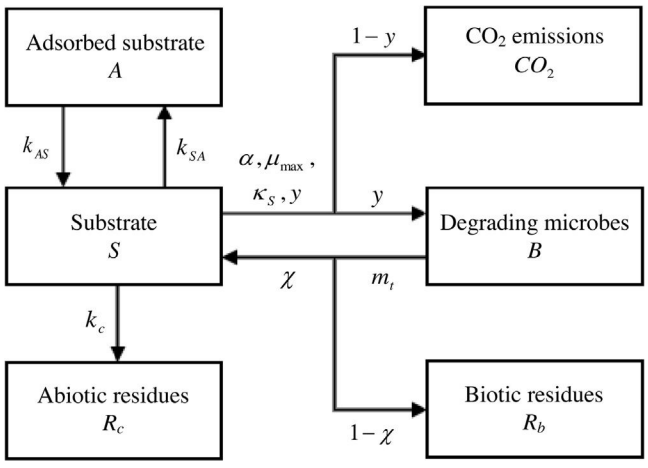

Fig. 2. Biochemical model for 2,4-D corresponding to Eqs. (2)–(8).

measurements of *tfda* sequences concentration associated with 2,4-D degradation. We assume that one *tfda* sequence corresponds to one microorganism, with an average cell dry weight of 2.8×10^{-13} g and the average molecular formula $C_5H_7O_2N$ (Dechesne et al., 2010). Note that the removal rate of pesticide by degraders $\mu B(t)/y$, used to define $\tau_{bio}(t)$ is the quantity primarily calibrated by the optimization procedure. As such, its value does not depend on the evaluated initial concentration of degraders. It will be further

used as a basis of comparison between degradation efficiency and the other sorption and transport parameters. Abiotic parameters will be kept equal to their previously determined values (Section 2.2.1). For this experiment, the ^{14}C non-extractable residues *NER* are attributed to the sum of the irreversibly attached abiotic residues R_c, the living biomass B and the biotic residues R_b (Barriuso et al., 2008):

$$NER = R_c + R_b + B \tag{10}$$

2.2.3. 2,4-D diffusion

Transport of 2,4-D by diffusion is a major control of 2,4-D fate when the 2,4-D and its degraders are initially separated or co-localized (Fig. 1, columns c and d). Since no degrading microorganisms were detected in the soil outside of the initially inoculated cube at any time of the experiments, degraders B and biogenic residues R_b are considered immobile. We spatialize Eqs. (2)–(8) such that all concentrations now depend on the time t and on the position in the soil core $\boldsymbol{x}$. The mass balance for S then writes:

$$\frac{\partial S}{\partial t} = \nabla(d\nabla S) - k_{SA}S + k_{AS}A - k_c S - \mu B + m_t \chi B \tag{11}$$

where d is the effective diffusion coefficient of 2,4-D in the soil solution. d is assumed to be uniform. Zero-flux boundary conditions are imposed on the soil core edges Γ_{lim}:

$$\nabla S = 0 \text{ on } \Gamma_{\text{lim}} \tag{12}$$

We define the characteristic diffusion time as:

$$\tau_{diff} = \lambda^2/d \tag{13}$$

with λ the characteristic diffusion length equal to the initial separation distance between the microbial hotspot and the 2,4-D injection cube. Furthermore, the transport and biological dynamics will be compared in terms of the Damköhler number (Boucher and Alves, 1959):

$$Da = \tau_{diff}/\tau_{bio} \tag{14}$$

Calibration of d will be performed on the separated 2,4-D and degrader experiment (Fig. 1, column c) with biotic and abiotic parameters fixed at their values according to the methodology of the previous sections.

The resulting integrated model for 2,4-D transport and reactivity will finally be validated against the co-localized 2,4-D and degraders experiment (Fig. 1, column d). Commensurable influences of chemical, biological and diffusion processes make this experiment the most suited for model validation. With these initial conditions, the competition between diffusion and biodegradation is different from the previous case of initial separation of degraders and substrate. Indeed, 2,4-D can be degraded before diffusing out of the microbial hotspot. Comparison will be established in both the separated and the co-localized cases on repartition maps of *S*, *A* and *NER* at the three measurement dates (days 1, 7 and 14) and on the daily measurements of CO_2 emissions at the core scale. Calibration sequence is synthesized in the last 3 rows of Fig. 1.

2.3. Simulation methods

Diffusion is simulated with a finite-difference scheme (Iserles, 2008). Simulations are performed in a cubic-like domain and not a cylindrical domain because of the marginal influence of the domain shape. In fact, concentration profiles are substantially smoothed out by diffusion before reaching the boundaries. Soil cores are discretized by a $12 \times 12 \times 6$ grid obtained by subdividing the $6 \times 6 \times 3$ grid of the experimental cores. Each experimental soil cube corresponds to eight voxels. Discretization is validated by a convergence analysis on the calibrated value of the diffusion coefficient. Diffusion is coupled to biochemical reactions (Steefel and MacQuarrie, 1996). Reaction rates are integrated with the 4th order Runge-Kutta ode45 method of MATLAB.

Table 1
Admissible range for calibration and calibrated values of the chemical, biological and transport model parameters (Section 2.2).

Parameters	Admissible range for calibration	Calibrated value
k_{SA} [day^{-1}]	[10^{-4}–10]	0.09
k_{AS} [day^{-1}]	[10^{-4}–10]	4.4
k_c [day^{-1}]	[10^{-4}–10]	0.01
α[day^{-1}]	[10^{-2}–10]	0.93
$\mu_{\max}$ [day^{-1}]	[10^{-2}–10]	0.6
$\mu_{\max}/\kappa_S$[g_{soil}·day^{-1}·μgC^{-1}]	[10^{-2}–100]	1.7
y [−]	[0.05–1]	0.52
m_t [day^{-1}]	[10^{-2}–10]	0.06
χ [−]	[0.05–1]	0.60
d [m^2/day]	[10^{-7}–7.10^{-5}]	6.0 10^{-6}

2.4. Calibration method

We express the instantaneous discrepancy over the soil core between measured and simulated ^{14}C as fraction $X = S$, A, *NER* or CO_2 as:

$$[J_X(t)]^2 = \sum_{i=1}^{n_{cubes}} \left(\frac{m_{cube}^{\exp}(X,t,i) - m_{cube}^{\text{mod}}(X,t,i)}{\sigma(X)} \right)^2 \tag{15}$$

where $m_{cube}^{\exp}(X,t,i)$ and $m_{cube}^{\text{mod}}(X,t,i)$ are the experimental and simulated mass of ^{14}C as fraction X in cube i ($i = 1,\ldots,n_{cubes}$) and $\sigma(X)$ is the standard deviation on the measurement error of X (Tarantola, 2004). The measured values $m_{cube}^{\exp}(X,t,i)$ are obtained as the average of 3 replicated experiments. $\sigma(X)$ is considered identical for all measured quantities X. Models are calibrated by minimizing the global misfit function J cumulating quadratic errors on *S*, *A*, *NER* and CO_2 over all the sampling dates:

$$J = \sum_X \sum_{j=1}^{n_t(X)} \left[J_X(t_j) \right]^2 \tag{16}$$

where $n_t(X)$ is the total number of sampling times t_j for fraction X. Because of some non-convexity of the objective function, optimization is performed using the simulated annealing Monte-Carlo method of MATLAB. Admissible parameter intervals are determined by extending intervals found in the literature (Section 4.1) and are listed in Table 1. Parameters defined over several orders of magnitude (k_{SA}, k_{AS}, k_c, α, $\mu_{\max}$, κ_S, m_t, d) are optimized by the logarithm of their value to estimate correctly their order of magnitude and precise value (Tarantola, 2004). Numerical parameters for simulated annealing are kept equal to their default values. Calibration is performed in successive steps using the complementarity of the experiments. Only a limited number of parameters are determined at each step, where parameter non-unicity is no longer critical.

2.5. Exploratory simulations

To further investigate the coupling between diffusive transport and biodegradation, the calibrated model is used to predict the fate of a 2,4-D addition under various physical, chemical and biological conditions.

We first evaluate the influence of different soil core water potentials and initial distances between 2,4-D and degraders. The

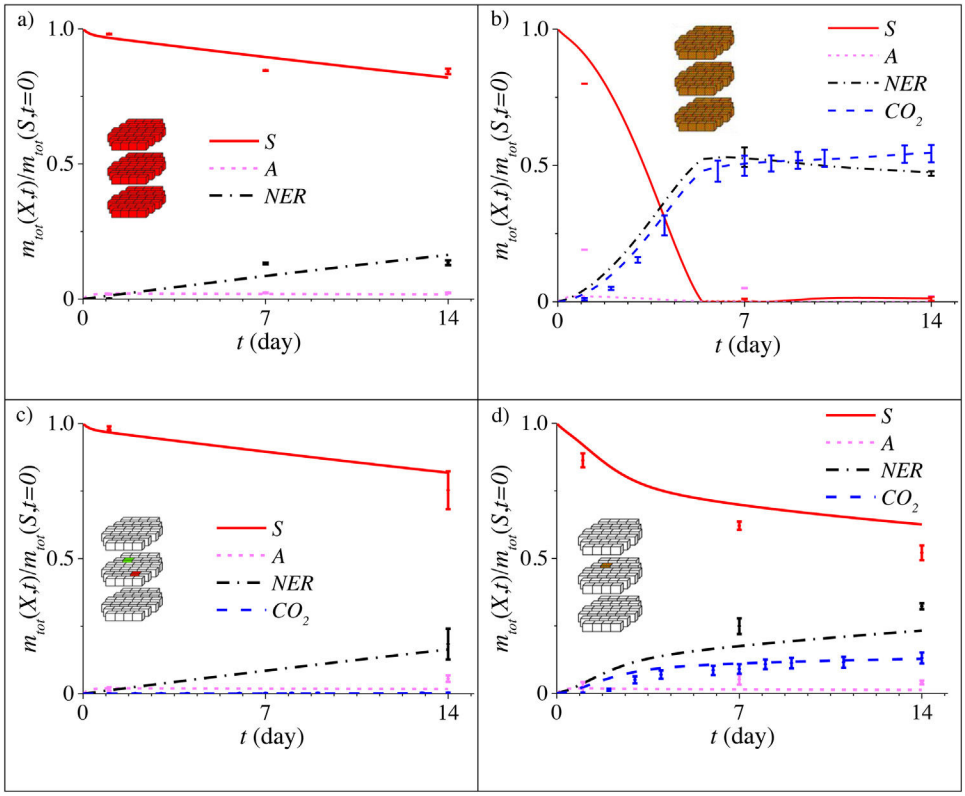

Fig. 3. Core scale ^{14}C repartition as $CaCl_2$-extractable residues (*S*), methanol extractable residues (*A*) and non-extractable residues (*NER*) for a) the uniform 2,4-D, no degraders experiment, b) the uniform 2,4-D, uniform degraders experiment, c) the separated 2,4-D and degraders experiment and d) the co-localized 2,4-D and degraders experiment. Points represent experimental data from Pinheiro et al. (2015) and lines represent the results of the calibrated model. The model results are obtained through calibration for a), b) and c), and by blind prediction for d).

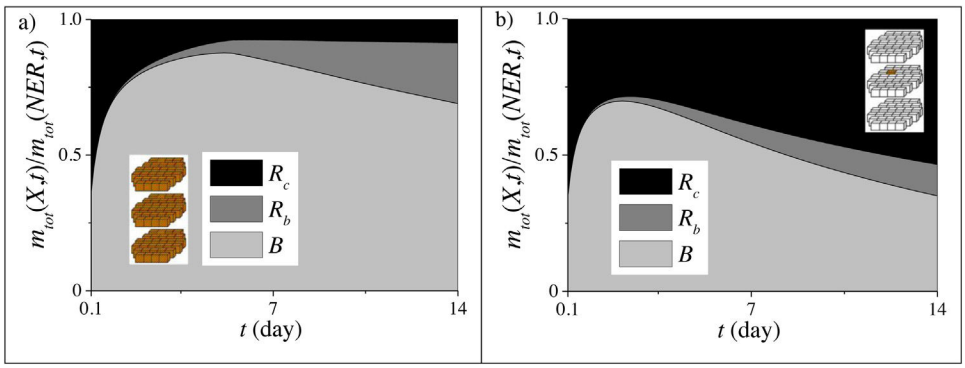

Fig. 4. Model predicted composition of ^{14}C Non-Extractable Residues *NER* at the core scale as abiotic residues (R_c), biotic residues (R_b) and living degraders (*B*) for a) the uniform 2,4-D, uniform degraders experiment and b) the co-localized 2,4-D and degraders experiment. Results for the separated 2,4-D and degraders configuration are not represented because biological degradation remains marginal in this experiment.

effective diffusion coefficient for 2,4-D is related to the water content through (Grathwohl, 1998):

$$d = d_0 \phi \eta \tag{17}$$

where d_0 is the diffusion coefficient of 2,4-D in water, ϕ is the effective porosity assimilated to the product of soil porosity and water content, and η is the ratio of pore constrictivity to tortuosity assumed to remain constant with water content. In addition to the two experimental initial conditions where 2,4-D and degraders are respectively separated by $l = 2.6$ cm and co-localized (Fig. 1c and d), we consider two intermediary configurations where degraders and pesticide are separated by $l = 0.9$ cm and $l = 1.7$ cm. Initial 2,4-D and degraders concentrations are kept equal to their experimental values. We limit the role of water content to its impact on bulk pesticide diffusion. We do not consider more complex influences on sorption and biological dynamics (Juwarkar et al., 2010) or on transport dynamics, for instance disconnections between soil clusters at low saturation levels (Vogel et al., 2015).

In a second time, we evaluate the relative effects of chemical interactions and biological degradation on the long-term fate of 2,4-D in the soil cores. Biological activity is maximized by considering instantaneous mineralization of the 2,4-D diffusing into the degraders cube. Chemical interactions are minimized by setting $k_{SA} = k_{AS} = k_c = 0$. Incubation is simulated until no more 2,4-D remains in solution.

Finally, we investigate the influence of the initial 2,4-D concentration on its biodegradation. Simulations are performed in the co-localized 2,4-D and degraders configuration where the interplay

between the different processes is the most important. We consider three different initial 2,4-D concentrations in the amended soil cube (0.06, 0.21 and 1.3 $\mu gC\, g_{soil}^{-1}$, corresponding to 0.6, 2 and 15 $kg_{2,4-D}.ha^{-1}$) in addition to the experimental concentration of 0.66 $\mu gC\, g_{soil}^{-1}$ (Fig. 1, 4th row). These 2,4-D concentrations are realistic since agronomic doses range between 0.3 and 2.3 $kg_{2,4-D}.ha^{-1}$ of 2,4-D (Willems et al., 1996) (Section 4.2). Toxicity effects of 2,4-D on soil microorganisms will not be considered as they have been observed only at much higher concentrations (from 15 $\mu gC\, g_{soil}^{-1}$ (Parker and Doxtader, 1983)).

3. Results

We present successively the results of the calibration/validation procedure according to the organization defined in Section 2.2 and the results of the exploratory simulations obtained in the conditions given by Section 2.5. Chemical, biological and diffusion dynamics are systematically compared by their characteristic times. ^{14}C repartition at the core scale as the fraction $X = S, A, NER$ or CO_2 is expressed as:

$$m_{tot}(X,t) = \sum_{i=1}^{n_{cubes}} m_{cube}(X,t,i) \quad (18)$$

3.1. Calibration

Calibration is performed sequentially according to the procedure defined in Section 2.2 and synthesized in Fig. 1. The experiment concerned by each calibration stage is recalled in brackets in the subsection title and refers to the name given in Fig. 1. The experimental data points and standard deviations are those obtained by Pinheiro et al. (2015).

3.1.1. 2,4-D chemical interaction with the soil matrix (Uniform 2,4-D – No degraders)

2,4-D reversibly sorbed fraction A reaches equilibrium with the solubilized fraction S in less than one day (Fig. 3a). The maximum concentration of A represents 2% of the added ^{14}C mass. This fast, limited reaction is expressed by the small partition coefficient k_{SA}/k_{AS}=0.02 (Table 1) associated with the characteristic desorption time (Section 2.2.1) $\tau_{desorption} = 1/k_{AS} = 0.2$day (Table 2). Retardation of 2,4-D transport would thus remain smaller than one day. Formation of irreversibly bound abiotic residues R_c is slower with a characteristic time evaluated at $\tau_c = 1/k_c = 77$ days (larger than the 14 days duration of the laboratory experiments). R_c eventually represents 13% of the added ^{14}C mass at day 14. Given the limited number of experimental data points, the linear assumption for reversible and irreversible abiotic attachment (Eqs. (1)–(3)) is plausible even though limitations in the number of attachment sites cannot be completely ruled out.

3.1.2. 2,4-D biodegradation (Uniform 2,4-D – uniform degraders)

2,4-D is consumed by degraders leading to an equal partition of the added ^{14}C mass between Non-Extractable Residues NER and CO_2 emissions at day 7 (Fig. 3b). From day 7 to day 14, NER are slowly mineralized. Their concentration drops from 53% to 47% of the added ^{14}C mass. Measured concentrations of reversibly attached 2,4-D A are larger than in the Uniform 2,4-D – No degraders experiment, especially at early times (15% versus 2% at day 1). This may be linked to the absence of sterilization process in this specific experiment impacting the sorption properties of the core. NER concentrations as well as CO_2 emissions are however well captured by the calibrated biological model.

Incorporation of the biological accommodation rate α defined in Eq. (8) is necessary to capture the mineralization lag time observed at the beginning of the experiments. After this first phase, biodegradation is the dominant control of 2,4-D fate, as indicated by the large mineralized fraction. The model also predicts a NER composition dominated by biogenic residues (69% living degraders B, 22% biotic bound residues R_b, 9% abiotic bound residues R_c at day 14 (Fig. 4a)). Most abiotic residues are formed at the beginning of the incubation during the biological lag time. Slow remobilization of NER and continued mineralization after day 7 (Fig. 3b) originate from decaying biomass releasing available substrate into the solution (Fig. 5, plain line).

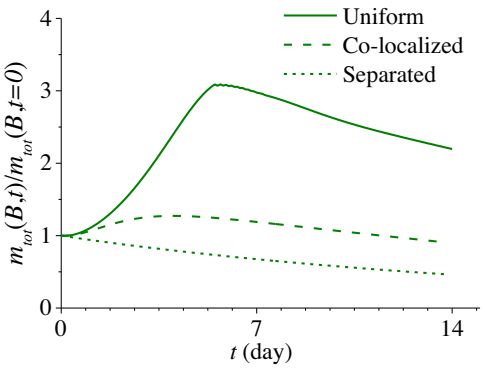

Fig. 5. Model predicted living degraders mass (B) in the soil core for the uniform 2,4-D, uniform degraders experiment (plain line, Section 3.1.2), the separated 2,4-D and degraders experiment (dotted line, Section 3.1.3) and the co-localized 2,4-D and degraders experiment (dashed line, Section 3.1.4).

Biotic and abiotic processes may be further compared in terms of characteristic times. After the microbial adaptation phase of around one day, degradation rates increase with the growth of degraders. As a consequence, degradation speeds up and its characteristic time τ_{bio} (Eq. (9)) decreases to 1.5 h at day 7. At this stage, the degradation is three orders of magnitude faster than the irreversible attachment (τ_c=77 days,

(Table 2). The 2,4-D remaining in the soil core is efficiently consumed by the degraders with comparatively negligible irreversible sorption. After day 5, most 2,4-D has been degraded and can no longer sustain the degrader growth. The degraders concentration peaks around 5 days and slowly decreases with a characteristic death time τ_{death} =17 days. In such conditions (i.e. without any transport mechanisms), most of the substrate is efficiently degraded before getting irreversibly sorbed.

3.1.3. 2,4-D diffusion (Separated 2,4-D and degraders)

2,4-D diffusion dilutes all species S, A and NER either directly for the labile S or indirectly for the immobile A and NER. At day 14, degradation, sorption and diffusion have reduced the maximum labile 2,4-D concentration to less than 2% of its initial value (Fig. 6). At core scale, the added ^{14}C mass remains mostly in solution (76% at day 14, Fig. 3c). The reversibly fixed mass A remains low (6%) because of the small partition coefficient k_{SA}/k_{AS}. The ^{14}C mass as Non-Extractible Residues (NER) is much larger (17%). As most 2,4-D is located outside of the degraders hotspot, mineralization is marginal with only 0.2% of the added ^{14}C mass converted into CO_2. We calibrate the effective 2,4-D diffusion coefficient using the previously obtained chemical and biological parameters. The calibrated model provides good estimates of ^{14}C repartition both at cube scale (Fig. 6) and at core scale (Fig. 3c). The underestimation of reversible and irreversible sorptions, which conversely turns into an overestimation of the remaining concentrations in solution, might come from the overall lower 2,4-D concentrations involved in this experiment, with only one amended soil cube, as compared to the Uniform 2,4-D – No degraders experiment, where all soil cubes are amended. The calibrated value of the effective 2,4-D

Table 2
Characteristic chemical, biological and diffusion times for 2,4-D pesticide. λ is the characteristic diffusion distance, equal to the initial separation distance between 2,4-D and degraders for the separated distribution, and to the characteristic scale of the degraders cube for the co-localized distribution.

	Characteristic time [d]	t = 1 day	t = 7 day	t = 14 day
	$\tau_{sorption} = 1/k_{SA}$	11		
	$\tau_{desorption} = 1/k_{AS}$	0.2		
	$\tau_c = 1/k_c$	77		
	$\tau_{death} = 1/m_t$	17		
Uniform 2,4-D Uniform degraders	$\tau_{bio} = \frac{yS(t)}{\mu B(t)}$	8.8	0.05	1
Separated 2,4-D and degraders	$\tau_{diff} = \lambda^2/d$	108		
λ = 2.6 cm	$\tau_{bio} = \frac{yS(t)}{\mu B(t)}$	7.0	3.7	5.2
Co-localized 2,4-D and degraders	$\tau_{diff} = \lambda^2/d$	6		
λ = 0.6 cm	$\tau_{bio} = \frac{yS(t)}{\mu B(t)}$	3.9	1.7	2.5

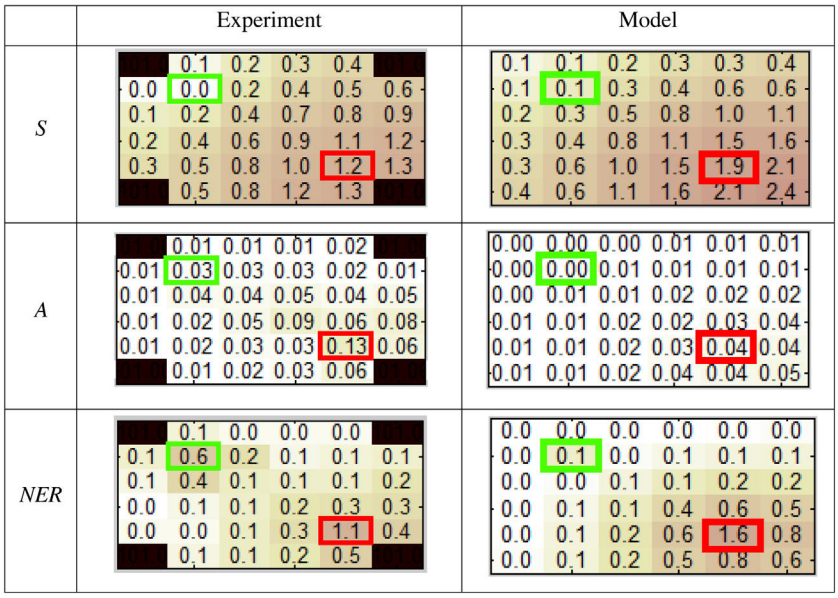

Fig. 6. For the separated 2,4-D and degraders experiment, ^{14}C repartition in the middle layer of the soil core at day 14 as labile 2,4-D (*S*), sorbed 2,4-D (*A*) and Non-Extractable Residues (*NER*). Values are given in percentage of the added ^{14}C mass. Degraders and 2,4-D initial locations are framed in green and red respectively. (For interpretation of the references to colour in this figure legend, the reader is referred to the web version of this article.)

diffusion coefficient d is 6.10^{-6} m^2/day. We validate the spatial discretization by a convergence analysis on the calibrated value of the diffusion coefficient. While the calibrated value of d evolves from 1×10^{-5} m^2/d on a $6 \times 6 \times 3$ grid to 0.6×10^{-5} m^2/s on the refined $12 \times 12 \times 6$ grid, it is only marginally different at 0.5×10^{-5} m^2/s on a $18 \times 18 \times 9$ grid.

To better understand the origin of the low degradation rate, we compare the characteristic diffusion and degradation times. With τ_{diff}=108 days and τ_{bio} ranging from 3.7 to 7 days (Table 2), degradation remains consistently transport-limited (Damköhler number $Da \geq 10$, Eq. (14)). We illustrate this point by quantifying the amount of substrate diffused to the degraders cube (hotspot) as a function of time with negligible chemical interactions ($k_{SA} = k_{AS} = k_c = 0$).This can be estimated by the First-Passage Time Distribution computed numerically by solving the diffusion equation with the initial and boundary conditions of the experiment (Havlin and Ben-Avraham, 1987). As shown in Appendix B, the potential delivery of substrate to the hotspot is slow and spreads over a wide range of time expressing the dilution of the substrate throughout the soil core. Within the 14 days duration of the experiment, the cumulated quantity of substrate that can diffuse to the hotspot is only 1%. The amount of 2,4-D effectively reaching the degraders cube (hotspot) is even smaller due to irreversible abiotic attachment. Even though attachment is slow, it occurs everywhere in the core and further limits the amount of 2,4-D available for degradation. Finally, degradation is reduced by the decrease of the biological activity. Not enough substrate reaches the hotspot to sustain the degraders population. The degraders population continuously decreases and drops to half of its initial value at day 14 (Fig. 5, dotted line).

3.1.4. Validation (Co-localized 2,4-D and degraders)

At day 14, 13% of the added ^{14}C mass have been mineralized (Fig. 3d). 52% remain in solution in the hotspot or immediately next to it (Fig. 7). 32% are in the Non-Extractible Residues (NER). This percentage is larger than in the separated 2,4-D and degraders experiment due to enhanced formation of biogenic residues. Mineralization and formation of half of the overall NER occur directly in the degrader hotspot. We recall that the results of the model are not obtained through calibration but by blind prediction. Mineralization rates are well evaluated, demonstrating the relevance of the biological model (Eqs. (4)–(8)). The slight underestimation of reversible and irreversible sorptions is similar to the one observed in the Separated 2,4-D and degraders experiment (Section 3.1.3).

The model predicts a drop of 2,4-D concentration in the hotspot to 27% of the added ^{14}C at day 1, 9% at day 2 and 4% at day 3 (results not shown). This sharp drop comes from biodegradation and from

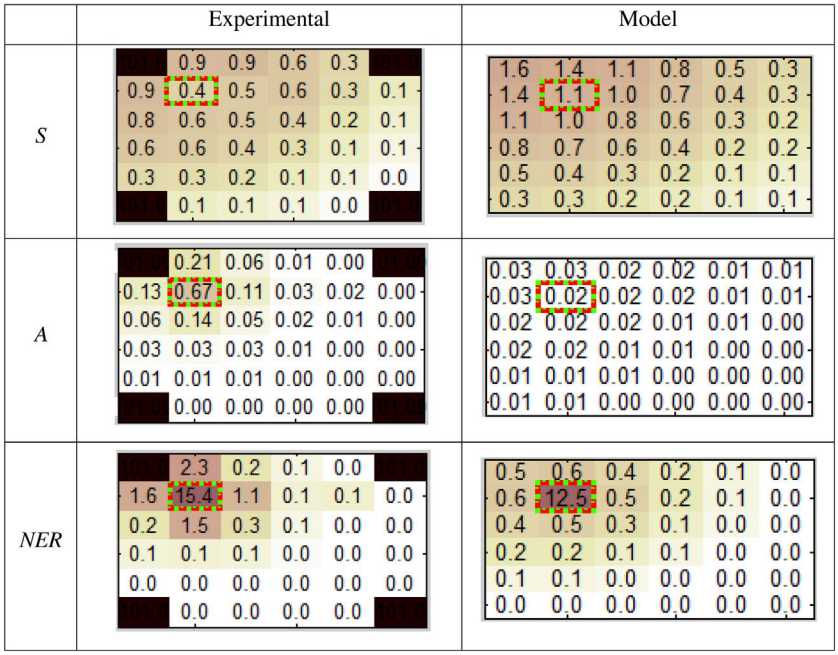

Fig. 7. For the co-localized 2,4-D and degraders experiment, ^{14}C repartition in the middle layer of the soil core at day 14 as labile 2,4-D (*S*), sorbed 2,4-D (*A*) and Non-Extractable Residues (*NER*). Values are given in percentage of the added ^{14}C mass. Degraders and 2,4-D initial location is framed in green and red. (For interpretation of the references to colour in this figure legend, the reader is referred to the web version of this article.)

diffusion out of the hotspot. The similar characteristic diffusion and degradation times show that both processes are important (τ_{diff} = 6.0 d, τ_{bio}=3.9 d at day 1 (Table 2)).

After day 3, 2,4-D concentration in the hotspot becomes smaller than the concentrations in the surrounding cubes, resulting in an inversion of substrate gradients, in a backward diffusive flux towards the hotspot, and in a sustained rate of 2,4-D mineralization (Fig. 3d). As in the previous experiment where degraders and 2,4-D are separated, substrate dilution by diffusion promotes irreversible abiotic bounding. Abiotic NER eventually represent half of the total NER at day 14 (Fig. 4b).

As an intermediary conclusion, the biochemical transport model of Eqs. (4)–(12) has been successfully calibrated on the experiments by Pinheiro et al. (2015), as shown by its good performances against the three experiments used for calibration and the fourth experiment used as an independent validation.

3.2. Exploratory simulations

We use the model successfully calibrated in Section 3.1 to further investigate the biological, chemical and physical constrains on 2,4-D degradation. Simulations performed under various water potentials and initial separation distances between 2,4-D and degraders show the role of the diffusion-induced dilution. The relative influence of the chemical and biological processes is then illustrated by minimizing the efficiency of sorption and maximizing the efficiency of degradation for the same simulation conditions. Finally, we investigate the influence of the initial concentration of 2,4-D on its biodegradation.

3.2.1. Influence of soil core water potential and initial distance between 2,4-D and degraders

We use Eq. (17) and the calibrated value of $d = 6 \times 10^{-6}$ m^2/d at a water potential of −31.6 kPa to estimate the diffusion coefficients associated with a large range of soil core water potential. Estimated values of d then vary from 3×10^{-6} m^2/d at −1585 kPa (wilting point) to 9×10^{-6} m^2/d at −1 kPa (near saturation).

Fig. 8a synthesizes the simulation results as cumulated ^{14}C mineralization at day 14. Mineralization is first controlled by the initial separation distance between degraders and substrate. It is maximal when degraders and substrate are initially co-localized (black columns of Fig. 8a). At an initial distance of 2.6 cm, it is reduced by a factor of 55 near saturation (−1 kPa) and by 1100 at the wilting point (−1585 kPa). These results show two well-differentiated regimes. When degraders and substrate are initially co-localized, degradation can be quite effective as shown by the high mineralization. When degraders and substrate are initially separated, degradation sharply drops and becomes negligible (less than a few percent) at least for the first 14 days of the simulation.

Sensitivity of mineralization to water potential is comparatively smaller and is limited to a factor of 2 to 10. It is however quite different depending on the initial distance between substrate and degraders. When degraders and substrate are initially co-localized, degradation is higher in dry conditions when slower diffusion keeps substrate for a longer time at the hotspot (larger Damköhler values). When degraders and substrate are initially separated, it is the opposite. The little degradation is higher in wet conditions, when faster diffusion promotes the delivery of substrate to the degraders. This shows the two opposite effects of water potential on degradation. Both effects balance for an initial separation distance l of 0.9 cm (grey columns of Fig. 8a). At lower water contents, the negative effect of the larger transit time of the substrate to the hotspot is compensated by the positive effect of the larger residence time in the hotspot. These antagonistic effects of water potential on degradation are consistent with those observed by Vogel et al. (2015) in their simulations of dissolved organic carbon (DOC) biodegradation at the pore scale. The authors noted that an increased delay in DOC transport by diffusion, coming from a lower water content or a higher pore tortuosity, results either in limiting or stimulating degraders activity depending on the initial distance between DOC and degraders.

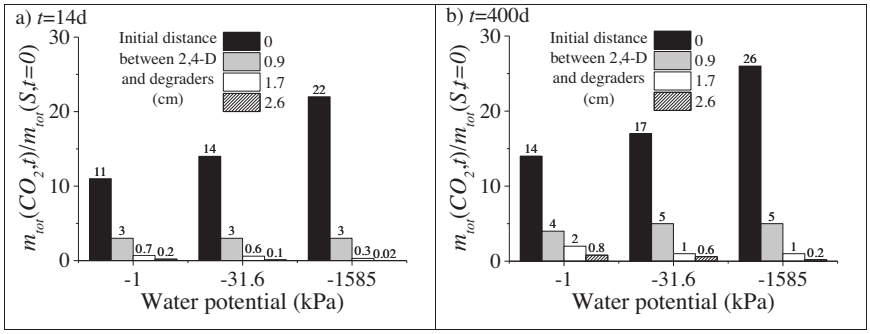

Fig. 8. Predicted cumulated mineralization at a) $t = 14$ days and b) $t = 400$ days, as a function of soil core water potential and of the initial separation distance between the 2,4-D and degraders. Mineralization values are given in% of added ^{14}C. −1 kPa corresponds to near saturation, −31.6 kPa to field capacity and −1585 kPa to the wilting point.

3.2.2. Relative effects of chemical interactions and biological degradation

In the two-weeks duration of the experiments by Pinheiro et al. (2015), the previous section has shown that degradation is mainly transport-limited when 2,4-D and degraders are heterogeneously distributed. More than half of the added 2,4-D remains in the soil solution after 14 days of incubation (Fig. 3c and d). We use our calibrated model to investigate the long term fate of the 2,4-D addition in the soil cores.

Incubation is simulated on a period of 400 days. We systematically check that no 2,4-D remains in solution at this date. Results are synthesized as cumulated ^{14}C mineralization in Fig. 8b. The model predicts that mineralization only marginally increases between day 14 (Fig. 8a) and day 400 (Fig. 8b). The maximum increase from 22% to 26% is obtained in the driest conditions when degraders and substrate are initially co-localized. When degraders and substrate are initially separated, or when the water content is higher, this increase is even more limited. In other words, most degradation occurs within the first 14 days following the beginning of incubation. The large pool of available substrate remaining in the soil cores at day 14 indicates that degradation then becomes limited by chemical and biological processes, i.e. irreversible abiotic bonding and decrease of biological activity due to degraders decay.

We analyze the respective contributions of these different dynamics by maximizing biological activity and minimizing chemical interactions (Section 2.5). Biological activity is maximized by considering instantaneous mineralization of the 2,4-D diffusing into the degraders cube. Chemical interactions are minimized by setting $k_{SA} = k_{AS} = k_c = 0$.We consider the case where degraders and 2,4-D are initially separated by 2.6 cm and the water potential is equal to −31.6 kPa (conditions of the Separated 2,4-D and degraders experiment by Pinheiro et al. (2015)). Results are presented as cumulated ^{14}C mineralization over time on Fig. 9. Core-scale mineralization reaches its maximal potential value of 70% around day 1000 (Fig. 9, dash-dotted line). In this case, degradation is solely transport-limited and the slow mineralization comes from the broad First Passage Time Distribution (FPTD) associated with diffusion (Appendix B). In fact, degradation is exactly equal to the product of the cumulated FPTD by the maximal mineralization capacity (Appendix C).

When biological activity is kept maximal but the sorption limitations are introduced, total mineralization drops from 70% to 17% (Fig. 9, dotted line). Although being much slower than biodegradation, irreversible attachment occurs everywhere in the column and benefits from 2,4-D diffusion-induced dilution. The maximal mineralization value is reached around 300 days due to the characteristic time of irreversible attachment $\tau_c = 77$ days (Table 2).

Finally, when biological limitations are introduced, total mineralization sharply drops to 1% and 0.6% respectively without and with chemical interactions (Fig. 9, dashed and plain lines). Maximal degradation is reached after only 130 days because of degraders decay. Following 2,4-D dilution and chemical trapping, the amount of substrate reaching the hotspot is not sufficient to maintain the initial degraders population. With a characteristic decay time $\tau_{death} = 17$ days (Table 2), degraders population at day 130 only represent 0.1% of its initial value.

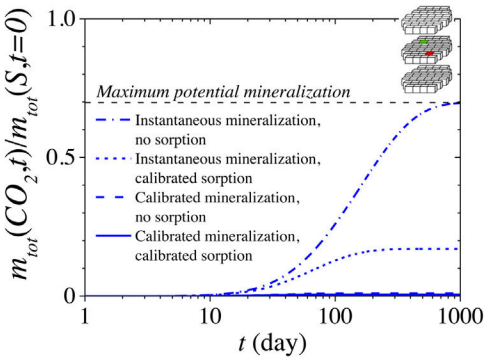

Fig. 9. Predicted cumulated ^{14}C mineralization for the separated 2,4-D and degraders experiment (Section 3.1.3) for different biochemical models (Section 3.2.2). Calibrated mineralization refers to the calibrated biological model. Instantaneous mineralization refers to the maximized biodegradation model where all 2,4-D reaching the microbial hotspot is immediately converted into CO_2 and biotic residues R_b. Sorption refers to reversible and irreversible 2,4-D chemical attachment to the soil matrix.

These results show the importance of transport processes during the early times of incubation. When substrate and degraders are initially co-localized, degradation is substantial until substrate diffuses out of the hotspot. When separated, degradation is strongly limited by dilution, microbial decay and abiotic trapping.

3.2.3. Impact of initial 2,4-D concentrations

We determine the sensitivity of the degradation of 2,4-D to its initial concentration in the previously calibrated model, in the configuration where 2,4-D is introduced in the microbial hotspot. We consider four different initial 2,4-D concentrations and a fixed initial concentration of degraders. In a first phase (first three days of incubation), degradation rates are high whatever the initial 2,4-D concentration (Fig. 10a). Most pesticides are located in the hotspot and are available for degradation. Degradation is more effective when there are relatively more degraders than pesticides. In other words, the relative degradation, defined as the degraded quantity of pesticide over its initial quantity, increases for lower pesticide concentration. Even though pesticide degradation is high in all cases, degraders display evolving behaviors. Either degraders first multiply as long as pesticides are concentrated enough (Fig. 10b, dashed line), or degraders population directly decays when pesticides are

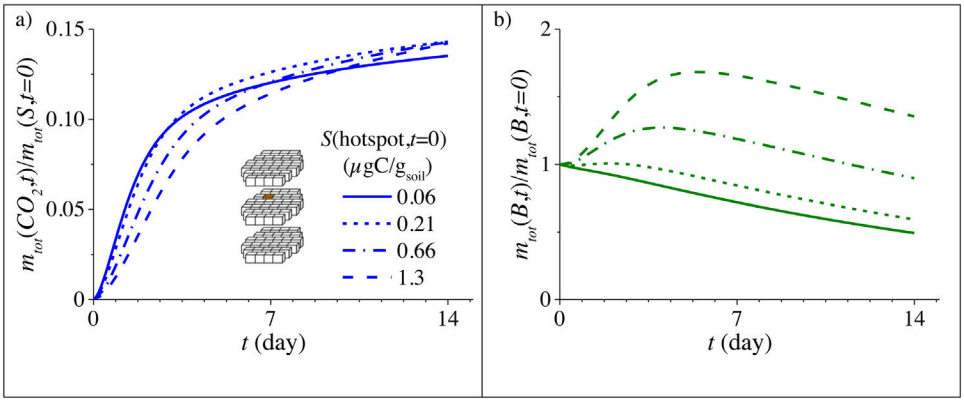

Fig. 10. a) Simulated cumulated ^{14}C mineralization and b) simulated living degrader mass for the co-localized 2,4-D and degraders configuration and four different initial concentrations of 2,4-D in the hotspot. S(hotspot,t = 0) = 0.66 μgC g$_{soil}^{-1}$ corresponds to the experimental conditions of Pinheiro et al. (2015).

not abundant enough to sustain microorganisms (Fig. 10b, plain line).

In a second phase (approximately after day 3), mineralization becomes limited by the smaller quantity of substrate remaining in the hotspot. Degradation globally slows down and the degrader concentration decreases. While low initial concentrations of 2,4-D have promoted in the first phase high relative degradation because the ratio of degraders to substrate was in favor of substrate, it becomes the opposite in the second phase. Degraders have continuously decreased and are relatively few to degrade the remaining pesticides. However, at high initial concentrations of 2,4-D, degraders have multiplied in the first phase and are comparatively more abundant to degrade the remaining pesticides in the second phase.

Eventually, these two opposite effects almost completely compensate and relative mineralization reaches very similar levels whatever the initial 2,4-D concentration at day 14 (between 13% and 14% added ^{14}C, Fig. 10a) and at day 400 (minimum 15% for the lowest concentration of 0.06 μgC g$_{soil}^{-1}$, maximum 18% for the highest concentration of 1.3 μgC g$_{soil}^{-1}$). Similar results have been obtained by Vieublé Gonod (2002), who observed less relative mineralization at higher initial pesticide concentration in the first few days of the experiment. Also the relative 2,4-D mineralization after 15 days was not sensitive to the initial pesticide concentration as earlier observed by Ou et al. (1978) and Parker and Doxtader (1983).

4. Discussion

We first compare our calibration results for the different parameters with previous published values. Then we discuss the relevance of the concentration levels and distributions for 2,4-D and degraders considered in this study from a field perspective. We further propose plausible scenarios of efficient degradation despite diffusion-limited transport, concentration dilution and abiotic trapping. The first scenario is based on a more homogeneous distribution of degraders, the second on microbial mobility, and the third on a fast, intermittent transport process (e.g. convection) delivering the substrate directly to the degraders hotspot.

4.1. Comparison between estimated and previously published parameter values

Parameter values resulting from calibration (Table 1) are close to previously published results. While most models use instantaneous equilibrium for reversible sorption, some authors like Shareef and Shaw (2008) have integrated slow and fast adsorption/desorption kinetics. Our calibrated values of adsorption rate $k_{SA} = 0.09$ d^{-1} and desorption rate $k_{AS} = 4.4$d^{-1} fall within the ranges of [0.02–48] d^{-1} and [5.10^{-5}–130] d^{-1} obtained for 2,4 D in different soils by Shareef and Shaw (2008). The calibrated formation rate of irreversibly bound abiotic residues $k_c = 0.01$ d^{-1} is within the range of [9.10^{-4}–0.58] d^{-1} found by Matthies et al. (2008).

The estimated value of the maximum growth rate μ_{max} (0.6 d^{-1}) is similar to the one found by Geng et al. (2015) for microorganisms that degrade PAH (0.5 d^{-1}) but is smaller than the one found by Kästner et al. (2013) for microorganisms that degrade 2,4-D (2.6 d^{-1}). Except for μ_{max}, our results ($m_t = 0.06$ d^{-1}, $\kappa_S = 0.37$ μgC g$_{soil}^{-1}$, $y = 0.52$) are close to those reported by Kästner et al. (2013) ($m_t = 0.07$ d^{-1}, $\kappa_S = 0.42$ μgC g$_{soil}^{-1}$, $y = 0.5$). The calibrated ratio $\mu_{max}/\kappa_S = 1.7$ g$_{soil}$ d^{-1} μgC^{-1} is smaller than the ones obtained by Tuxen et al. (2002) for 2,4-D degraders ([4.5–100] g$_{soil}$ d^{-1} μgC^{-1}). The calibrated recycling coefficient $\chi = 0.6$ is equal to the one found by Miltner et al. (2012) and is also within the range of values obtained by Monga et al. (2014) [0.2-0.8] for different species of microorganisms. Our calibrated mortality rate $m_t = 0.06$d^{-1} is however lower than the ones reported by Monga et al. (2014) [0.2–1.5 d^{-1}].

Finally, our calibrated diffusion coefficient $d = 6.0 \times 10^{-6}$ m^2 d^{-1} is one order of magnitude smaller than the diffusion coefficient of 2,4-D in water (6.9×10^{-5} m^2 d^{-1} (Saxena et al., 1974b)) and falls just below the range obtained by Saxena et al. (1974a) for 2,4-D in saturated porous media [6.3×10^{-6}–1.4×10^{-5} m^2 d^{-1}]. It is also similar to the ones obtained by Villaverde et al. (2009) at −8 kPa for azoxystrobin, chlorotoluron and atrazine (respectively 4.3×10^{-6}, 8.6×10^{-6} and 1.3×10^{-5} m^2 d^{-1}) and by Dechesne et al. (2010) at −8 kPa for benzoate (3.58×10^{-6} m^2 d^{-1}).

4.2. Influence of initial 2,4-D and degraders concentrations

The initial 2,4-D concentration of 0.66 μgC g$_{soil}^{-1}$ used in the homogeneous experiments of Pinheiro et al. (2015) (Fig. 1a–b) corresponds to 7.4 kg$_{2,4-D}$.ha^{-1}. For the heterogeneous experiments, only one soil cube is amended with an initial 2,4-D concentration of 0.66 μgC g$_{soil}^{-1}$ (Fig. 1c–d). The corresponding 2,4-D concentration at the soil core scale (i.e. the added mass of 2,4-D divided by the volume of the soil core) is 0.06 kg$_{2,4-D}$.ha^{-1}. These 2,4-D concentrations are realistic since agronomic doses range between 0.3 and 2.3 kg$_{2,4-D}$.ha^{-1} of 2,4-D (Willems et al., 1996). Furthermore, when applied to soils, pesticides are not homogeneously spread because of their formulation, their mode of delivery and agricultural practices. For example, Walker and Brown (1983) showed that pesticide application by conventional farm sprayers is very variable in initial deposition with recovery of simazine between 6 times below and 3 times above the theoretical added agronomic dose and coefficients

of variation just after application that can reach 60%. Müller et al. (2003) also observed a small scale variability of atrazine concentrations in an allophanic soil just after addition (coefficient of variation of 35%). Thus, spots with smaller or higher 2,4-D concentrations are present in soil.

Initial quantities of degrading microorganisms are also realistic since we chose to work with soil indigenous microorganisms rather than inoculated microorganisms to consider the complexity of the soil community and potential cooperation between species (microbial consortium) necessary in certain cases to ensure complete degradation of pesticides. Pesticide degraders generally represent only a few percents of the total soil microflora (Fournier et al., 1981; Monard et al., 2012) and are generally heterogeneously distributed in soils, leaving soil volumes without degradation potential (Gonod et al., 2003). In soils that have never been treated with 2,4-D, the number of degraders is initially low and ranges between 10^3 and 1.7 10^3 CFU (colony forming unit) g^{-1} soil (Fournier, 1980; Holben et al., 1992; Loos et al., 1979; Shaw and Burns, 1998; Xia et al., 1995). Initial degrading microorganisms may be more abundant in soils regularly treated with pesticides (Fournier et al., 1981). Using direct DNA extraction from soil and PCR amplification, Gonod et al. (2006) and Pinheiro et al. (2015) found 10^5 and 4.65 10^5 *tfdA* genes g^{-1} soil respectively in the same soil used in this work just after sampling. After 2,4-D addition, degrading microorganisms increased and reached a maximum of 1.25 to 2.87 10^6 *tfdA* genes g^{-1} soil. Maximum degrading microbial biomass may represent a few percent of the added carbon *via* 2,4-D, 4.2% (Ou, 1984) to 12% (Gonod et al., 2006; Soulas et al., 1984). Initial quantities of degraders also impact the duration of the lag phase (Estrella et al., 1993). We did not test the impact of degraders quantity because, in our model, 2,4-D biodegradation is directly proportional to the degrading biomass.

4.3. Plausible degradation scenarios

Difference of degradation rates in the experiments of Pinheiro et al. (2015) come from the ambiguous role of diffusion as a transport mechanism. On one hand, diffusion provides residence times large enough for degradation to be substantial when substrate and degraders are at the same place. On the other hand, diffusion-induced dilution results in low probabilities of contact between substrate and degraders. Additional physical or biological processes could enhance degradation by increasing this probability of contact. We propose three plausible scenarios where degradation can remain substantial despite diffusion-induced dilution.

The simplest scenario consists in a more homogeneous repartition of degraders in the soil volume to increase the probability of contact between substrate and degraders. For instance, Dechesne et al. (2010) have shown that under diffusion-controlled transfer of substrate, degradation is more important when degraders are distributed between a large number of hotspots than when grouped into a single hotspot. However, additional environmental constraints may invalidate this scenario, for instance microbial interspecies relations like syntrophy (Kim et al., 2008), predation (Balagaddé et al., 2008) or mutual exclusion (Kerr et al., 2002) where a spatial structure of the microbial consortia would emerge (Wang and Or, 2014).

In the second scenario, degraders and substrate are heterogeneously distributed and initially separated but both mobile. Limitation of degradation because of substrate dilution could be counterbalanced by degraders mobility increasing access of microbes to the substrate. While 2,4-D degraders mobility was not observed in the experiments of Pinheiro et al. (2015), it has been found in other studies (e.g. Pallud et al., 2004) in association with higher water content and/or development of microbial hotspots with higher 2,4-D concentrations.

Finally, degraders and substrate can be heterogeneously distributed but initially located at the same place. This raises the question of how substrates are delivered to the degraders hotspot in the first place. Convection by infiltrating water could be such a delivery mechanism. Convection is fast enough to enable localized delivery of high concentrations. However, fast convection would also flush the substrates past the degraders hotspot, reducing the contact time and thus the degradation. Increased contact time may then come from degraders being flushed together with substrates by convection, or alternatively by intermittent convection allowing substrates to remain at the hotspot long enough for degradation to take place. Other intermittent, localizing mechanisms could also be considered, as for instance soil tillage or bioturbation incorporating pesticide at a soil depth where less specific microorganisms are present (Vieublé-Gonod et al., 2009). Intermittency might not only constrain degradation physically but also biologically. Regular substrate delivery would contribute to maintain the degraders population and the degradation function (Estrella et al., 1993).

5. Conclusions

We investigate the temporal constraints on 2,4-D pesticide biodegradation in soils as influenced by spatially distributed microorganisms. An integrated reactive transport model is calibrated and validated on a set of laboratory experiments performed by Pinheiro et al. (2015). In these experiments, the fate of a 2,4-D addition in reconstructed soil columns is monitored for various initial distributions of 2,4-D and soil degraders. We use the complementarity of these experiments to unambiguously identify the chemical, biological and physical components of the model. Calibration consistency is supported by the good results of the model on the experiments of Pinheiro et al. (2015), as well as by the agreement between the fitted parameters for the different model components and previously published values.

Reversible 2,4-D sorption is the fastest process with a characteristic time of a few hours, but sorbed concentrations remain limited to a few percents of aqueous 2,4-D concentrations. Degradation is slower with characteristic times ranging from a few hours to a few days during the two-weeks duration of the experiments. Degradation also requires about one day to react to substrate availability. Irreversible abiotic attachment is much slower with a characteristic timescale of some months. As a consequence, degradation outcompetes abiotic entrapment when 2,4-D and degraders are in contact. 2,4-D is efficiently degraded for uniform spatial distributions of pesticide and degraders. However, degradation rates become more variable for heterogeneous repartitions. When 2,4-D and degraders are initially co-localized, most degradation occurs within the characteristic diffusion time of three days after which 2,4-D has diffused away from the hotspot. When 2,4-D and degraders are initially separated, degradation is limited by the small amount of pesticide reaching the degraders hotspot. For a separation distance of 3 cm, the characteristic diffusion time is around two months, corresponding to only 3% of the added pesticide mass potentially reaching the hotspot within the 14 days duration of the experiment.

A simple sensitivity analysis shows that the initial separation distance between pesticides and degraders is the major control of degradation. Mineralization decreases by up to a factor of 200 when this distance increases from 0 to 3 cm. Influence of water content on mineralization is comparatively smaller (up to factor of 4) and qualitatively depends on the initial distance between substrate and degraders. For initially separated degraders and substrate, degradation remains limited in all cases, but is relatively less limited when faster diffusion promotes the delivery of substrate to the degraders. However, when degraders and substrate are initially co-localized, degradation is always substantial. It is even somewhat higher in dry

conditions when smaller diffusion keeps substrate for a longer time at the hotspot. The influence of the initial pesticide concentration is comparatively marginal. While the development of degraders and the rate of degradation may follow different paths, the proportion of pesticide degraded is very similar after 14 days (between 15 and 18% added ^{14}C). Initially lower degradation rates at high concentration of pesticide are compensated after a few days by the fast development of the degraders population.

Simulations further confirms the importance of substrate diffusive transport limitations by showing that most degradation occurs within the first two weeks of incubation. After this period of time, degradation becomes limited by microbial decay and 2,4-D abiotic trapping. Any process enhancing dilution in the full soil core volume would further limit degradation.

Because degradation only occurs when pesticides and degraders are initially co-localized, we propose that heterogeneous spatial repartitions of microorganisms could be coupled to fast, intermittent transport processes like convection, soil tillage or bioturbation. These processes should be fast enough to overcome diffusion-induced dilution, and intermittent for pesticide to remain at the same place long enough for degradation to take place. Microbial mobility might also promote degradation by increasing the probability of contact between pesticides and degraders.

Acknowledgements

The ANR is acknowledged for its funding through its projects Soilμ-3D under the no. ANR-15-CE01-0006 for providing the agro-ecological and laboratory framework and H2MNO4 under the no. ANR-12-MONU-0012-01 for the confrontation to reactive-transport modeling.

Appendix A. Soil core cutting procedure

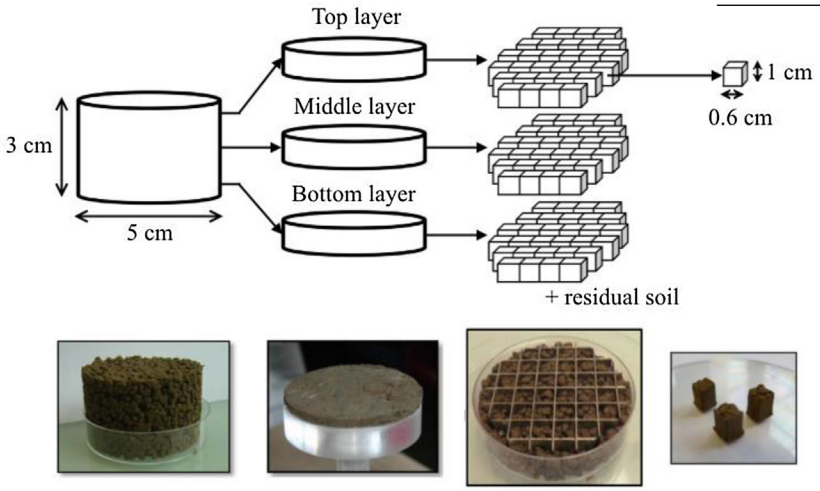

Soil core cutting procedure for the heterogeneous distributions of microorganisms and 2,4-D experiments (Adapted from Pinheiro et al. (2015)). Cutting issues 32 soil cubes for each of the layers.

Appendix B. First-passage time of 2,4-D at the degraders cube for the separated experiment

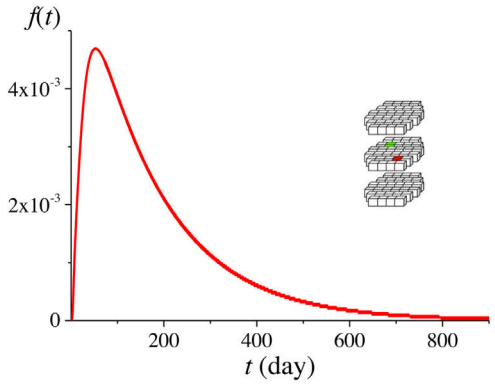

Probability density function of first passage time at the degraders hotspot of 2,4-D initially separated from the degraders by 2.6 cm (Section 3.1.3).

Appendix C. Maximal mineralization

Mineralization is not equal to substrate uptake by degraders due to formation of living biomass. Furthermore, part of the substrate is stored within the cells and released in solution upon their death, making it available again for mineralization. These two processes must be taken into account to evaluate the maximal mineralization of a given amount of substrate reaching the degraders. We consider that this mineralization is instantaneous, such that substrate cannot diffuse out of the hotspot or get sorbed. The maximal mineralization of an amount $S(t)$ of 2,4-D reaching the microbial hotspot thus writes:

$$CO_2(t) = (1-y)S(t) + (1-y)\chi y S(t) + (1-y)\chi^2 y^2 S(t) + \ldots \quad (19)$$

with y the yield coefficient ($0 < y < 1$) and χ the partition coefficient between recycled and non-recycled dead biomass ($0 < \chi < 1$) (Eqs. (4)–(7)). The first term corresponds to the microbial uptake of $S(t)$. The second term corresponds to the microbial uptake of the amount of substrate $\chi y S(t)$ stored within the cells during the first step and released upon their death, and so on. The maximum mineralization thus corresponds to the sum of a converging geometric sequence and is given by:

$$CO_2(t) = \frac{1-y}{1-\chi y} S(t) \quad (20)$$

Using the calibrated values $y = 0.52$ and $\chi = 0.60$ (Table 1), the maximum mineralization is equal to 70% of the amount of substrate reaching the microbial hotspot. Note that for negligible chemical interactions of 2,4-D with soil ($k_{SA} = k_{AS} = k_c = 0$), the amount of substrate reaching the degraders cube is given by the First Passage Time Distribution (FPTD, Section 3.1.3). In this case, the maximum cumulated mineralization corresponds to 70% of the cumulated FPTD.

References

Balagaddé, F.K., Song, H., Ozaki, J., Collins, C.H., Barnet, M., Arnold, F.H., Quake, S.R., You, L., 2008. A synthetic Escherichia coli predator–prey ecosystem. Mol. Syst. Biol. 4, 1.

Barriuso, E., Koskinen, W.C., Sadowsky, M.J., 2004. Solvent extraction characterization of bioavailability of atrazine residues in soils. J. Agric. Food Chem. 52 (21), 6552–6556.

Barriuso, E., Benoit, P., Dubus, I.G., 2008. Formation of pesticide nonextractable (Bound) residues in soil: magnitude, controlling factors and reversibility. Environ. Sci. Technol. 42 (6), 1845–1854.

Boucher, D.F., Alves, G.E., 1959. Dimensionless numbers. Chem. Eng. Prog. 55, 55–64.

Chenu, C., Hassink, J., Bloem, J., 2001. Short-term changes in the spatial distribution of microorganisms in soil aggregates as affected by glucose addition. Biol. Fert. Soils 34 (5), 349–356.

Dechesne, A., Owsianiak, M., Bazire, A., Grundmann, G.L., Binning, P.J., Smets, B.F., 2010. Biodegradation in a partially saturated sand matrix: compounding effects of water content, bacterial spatial distribution, and motility. Environ. Sci. Technol. 44 (7), 2386–2392.

Estrella, M.R., Brusseau, M.L., Maier, R.S., Pepper, I.L., Wierenga, P.J., Miller, R.M., 1993. Biodegradation, sorption, and transport of 2, 4-dichlorophenoxyacetic acid in saturated and unsaturated soils. Appl. Environ. Microbiol. 59 (12), 4266–4273.

Filipović, V., Coquet, Y., Pot, V., Houot, S., Benoit, P., 2014. Modeling the effect of soil structure on water flow and isoproturon dynamics in an agricultural field receiving repeated urban waste compost application. Sci. Total Environ. 499, 546–559.

Fournier, J., Codaccioni, P., Soulas, G., 1981. Soil adaptation to 2, 4-D degradation in relation to the application rates and the metabolic behaviour of the degrading microflora. Chemosphere 10 (8), 977–984.

Fournier, J., 1980. Enumeration of the soil micro-organisms able to degrade 2, 4-D by metabolism or co-metabolism. Chemosphere 9 (3), 169–174.

Geng, C., Haudin, C.-S., Zhang, Y., Lashermes, G., Houot, S., Garnier, P., 2015. Modeling the release of organic contaminants during compost decomposition in soil. Chemosphere 119, 423–431.

Gevao, B., Semple, K.T., Jones, K.C., 2000. Bound pesticide residues in soils: a review. Environ. Pollut. 108 (1), 3–14.

Gonod, L.V., Chenu, C., Soulas, G., 2003. Spatial variability of 2,4-dichlorophenoxyacetic acid (2,4-D) mineralisation potential at a millimetre scale in soil. Soil Biol. Biochem. 35 (3), 373–382.

Gonod, L.V., Martin-Laurent, F., Chenu, C., 2006. 2,4-D impact on bacterial communities, and the activity and genetic potential of 2,4-D degrading communities in soil. FEMS Microbiol. Ecol. 58 (3), 529–537.

Grathwohl, P., 1998. Diffusion in Natural Porous Media, 1. Springer, US (207 pp).

Greer, L.E., Shelton, D.R., 1992. Effect of inoculant strain and organic matter content on kinetics of 2,4-dichlorophenoxyacetic acid degradation in soil. Appl. Environ. Microbiol. 58 (5), 1459–1465.

Havlin, S., Ben-Avraham, D., 1987. Diffusion in disordered media. Adv. Phys. 36 (6), 695–798.

Holben, W.E., Schroeter, B.M., Calabrese, V.G., Olsen, R.H., Kukor, J.K., Biederbeck, V.O., Smith, A.E., Tiedje, J.M., 1992. Gene probe analysis of soil microbial populations selected by amendment with 2,4-dichlorophenoxyacetic acid. Appl. Environ. Microbiol. 58 (12), 3941–3948.

Iserles, A., 2008. A First Course in the Numerical Analysis of Differential Equations Cambridge Texts in Applied Mathematics. Cambridge University Press (480 pp).

Juwarkar, A., Singh, S., Mudhoo, A., 2010. A comprehensive overview of elements in bioremediation. Rev. Environ. Sci. Bio/Technol. 9 (3), 215–288.

Kästner, M., Nowak, K.M., Miltner, A., Trapp, S., Schäffer, A., 2013. Classification and modelling of nonextractable residue (NER) formation of xenobiotics in soil—a synthesis. Crit. Rev. Environ. Sci. Technol. 44 (19), 2107–2171.

Kerr, B., Riley, M.A., Feldman, M.W., Bohannan, B.J.M., 2002. Local dispersal promotes biodiversity in a real-life game of rock-paper-scissors. Nature 418 (6894), 171–174.

Kim, H.J., Boedicker, J.Q., Choi, J.W., Ismagilov, R.F., 2008. Defined spatial structure stabilizes a synthetic multispecies bacterial community. Proc. Natl. Acad. Sci. 105 (47), 18188–18193.

Loos, M.A., Schlosser, I.F., Mapham, W.R., 1979. Phenoxy herbicide degradation in soils: quantitative studies of 2,4-D- and MCPA-degrading microbial populations. Soil Biol. Biochem. 11 (4), 377–385.

Müller, K., Smith, R.E., James, T.K., Holland, P.T., Rahman, A., 2003. Spatial variability of atrazine dissipation in an allophanic soil. Pest Manage. Sci. 59 (8), 893–903.

Manzoni, S., Porporato, A., 2007. A theoretical analysis of nonlinearities and feedbacks in soil carbon and nitrogen cycles. Soil Biol. Biochem. 39 (7), 1542–1556.

Matthies, M., Witt, J., Klasmeier, J., 2008. Determination of soil biodegradation half-lives from simulation testing under aerobic laboratory conditions: a kinetic model approach. Environ. Pollut. 156 (1), 99–105.

Miltner, A., Bombach, P., Schmidt-Brücken, B., Kästner, M., 2012. SOM genesis: microbial biomass as a significant source. Biogeochemistry 111 (1-3), 41–55.

Monard, C., Mchergui, C., Nunan, N., Martin-Laurent, F., Vieublé Gonod, L., 2012. Impact of soil matric potential on the fine-scale spatial distribution and activity of specific microbial degrader communities. FEMS Microbiol. Ecol. 81 (3), 673–683.

Monga, O., Garnier, P., Pot, V., Coucheney, E., Nunan, N., Otten, W., Chenu, C., 2014. Simulating microbial degradation of organic matter in a simple porous system using the 3-D diffusion-based model MOSAIC. Biogeosciences 11 (8).

Murphy, E.M., Ginn, T.R., 2000. Modeling microbial processes in porous media. Hydrogeol. J. 8, 142–158.

Murphy, E.M., Ginn, T.R., Chilakapati, A., Resch, C.T., Phillips, J.L., Wietsma, T.W., Spadoni, C.M., 1997. The influence of physical heterogeneity on microbial degradation and distribution in porous media. Water Resour. Res. 33 (5), 1087–1103.

Ogram, A.V., Jessup, R.E., Ou, L.T., Rao, P.S., 1985. Effects of sorption on biological degradation rates of (2,4-dichlorophenoxy) acetic acid in soils. Appl. Environ. Microbiol. 49 (3), 582–587.

Or, D., Smets, B.F., Wraith, J.M., Dechesne, A., Friedman, S.P., 2007. Physical constraints affecting bacterial habitats and activity in unsaturated porous media–a review. Adv. Water Resour. 30 (6–7), 1505–1527.

Ou, L.-T., Davidson, J.M., Rothwell, D.F., 1978. Response of soil microflora to high 2, 4-D applications. Soil Biol. Biochem. 10 (5), 443–445.

Ou, L.-T., 1984. 2,4-D degradation and 2,4-D degrading microorganisls in soils. Soil Sci. 137 (2), 100–107.

Pallud, C., Dechesne, A., Gaudet, J.P., Debouzie, D., Grundmann, G.L., 2004. Modification of spatial distribution of 2,4-dichlorophenoxyacetic acid degrader microhabitats during growth in soil columns. Appl. Environ. Microbiol. 70 (5), 2709–2716.

Parker, L.W., Doxtader, K.G., 1983. Kinetics of the microbial degradation of 2,4-D in soil: effects of temperature and moisture1. J. Environ. Qual. 12 (4), 553–558.

Patarinska, T., Dochain, D., Agathos, S.N., Ganovski, L., 2000. Modelling of continuous microbial cultivation taking into account the memory effects. Bioprocess. Eng. 22 (6), 517–527.

Pinheiro, M., Garnier, P., Beguet, J., Martin Laurent, F., Vieublé Gonod, L., 2015. The millimetre-scale distribution of 2,4-D and its degraders drives the fate of 2,4-D at the soil core scale. Soil Biol. Biochem. 88 (0), 90–100.

Pirt, S.J., 1975. Principles of Microbe and Cell Cultivation. Blackwell Scientific Publications, Oxford, UK (274 pp).

Rosenbom, A.E., Binning, P.J., Aamand, J., Dechesne, A., Smets, B.F., Johnsen, A.R., 2014. Does microbial centimeter-scale heterogeneity impact MCPA degradation in and leaching from a loamy agricultural soil? Sci. Total Environ. 472, 90–98.

Saxena, S., Boersma, L., Lindstrom, F., Young, J., 1974a. Effect of pore size on diffusion coefficients in porous media. Soil Sci. 117 (2), 80–86.

Saxena, S., Boersma, L., Lindstrom, F., Young, J., 1974b. The self-diffusion coefficients of 45CA and 2, 4 dichlorophenoxyacetic acid. Soil Sci. 117 (1), 14–20.

Shareef, K., Shaw, G., 2008. Sorption kinetics of 2,4-D and carbaryl in selected agricultural soils of northern Iraq: application of a dual-rate model. Chemosphere 72 (1), 8–15.

Shaw, L.J., Burns, R.G., 1998. Biodegradation of 2,4-D in a noncontaminated grassland soil profile. J. Environ. Qual. 27 (6), 1464–1471.

Sims, G.K., Radosevich, M., He, X.T., Traina, S.J., 1991. The effects of sorption on the bioavailability of pesticides. In: Betts, W.B. (Ed.), Biodegradation. Springer Series in Applied Biology, Springer London, pp. 119–137.

Soulas, G., Chaussod, R., Verguet, A., 1984. Chloroform fumigation technique as a means of determining the size of specialized soil microbial populations: application to pesticide-degrading microorganisms. Soil Biol. Biochem. 16 (5), 497–501.

Steefel, C.I., MacQuarrie, K.T.B., 1996. Approaches to modeling of reactive transport in porous media. Rev. Mineral. Geochem. 34 (1), 85–129.

Tarantola, A., 2004. Inverse Problem Theory and Methods for Model Parameter Estimation. SIAM Philadelphia (342 pp).

Tuxen, N., de Lipthay, J.R., Albrechtsen, H.-J., Aamand, J., Bjerg, P.L., 2002. Effect of exposure history on microbial herbicide degradation in an aerobic aquifer affected by a point source. Environ. Sci. Technol. 36 (10), 2205–2212.

Vieublé Gonod, L., 2002. Variabilité spatiale de la minéralisation de substrats carbonés (2,4-D, leucine, lysine) dans la matrice solide du sol, 1 vol. (viii-250 p.) pp.

Vieublé-Gonod, L., Benoit, P., Cohen, N., Houot, S., 2009. Spatial and temporal heterogeneity of soil microorganisms and isoproturon degrading activity in a tilled soil amended with urban waste composts. Soil Biol. Biochem. 41 (12), 2558–2567.

Villaverde, J., van Beinum, W., Beulke, S., Brown, C.D., 2009. The kinetics of sorption by retarded diffusion into soil aggregate pores. Environ. Sci. Technol. 43 (21), 8227–8232.
Vogel, L.E., Makowski, D., Garnier, P., Vieublé-Gonod, L., Coquet, Y., Raynaud, X., Nunan, N., Chenu, C., Falconer, R., Pot, V., 2015. Modeling the effect of soil meso- and macropores topology on the biodegradation of a soluble carbon substrate. Adv. Water Resour. 83, 123–136.
Walker, A., Brown, P.A., 1983. Spatial variability in herbicide degradation rates and residues in soil. Crop Prot. 2 (1), 17–25.
Wang, G., Or, D., 2014. Trophic interactions induce spatial self-organization of microbial consortia on rough surfaces. Sci. Rep. 4, 6757.
Willems, H.P.L., Lewis, K.J., Dyson, J.S., Lewis, F.J., 1996. Mineralization of 2,4-D and atrazine in the unsaturated zone of a sandy loam soil. Soil Biol. Biochem. 28 (8), 989–996.
Xia, X., Bollinger, J., Ogram, A., 1995. Molecular genetic analysis of the response of three soil microbial communities to the application of 2, 4-D. Mol. Ecol. 4 (1), 17–28.

3 Bilan

Nous avons calibré avec succès un modèle couplant diffusion, sorption et biodégradation d'un pesticide dans le sol à partir de la série d'expériences de laboratoire réalisée par Pinheiro *et al.* (2015). Les résultats de la calibration ainsi que de scénarios basés sur le modèle calibré ont notamment mis en évidence le rôle fondamental des conditions initiales dans la biodégradation du pesticide. Lorsque le pesticide et les dégradeurs sont au même emplacement au début de l'incubation, la minéralisation du pesticide est importante, pouvant atteindre un tiers de sa valeur maximale potentielle. La majorité de la dégradation prend alors place durant les premiers jours d'incubation, avant que le pesticide ne diffuse en dehors du hotspot bactérien. Lorsque les dégradeurs et le pesticide sont initialement séparés, ou lorsque le pesticide a diffusé en dehors du hotspot, la dégradation devient fortement limitée par la dilution et la sorption du pesticide dans le reste de le colonne de sol, ainsi que par la décroissance de la population bactérienne.

Dans cette étude, la capacité à décrire le processus de diffusion, centrale dans les chapitres précédents, apparaît donc moins importante que l'identification des conditions initiales. Parce que la dégradation ne prend place que lorsque le pesticide et les dégradeurs sont initialement au même endroit, nous proposons qu'une répartition hétérogène de microorganismes pourrait être couplée à un phénomène de transport intermittent comme l'advection. En effet, ce processus doit être suffisamment rapide pour contrer la dilution induite par la diffusion, mais aussi intermittent afin que le pesticide puisse demeurer suffisamment longtemps au contact des microorganismes pour pouvoir être dégradé.

Conclusion générale

Le transport d'un contaminant au sein du milieu souterrain résulte d'un couplage entre processus de transport et réactivité chimique ou biologique. Les modèles reposant sur une description détaillée de ce couplage se heurtent à difficultés de calibration dues à des données expérimentales très parcellaires. Dans cette thèse, nous avons suivi une approche alternative de modèles équivalents parcimonieux, simples à implémenter et calibrables de manière déterministe sur des données de terrain. Nous nous sommes intéressés aux milieux où le processus à l'origine de la dispersion est essentiellement diffusif, comme les sols ou les aquifères fracturés. La diffusion se prête en effet à une approche parcimonieuse, de part son effet homogénéisant qui réduit les gradients de concentration et efface en partie l'effet de l'hétérogénéité du milieu géologique. Nous nous sommes concentrés sur la possibilité d'utiliser des modèles calibrables à partir d'une donnée de temps de transit, comme la courbe de restitution d'un essai de traçage, comme proxy pour simuler du transport réactif. En effet, de tels modèles se sont révélés très efficaces pour des applications de transport conservatif et leur possible extension au transport réactif présente un intérêt certain.

Dans le Chapitre 2, nous avons comparé un modèle de référence, le modèle MINC (Multiple INteracting Continua (Pruess and Narasimhan 1985)), qui simule des échanges entre une porosité advective "mobile" et des inclusions diffusives "immobiles", au modèle simplifié équivalent MRMT (Multiple Rate Mass Transfer (Haggerty and Gorelick 1995)) pour du transport réactif. Le modèle MRMT représente les échanges mobile-immobiles par une distribution de coefficients d'échange calibrable sur la courbe de restitution d'un essai de traçage. L'équivalence entre MINC et MRMT est définie comme l'identité des concentrations d'un soluté conservatif dans la zone advective, et ainsi l'identité des courbes de restitution. Cette identité qui a été formellement démontrée par Haggerty and Gorelick (1995) n'assure pas la conservation de la distribution des concentrations immobiles. Nous avons cependant montré les modèles MINC et MRMT donnent des taux de réaction qui bien que différents restent très similaires (de Dreuzy et al. 2013). Cette proximité est due à la bonne estimation de la distribution des concentrations immobiles par MRMT, et notamment du second moment de cette distribution. Les déviations entre MINC et MRMT apparaissent principalement lorsque des gradients initiaux forts accentuent l'influence de la structure du domaine immobile. Dans certains cas, des "concentrations" MRMT négatives peuvent même apparaître, rappelant que ces "concentrations" sont avant tout un produit mathématique de la relation d'équivalence entre MINC et MRMT.

Dans le Chapitre 3, nous avons évalué la possibilité d'utiliser le modèle MRMT pour estimer l'effet sur la macrodispersion de structures immobiles plus complexes que celle, linéaire, de MINC. Ces structures peuvent être par exemple celles des bras morts d'un réseau de fractures ou d'une porosité de dissolution, présentant des boucles, des jonctions et des embranchements. Nous avons introduit le modèle SINC (Structured INteracting Contina) généralisant le modèle MINC à n'importe quelle organisation des zones immobiles entre elles et avec la zone mobile (Babey et al. 2015). SINC repose sur la description des échanges entre les différentes zones par une matrice d'interactions définissant un graphe. Nous avons démontré algébriquement qu'un modèle SINC, quelle que soit sa structure (i.e. quelle que soit l'organisation de ses zones immobiles), est formellement équivalent à un modèle MRMT unique (i.e. production des mêmes courbes de restitution). Ce modèle MRMT équivalent possède un nombre de taux d'échange égal au nombre de zones immobiles du modèle SINC de référence. De plus, dû à l'homogénéisation opérée par la diffusion, un petit nombre de taux d'échange peut concentrer la majorité de la porosité diffusive (e.g. 5 taux d'échange correspondant à plus de 95% de la porosité immobile). Nous avons donc développé des méthodes permettant d'identifier des modèles MRMT réduits, possédant un nombre limité de taux d'échange défini par l'utilisateur, à partir d'une donnée de temps de résidence. Nous avons montré que des modèles MRMT à 5 taux d'échange pouvaient reproduire la macro-dispersion d'un soluté avec une erreur de 0.1%. Ce résultat renforce l'intérêt de MRMT, même faiblement paramétré, comme modèle généraliste pour estimer des échanges mobile-immobiles.

Nous avons étudié dans le Chapitre 4 la possibilité d'utiliser une information de temps de transit, comme la courbe de restitution d'un essai de traçage, pour prédire du transport réactif dans des structures immobiles complexes (Babey et al. 2016). Nous avons utilisé le modèle SINC comme modèle de référence et MRMT comme modèle équivalent, exploitant les méthodes d'identification proposées dans le chapitre précédent. Nous avons montré que MRMT fournit de très bonnes estimations d'une réactivité hétérogène et non-linéaire pour une expérience de flush. Les taux de dissolution d'un minéral et de sorption dans SINC et MRMT diffèrent au maximum de 10%, et restent généralement inférieur à 1%. Ce résultat s'explique d'une part par la bonne représentation par MRMT des échanges mobile-immobile rapides par un grand nombre de taux d'échange, d'autre part par l'homogénéisation opérée aux temps longs par la diffusion dans les parties plus reculées de la structure immobile. La bonne estimation des distributions de concentration par MRMT suggère que son usage comme proxy pour du transport réactif resterait valide pour d'autres réactions que la dissolution/sorption

testées. De plus, comme dans le Chapitre 3, nous avons montré que des modèles MRMT simplifiés, ne possédant qu'un faible nombre de taux d'échange (< 5), donnent déjà de très bonnes estimations des taux de réaction. Comme dans le Chapitre 2, des gradients de concentration forts dans le domaine immobile soulignent l'effet de la structure et accentuent les différences entre SINC et MRMT. L'utilisation de MRMT comme proxy pour le transport réactif est donc conditionnée à des gradients de concentration dans le domaine immobile restant principalement contrôlés par les échanges mobile-immobile.

Dans le Chapitre 5, nous nous sommes éloignés des modèles mobile-immobiles pour nous concentrer sur le rôle des conditions initiales dans le couplage entre diffusion et réactivité biochimique (Babey et al. 2017). Nos travaux sont basés sur une série d'expériences de laboratoire réalisées par Pinheiro et al. (2015) où l'évolution d'un apport de pesticide (2,4-D) est suivie dans des colonnes de sol pour différentes distributions initiales de pesticide et de dégradeurs microbiens. Nous avons proposé et calibré un modèle de ces expériences couplant diffusion, sorption et biodégradation du pesticide. Nous montrons le rôle fondamental des conditions initiales dans la biodégradation du pesticide, celle-ci ne prenant place que lorsque le pesticide se trouve initialement dans le hotspot bactérien. Lorsque le pesticide et les dégradeurs sont séparés, la dilution induite par la diffusion favorise la sorption et limite la quantité de pesticide atteignant les dégradeurs. Pour cette problématique, la caractérisation du processus de diffusion qui était centrale dans les chapitres précédents apparaît moins importante que celle des conditions initiales et du processus amenant à ces conditions. Un tel processus pourrait être de l'advection intermittente. Dans ce cas, l'hétérogénéité spatiale de la distribution des dégradeurs microbiens serait couplée à une intermittence temporelle du processus de transport du pesticide.

Ces différents travaux offrent un certain nombre de perspectives. Un premier axe consisterait à approfondir la compréhension de la transition algébrique de SINC à MRMT. L'objectif serait d'une part de déterminer la relation entre les coefficients du MRMT et les structures de porosité, en faisant par exemple appel aux approches du domaine de l'identification des systèmes (Rapaport et al. 2016). L'identification du "sens physique" des paramètres MRMT permettrait de les détacher (au moins partiellement) des conditions de leur calibration, et irait ainsi dans le sens d'applications de terrain. Un autre objectif serait de déterminer l'origine de la conservation du second moment de la distribution des concentrations par la relation d'équivalence SINC-MRMT. Cette conservation a été observée dans toutes nos expériences

numériques quelle que soit l'organisation des zones immobiles dans SINC, mais sa justification analytique reste à apporter.

Un second axe de perspectives serait d'étendre les approches parcimonieuses développées ici pour du transport essentiellement diffusif à d'autre processus de transport, notamment l'advection. Il pourrait s'agir de considérer une porosité mobile plus complexe, constituée par exemple de plusieurs zones mobiles présentant une certaine structure. Là où la diffusion réduit la signature d'une structure immobile sur le transport conservatif et réactif à quelques temps d'échange caractéristiques, on peut s'attendre à ce qu'une structure advective possède une influence beaucoup plus prononcée mettant davantage au défi une approche parcimonieuse. Une autre piste serait l'extension de la dégradation des pesticides à des modèles de sol plus complexes plus proches des structures double porosité. Une telle extension pourrait être réalisée soit en intégrant une double porosité dans le modèle calibré dans le Chapitre 5, soit en utilisant ce modèle calibré comme une zone diffusive en interaction avec une zone advective additionnelle.

Enfin, un dernier axe serait le passage à une échelle plus large des approches développées dans cette thèse plutôt pour de la petite échelle (échelle du pore à celle du mètre). Il s'agirait d'une part d'interpréter ce qui peut constituer des zones immobiles, e.g. aquitards. D'autre part, d'autres types de données pourraient être utilisés comme les traceurs atmosphériques ou les ratios isotopiques. Ces derniers en particulier se révèlent prometteurs pour l'étude du transport réactif, car permettant de distinguer les variations de concentrations venant du mélange et de la réactivité.

Bibliographie

Altman, S. J., M. Uchida, V. C. Tidwell, C. M. Boney, and B. P. Chambers. 2004. Use of X-ray absorption imaging to examine heterogeneous diffusion in fractured crystalline rocks. Journal of Contaminant Hydrology **69**:1-26.

Anderson, M. P., and W. W. Woessner. 1990. Applied groundwater modeling: Simulation of Flow and Advective Transport. Academic Press.

Andersson, P., J. Byegard, E.-L. Tullborg, T. Doe, J. Hermanson, and A. Winberg. 2004. In situ tracer tests to determine retention properties of a block scale fracture network in granitic rock at the Aspo Hard Rock Laboratory, Sweden. Journal of Contaminant Hydrology **70**:271-297.

Arbogast, T., S. Bryant, C. Dawson, F. Saaf, C. Wang, and M. Wheeler. 1996. Computational methods for multiphase flow and reactive transport problems arising in subsurface contaminant remediation. Journal of Computational and Applied Mathematics **74**:19-32.

Arbogast, T., J. Douglas, and U. Hornung. 1990. Derivation of the double porosity model of single-phase flow via homogenization theory. Siam Journal on Mathematical Analysis **21**:823-836.

Babey, T., J.-R. de Dreuzy, and T. R. Ginn. 2016. From conservative to reactive transport under diffusion-controlled conditions. Water Resources Research **52**:3685-3700.

Babey, T., J. R. de Dreuzy, and C. Casenave. 2015. Multi-Rate Mass Transfer (MRMT) models for general diffusive porosity structures. Advances in Water Resources **76**:146-156.

Babey, T., L. Vieublé-Gonod, A. Rapaport, M. Pinheiro, P. Garnier, and J.-R. de Dreuzy. 2017. Spatiotemporal simulations of 2,4-D pesticide degradation by microorganisms in 3D soil-core experiments. Ecological Modelling **344**:48-61.

Ball, W. P., and P. V. Roberts. 1991. Long-term sorption of halogenated organic chemicals by aquifer material. 2. Intraparticle diffusion. Environmental Science & Technology **25**:1237-1249.

Barenblatt, G. I., I. P. Zheltov, and I. N. Kochina. 1960. Basic concept in the theory of seepage of homogeneous liquids in fissured rocks. J. Appl. Math. **24**:1286-1303.

Battiato, I., D. M. Tartakovsky, A. M. Tartakovsky, and T. D. Scheibe. 2011. Hybrid models of reactive transport in porous and fractured media. Advances in Water Resources **34**:1140-1150.

Bear, J. 1973. Dynamics of Fluids in Porous Media. Dover Publications.

Bear, J., C.-F. Tsang, and G. d. Marsily, editors. 1993. Flow and Contaminant Transport in Fractured Rock. Academic Press.

Benson, D. A., R. Schumer, M. M. Meerschaert, and S. W. Wheatcraft. 2001. Fractional dispersion, Lévy motion, and the MADE tracer test. Transport in Porous Media **42**:211-240.

Benson, D. A., S. W. Wheatcraft, and M. M. Meerschaert. 2000. Application of a fractional advection-dispersion equation. Water Resources Research **36**:1403-1412.

Berkowitz, B., A. Cortis, M. Dentz, and H. Scher. 2006. Modeling non-Fickian transport in geological formations as a continuous time random walk. Reviews of Geophysics **44**.

Berkowitz, B., and H. Scher. 1998. Theory of anomalous chemical transport in random fracture networks. Physical Review E **57**:5858-5869.

Berkowitz, B., H. Scher, and S. Silliman. 2000. Anomalous transport in laboratory-scale, heterogeneous porous media. Water Resources Research **36**.

Bethke, C. M., and T. M. Johnson. 2008. Groundwater age and groundwater age dating. Annual Review of Earth and Planetary Sciences **36**:121-152.

Bouchaud, J.-P., and A. Georges. 1990. Anomalous diffusion in disordered media: Statistical mechanisms, models and physical applications. Physics Reports **195**:127-293.

Briggs, M. A., F. D. Day-Lewis, J. P. Zarnetske, and J. W. Harvey. 2015. A physical explanation for the development of redox microzones in hyporheic flow. Geophysical Research Letters **42**:4402-4410.

Burns, D. A., J. J. McDonnell, R. P. Hooper, N. E. Peters, J. E. Freer, C. Kendall, and K. Beven. 2001. Quantifying contributions to storm runoff through end-member mixing analysis and hydrologic measurements at the Panola Mountain Research Watershed (Georgia, USA). Hydrological Processes **15**:1903-1924.

Carrera, J., X. Sánchez-Vila, I. Benet, A. Medina, G. Galarza, and J. Guimerà. 1998. On matrix diffusion: formulations, solution methods and qualitative effects. Hydrogeology Journal **6**:178-190.

Carrera, J., E. Vázquez-Suñé, O. Castillo, and X. Sánchez-Vila. 2004. A methodology to compute mixing ratios with uncertain end-members. Water Resources Research **40**:n/a-n/a.

Clauser, C. 1992. Permeability of crystalline rock. Eos Trans. AGU **73**:237-238.

Coats, K. H., and B. D. Smith. 1964. Dead-end pore volume and dispersion in porous media. Society of Petroleum Engineers Journal **4**:73-84.

Conca, L. J., and J. Wright. 2012. Diffusion And Flow In Gravel, Soil, And Whole Rock. Applied Hydrogeology **1**:5-24.

Crank, J. 2002. The mathematics of diffusion. Oxford University Press, Oxford.

Dagan, G. 1989. Flow and Transport in Porous Formations. Springer Verlag.

de Dreuzy, J. R., and J. Carrera. 2015. On the validity of effective formulations for transport through heterogeneous porous media. Hydrol. Earth Syst. Sci. Discuss. **12**:12281-12310.

de Dreuzy, J. R., A. Rapaport, T. Babey, and J. Harmand. 2013. Influence of porosity structures on mixing-induced reactivity at chemical equilibrium in mobile/immobile Multi-Rate Mass Transfer (MRMT) and Multiple INteracting Continua (MINC) models. Water Reosurces Research.

de Gennes, P. G. 1983. Hydrodynamic dispersion in unsaturated porous media. Journal of Fluid Mechanics **136**:189-200.

de Marsily, G., F. Delay, J. Gonçalvez, P. Renard, V. Teles, and S. Violette. 2005. Dealing with spatial heterogeneity. Hydrogeology Journal **13**:161-183.

de Marsily, G., J. P. Delhomme, F. Delay, and A. Buoro. 1999. 40 years of inverse problems in hydrogeology. Comptes Rendus De L Academie Des Sciences Serie Ii Fascicule a-Sciences De La Terre Et Des Planetes **329**:73-87.

de Simoni, M., J. Carrera, X. Sanchez-Vila, and A. Guadagnini. 2005. A procedure for the solution of multicomponent reactive transport problems. Water Resources Research **41**.

Dechesne, A., M. Owsianiak, A. Bazire, G. L. Grundmann, P. J. Binning, and B. F. Smets. 2010. Biodegradation in a Partially Saturated Sand Matrix: Compounding Effects of Water Content, Bacterial Spatial Distribution, and Motility. Environmental Science & Technology **44**:2386-2392.

Dentz, M., A. Cortis, H. Scher, and B. Berkowitz. 2004. Time behavior of solute transport in heterogeneous media: transition from anomalous to normal transport. Advances in Water Resources **27**:155-173.

Dietrich, P., R. Helmig, M. Sauter, H. Hötzl, J. Köngeter, and G. Teutsch. 2005. Flow and transport in fractured porous media. Springer Science & Business Media.

Doherty, J. 2003. Ground water model calibration using pilot points and regularization. Ground Water **41**:170-177.

Donado, L. D., X. Sanchez-Vila, M. Dentz, J. Carrera, and D. Bolster. 2009. Multicomponent reactive transport in multicontinuum media. Water Resources Research **45**.

Englert, A., S. S. Hubbard, K. H. Williams, L. Li, and C. I. Steefel. 2009. Feedbacks Between Hydrological Heterogeneity and Bioremediation Induced Biogeochemical Transformations. Environmental Science & Technology **43**:5197-5204.

Evans, C., and T. D. Davies. 1998. Causes of concentration/discharge hysteresis and its potential as a tool for analysis of episode hydrochemistry. Water Resources Research **34**:129-137.

Fetter, C. W. 2008. Contaminant Hydrogeology (2nd edition). Waveland Pr Inc, New York.

Flekkøy, E. G., A. Malthe-Sørenssen, and B. Jamtveit. 2002. Modeling hydrofracture. J. Geophys. Res. **107**:2151.

Freeze, A., and J. Cherry. 1979. Groundwater. Prentice Hall.

Freeze, R. A., J. Massmann, L. Smith, T. Sperling, and B. James. 1990. Hydrogeological Decision-Analysis .1. a Framework. Ground Water **28**:738-766.

Frippiat, C. C., and A. E. Holeyman. 2008. A comparative review of upscaling methods for solute transport in heterogeneous porous media. Journal of Hydrology **362**:150-176.

Gelhar, L. W., C. Welty, and K. R. Rhefeldt. 1992. A Critical Review of Data on Field-Scale Dispersion in Aquifers. Water Resources Research **28**:1955-1974.

Golfier, F., B. D. Wood, L. Orgogozo, M. Quintard, and M. Bues. 2009. Biofilms in porous media: Development of macroscopic transport equations via volume averaging with closure for local mass equilibrium conditions. Advances in Water Resources **32**:463-485.

Golfier, F., C. Zarcone, B. Bazin, R. Lenormand, D. Lasseux, and M. Quintard. 2002. On the ability of a Darcy-scale model to capture wormhole formation during the dissolution of a porous medium. Journal of Fluid Mechanics **457**:213-254.

Gonod, L. V., C. Chenu, and G. Soulas. 2003. Spatial variability of 2,4-dichlorophenoxyacetic acid (2,4-D) mineralisation potential at a millimetre scale in soil. Soil Biology and Biochemistry **35**:373-382.

Gonod, L. V., F. Martin-Laurent, and C. Chenu. 2006. 2,4-D impact on bacterial communities, and the activity and genetic potential of 2,4-D degrading communities in soil. FEMS Microbiology Ecology **58**:529-537.

Gouze, P., Y. Melean, T. Le Borgne, M. Dentz, and J. Carrera. 2008. Non-Fickian dispersion in porous media explained by heterogeneous microscale matrix diffusion. Water Resources Research **44**:19.

Grisak, G. E., and J. F. Pickens. 1980. Solute transport through fractured media .1. the effect of matrix diffusion. Water Resources Research **16**:719-730.

Grisak, G. E., J. F. Pickens, and J. A. Cherry. 1980. Solute transport through fractured media .2. Column study of fractured till. Water Resources Research **16**:731-739.

Haggerty, R. 2001. Matrix diffusion: Heavy-tailed residence time distributions and their influence on radionuclide retention. Radionuclide Retention in Geologic Media:81.

Haggerty, R., S. W. Fleming, L. C. Meigs, and S. A. McKenna. 2001. Tracer tests in a fractured dolomite 2. Analysis of mass transfer in single-well injection-withdrawal tests. Water Resources Research **37**.

Haggerty, R., and S. M. Gorelick. 1995. Multiple-rate mass transfer for modeling diffusion and surface reactions in media with pore-scale heterogeneity. Water Resources Research **31**:2383-2400.

Haggerty, R., C. F. Harvey, C. F. von Schwerin, and L. C. Meigs. 2004. What controls the apparent timescale of solute mass transfer in aquifers and soils? A comparison of experimental results. Water Resources Research **40**.

Harvey, C., and S. M. Gorelick. 2000. Rate-limited mass transfer or macrodispersion: Which dominates plume evolution at the Macrodispersion Experiment (MADE) site? Water Resources Research **36**:637.

Hay, M. B., D. L. Stoliker, J. A. Davis, and J. M. Zachara. 2011. Characterization of the intragranular water regime within subsurface sediments: Pore volume, surface area, and mass transfer limitations. Water Resources Research **47**:n/a-n/a.

Hem, J. D. 1985. Study and interpretation of the chemical characteristics of natural water. Department of the Interior, US Geological Survey.

Hill, M., and C. Tiedeman. 2006. Effective groundwater model calibration Wiley.

Hornung, U. 1997. Homogenization and Porous Media. Springer Science & Business Media.

Hsieh, P. A. 1998. Scale effects in fluid flow through fractured geological media. Pages 335-353 Scale dependence and scale invariance in hydrology. Cambridge University Press.

Hu, Q., and J. S. Y. Wang. 2003. Aqueous-Phase Diffusion in Unsaturated Geologic Media: A Review. Critical Reviews in Environmental Science and Technology **33**:275-297.

Hunt, A., and R. Ewing. 2009. Effects of Multi-Scale Heterogeneity. Pages 287-306 Percolation Theory for Flow in Porous Media.

Jardine, P. M., W. E. Sanford, J. P. Gwo, O. C. Reedy, D. S. Hicks, J. S. Riggs, and W. B. Bailey. 1999. Quantifying diffusive mass transfer in fractured shale bedrock. Water Resources Research **35**:2015-2030.

Johnson, N. M., G. E. Likens, F. H. Bormann, D. W. Fisher, and R. S. Pierce. 1969. A Working Model for the Variation in Stream Water Chemistry at the Hubbard Brook Experimental Forest, New Hampshire. Water Resources Research **5**:1353-1363.

Johnson, R. L., J. A. Cherry, and J. F. Pankow. 1989. Diffusive contaminant transport in natural clay: a field example and implications for clay-lined waste disposal sites. Environmental Science & Technology **23**:340-349.

Karimi-Fard, M., L. J. Durlofsky, and K. Aziz. 2003. An Efficient Discrete Fracture Model Applicable for General Purpose Reservoir Simulators. Society of Petroleum Engineers.

Karimi-Fard, M., B. Gong, and L. J. Durlofsky. 2006. Generation of coarse-scale continuum flow models from detailed fracture characterizations. Water Resources Research **42**.

Knorr, B., P. Maloszewski, F. Krämer, and C. Stumpp. 2016. Diffusive mass exchange of non-reactive substances in dual-porosity porous systems – column experiments under saturated conditions. Hydrological Processes **30**:914-926.

Le Borgne, T., and P. Gouze. 2008. Non-Fickian dispersion in porous media: 2. Model validation from measurements at different scales. Water Resources Research **44**.

Levy, M., and B. Berkowitz. 2003. Measurement and analysis of non-Fickian dispersion in heterogeneous porous media. Journal of Contaminant Hydrology **64**:203-226.

Li, L., C. A. Peters, and M. A. Celia. 2007. Effects of mineral spatial distribution on reaction rates in porous media. Water Resources Research **43**.

Luquot, L., O. Rodriguez, and P. Gouze. 2014. Experimental Characterization of Porosity Structure and Transport Property Changes in Limestone Undergoing Different Dissolution Regimes. Transport in Porous Media **101**:507-532.

Magnico, P., C. Leroy, J. P. Bouchaud, C. Gauthier, and J. P. Hulin. 1993. Tracer dispersion in porous media with a double porosity. Physics of Fluids A: Fluid Dynamics **5**:46-57.

Maloszewski, P., and A. Zuber. 1985. On the theory of tracer experiments in fissured rocks with a porous matrix. Journal of Hydrology **79**:333-358.

Margolin, G., M. Dentz, and B. Berkowitz. 2003. Continuous time random walk and multirate mass transfer modeling of sorption. Chemical Physics **295**:71-80.

McKenna, S. A., L. C. Meigs, and R. Haggerty. 2001. Tracer tests in a fractured dolomite 3. Double-porosity, multiple-rate mass transfer processes in convergent flow tracer tests. Water Resources Research **37**.

McLaughlin, D., and L. R. Townley. 1996. A reassessment of the groundwater inverse problem. Water Resources Research **32**.

Meigs, L. C., and R. L. Beauheim. 2001. Tracer tests in a fractured dolomite 1. Experimental design and observed tracer recoveries. Water Resources Research **37**.

Miller, C. T., and W. G. Gray. 2002. Hydrogeological research: Just getting started. Ground Water **40**:224-231.

Molson, J., M. Aubertin, and B. Bussière. 2012. Reactive transport modelling of acid mine drainage within discretely fractured porous media: Plume evolution from a surface source zone. Environmental Modelling & Software **38**:259-270.

Murphy, E. M., T. R. Ginn, A. Chilakapati, C. T. Resch, J. L. Phillips, T. W. Wietsma, and C. M. Spadoni. 1997. The influence of physical heterogeneity on microbial degradation and distribution in porous media. Water Resources Research **33**:1087-1103.

Neretnieks, I. 1980. Diffusion in the Rock Matrix: An Important Factor in Radionucleside Retardation? Journal of Geophysical Research **85**:4379-4397.

Neuman, S. P., and D. M. Tartakovsky. 2009. Perspective on theories of non-Fickian transport in heterogeneous media. Advances in Water Resources **32**:670-680.

Noetinger, B., and G. Zargar. 2004. Multiscale description and upscaling of fluid flow in subsurface reservoirs. Oil & Gas Science and Technology-Revue De L Institut Francais Du Petrole **59**:119-139.

Nye, P. H. 1980. Diffusion of Ions and Uncharged Solutes in Soils and Soil Clays. Pages 225-272 *in* N. C. Brady, editor. Advances in Agronomy. Academic Press.

Or, D., B. F. Smets, J. M. Wraith, A. Dechesne, and S. P. Friedman. 2007. Physical constraints affecting bacterial habitats and activity in unsaturated porous media – a review. Advances in Water Resources **30**:1505-1527.

Orgogozo, L., F. Golfier, M. A. Bues, M. Quintard, and T. Kone. 2013. A dual-porosity theory for solute transport in biofilm-coated porous media. Advances in Water Resources **62**:266-279.

Pinder, G. F., and M. A. Celia. 2006. Subsurface Hydrology. Wiley.

Pinheiro, M., P. Garnier, J. Beguet, F. Martin Laurent, and L. Vieublé Gonod. 2015. The millimetre-scale distribution of 2,4-D and its degraders drives the fate of 2,4-D at the soil core scale. Soil Biology and Biochemistry **88**:90-100.

Pruess, K. 1992. Brief Guide to the MINC - Method for Modeling Flow and Transport in Fractured Media. Earth Sciences Division, Lawrence Berkeley National Laboratory. Berkeley CA USA.

Pruess, K., and T. N. Narasimhan. 1985. A practical method for modeling fluid and heat-flow in fractured porous-media. Society of Petroleum Engineers Journal **25**:14-26.

Quintard, M., and S. Whitaker. 1993. Transport in ordered and disordered porous-media - volume-averaged equations, closure problems, and comparison with experiment. Chemical Engineering Science **48**:2537-2564.

Rao, P. S. C., D. E. Rolston, R. E. Jessup, and J. M. Davidson. 1980. Solute transport in aggregated porous-media - theoretical and experimental evaluation. Soil Science Society of America Journal **44**:1139-1146.

Rapaport, A., A. Rojas-Palma, J.-R. De Dreuzy, and H. Ramirez. 2016. Equivalence of finite dimensional input-output models of solute transport and diffusion in geosciences. arXiv preprint arXiv:1606.06438.

Refsgaard, J. C., A. L. Hojberg, I. Moller, M. Hansen, and V. Sondergaard. 2010. Groundwater Modeling in Integrated Water Resources Management-Visions for 2020. Ground Water **48**:633-648.

Rehfeldt, K. R., J. M. Boggs, and L. W. Gelhar. 1992. Field study of dispersion in a heterogeneous aquifer, 3, geostatistical analysis of hydraulic conductivity. Water Resources Research **28**.

Renard, P., and G. de Marsily. 1997. Calculating equivalent permeability: a review. Advances in Water Resources **20**:253-278.

Roubinet, D., and D. M. Tartakovsky. 2013. Hybrid modeling of heterogeneous geochemical reactions in fractured porous media. Water Resources Research **49**:7945-7956.

Rubin, J. 1983. Transport of reacting solutes in porous-media - relation between mathematical nature of problem formulation and chemical nature of reactions. Water Resources Research **19**:1231-1252.

Sawyer, A. H. 2015. Enhanced removal of groundwater-borne nitrate in heterogeneous aquatic sediments. Geophysical Research Letters **42**:403-410.

Scheibe, T. D., Z. Hou, B. J. Palmer, and A. M. Tartakovsky. 2013. Pore-scale simulation of intragranular diffusion: Effects of incomplete mixing on macroscopic manifestations. Water Resources Research **49**:4277-4294.

Scholl, M. A. 2000. Effects of heterogeneity in aquifer permeability and biomass on biodegradation rate calculations - Results from numerical simulations. Ground Water **38**:702-712.

Shapiro, A. M. 2001. Effective matrix diffusion in kilometer-scale transport in fractured crystalline rock. Water Resources Research **37**.

Soler-Sagarra, J., L. Luquot, L. Martínez-Pérez, M. W. Saaltink, F. De Gaspari, and J. Carrera. 2016. Simulation of chemical reaction localization using a multi-porosity reactive transport approach. International Journal of Greenhouse Gas Control **48, Part 1**:59-68.

Sornette, A., P. Davy, and D. Sornette. 1993. Fault Growth in Brittle-Ductile Experiments and the Mechanics of Continental Collisions. Journal of Geophysical Research-Solid Earth **98**:12111-12139.

Sposito, G. 2008. Scale dependence and scale invariance in hydrology. Cambridge University Press.

Steefel, C. I., and P. C. Lichtner. 1994. Diffusion and reaction in rock matrix bordering a hyperalkaline fluid-filled fracture. Geochimica et Cosmochimica Acta **58**:3595-3612.

Sudicky, E. A., and E. O. Frind. 1982. Contaminant transport in fractured porous-media - analytical solutions for a system of parallel fractures. Water Resources Research **18**:1634-1642.

Tang, D. H., E. O. Frind, and E. A. Sudicky. 1981. Contaminant transport in fractured porous-media - analytical solution for a single fracture. Water Resources Research **17**:555-564.

Tonkin, M., J. Doherty, and C. Moore. 2007. Efficient nonlinear predictive error variance for highly parameterized models. Water Resources Research **43**.

van Genuchten, M. T., and P. J. Wierenga. 1977. Mass Transfer Studies in Sorbing Porous Media: II. Experimental Evaluation with Tritium (3H2O)1. Soil Science Society of America Journal **41**:272-278.

Villermaux, J. 1987. Chemical-engineering approach to dynamic modeling of linear chromatography - a flexible method for representing complex phenomena from simple concepts. Journal of Chromatography **406**:11-26.

Vogel, L. E., D. Makowski, P. Garnier, L. Vieublé-Gonod, Y. Coquet, X. Raynaud, N. Nunan, C. Chenu, R. Falconer, and V. Pot. 2015. Modeling the effect of soil meso-

and macropores topology on the biodegradation of a soluble carbon substrate. Advances in Water Resources **83**:123-136.

Warren, J. E., and P. J. Root. 1963. The Behavior of Naturally Fractured Reservoirs. Society of Petroleum Engineers Journal **3**:245-255.

Willmann, M., J. Carrera, X. Sanchez-Vila, O. Silva, and M. Dentz. 2010. Coupling of mass transfer and reactive transport for nonlinear reactions in heterogeneous media. Water Resources Research **46**:15.

Wood, B. D. B. D., M. Quintard, and S. Whitaker. 2004. Estimation of adsorption rate coefficients based on the Smoluchowski equation. Chemical Engineering Science **59**:1905-1921.

Wood, W. W., T. F. Kraemer, and P. P. Hearn. 1990. Intragranular Diffusion: An Important Mechanism Influencing Solute Transport in Clastic Aquifers? Science **247**:1569-1572.

Wu, S. C., and P. M. Gschwend. 1986. Sorption kinetics of hydrophobic organic-compounds to natural sediments and soils. Environmental Science & Technology **20**:717-725.

Wu, W. M., J. Carley, M. Fienen, T. Mehlhorn, K. Lowe, J. Nyman, J. Luo, M. E. Gentile, R. Rajan, D. Wagner, R. F. Hickey, B. H. Gu, D. Watson, O. A. Cirpka, P. K. Kitanidis, P. M. Jardine, and C. S. Criddle. 2006a. Pilot-scale in situ bioremediation of uranium in a highly contaminated aquifer. 1. Conditioning of a treatment zone. Environmental Science & Technology **40**:3978-3985.

Wu, W. M., J. Carley, T. Gentry, M. A. Ginder-Vogel, M. Fienen, T. Mehlhorn, H. Yan, S. Caroll, M. N. Pace, J. Nyman, J. Luo, M. E. Gentile, M. W. Fields, R. F. Hickey, B. H. Gu, D. Watson, O. A. Cirpka, J. Z. Zhou, S. Fendorf, P. K. Kitanidis, P. M. Jardine, and C. S. Criddle. 2006b. Pilot-scale in situ bioremedation of uranium in a highly contaminated aquifer. 2. Reduction of U(VI) and geochemical control of U(VI) bioavailability. Environmental Science & Technology **40**:3986-3995.

Wu, Y. S., H. H. Liu, and G. S. Bodvarsson. 2004. A triple-continuum approach for modeling flow and transport processes in fractured rock. Journal of Contaminant Hydrology **73**:145-179.

Zheng, C., and G. D. Bennett. 2002. Applied contaminant transport modeling, 2nd edition. Wiley Interscience.

Zimmerman, D. A., G. d. Marsily, C. A. Gotway, M. G. Marietta, C. L. Axness, R. L. Beauheim, R. L. Bras, J. Carrera, G. Dagan, P. B. Davies, D. P. Gallegos, A. Galli, J. Gomex-Hernandez, P. Gringrod, A. L. Gutjahr, P. K. Kitanidis, A. M. Lavenue, D. McLaughlin, S. P. Neuman, B. S. Ramarao, C. Ravenne, and Y. Rubin. 1998. A comparison of seven geostatistically based inverse approaches to estimate transmissivities for modeling advective transport by groundwater flow. Water Resources Research **34**:1373-1413.

Zinn, B., L. C. Meigs, C. F. Harvey, R. Haggerty, W. J. Peplinski, and C. F. Von Schwerin. 2004. Experimental visualization of solute transport and mass transfer processes in two-dimensional conductivity fields with connected regions of high conductivity. Environmental Science & Technology **38**:3916-3926.